

Quantum manipulation of a single trapped molecular ion

Inauguraldissertation

zur

Erlangung der Würde eines Doktors der Philosophie

vorgelegt der

Philosophisch-Naturwissenschaftlichen Fakultät

der Universität Basel

von

Kaveh Najafian

2021

Originaldokument gespeichert auf dem Dokumentenserver der
Universität Basel edoc.unibas.ch

This work is licensed under a Creative Commons
Attribution-NonCommercial 4.0 International License.



Genehmigt von der Philosophisch-Naturwissenschaftlichen Fakultät

auf Antrag von

Prof. Dr. Stefan Willitsch, Prof. Dr. Anatole von Lilienfeld und
Prof. Dr. Michael Drewsen

Basel, 15.12.2020

Prof. Dr. Martin Spiess

Abstract

The controlled manipulation of quantum states of single trapped atomic ions forms the basis of some of the most precise measurements performed to date with proven applications in fundamental physics, time keeping and quantum computing. In this thesis, we extend the toolbox of coherent manipulation of single trapped ions to molecular ions with potential applications including measuring a possible time variation of the proton-to-electron mass ratio, m_p/m_e , the implementation of new frequency standards in the mid-infrared regime and the realization of noise-insensitive qubits. We describe in detail the theoretical modeling of molecular energy levels, systematic shifts and transition strengths for the identification of molecular transitions which are useful as a new clock standard and as a molecular qubit. The homonuclear diatomic molecule N_2^+ is found to form a noise-insensitive system with clock transitions suitable for precision measurements over a wide range of frequencies. We further describe the experimental implementation of a single-molecule trapped-ion experiment for precision measurements including the design, manufacturing and characterization of a new ion trap and the electronic circuits required for stable operation. We describe several techniques used for laser stabilization and present the techniques developed for cooling the molecular ion from an initial temperature of over 1000 K to the motional ground state of the trap below 10 μ K. A new state readout technique is presented which relies on phase-sensitive forces to non-destructively read out and prepare the internal state of the molecule from a large number of possible states. The demonstration of state readout and state preparation of a single ground-state-cooled N_2^+ ion signifies the successful implementation of all necessary prerequisites for precision measurements and coherent manipulations of single molecular ions.

Contents

1	Introduction	1
2	Qubits and Clock Transitions in a Homonuclear Diatomic Molecule	9
2.1	Energy levels of a diatomic molecule	11
2.1.1	The molecular Hamiltonian	11
2.1.2	The effective Hamiltonian	18
	The vibrational Hamiltonian	18
	The rotational Hamiltonian	20
	The rovibrational interaction	20
	The spin-rotation Hamiltonian	24
	The hyperfine Hamiltonian	25
2.1.3	Interaction with external fields	28
	On the signs of the Zeeman interaction	29
	The g-tensor	32
	The electron spin Zeeman interaction	32
	The rotational Zeeman interaction	37
	The nuclear spin Zeeman interaction	39
	The anisotropic electron spin Zeeman interaction	40
2.1.4	Numerical evaluation of the effective Hamiltonian	46
2.1.5	Magic clock transitions and state mixing	48
2.2	The theory of dipole-forbidden transitions	53
2.2.1	Transition moments and Rabi frequencies	53
2.2.2	Magnetic dipole transitions and matrix elements	56
2.2.3	Electric quadrupole transitions and matrix elements	57
2.2.4	Vibrational transition moments	58
2.3	Clock transitions and qubits in N_2^+	62
2.3.1	Zeeman transitions, $\Delta M_F = \pm 1$	62

2.3.2	Hyperfine transitions, $\Delta F = \pm 1$	64
2.3.3	Fine structure transitions, $\Delta J = \pm 1$	65
2.3.4	Rotational transitions, $\Delta N = \pm 2$	68
2.3.5	Vibrational transitions, $\Delta v = 1$	70
2.4	Systematic shifts and uncertainties	73
2.4.1	Residual Zeeman shift	73
2.4.2	Ac-Stark shifts	74
2.4.3	Electric quadrupole shifts	76
2.4.4	Statistical uncertainty	79
2.5	Summary	80
3	Building a Molecular Clock Experiment for N_2^+	83
3.1	A new trap for single molecule manipulations	84
3.1.1	The linear Paul trap	85
	The secular motion	85
	The micromotion	86
3.1.2	Axial RF gradients	88
3.1.3	Trap design	91
	Electrode radius	91
	Compensation electrodes	93
3.1.4	Trap manufacturing	95
3.2	Trap electronics	97
3.2.1	Helical resonator design and characterisation	98
3.2.2	Trap voltage supply	100
3.2.3	Axial micromotion compensation circuit	101
3.3	Laser stabilisation for precision spectroscopy	103
3.3.1	Pound-Drever-Hall locking to a cavity	106
3.3.2	Linewidth characterisation using the in-loop error signal	110
3.3.3	The frequency comb	112
3.3.4	Locking and characterising a QCL using a gas cell	116
3.3.5	Single-laser Raman transitions	118
3.4	Experiment peripherals	121
3.4.1	Control electronics	121
3.4.2	Chamber layout	122
3.4.3	Magnetic field coils	123
3.5	Summary	124

4	Motional State Dynamics of N_2^+ in an Ion Trap	127
4.1	From ionization to the Doppler limit	128
4.2	Reduction of Ca^+ from the trap	129
4.2.1	Characterizing ion decay	131
4.2.2	Heating mechanism	133
4.3	Sympathetic sideband cooling	136
4.3.1	The N_2^+ motional modes	136
4.3.2	Sideband-cooling sequence	137
4.3.3	Heating rates	140
4.3.4	Coherence times	140
4.4	Summary	144
5	Non-destructive Molecular State Detection	145
5.1	The optical lattice	147
5.2	The ac-Stark shift	149
5.2.1	Ac-Stark shift of N_2^+	149
5.2.2	Ac-Stark shift of Ca^+	153
5.3	Motional excitation by the optical lattice	157
5.3.1	Numerical simulation of the motional excitation	158
5.3.2	'Quantum simulation' using N_2H^+	161
5.3.3	Example signal	165
5.4	Single-molecule experiments	168
5.4.1	Identifying molecular states	168
5.4.2	State preparation	169
5.4.3	Molecular dipole-allowed spectroscopy	172
5.4.4	Tracing reactions and inelastic scattering events	173
5.4.5	Partial state readout	175
5.5	Summary	178
6	Conclusions and Outlook	179
A	Standard Results from Spherical Tensor Algebra	183
B	Alternative Derivations of Matrix Expressions	187
B.1	The spin-Zeeman interaction in Hund's case (a).	187
B.2	The spin-Zeeman interaction in a case (b) \rightarrow (a) transformation	189
B.3	The rotational Zeeman interaction in the uncoupled basis	192
B.4	The anisotropic spin-Zeeman Hamiltonian in Hund's case (a)	196

B.5	The E1 operator in a combined Hund's case (<i>a</i>) and (<i>b</i>) basis.	197
C	Table of Magic Transitions	201
D	Sideband Cooling Simulations	205
	Bibliography	209

Introduction

1

” *If you’re teaching today what you were teaching five years ago, either the field is dead or you are.*

— **Noam Chomsky**
about the field of linguistics

At the heart of the scientific endeavour lies the search for scientific truths about the nature of our universe. In the natural sciences these truths take the form of mathematical models which can be used to describe and predict measurable natural phenomena. As what is measurable is constantly advancing, so are the scientific models and hence the truths which are deduced from them. The extension of measurements into new frontiers of the natural world is therefore a pursuit that can both strengthen, expand and overturn existing models. Scientific truth, as defined by an empiricist epistemic view, is therefore the models which currently best describe observations about the natural world, reflecting a humility toward our understanding which does not impose upon the universe an absolute, unchanging truth.

The physical laws of our universe, just like our understanding thereof, may themselves be subject to change, over vast distances or time spans, between the microscopic and the macroscopic [1]. A great effort is therefore undertaken in several branches of physics to establish the universality of our physical laws and the fundamental constants which quantify them. In the field of astrophysics, the time and space variation of physical law can be tested under vastly different conditions, varying several billion years in time and billions of light years in space, as the radiation reaching us now from the (metaphorical) corners of the universe reflect the conditions of the early universe and the present, all at once. As an alternative approach, the extension of measurements into new frontiers of physics

may be preformed in a laboratory environment, under well controlled conditions, free from external interference [2]. This approach benefits from an increased precision in the measurement, although within a more constrained region of time and space.

The four, currently well established, fundamental forces of the universe are, the 'electromagnetic interaction' which enables light and holds together atoms and molecules, the 'weak interaction' which is responsible for radioactive decay of atomic nuclei, the 'strong interaction' which binds together quarks to form nucleons and also binds nucleons to form atomic nuclei and 'gravity' which makes it difficult to get out of bed in the morning. As our everyday domain of the universe is well described by these four forces, to reach into new frontiers of physics requires increasingly extreme conditions. Dark matter is observed at galactic scales, supersymmetry is probed at energies comparable to the young universe fractions of a second after the big bang and drifting fundamental constants are sought in the high precision measurements that can only be reached with temperatures close to absolute zero [2, 3].

Of the four fundamental forces, the electromagnetic force is the most readily controllable. Our understanding of the remaining three fundamental forces is intimately linked to the interaction of matter with electromagnetic fields, whether it is the detection of gravitational waves by the enormous laser interferometer, LIGO [4], or the discovery of the Higgs particle in the calorimeters of the Large Hadron Collider (LHC) at CERN [5, 6]. Spectroscopy, i.e. the study of the interaction between matter and electromagnetic radiation, has provided us a window into the inner workings of the universe, in fields ranging from astronomy and atmospheric science to biology and medicine.

A major milestone is reached in the field of spectroscopy when we are able to isolate single atoms, molecules or subatomic particles and manipulate them with a high level of control. Such a system allows for long interrogation times and is free from collisions and ensemble interactions. It is also more easily cooled to temperatures close to absolute zero to further reduce uncertainties associated with the motion of particles. Single trapped atomic ions have been utilized with tremendous success in the past 20 years, for a vast array of experiments in fundamental and applied physics.

Currently, the precision of spectroscopic experiments on single trapped atomic ions have reached a relative uncertainty of 10^{-19} in the transition frequency between two energy levels [7, 8], corresponding to a number with 18 significant digits after the decimal point. In comparison, 18 decimals in the number π , i.e. $\pi \approx 3.141592653589793238$, would allow determination of the circumference of a sphere the size of earth to an error smaller than the size of a single hydrogen atom. With such a precision, these systems are suitable for putting new limits on the existence of higher dimensions, fifth fundamental forces as well as searches for dark matter and drifting fundamental constants [9, 10, 11]. This well-controlled model system may also serve as a stable time reference [12] to which other experiments are compared and may therefore aid in the discovery of new phenomena in other fields of science.

Measuring time requires a stable oscillating process¹, relatively insensitive to outside interference, which can be counted and thus forms a clock. The natural oscillation frequencies of a quantum particle, such as the frequency difference between two energy levels in an atom, can therefore be used as a stable time reference. Used as a clock, the atomic system mentioned above shows an error of less than 1 second every 30 billion years, twice the current estimate of the age of the universe. Historically, there exists a close relationship between scientific discoveries in physics and advances in time keeping whereby many discoveries can be attributed to improvements in clocks [13]. The technique of very-long-baseline interferometry (VLBI), which was recently employed to photograph a black hole [14], relies on extremely precise clocks to function.

The precise control of single quantum particles is also one of the most successful platforms for quantum computers [15, 16, 17], a new information processor which utilizes quantum effects, such as entanglement and superposition, to speed up certain calculations that are beyond the abilities of classical computers [18]. Such a device is also suitable for simulating large quantum systems such as molecules in what is typically termed a quantum simulator [19]. The folding of proteins into their lowest energy configuration has been a long standing problem in the field of biochemistry, which is not easily predicted on a classical computer, and would greatly benefit from quantum simulation [20]. The basic building

¹Non-oscillatory processes such as the decay of radioactive particles may also be used as a measure of time, as e.g. in carbon dating.

block of the quantum computer is the qubit, a quantum mechanical analogue of the classical bit. These building blocks benefit from the increased control and precise manipulation of single isolated particles in a well controlled environment.

It is no surprise then that single trapped atomic ions constitute one of the most promising platforms for pushing the boundaries of fundamental and applied physics. The essential building blocks of such an experiment are,

- State initialization: The production of the single trapped particle into a specific internal state which is a suitable starting point for the experiment.
- Cooling: The reduction of the kinetic energy of the particle to reduce Doppler broadening and other systematic shifts in the measurement.
- State manipulation: The manipulation of internal states of the particle using a well defined electromagnetic field produced by a stable oscillator. Alternatively, as in the case of a chemical reaction experiment, state changes can be induced by collisions.
- State detection: The readout of the internal state of the trapped particle to determine the success or failure of the state manipulation pulse.

By extending the field of molecular spectroscopy into the domain of single trapped molecular ions, similar advances are expected as those achieved by single-atom experiments [21, 22, 23, 24, 25]. The most precise spectroscopy on molecular ions is currently behind their atomic counterparts by several orders of magnitude [26]. This reflects the challenge posed by the complex system of energies, which includes vibrations and rotations and makes all the building blocks listed above, except perhaps the state manipulation, more challenging in the molecule than in the atom. Many widely spaced energy levels can be populated and thus, apart from a few special cases [27, 28, 29], the laser cooling of molecular ions is not feasible. Molecular state detection and initialization into a specific state is also challenging for the same reason. Nevertheless, these experimental challenges may be overcome and the potential benefits of using molecular ions as probes of fundamental physics, qubits and clocks are many [30, 31].

The molecular energies are more sensitive than their atomic counterparts to certain fundamental physical constants and can therefore be used to measure these constants to a better precision given a similar spectroscopic uncertainty [32, 33]. One such constant is the ratio of masses between the proton and the electron $\mu_m = m_p/m_e \approx 1836$. The mass of the proton originates mainly from the binding energy of the quarks and therefore, according to extensions of the standard model and general relativity, this mass ratio may change over time [2]. The atomic energies show a low sensitivity to the masses of the subatomic particles as the electromagnetic interaction between charges dominate the energy splitting in these systems [13]. The molecular rotational and vibrational energies, however, depend on the molecular moments of inertia and vibrational frequencies, respectively, which depend on the mass of the nuclei and therefore the transition frequencies are several orders of magnitude more sensitive to μ_m than atomic transitions [32, 34, 33, 35, 36].

The time variation of the proton-to-electron mass ratio has been constrained by comparing several lines with different sensitivity to μ_m in the absorption spectra of methanol from distant quasars, with a look-back time of ~ 7.5 billion years. This study did not find a significant temporal variation of μ_m up to $\dot{\mu}_m/\mu_m < 10^{-17}$ per year² [37]. By comparing the frequency ratio of two transitions in Yb^+ ions in the laboratory, the time variation was limited to $\dot{\mu}_m/\mu_m < 10^{-16} \text{ yr}^{-1}$ using a single trapped atomic ion [9]. The current limit from laboratory measurements of trapped molecules comes from comparing the frequencies of a SF_6 molecular clock to an atomic clock with a resulting temporal constraint of $\dot{\mu}_m/\mu_m < 10^{-14} \text{ yr}^{-1}$ [38].

The complexity of molecular energies means that suitable transitions can be found in a broad range of frequencies ranging from 1 MHz to 100's of THz which are extra insensitive to experimental noise. These transitions, termed clock transitions after their suitability for time keeping, have therefore been proposed as new frequency standards [39, 40, 21] and as stable qubit states [41].

The goal of this thesis is therefore the determination of the usefulness of a single molecular ion for the purposes detailed above. We wish to

²Assuming a linear time variation.

determine the utility of the molecular energy levels for precision measurements, with the purpose of finding drifting fundamental constants, as a clock standard and as a molecular qubit. We also wish to establish the difficulty in the implementation of such an experiment in order to assess whether such an experiment is feasible and worthwhile. All of the necessary building blocks will be implemented in order to establish, experimentally, which part of the system needs to be improved in order to reach the ultimate goal of an experiment with full control over a single molecule.

The thesis is structured as follows. In Chapter 2, we shall treat the full complexity of the molecule theoretically, to the best of our abilities, not as a hindrance but an opportunity to implement a stable and versatile experiment for precision measurements. After briefly reviewing the molecular Hamiltonian and the approximations which enable its calculation, we proceed to define the effective Hamiltonian for our model system, N_2^+ . Several terms of the Hamiltonian are derived explicitly, particularly for describing the interaction of the molecule with external magnetic fields. By solving this Hamiltonian numerically we obtain the energies of the molecular levels. We shall also treat the theory of transitions between these levels in the same formalism that was used to obtain the energies. Armed with this theory, we can then proceed to explore the landscape of transitions in the molecule and present the benefits and drawbacks of each class of transitions, rotational, vibrational, hyperfine and Zeeman transitions, for precision measurements and as qubit states. Finally we consider additional systematic and statistical uncertainties in the molecule which may limit the attainable precision under realistic experimental conditions. We shall see that the homonuclear diatomic molecule serves as a stable and versatile system suitable for precision measurements and as qubit states with a relatively modest experimental overhead.

In Chapter 3, we describe the implementation of such an experiment for a single N_2^+ ion co-trapped with a single laser cooled Ca^+ ion for sympathetic cooling of its kinetic energy and detection of its internal state. We begin with the description of the ion trap and the design of a new trap focusing on a low heating rate to allow long probe times. The electronics that were built for stable trap operation are then described. We proceed to describe some techniques that may be used for stabilizing a molecular

probe laser for precision measurements. This chapter ends with a short description of additional parts of the experiment.

The first results from the implementation of the single $\text{Ca}^+ - \text{N}_2^+$ experiment are presented in Chapter 4, where we describe the techniques for cooling the initial energy of the molecule from 1000 K to close to absolute zero near $10 \mu\text{K}$ in several stages. The initial cooling from ionization temperatures to a few mK is achieved through sympathetic cooling using several laser cooled co-trapped Ca^+ . The technique that was developed for reducing the number of Ca^+ to a single one is then presented. Finally we describe the resolved sideband cooling of the motional mode of both ions to the ground state of the trap and characterize the heating rates and coherence times of the system.

In Chapter 5 we describe the state readout technique that was developed to determine the internal state of the molecule without losing the state. This technique relies on entanglement of the internal molecular state with the motional modes of the $\text{Ca}^+ - \text{N}_2^+$ string. Although such schemes have been previously proposed and implemented, we describe and implement a version of this scheme which is especially suitable for the detection of quantum states in the complex landscape of molecular energy levels. We first theoretically determine the ac-Stark shift that both atomic and molecular ions are subjected to from the state-readout laser. We then simulate the effect of this shift on the motional modes of the two-ion string by a classical numerical simulation as well as a quantum simulation using N_2H^+ . Finally we present the results of several experiments performed on a single N_2^+ ion. We determine the initial rovibrational states after ionization, perform nondestructive spectroscopy on a dipole allowed transition and present a simplified method to determine the internal state of a molecule with a limited knowledge of the transition strengths.

Some concluding remarks and a future outlook are presented in Chapter 6.

Qubits and Clock Transitions in a Homonuclear Diatomic Molecule

“ *It's not rocket science. Well, it is rocket science but you'll get the hang of it.* ”

— **Stefan Willitsch**
first meeting with a new PhD student

In this chapter we develop the theory of energy levels, transition strengths and systematic shifts of a diatomic molecule in the presence of a magnetic field. We are interested in the behaviour of a single, trapped molecule in a vacuum environment, practically free from collisions. The state dynamics are thus only due to interactions with electromagnetic fields. We shall estimate the limiting uncertainties of the molecular transition frequencies and assess the usefulness of these transitions for testing fundamental physics and as a molecular clock. We shall also consider the stability of these transitions as noise-insensitive qubit states.

There is extensive literature on the subject of energy states and transitions in diatomic molecules. The theoretical foundation of this chapter is based on *Brown & Carrington* [42] with complementary works on the theory of spherical tensor algebra by *R. Zare* [43] and the theory of forbidden transitions by *D. Papoušek* [44]. Other great works include Refs. [45, 46, 47]. The contribution of this chapter to the well-established theory is therefore only to combine the tools for treating molecular energies, forbidden transitions and systematic shifts in a single, consistent framework. This chapter may also serve as a guide to show, in detail, how to

use the formalism of spherical tensor algebra in combination with bra-ket notation to gain deep insights into the subject of molecular lines and forbidden transitions.

We start the analysis by briefly describing the method of constructing a Hamiltonian and a basis set suitable for our system. We then construct an 'effective' Hamiltonian starting with the internal interactions between the electrons and the nuclei. To this we add interactions with external, static fields and finally we add time-varying fields in the form of electromagnetic radiation to predict state dynamics. By means of several example derivations, we will show how to derive matrix expressions for the Hamiltonian interactions in a suitable basis.

We then present the results of our calculations for the N_2^+ molecule in its electronic ground state, $X^2\Sigma_g^+$. The results show that often neglected elements in the Hamiltonian lead to significant changes in the measured spectrum by inducing transitions that would otherwise be forbidden. Such terms also enable 'magic' transitions that are particularly insensitive to experimental noise. We present different classes of transitions from Zeeman transitions of ~ 1 MHz to rovibrational transitions of ~ 100 THz, and explore their susceptibility to magnetic fields. Finally we assess the suitability of the N_2^+ molecular transitions as clock and qubit states by estimating other sources of systematic shifts and uncertainties.

2.1 Energy levels of a diatomic molecule

The purpose of this section is to provide a short background on the molecular Hamiltonian and to introduce the techniques that can be used to solve it, such as wavefunction separation, perturbation theory and the 'effective' Hamiltonian approach. We will then consider the hierarchy of angular momentum couplings and determine the basis states that are suitable for evaluating the Hamiltonian.

2.1.1 The molecular Hamiltonian

The Hamiltonian for a system of particles represents the total energy of the system and can be written as the sum of the kinetic and potential energies of each particle. A simplified molecular Hamiltonian, in the absence of external fields, may take the form [42],

$$\begin{aligned}\mathcal{H}_{\text{tot}} &= \sum_i \frac{1}{2m_i} \mathbf{P}_i^2 + \frac{1}{2 \sum_{\alpha} M_{\alpha}} \sum_{i,j} \mathbf{P}_i \cdot \mathbf{P}_j \\ &+ \sum_{i < j} \frac{e^2}{4\pi\epsilon_0 R_{ij}} + \sum_{\alpha, i} \frac{Z_{\alpha} e^2}{4\pi\epsilon_0 R_{i\alpha}} \\ &+ \mathcal{H}(\mathbf{S}_i) + \mathcal{H}(\mathbf{I}_{\alpha}) \\ &+ \sum_{\alpha} \frac{1}{2M_{\alpha}} \mathbf{P}_{\alpha}^2 + \sum_{\alpha < \beta} \frac{Z_{\alpha} Z_{\beta} e^2}{4\pi\epsilon_0 R_{\alpha\beta}}.\end{aligned}\tag{2.1}$$

Here, the (i, j) and (α, β) -indices refer to the electrons and the nuclei, respectively. The momentum operator, \mathbf{P}_i , then represents the momentum of electron i . The masses of electrons and nuclei are denoted m_i and M_{α} , respectively, and e and Z_{α} denote their respective charges. $R_{\alpha\beta}$ is the spatial coordinate between two particles and ϵ_0 is the vacuum permittivity. The first two terms therefore describe the kinetic energy of the electrons. The next two terms describe the Coulomb potential between different electrons and between the electrons and nuclei. The next two terms, which are not written explicitly¹, represent the interaction between the electron and nuclear spins and the system as a whole. The last two terms

¹If these two terms were written out explicitly this expression would be very lengthy.

in this Hamiltonian represent the kinetic energy of the nuclei and the Coulomb energy between different nuclei.

By solving the Schrödinger wave equation with appropriate boundary conditions, we can find the wavefunctions, Ψ_{evrs} , that fully describe the system, with energies, E_{evrs} , given by,

$$\mathcal{H}_{\text{tot}}\Psi_{evrs} = E_{evrs}\Psi_{evrs}. \quad (2.2)$$

The subscript *evrs* suggests that this wavefunction is a combined function of the electronic, vibrational, rotational and spin coordinates. By solving the time-dependent wave equation we obtain the time evolution of our wavefunctions under, e.g., the influence of an electromagnetic field,

$$\mathcal{H}_{\text{tot}}(t)\Psi_{evrs}(t) = i\hbar\frac{\partial}{\partial t}\Psi_{evrs}(t), \quad (2.3)$$

where, $\mathcal{H}_{\text{tot}}(t)$ now includes a term corresponding to the interaction with an external field.

Exact solutions to Eq. (2.2), using the Hamiltonian of Eq. (2.1), are beyond the capabilities of even the most powerful classical computers today. Even the simplest molecule, H_2^+ , consisting of two protons and one electron, can only be solved for after making certain assumptions [45]. The most common starting point is the Born-Oppenheimer approximation which treats the electronic and nuclear wavefunctions as separable, i.e.,

$$\Psi_{evrs} = \psi_e\phi_{vrs}. \quad (2.4)$$

Each part can then be solved individually as,

$$\mathcal{H}_e\psi_e = E_e\psi_e, \quad (2.5)$$

and analogously for \mathcal{H}_{vrs} . In the Hamiltonian, this separation into an electronic and a nuclear part, $\mathcal{H}_{\text{tot}} = \mathcal{H}_e + \mathcal{H}_{vrs}$, is imposed by the approximation that the electronic wavefunctions are independent of the nuclear momenta and thus follow the motion of the nuclei adiabatically. The nuclear coordinate, $R_{\alpha\beta}$, is then reduced to a parameter in the electronic Hamiltonian \mathcal{H}_e . The electronic Schrödinger equation can then be solved exactly for H_2^+ and approximately for other diatomic molecules. The solutions are commonly presented as Born-Oppenheimer potentials

for each electronic state describing the effective potential experienced by the nuclei.

Such a separation of the total wavefunction most of the time involves the approximation that the Hamiltonian acting on one part of the separated wavefunction does not significantly influence the other part. By perturbation theory, the interaction between the two subsystems that was neglected in the separation can be added as correction terms in the Hamiltonian up to any desired accuracy. As an example of an exact separation, in the absence of external fields, the translational motion of the molecule can be rigorously and exactly separated from the spin-rovibronic wavefunction by transforming the Hamiltonian, Eq. (2.2), to a reference frame co-moving with the molecule. In the presence of an external field this separation is no longer exact.

The separation of the vibrational and rotational motion of the nuclei can be achieved, in a similar manner as the separation of electronic and nuclear motion, by separating the wavefunction, Ψ_{vr} , in a radial (vibrational) part, $\chi(R)$, and an angular (rotational) part, $\Theta(\theta)$. The wave equation for the radial wavefunction is then,

$$\frac{\hbar^2}{2\mu} \frac{1}{R^2} \frac{d}{dR} R^2 \frac{d\chi(R)}{dR} + [E_{evr} - V - B(R)J(J+1)] \chi(R) = 0. \quad (2.6)$$

Here, μ represents the reduced mass of the two nuclei and J is the quantum number associated with rotations. The potential, V , includes the Born-Oppenheimer potential for the nuclei in a given electronic state. By assuming a harmonic potential experienced by the nuclei and neglecting the angular part, $J(J+1)$, the vibrational wave equation can be solved and describes harmonic oscillator states with associated quantum number v .

Anharmonic corrections to the potential are then introduced as perturbations to these first-order Harmonic oscillator solutions. One general potential function that includes anharmonic corrections, up to any desired order, was introduced by *Dunham* [48],

$$V(\xi) = a_0 \xi^2 [1 + a_1 \xi + a_2 \xi^2 + \dots], \quad (2.7)$$

where $\xi = (R - R_e)/R_e$ is a dimensionless coordinate describing the excursions of the internuclear distance, R , from the equilibrium bond length, R_e . Here, $a_0 = h\omega_e/4B_e$ is given in terms of the oscillator frequency, ω_e , and the equilibrium rotational constant, B_e , where h is the Planck constant. The first term, corresponding to the Harmonic oscillator potential, is solved in the wave equation and higher order constants, $a_{n \neq 0}$, assumed to be small compared to a_0 , are added as perturbations².

The neglected angular part of the Hamiltonian, $B(R)J(J + 1)$, can also be added as a perturbation to the zero-order Hamiltonian by expressing the rotational constant in terms of its series expansion in ξ ,

$$B(R) = \frac{\hbar}{2\mu R^2} = \frac{\hbar}{2\mu R_e^2} [1 + c_1\xi + c_2\xi^2 + \dots], \quad (2.8)$$

where $c_n = (-1)^n(n + 1)$. By perturbation theory, it can then be shown that the energies of the vibrating rotor, thus described, are given by an infinite series in increasing orders of the vibrational and rotational quantum numbers,

$$E_{v,J} = \sum_{kl} Y_{kl}(v + 1/2)^k (J(J + 1))^l. \quad (2.9)$$

The values of the Y_{kl} coefficients can be derived explicitly in terms of the molecular constants. Physically, the first term including Y_{00} , which has no rotational or vibrational dependence, represents only a correction to the energy of the electronic state. The $Y_{10} = \omega_e$ term is the Harmonic oscillator energy and the $Y_{01} = B_e$ term represents the energy of a rigid rotor. Cross terms also appear, which couple the rotations and vibrations such as the $Y_{11}(v + 1/2)(J(J + 1))$ term which represents the change in the rotational moment of inertia upon vibrational excitation. The $Y_{02} = 4B_e^3/\omega_e^2$ term is the first order correction to the rigid-rotor energies with $E^{02} \propto J^2(J + 1)^2$, and therefore corresponds to a centrifugal distortion correction.

²Another commonly used potential is the Morse potential which in some cases better reproduces the B.O. potentials, especially in the limit of $R \rightarrow \infty$. The potential function is, $V = D(1 - e^{-\beta(R - R_e)})^2$, where D is the dissociation energy and β is a constant. The solutions of the vibrational wave equation are then equivalent to the anharmonic potential in Eq. (2.7) up to second order, but does not include higher order terms.

To reiterate, we have seen how a separation of wavefunctions can help us to find solutions to the molecular Hamiltonian and that the neglected interactions can be added as perturbations to these zero-order solutions. Another useful technique for solving the Hamiltonian presents itself naturally from a series expansion like the one in Eq. (2.9). Often we are only interested in the energies of a particular sub-manifold of the molecular states such as the vibrational states of a single electronic state or the rotational states of a single vibrational state. The electronic, vibrational and rotational wave equations are then unnecessary to solve for every state and we may instead transform to an 'effective' Hamiltonian which only acts within a particular sub-space of the molecular wavefunction. An example is given below.

We have seen that rovibrational coupling terms, in the expansion of Eq. (2.9), connect together the vibrational and rotational basis states, $|v, J\rangle$, by perturbing the zero-order solutions to the separated wave equation. We note that the rotational state dependence of all energy contributions with coefficients $Y_{n,0}$ for $n = 0, 1, \dots$ scale the same way, as $J(J + 1)$. The opportunity then presents itself to change the rotational constant, B_e , into an 'effective' rotational parameter, which depends on the vibrational state, in order to absorb all the terms that scale as $J(J + 1)$ into a single parameter, B_v . Thus, for example, the Y_{11} contribution which couples the rotational and vibrational states is added to the rotational constant $B_v = B_e + Y_{11}(v + 1/2) + \dots$

The Hamiltonian expressed in this manner will have the same eigenvalues as the 'real' Hamiltonian but is simplified to only act on the separated basis functions, $|v\rangle|J\rangle$, with a different effective rotational constant for each vibrational state. The effective rotational Hamiltonian then only has diagonal values in v , i.e. it does not couple different vibrational states, but nonetheless gives the correct energy eigenvalues including the off-diagonal contributions. This Hamiltonian can then act on the separated basis states, $|J\rangle$, without considering vibrational states and will give the correct rotational splitting. It can be proven rigorously by perturbation theory [42] or through a contact transformation [49] that the eigenvalues, thus produced, are equivalent to the eigenvalues of the real Hamiltonian.

Since we have separated the basis states $|v\rangle|J\rangle$ and absorbed all terms that couple them together in effective constants, v and J cease to be good quantum numbers of the real Hamiltonian. A better approximation to our real wavefunction can then be expressed as a linear combination of the zero-order separated basis states,

$$|\psi_k\rangle_p = \sum_i c_i^k |\phi_i\rangle. \quad (2.10)$$

The subscript p suggests that these wavefunctions are perturbed by terms which mix the zero-order basis states, $|\phi_i\rangle$, with mixing amplitudes, c_i^k . The perturbed wavefunctions, as they are no longer eigenfunctions of the real Hamiltonian, are therefore not necessarily mutually orthogonal.

The effective Hamiltonian is also a good meeting point between experiment and theory since a spectrum typically provides only frequencies and transition strengths. Thus, e.g., all the terms that scale as $J(J+1)$ are naturally grouped together and each individual contribution is hard to separate in a spectroscopic experiment. In this case, a comparison of different isotopes of the same molecule can help separate the contributions to each parameter, as different contributions often have different mass dependence.

The molecular basis we choose decides which zero-order solutions are considered for our wavefunction, and thus also which quantum numbers are useful to represent our interactions. The closer our quantum numbers are to 'good' quantum numbers, i.e. to operators that commute with the real Hamiltonian, the better is our approximation of the energy states. It is important to keep in mind that in the end, only the observables are physical and every label we put on the orbital, vibrational, rotational and spin coordinates are essentially for bookkeeping and for gaining intuition about the physical mechanisms. Symmetries and conservation laws concern the real wavefunction Ψ_{evrs} and not the near quantum numbers which we use to describe it. We must therefore keep an eye on the breakdown of these approximations and not treat them as inviolable.

We use $|\eta\Lambda\rangle$ as the Born-Oppenheimer electronic basis states where Λ is the projection of the electronic angular momentum of an electronic state, $^{2S+1}\Lambda_{u/g}^{\pm}$, on the internuclear axis and η denotes any other quantum numbers necessary to describe the electronic state. The vibrational

basis states are denoted $|v\rangle$ where v is the harmonic oscillator quantum number. For better approximations to our combined orbital, rotational and spin-angular-momentum wavefunctions, we treat them in a coupled representation and not as separable. We use common angular-momentum-coupling hierarchies called 'Hund's cases'. The Hund's cases represent the order of coupling strengths between orbital angular momentum, Λ , rotational angular momentum, N , electron spin angular momentum, S , and nuclear spin angular momentum, I , for a few limiting cases. The order of the coupling then determines which intermediate quantum numbers are useful for describing our system.

The molecular nitrogen ion, N_2^+ , in the electronic ground state, $X^2\Sigma_g^+$, can be described reasonably well within Hund's case (b_{β_J}) [50] where the rotational and electron spin angular momentum are weakly coupled to the molecular axis. The coupling order is given by,

$$\mathbf{N} + \mathbf{S} = \mathbf{J}, \quad (2.11)$$

$$\mathbf{J} + \mathbf{I} = \mathbf{F}. \quad (2.12)$$

Here, \mathbf{J} is the 'fine-structure' angular momentum³ resulting from the coupling between the electron spin and the rotation, and \mathbf{F} is the total 'hyperfine-structure' angular momentum including the nuclear spin \mathbf{I} . The coupling to the nuclear spin determines the subscript of the notation that describes the Hund's cases, e.g. (b_α) or (b_{β_J}), where α and β imply that the nuclear spin is strongly or weakly coupled to the molecular axis respectively. The additional subscript in case (b_{β_J}) then gives the angular momentum vector to which the nuclear spin couples, in this case J .

The set of quantum numbers that label the Hund's case (b_{β_J}) basis is then,

$$|\phi_i\rangle = |\eta, \Lambda, v, N, S, J, I, F, M_F\rangle. \quad (2.13)$$

Here, M_F , is the projection of the total angular momentum, \mathbf{F} , on the quantization axis and i is a compound index for all the quantum numbers. Due to the approximation of our wavefunction as this zero-order basis, only M_F remains a strictly good quantum number. The remaining six quantum numbers are used here as 'near' quantum numbers to label the

³Note that we have changed rotational quantum number from J to N when moving to the Hund's case (b) basis.

states. The bra-ket notation and spherical tensor algebra, used throughout this thesis, are so well established that we shall not have to deal with any explicit functional forms of the wavefunctions throughout the length of this thesis.

As an effective Hamiltonian for N_2^+ , we shall construct here the spin-rovibrational energies in the $X^2\Sigma_g^+$ -state without considering other electronic states. We construct the following Hamiltonian for the electronic ground state [51, 23],

$$H = H_{\text{vib}} + H_{\text{rot}} + H_{\text{fs}} + H_{\text{hfs}} + H_z, \quad (2.14)$$

as the sum of a vibrational, rotational, fine-structure, hyperfine-structure and Zeeman Hamiltonian. These terms are given explicitly in the next section. The parameters in our Hamiltonian are effective parameters for the specific vibronic state obtained through comparison with experiment or numerical simulations. Figure 2.1 shows the spin-rovibrational structure of $^{14}N_2^+$ in the electronic ground state schematically.

2.1.2 The effective Hamiltonian

The vibrational Hamiltonian

We have seen in Section 2.1.1 that the rovibrational energies of a diatomic molecule can be obtained by assuming harmonic oscillator wavefunctions with anharmonic and rotational terms introduced as perturbations, as described by Eq. (2.9). Neglecting the rotations, the vibrational energies, in units of frequency, are to second order [42],

$$G(v) = \omega_e(v + 1/2) + \omega_e x_e(v + 1/2)^2 + \omega_e y_e(v + 1/2)^3. \quad (2.15)$$

In the effective Hamiltonian approximation of Eq. (2.15), the off-diagonal terms in the Hamiltonian have been transformed away and the transition frequencies may be written as $\Delta E_{\text{vib}} = G(v') - G(v)$. These constants are given in Table 2.2 and Table 2.3 for $^{14}N_2^+$ and $^{15}N_2^+$, respectively. As the constants are obtained from experiments, they are effective constants which include corrections due to breakdown of the Born-Oppenheimer approximation.

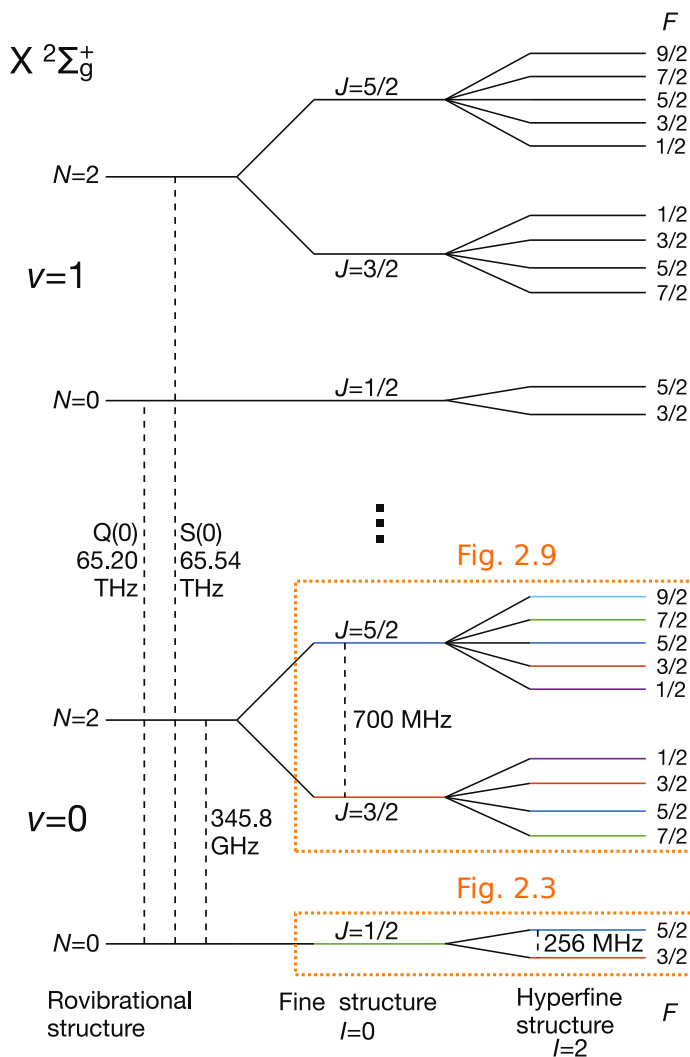


Fig. 2.1. A simplified energy-level diagram (not to scale) of $^{14}\text{N}_2^+$ in the electronic ground state, $X^2\Sigma_g^+$, including two rotational states, $N = 0, 2$, of the $v = 0, 1$ vibrational states. Both nuclear-spin states, $I = 0, 2$ are shown. The Zeeman structure is not included. The dotted boxes refer to the levels included in Figures 2.3 and 2.9 where the Zeeman-structure is presented. The color code of these levels matches the one used in said figures.

The rotational Hamiltonian

The effective rotational Hamiltonian, H_{rot} , associated with the quantum number N , is added as a perturbation to the vibrational energies, as described by Eq. (2.9). The Hamiltonian operator is,

$$H_{\text{rot}} = B(R) \cdot \hat{N}^2, \quad (2.16)$$

with diagonal matrix elements in the effective Hamiltonian (to second order) given by [42],

$$\langle \phi_i | H_{\text{rot}} | \phi_i \rangle = B_v N(N+1) - D_v (N(N+1))^2. \quad (2.17)$$

The first term represents the energy of a quantum-mechanical rigid rotor while the second term represents first order corrections to the rigid-rotor approximation. The rotational constant B_v , as obtained through experiments, is then an effective parameter that combines the effect of rotational angular momentum of both nuclei and electrons. The centrifugal distortion constant, D_v , includes the effects of the rovibrational coupling, as will be shown in Section 2.1.2.

The values of B_v and D_v are readily found in the literature but as we are also interested in the off-diagonal elements that mix rovibrational levels, this effective, diagonalized form of the Hamiltonian is not sufficient. In order to estimate the mixing amplitudes, the off-diagonal first order correction to H_{rot} , which we will denote H_{rovib} , is treated separately in the next section.⁴

The rovibrational interaction

We have seen in Eq. (2.9), that the first order correction to the rigid-rotor energies, $\propto Y_{02}$, gives rise to the first-order contribution to the centrifugal-distortion constant D_v . This interaction is also responsible for the first rovibrational mixing term which couples different vibrational states. The

⁴Since the transformed effective Hamiltonian already includes the contribution to the energies of the rovibrational interaction in the effective parameter, D_v , the reintroduction of this term might seem odd at first. We shall, however, see in the next section that the energy contribution to D_v is mainly due to the first order rovibrational correction and the centrifugal-distortion term can be replaced with H_{rovib} in the effective Hamiltonian.

mixing coefficients between rovibrational levels can be estimated as in Ref. [52].

As we have seen in Section 2.1.1, an operator that depends on the internuclear distance, R , can be expanded in a Taylor series around the equilibrium bond length R_e . Further, if we assume that the amplitude of vibrational motion is small compared to R_e , i.e. $\xi \ll 1$, we can neglect the higher order terms in the expansion. The rotational constant $B(R)$ expanded to second order around $(R - R_e)$ takes the form,

$$B(R) = B_e + \left. \frac{dB}{dR} \right|_{(R=R_e)} (R - R_e) + \left. \frac{d^2B}{dR^2} \right|_{(R=R_e)} (R - R_e)^2 + \dots \quad (2.18)$$

$B_e = B(R)|_{(R=R_e)}$ is the equilibrium rotational constant which in the low vibrational states may be approximated by $B_e \approx B_v$. The B_e term corresponds to the rigid rotor whereas the linear term in R causes the first-order rovibrational correction to the rotational energies and can be reintroduced as a perturbation to the diagonalized effective Hamiltonian.

We can find the value of dB/dR by first noting that $B(R) \propto R^{-2}$ and the deviation of $B(R)$ from the equilibrium bond length can be written,

$$B(R) = B_e \left(\frac{R_e}{R} \right)^2. \quad (2.19)$$

Taking the derivative with respect to R yields,

$$\left. \frac{dB}{dR} \right|_{(R=R_e)} = -2B_e \left. \frac{R_e^2}{R^3} \right|_{(R=R_e)} = -2 \frac{B_e}{R_e}. \quad (2.20)$$

In order to evaluate the effect of the operator $(R - R_e)$, from Eq. (2.18), on our basis states of Eq. (2.13), we first make some assumptions. We note that the spin-rotational basis states are independent of the internuclear distance R and therefore not impacted by this operator, i.e. we assume,

$$\begin{aligned} & \langle v', N', S', J', I', F', M'_F | R | v, N, S, J, I, F, M_F \rangle \\ & \approx \langle v' | R | v \rangle \langle N', S', J', I', F', M'_F | N, S, J, I, F, M_F \rangle. \end{aligned} \quad (2.21)$$

The validity of this approximation can be seen by observing the vibrational dependence of the effective spin-rotational and hyperfine constants in

Table 2.2. The difference between $v = 0$ and $v = 1$ in the constant γ_v are in the order of $\sim 1\%$ and this approximation is therefore justified.

Further, we approximate the vibrational wavefunctions, $|v\rangle$, as harmonic oscillator states. Like this, we can recognize the operator $(R - R_e) = \hat{x}$ as the normal-coordinate operator which is readily expressed in terms of the creation and annihilation operators, a^\dagger and a , as,

$$\hat{x} = \sqrt{\frac{\hbar}{2\mu\omega_e}}(a^\dagger + a). \quad (2.22)$$

Here μ refers to the reduced mass of the system and ω_e is the oscillation frequency. When acting on the Harmonic oscillator functions this operator gives,

$$\langle v'|(R - R_e)|v\rangle = \sqrt{\frac{\hbar}{2\mu\omega_e}}(\sqrt{v+1}\delta_{v'(v'+1)} + \sqrt{v}\delta_{v'(v'-1)}). \quad (2.23)$$

We can express the effective mass μ in the equilibrium constants $\mu = \hbar/(2R_e^2 B_e)$ and thus using Equations (2.20) and (2.23) we obtain,

$$\frac{dB}{dR}\langle v'|(R - R_e)|v\rangle = -2\sqrt{\frac{B_e^3}{\omega_e}}(\sqrt{v+1}\delta_{v'(v'+1)} + \sqrt{v}\delta_{v'(v'-1)}). \quad (2.24)$$

By the Kronecker delta expressions, δ , we see that this first-order rovibrational interaction mixes vibrational states of $\Delta v = \pm 1$. The second order contribution in Eq. (2.18) $\propto R^2$ will induce mixing of vibrational states $\Delta v = \pm 2$ and so on⁵. The rovibrational interaction Hamiltonian, $B(R) \cdot \hat{\mathbf{N}}^2$, has diagonal eigenvalues $B(R) \cdot N(N+1)$, and we therefore ob-

⁵As we saw in Section 2.1.1, we may expand the rotational constant, $B(R)$, in terms of the Dunham operator, $\hat{\xi} = (\hat{R} - R_e)/R_e$, which takes a dimensionless form. The analogue of Eq. (2.18) then takes the same form as in Eq. (2.8),

$$B(R) = B_e [1 - 2\xi + \dots].$$

tain the following Hamiltonian expression for the first order rovibrational interaction,

$$\begin{aligned} \langle v'N'|H_{\text{rovib}}|vN\rangle &= -2B_e\sqrt{\frac{B_e}{\omega_e}}\delta_{NN'} \\ &\times N(N+1)\left(\sqrt{v+1}\delta_{v,(v'+1)}+\sqrt{v}\delta_{v,(v'-1)}\right). \end{aligned} \quad (2.25)$$

Using the values $B_e \approx B_0 = 1.93 \text{ cm}^{-1}$ and $\omega_e \approx 2140 \text{ cm}^{-1}$ from Table 2.2, we find that $\sqrt{B_e/\omega_e} \approx 0.03$.

A simple analytical expression exists for the correction to the basis states, to first order in perturbation theory,

$$|a\rangle_p \approx |a^0\rangle + \frac{\langle a^0|H|b^0\rangle}{E_b - E_a}|b^0\rangle = c_a^a|a^0\rangle + c_b^a|b^0\rangle. \quad (2.26)$$

Here we have introduced the mixing coefficients from Eq. (2.10), c_i^a , which represent the mixing amplitude between the perturbed state $|\psi_a\rangle_p$ and the zero-order basis functions $|\phi_i\rangle$, normalized such that $\sum_i (c_i^a)^2 = 1$. By inserting our mixing Hamiltonian from Eq. (2.25), we obtain the vibrational mixing coefficients between $v = 0$ and $v = 1$,

$$\begin{aligned} |v=0\rangle_p &\approx \left(|v=0\rangle + 2\left(\frac{B_e}{\omega_e}\right)^{\frac{3}{2}} N(N+1)|v=1\rangle \right), \\ |v=1\rangle_p &\approx \left(|v=1\rangle - 2\left(\frac{B_e}{\omega_e}\right)^{\frac{3}{2}} N(N+1)|v=0\rangle \right). \end{aligned} \quad (2.27)$$

In this approximation the mixing coefficients c_1^0 and c_0^1 are equal in magnitude but opposite in sign.

To obtain the mixing coefficients to all orders, we diagonalize the Hamiltonian numerically, $H_{\text{tot}} = \Delta G_{01} + B_e \cdot N(N+1) + H_{\text{rovib}}$. In Table 2.1 we present the calculated mixing coefficients between $v = (0, 1, 2)$ in $N = (0, 2)$. First, we note that the rotational ground state, $N = 0$, prohibits rovibrational mixing as expected in the absence of rotations. Mixing coefficients between $v = 0$ and $v = 1$ is of order 10^{-4} in $N = 2$ and shifts the energy levels by $\sim 6 \text{ MHz}$ in $N = 2$, or $(N(N+1))^2 \cdot 0.177 \text{ MHz}$, compared to the unmixed levels. This is also what we get from the centrifugal distortion constant $D_0 \approx 0.179 \text{ MHz}$, from Table 2.2. We

	$v = 0$ $N = 0$	$v = 0$ $N = 2$	$v = 1$ $N = 0$	$v = 1$ $N = 2$	$v = 2$ $N = 0$	$v = 2$ $N = 2$
$v = 0, N = 0$	1	0	0	0	0	0
$v = 0, N = 2$	0	0.999	0	$3.15 \cdot 10^{-4}$	0	$-6.93 \cdot 10^{-8}$
$v = 1, N = 0$	0	0	1	0	0	0
$v = 1, N = 2$	0	$3.11 \cdot 10^{-4}$	0	-0.999	0	$4.39 \cdot 10^{-4}$
$v = 2, N = 0$	0	0	0	0	1	0
$v = 2, N = 2$	0	$6.72 \cdot 10^{-8}$	0	$-4.33 \cdot 10^{-4}$	0	-0.990

Tab. 2.1. Mixing of vibrational states due to the first-order rovibrational interaction. Columns represent the perturbed rovibrationally mixed functions $|v, N\rangle_p$ and the rows represent the orthogonal zero-order basis states $|v\rangle|N\rangle$. A basis set of $N = 0, 2, \dots, 100$ and $v = 0, 1, 2$ was used to ensure convergence.

therefore find that the main contribution to the effective centrifugal distortion constant, D_v , comes from this first-order rovibrational interaction and that the other contributions to Y_{n2} for $n \neq 0$, are small⁶.

The spin-rotation Hamiltonian

Fine-structure terms in the effective Hamiltonian, H_{fs} , arise from coupling between the electron spin magnetic moment with the magnetic moment generated by the rotating molecule and the electron orbital motion.

The spin-rotation-coupling Hamiltonian, $H_{\text{fs}} = \gamma_v \hat{\mathbf{N}} \cdot \hat{\mathbf{S}}$, is diagonal in the Hund's case (b) basis with diagonal matrix elements given by [51],

$$\langle \phi_i | H_{\text{fs}} | \phi_i \rangle = \gamma_{v,N} (J(J+1) - N(N+1) - S(S+1)) / 2. \quad (2.28)$$

The coupling constant $\gamma_{v,N}$ also includes a centrifugal distortion term, $\gamma_{v,N} = \gamma_v + \gamma_{Dv} N(N+1)$, which arises, as in the rotational Hamiltonian, from the radial expansion of $\gamma(R)$.

The spin-orbit interaction does not appear in our Hamiltonian as the projection of the orbital angular momentum is zero in a pure Σ state. Even so, a residual angular momentum appears due to mixing of electronic

⁶The centrifugal distortion energy is typically much smaller than the vibrational and rotational spacing and the D_v term can be kept or removed from the estimation of the vibrational mixing coefficients with no significant impact on the obtained mixing coefficients. However, in order to keep the treatment consistent we remove the centrifugal distortion term from the diagonalization.

states and is included in the effective coupling constant $\gamma_{v,N}$ to second order [42]. Due to the relative weakness of the rotational magnetic moment, this second order contribution is often the dominant contribution to $\gamma_{v,N}$ [53]. We shall see in Section 2.1.3 how this contribution to $\gamma_{v,N}$ can be used to estimate the Zeeman shift due to unquenched orbital angular momentum.

The hyperfine Hamiltonian

The 'hyperfine' interaction refers to interactions between the spin-rotational electric and magnetic moments and the magnetic dipole and electric quadrupole moment of the nuclei. Due to the mass ratio between the electrons and protons of ~ 1800 , the nuclear magnetic moment is three orders of magnitude smaller than that of the electron spin and these terms can be added to our spin-rotational Hamiltonian perturbatively.

Each $^{14}\text{N}_2^+$ atom has a nuclear spin of 1. The total nuclear spin, I , can then take the values $I = 0, 1, 2$. In N_2^+ , even (odd) values of I allow for only even (odd) rotational quantum numbers, N , due to the total permutation symmetry of the molecular wavefunction. Here, we will only consider the nuclear-spin species $I = 0, 2$ which are associated with the rotational ground state. We will also consider the case of $^{15}\text{N}_2^+$ as this isotope is particularly useful for experimental reasons.

The effective hyperfine-interaction Hamiltonian has four contributions,

$$H_{\text{hfs}} = H_t + H_{b_F} + H_{eQ} + H_{C_I}. \quad (2.29)$$

The matrix elements for these four terms have been derived elsewhere [51], and here we shall simply give the results. In Section 2.1.3, we will show how such matrix elements are derived.

H_t is the dipolar hyperfine interaction which represents a magnetic dipole-dipole coupling between the electron and nuclear spins. The Hamiltonian operator is given in spherical tensor notation as $H_t = -\sqrt{10}T^1(\mathbf{I}) \cdot T^1(\mathbf{S}, C^2)$

[54], where C^2 represents a second rank spherical harmonic [54]. The matrix elements are,

$$\begin{aligned}
& \langle v', N', S', J', I', F', M'_F | H_t | v, N, S, J, I, F, M_F \rangle \\
&= t_{v,N} \delta_{vv'} \delta_{SS'} \delta_{II'} \delta_{FF'} \delta_{M_F M'_F} (-1)^{J+I+F+N'+1} \\
&\times \sqrt{30I(I+1)(2I+1)S(S+1)(2S+1)} \\
&\times \sqrt{(2J+1)(2J'+1)(2N+1)(2N'+1)} \\
&\times \begin{Bmatrix} I & J' & F' \\ J & I & 1 \end{Bmatrix} \begin{Bmatrix} N' & N & 2 \\ S & S & 1 \\ J' & J & 1 \end{Bmatrix} \begin{pmatrix} N' & 2 & N \\ 0 & 0 & 0 \end{pmatrix}. \quad (2.30)
\end{aligned}$$

The effective coupling constant also includes a centrifugal distortion correction $t_{v,N} = t_v + t_N N(N+1)$. Note that this Hamiltonian exhibits nonzero off-diagonal matrix elements for states of different J and N quantum numbers and we say that this expression 'mixes' different J and N quantum numbers.

H_{b_F} is the Fermi-contact interaction which represents the coupling between the electron and nuclear spins at the position of the nuclei. The Hamiltonian operator in spherical tensor notation is given by $H_{b_F} = b_F T^1(\mathbf{I}) \cdot T^1(\mathbf{S})$ [54]. This term is therefore only present for electronic states with some Σ character i.e. electronic states with a nonzero probability density at the nucleus⁷. The matrix elements are given by,

$$\begin{aligned}
& \langle v', N', S', J', I', F', M'_F | H_{b_F} | v, N, S, J, I, F, M_F \rangle \\
&= b_{F,v} \delta_{vv'} \delta_{NN'} \delta_{SS'} \delta_{II'} \delta_{FF'} \delta_{M_F M'_F} (-1)^{F+I+J'+J+N+S+1} \\
&\times \sqrt{I(I+1)(2I+1)S(S+1)(2S+1)(2J+1)(2J'+1)} \\
&\times \begin{Bmatrix} I & J' & F' \\ J & I & 1 \end{Bmatrix} \begin{Bmatrix} S & J' & N \\ J & S & 1 \end{Bmatrix}. \quad (2.31)
\end{aligned}$$

This term has off-diagonal elements in J .

H_{eqQ} is the electric-quadrupole hyperfine interaction and represents a shift of the energies due to interaction of the electrons with the electric-

⁷Inside the nucleus, the magnetic field from the nucleus takes on a different form than a point magnetic dipole and the interaction can not be adequately described by H_t . [45]

quadrupole charge distribution of the nuclei. The spherical tensor form of the Hamiltonian operator is [51]

$$H_{eqQ} = -e \sum_{\alpha} T^2(\nabla \mathbf{E}_{\alpha}) \cdot T^2(\mathbf{Q}_{\alpha}). \quad (2.32)$$

This expression has off-diagonal matrix elements in N , J and I , where $I_1 = 1$ is the nuclear spin of a ^{14}N atom. The matrix elements are given by,

$$\begin{aligned} & \langle v', N', S', J', I', F', M'_F | H_{eqQ} | v, N, S, J, I, F, M_F \rangle \\ &= \frac{eqQ_v}{2} \delta_{vv'} \delta_{SS'} \delta_{FF'} \delta_{M_F M'_F} \\ & \times \frac{(-1)^I + (-1)^{I'}}{2} (-1)^{F+2J+I'+2I_1+S+2N'} \\ & \times \sqrt{(2I+1)(2I'+1)(2J+1)(2J'+1)(2N+1)(2N'+1)} \\ & \times \begin{Bmatrix} I' & 2 & I \\ J & F & J' \end{Bmatrix} \begin{Bmatrix} 1 & 2 & 1 \\ I & 1 & I' \end{Bmatrix} \begin{Bmatrix} N' & 2 & N \\ J & S & J' \end{Bmatrix} \\ & \times \begin{pmatrix} N' & 2 & N \\ 0 & 0 & 0 \end{pmatrix} \begin{pmatrix} I_1 & 2 & I_1 \\ -I_1 & 0 & I_1 \end{pmatrix}^{-1}. \end{aligned} \quad (2.33)$$

Finally, H_{c_I} is the nuclear-spin rotation interaction, analogous to the electron-spin rotation coupling from Section 2.1.2, with operator form $H_{c_I} = c_I T^1(\mathbf{I}) \cdot T^1(\mathbf{N})$ [51]. This interaction Hamiltonian mixes different J quantum numbers and takes the form,

$$\begin{aligned} & \langle v', N', S', J', I', F', M'_F | H_{c_I} | v, N, S, J, I, F, M_F \rangle \\ &= c_I \delta_{vv'} \delta_{NN'} \delta_{SS'} \delta_{II'} \delta_{FF'} \delta_{M_F M'_F} (-1)^{F+I+J'+J+N+S+1} \\ & \times \sqrt{I(I+1)(2I+1)N(N+1)(2N+1)(2J+1)(2J'+1)} \\ & \times \begin{Bmatrix} J & 1 & J' \\ I & F & I \end{Bmatrix} \begin{Bmatrix} N & 1 & N \\ J' & S & J \end{Bmatrix}. \end{aligned} \quad (2.34)$$

All the effective coupling constants for $^{14}\text{N}_2^+$ are given in Table 2.2.

2.1.3 Interaction with external fields

In this section, we aim to illustrate the methods for deriving a Hamiltonian expression by means of several examples. We will see how to derive matrix elements in both Hund's case (a) and case (b), in coupled and uncoupled representations. The hope is that this section will serve as a short reference for the different techniques and manipulations that are helpful in deriving matrix elements. We employ the methods of spherical tensor algebra and bra-ket notation which are rigorously derived and described in length by *Brown and Carrington* [42] and *R. Zare* [43].

We shall derive matrix expressions for the interaction between the magnetic moments of our molecule and an external magnetic field. These expressions are useful both in the evaluation of the Zeeman effect, in a static magnetic field, and for calculating magnetic-dipole transition moments through interaction with an oscillating magnetic field. We therefore derive expressions for the general case and take note of the one-to-one correspondence between selection rules for magnetic dipole transitions and the breakdown of the Hund's case ($b_{\beta,J}$) approximation by the Zeeman Hamiltonian.

The N_2^+ molecule has four magnetic moments that should be considered in the interaction with an external magnetic field. The effective Zeeman Hamiltonian, H_z , therefore has four first-order contributions corresponding to the interaction of a magnetic field, \mathbf{B} , with the magnetic dipole moment associated with electron spin, \mathbf{S} , molecular rotation, \mathbf{N} , nuclear spins, \mathbf{I} , and orbital angular momentum, \mathbf{L} [42, 54]. The magnetic moment of the electronic orbital motion vanishes in a pure Σ -state but should still be considered in the $X^2\Sigma_g^+$ ground state due to a residual angular momentum that might arise due to mixing of electronic states. Cross terms and terms of higher order in the magnetic field ($\propto B^2$) [55, 42] also appear in the effective Hamiltonian, but will not be considered here. A discussion of the neglected terms in the Zeeman Hamiltonian will follow in Section 2.4.1.

We construct the following Hamiltonian,

$$H_z = -g_S\mu_B\mathbf{B}\cdot\mathbf{S} - g_N\mu_B\mathbf{B}\cdot\mathbf{N} - g_I\mu_N\mathbf{B}\cdot\mathbf{I} - g_l\mu_B\left(\hat{S}_x\hat{B}_x + \hat{S}_y\hat{B}_y\right) \quad (2.35)$$

Here, g_S , g_N and g_I are the g -factors for the electron spin, rotation and nuclear spin respectively and μ_B is the Bohr magneton. The final term, expressed here as the anisotropic correction to the electron spin Zeeman interaction, arises due to unquenched orbital magnetic moment and g_l is its corresponding g -factor. B_x and S_x refer to the x -axis contribution from the magnetic field and electron spin in the molecule-fixed frame of reference. Both the rotational and anisotropic spin g -factors, g_N and g_l , show a significant dependence on the vibrational state. This shift is on the order of 10^{-2} between $v = 0$ and $v = 1$ and we will show in Section 2.2.4 how this enables rovibrational transitions that are otherwise forbidden.

On the signs of the Zeeman interaction

In Eq. (2.35) we have chosen to adopt a convention where the Zeeman terms are all given the same sign. The correct physical properties are then obtained by imposing different signs in the corresponding g -factors g_S, g_N, g_I and g_l . This convention is physically intuitive and allows us to determine the signs of the interactions by a classical analogy [56].

As an example, we compare the magnetic dipole moment, $\hat{\mu}$, of a free proton and a free electron in relation to their spin angular momentum vector,

$$\hat{\mu}_p = g_p \mu_B \hat{I} / \hbar \quad (2.36)$$

$$\hat{\mu}_s = -g_S \mu_B \hat{S} / \hbar \quad (2.37)$$

These relations follow from the Dirac equation for the electron and protons. We see that the magnetic moments of the proton and the electron are aligned parallel and anti-parallel, respectively, to their spin vector. This means that in a magnetic field, the proton spin will experience a torque in the direction of the magnetic field and the electron spin will experience a torque in the opposite direction. This is readily understood by analogy with a classical current loop.

The classical current, defined as the movement of positive charges, will produce a magnetic dipole pointing in the direction given by the right-hand rule as shown in Figure 2.2a. The proton spin is analogous to the rotation of a positive charge around its own axis. Although such a

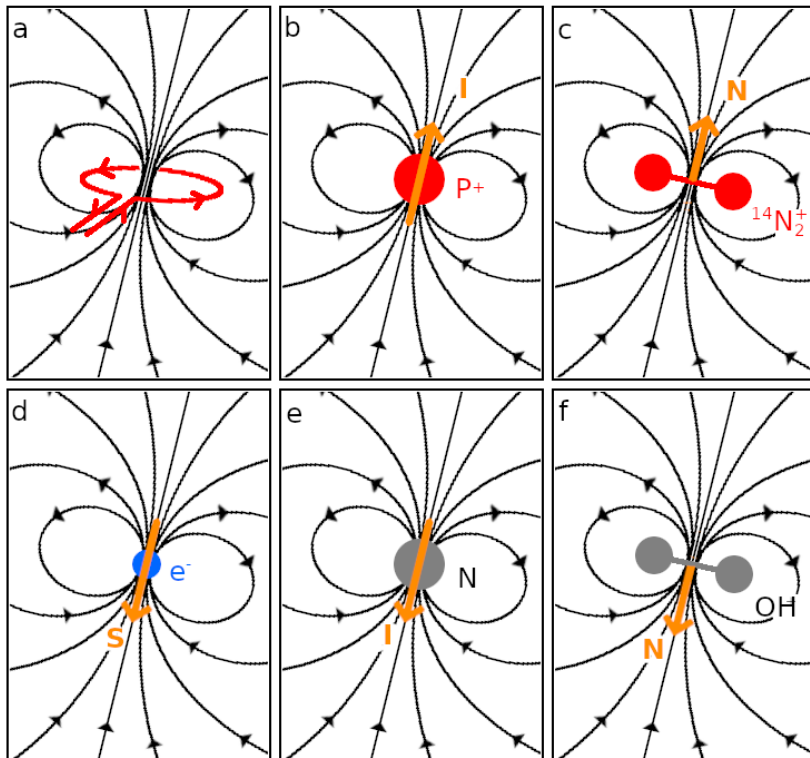


Fig. 2.2. The relationship between angular-momentum vectors (orange arrows) to the induced magnetic dipole for a) a classical current loop, b) a proton c) the rotation of a $^{14}\text{N}_2^+$ molecule d) an electron e) a neutron f) rotation of the OH molecule. The field direction (black arrows) is the same in all pictures while the angular momentum vector is inverted for the lower three figures.

rotation is nonphysical, the direction of its magnetic moment nevertheless agrees with the classical picture. We can apply a similar reasoning to all our Zeeman terms and adjust the sign of the g -factors accordingly.

The electron spin and orbital g -factors should be negative to reflect the fact that a negative charge produces a magnetic field opposite to its angular momentum vector. In the Hydrogen (^1H) nucleus this reasoning is also straightforward, but in any nuclei composed of several protons and neutrons the situation is more complicated and has to be calculated. The ^{14}N nucleus behaves more like the proton and the magnetic moment has a value of $\mu_I \approx 0.31\mu_N$. The ^{15}N nucleus has an additional neutron and behaves more like the free neutron with $\mu_I \approx -0.43\mu_N$, where μ_N is the nuclear magneton.

The rotational Zeeman term includes contributions from both the nuclei and electrons and by the above analogy we see that the nuclear contribution will always be positive as it corresponds to moving positive charges, given by [42],

$$g_N^{(\text{nuc.})} = \frac{m(Z_1 M_2^2 + Z_2 M_1^2)}{M_1 M_2 (M_1 + M_2)} \quad (2.38)$$

where Z_1 and M_1 are the charge and mass of the nucleus with index 1. The electronic contribution will largely cancel this nuclear contribution. An experiment or a numerical calculation can reveal whether g_N should be positive or negative depending on which contribution is larger. For example, in $^{14}\text{N}_2^+$ the contribution from the nuclei is larger than the electronic contribution, while in the ground state of the OH molecule the electronic contribution is larger [57].

The anisotropic correction term arises from a cross term in perturbation theory between the orbital magnetic moment $\mathbf{B} \cdot \mathbf{L}$ and the spin-orbit coupling $\mathbf{L} \cdot \mathbf{S}$. The contribution to the spin-rotation constant, γ_N , from the spin-orbit coupling arises due to a second order perturbation, where the sign information is lost and a physical intuition is difficult to attain. Instead, we rely on a numerical calculation by *Bruna & Grein* [58], where the anisotropic term is given the opposite sign as the electron-spin term.

The g -tensor

Just as we did with the sign of the Zeeman interaction, we may continue our 'abuse' of the effective g -factor to also include anisotropic effects. In any anisotropic environment, such as a molecule or a crystal lattice, the effective magnetic moment can be different along different directions corresponding to the effective magnetic field experienced by, e.g., the electron. Physically, the effect of magnetic shielding can be included by imposing different g -factors along different directions. The effective g -factor is then considered a tensor with 3×3 components. In most cases, the off-diagonal elements are ignored [54] and in the case of a diatomic molecule, $g_{xx} = g_{yy}$ due to the cylindrical symmetry. In our effective Hamiltonian of Eq. (2.35), we have included the effect of this cylindrical anisotropy through the additional g_l term where $g_l = g_{xx} = g_{yy}$. This term then reflects the magnetic moment of the residual orbital magnetic moment interacting with the electron spin.

The electron spin Zeeman interaction

We start by deriving a matrix expression for the interaction between the magnetic moment of the electron spin and an external magnetic field. Since N_2^+ has an unpaired electron and no electronic angular momentum in the $X^2\Sigma_g^+$ -state, this term is expected to have the biggest contribution to the Zeeman energies. The most basic representation of this Hamiltonian is the scalar product [54],

$$H_{Z,S} = -g_S\mu_B \mathbf{B} \cdot \mathbf{S}, \quad (2.39)$$

where $g_S\mu_B$ represents the magnetic moment of the electron. The effective constant g_S can differ from that of the free electron $g_e \approx 2.0023$ due to relativistic corrections or shielding corrections like the one discussed in the previous section.

The scalar product of two vectors $\mathbf{B} \cdot \mathbf{S}$ can be expressed in spherical tensor notation as the product of two first-rank tensors

$$T^1(\mathbf{B}) \cdot T^1(\mathbf{S}). \quad (2.40)$$

This is a shorthand notation for,

$$\sum_p (-1)^p T_p^1(\mathbf{B}) \cdot T_{-p}^1(\mathbf{S}), \quad (2.41)$$

where p specifies one of three tensor components related to the cartesian (X, Y, Z) components as,

$$T_0^1(\mathbf{S}) = S_Z \quad (2.42)$$

$$T_1^1(\mathbf{S}) = -\frac{1}{\sqrt{2}}(S_X + iS_Y) \quad (2.43)$$

$$T_{-1}^1(\mathbf{S}) = \frac{1}{\sqrt{2}}(S_X - iS_Y) \quad (2.44)$$

This definition ensures that the tensor components transform under rotations as,

$$T_p^k = \sum_{p'} D_{pp'}^k T_{p'}^k, \quad (2.45)$$

where $D_{pp'}^k$ is an irreducible representation of the rotation group of rank k or the so called 'rotation matrix' [42].

The Cartesian components, S_i , may refer to any orthonormal coordinate system and is usually chosen as either the lab-fixed coordinate system (subscript p), represented here by the uppercase Latin letters (X, Y, Z), in which lasers and external fields are defined or the molecule-fixed coordinate system (subscript q), represented by the lowercase letters (x, y, z), which rotates in space with the molecule. The z -component commonly refers to the principal molecular axis which, e.g., defines the molecular electric dipole moment or symmetry axis. Both coordinate systems have their origin at the center of mass of the molecule. Either coordinate system can be used in principle and should lead to the same matrix expressions as the other. The choice is often made to simplify the derivation.

The external magnetic field is defined in the space-fixed coordinates and in a Hund's case (b) system, the coupling of the electron spin to the

molecular axis is weak. Therefore this Hamiltonian is readily evaluated in lab-fixed coordinates⁸.

Using the list of standard results from spherical tensor algebra in Appendix A, the derivation of the matrix expression for this interaction is straightforward. The procedure is to successively decouple the matrix element from the coupled Hund's case ($b_{\beta,J}$) basis states $|N, S, J, I, F, M_F\rangle$ to the point where the operator $T^1(\mathbf{S})$ can act on a pure spin basis $|S\rangle$, for which the eigenvalues are known.

We begin by first applying the well known Wigner-Eckart (W.E.) theorem, from Eq. (A.6) in Appendix A, to obtain a reduced matrix element which no longer depends on the projection quantum number, M_F , or the magnetic field direction, p' .

$$\begin{aligned} \langle N', S', J', I', F', M'_F | \mathbf{B} \cdot \mathbf{S} | N, S, J, I, F, M_F \rangle = & \quad (2.46) \\ T_{-p'}^1(\mathbf{B}) (-1)^{p'} (-1)^{F' - M'_F} \begin{pmatrix} F' & 1 & F \\ -M'_F & p' & M_F \end{pmatrix} \\ \times \langle N', S', J', I', F' | T^1(\mathbf{S}) | N, S, J, I, F \rangle. \end{aligned}$$

The quantity in parenthesis is a Wigner 3j symbol [43]. The operator $T_{-p'}^1(\mathbf{B})$ represents the field strength and direction of the magnetic field and therefore does not impact our angular-momentum states other than by defining the space-fixed projection of the spin operator, p' ⁹. It can therefore be moved outside the bra-ket. The reduced matrix element no longer depends on the spatial coordinates, p , and we can drop the subscript from the spherical tensor operator $T^1(\mathbf{S})$.

In order to separate the electron-spin basis $|S\rangle$, we must first to decouple it from the nuclear spin and then from rotations, i.e., from the total

⁸The Hamiltonian expressed in this coordinate system is also suitable for evaluation in the Paschen-Back regime, where the external field is so strong that the magnetic moments decouple from each other, although a different uncoupled basis set should be used. A matrix element suitable for the Paschen-Back regime is derived for the rotational Zeeman effect in Appendix B.3.

⁹In order to keep the derived expressions general for static fields and linear laser polarization as well as for circularly polarized light, we have picked out a single tensor component from Eq. (2.41) and replaced the sum over p with an arbitrary component p' . This poses no problems if the magnetic field is adequately described by a single tensor component. If we wish to consider arbitrary polarizations of the incoming field, the sum over p can be reintroduced without additional changes to the derived expression.

angular momentum vectors F and J . This procedure corresponds to separating the coupled wavefunction into its constituent uncoupled basis functions and assumes that our spin operator does not act on the nuclear or rotational wavefunctions.

First, we apply Eq. (A.9), from Appendix A, which takes care of decoupling the nuclear spin, I , from the J angular momentum state. For a first rank tensor operator that only acts on the first part of the coupled, $F = J + I$, system, we have,

$$\begin{aligned} & \langle N', S', J', I', F' | T^1(\mathbf{S}) | N, S, J, I, F \rangle \\ &= \delta_{II'} (-1)^{F+J'+I'+1} \sqrt{(2F'+1)(2F+1)} \begin{Bmatrix} J' & F' & I \\ F & J & 1 \end{Bmatrix} \\ & \times \langle N', S', J' | T^1(\mathbf{S}) | N, S, J \rangle. \end{aligned} \quad (2.47)$$

The term in curly brackets is a Wigner 6j symbol [43]. In this equation, the Kronecker delta appears as a result of the orthogonality of our zero-order nuclear-spin basis. As we assume that the tensor operator does not act on these functions, we have $\langle I' | I \rangle = \delta_{I'I}$.

We further decouple the electron spin from the rotational angular momentum by applying a similar equation, Eq. (A.10), that takes care of decoupling for the case of a tensor operator acting on the second part of a coupled $J = N + S$ system,

$$\begin{aligned} & \langle N', S', J' | T^1(\mathbf{S}) | N, S, J \rangle \\ &= \delta_{NN'} (-1)^{J'+N+S+1} \sqrt{(2J'+1)(2J+1)} \begin{Bmatrix} S & J' & N \\ J & S & 1 \end{Bmatrix} \\ & \times \langle S' | T^1(\mathbf{S}) | S \rangle. \end{aligned} \quad (2.48)$$

Here, the Kronecker delta $\delta_{N'N}$ appears for the same reason as for the nuclear spin wavefunctions above, from the orthogonality of our zero-order rotational basis states.

The fully decoupled and projection-reduced matrix element is now evaluated through a standard result, Eq. (A.7) in Appendix A,

$$\langle S' | T^1(\mathbf{S}) | S \rangle = \delta_{S'S} \sqrt{S(S+1)(2S+1)}. \quad (2.49)$$

Here, the quantum numbers S are not operators and can be moved out of the bra-ket and the Kronecker delta condition $\delta_{S'S}$ results from the orthogonality of our zero-order spin basis states.

Finally putting together Equations (2.46), (2.47), (2.48) and (2.49) we find,

$$\begin{aligned}
& \langle N', S', J', I', F', M'_F | \mathbf{B} \cdot \mathbf{S} | N, S, J, I, F, M_F \rangle \\
& = T_{-p'}^1(\mathbf{B}) \delta_{NN'} \delta_{SS'} \delta_{II'} (-1)^{p'} (-1)^{F'+F-M'_F+2J'+N+S+I} \\
& \times \sqrt{(2F'+1)(2F+1)(2J'+1)(2J+1)S(S+1)(2S+1)} \\
& \times \begin{pmatrix} F' & 1 & F \\ -M'_F & p' & M_F \end{pmatrix} \begin{Bmatrix} J' & F' & I \\ F & J & 1 \end{Bmatrix} \begin{Bmatrix} S & J' & N \\ J & S & 1 \end{Bmatrix}. \quad (2.50)
\end{aligned}$$

The off-diagonal terms of this expression that lead to mixing of basis states can now be read from the delta conditions $\delta_{NN'} \delta_{SS'} \delta_{II'}$ and the triangle conditions of the Wigner 3j and 6j symbols. For example, by the sum rule $m_1 + m_2 + m_3 = 0$ in the lower row of the 3j symbol we see that nonzero $\Delta M_F = 0, \pm 1$ terms are obtained through the $p' = 0, \pm 1$ as expected for π - and σ -polarized light, respectively. There are no conditions that forbid $F' \neq F$ or $J' \neq J$ terms and this term therefore mixes states with the same value of N, S, I, M_F but different in the J and F quantum numbers.

We have yet to specify the form of $T_{-p'}^1(\mathbf{B})$ which could be static or oscillating in any direction. If we define the magnetic field to be static along the Z -direction of our lab-fixed coordinates, then $T_0^1(\mathbf{B}) = B_Z$ and we obtain,

$$\begin{aligned}
& \langle N', S', J', I', F', M'_F | \mathbf{B} \cdot \mathbf{S} | N, S, J, I, F, M_F \rangle \\
& = B_Z \delta_{NN'} \delta_{SS'} \delta_{II'} (-1)^{F'+F-M'_F+2J'+N+S+I} \\
& \times \sqrt{(2F'+1)(2F+1)(2J'+1)(2J+1)S(S+1)(2S+1)} \\
& \times \begin{pmatrix} F' & 1 & F \\ -M'_F & 0 & M_F \end{pmatrix} \begin{Bmatrix} J' & F' & I \\ F & J & 1 \end{Bmatrix} \begin{Bmatrix} S & J' & N \\ J & S & 1 \end{Bmatrix}. \quad (2.51)
\end{aligned}$$

This expression is identical to the matrix element derived for N_2^+ in Ref. [23] and for a nonlinear symmetric top molecule in Ref. [54].

In Appendix B.1, we have derived the matrix expression for this Hamiltonian in a Hund's case ($a_{\beta,J}$) basis which is useful for evaluating the first excited $A^2\Pi_u$ -state of N_2^+ . In Appendix B.2, we present another useful technique by transforming the case (b) basis into superpositions of the case (a) basis states. These expressions are useful in the intermediate case between Hund's case (a) and (b) or when an interaction is better described in different quantum numbers. We then show the equivalence of the expression derived in this way with Eq. (2.50) above.

The rotational Zeeman interaction

As the charges in the molecule rotate in space, a magnetic dipole moment is induced which will interact with the external magnetic field. The magnetic dipole induced by the nuclei are to a large degree cancelled by the magnetic dipole induced by the electrons which closely follow the nuclear rotation. The resulting magnetic dipole therefore depends on the specific molecule and electronic state and the corresponding g_N , can take both positive and negative values as mentioned in Section 2.1.3. The effective Hamiltonian expressed in spherical tensor notation reads [42],

$$H_{Z,N} = -g_N \mu_B T^1(\mathbf{B}) \cdot T^1(\mathbf{N}), \quad (2.52)$$

and is readily evaluated in space-fixed coordinates. Like before, we apply the W.E. theorem to remove the dependence on the lab-fixed projection and obtain the reduced matrix element,

$$\begin{aligned} & \langle N', S', J', I', F', M'_F | \mathbf{B} \cdot \mathbf{N} | N, S, J, I, F, M_F \rangle \\ &= T^1_{-p'}(\mathbf{B}) (-1)^{p'} (-1)^{F'-M'_F} \begin{pmatrix} F' & 1 & F \\ -M'_F & p' & M_F \end{pmatrix} \\ & \times \langle N', S', J', I', F' | T^1(\mathbf{N}) | N, S, J, I, F \rangle \end{aligned} \quad (2.53)$$

We decouple the angular momenta F and J in two steps, first applying Eq. (A.9) for a tensor operator that acts on the first part of a coupled scheme, $F = J + I$,

$$\begin{aligned} & \langle N', S', J', I', F' | T^1(\mathbf{N}) | N, S, J, I, F \rangle \\ &= \delta_{II'} (-1)^{F+J'+I'+1} \sqrt{(2F'+1)(2F+1)} \\ & \times \begin{Bmatrix} J' & F' & I \\ F & J & 1 \end{Bmatrix} \langle N', S', J' | T^1(\mathbf{N}) | N, S, J \rangle. \end{aligned} \quad (2.54)$$

We apply the same equation again to the remaining matrix element, this time to decouple the rotational angular momentum from the electron spin, $J = N + S$,

$$\begin{aligned} & \langle N', S', J' | T^1(\mathbf{N}) | N, S, J \rangle \\ &= \delta_{NN'} (-1)^{N'+S'+J+1} \sqrt{(2J'+1)(2J+1)} \\ & \times \begin{Bmatrix} N' & J' & S' \\ J & N & 1 \end{Bmatrix} \langle N' | T^1(\mathbf{N}) | N \rangle \end{aligned} \quad (2.55)$$

The fully decoupled matrix element is evaluated using Eq (A.7) as,

$$\langle N' | T^1(\mathbf{N}) | N \rangle = \delta_{N'N} \sqrt{N(N+1)(2N+1)}, \quad (2.56)$$

where once again the Kronecker delta implies orthogonality of the rotational basis states $\langle N' | N \rangle$. Putting together Equations (2.53), (2.54), (2.55) and (2.56), we obtain the matrix element,

$$\begin{aligned} & \langle N', S', J', I', F', M'_F | \mathbf{B} \cdot \mathbf{N} | N, S, J, I, F, M_F \rangle \\ &= T_{-p'}^1(\mathbf{B}) (-1)^{p'} \delta_{NN'} \delta_{SS'} \delta_{II'} (-1)^{F'+F-M'_F+J'+J+N'+S'+I} \\ & \times \sqrt{(2F'+1)(2F+1)(2J'+1)(2J+1)N(N+1)(2N+1)} \\ & \times \begin{pmatrix} F' & 1 & F \\ -M'_F & p' & M_F \end{pmatrix} \begin{Bmatrix} J' & F' & I \\ F & J & 1 \end{Bmatrix} \begin{Bmatrix} N & J' & S' \\ J & N & 1 \end{Bmatrix}. \end{aligned} \quad (2.57)$$

This matrix expression has nonzero values for $J' \neq J$ and $F' \neq F$. The matrix expression for the rotational Zeeman effect was derived in Ref. [54] for a symmetric top molecule, of which a diatomic molecule is a special case. By inserting $K = 0$, i.e. a vanishing rotational angular-momentum

projection on the molecular axis, and by defining the magnetic field direction as $T_0^1(\mathbf{B}) = B_Z$ both expressions agree.

This matrix element was derived in Appendix B.3 in the uncoupled basis to illustrate another useful technique and to show its equivalence with Eq. (2.57). The uncoupled form is particularly useful when the coupling operator includes projection quantum numbers that have been omitted in the coupled representation, e.g. for evaluation in the Paschen-Back regime.

The nuclear spin Zeeman interaction

Any unpaired spins in the atomic nuclei of the molecule have an associated magnetic moment. In the low-field regime we can consider both nuclei in a coupled representation, $I_1 + I_2 = I$, and consider the interaction with the total nuclear spin as a single quantum number. Due to the mass difference between the electron and nucleons, the nuclear magneton, μ_N , is $\sim 10^3$ times weaker than the Bohr magneton, μ_B .

The interaction with the total spin, I , is written in spherical tensor form as [54],

$$H_{Z,I} = -g_I \mu_N T^1(\mathbf{B}) \cdot T^1(\mathbf{I}). \quad (2.58)$$

As the nuclear spins do not couple strongly to the molecular axis in the subscript- β Hund's cases, it is readily evaluated in space-fixed coordinates.

We apply the W.E. theorem to obtain the reduced matrix element which no longer depends on the space projection, M_F ,

$$\begin{aligned} & \langle N', S', J', I', F', M'_F | \mathbf{B} \cdot \mathbf{I} | N, S, J, I, F, M_F \rangle \\ &= T_{-p'}^1(\mathbf{B}) (-1)^{p'} (-1)^{F' - M'_F} \begin{pmatrix} F' & 1 & F \\ -M'_F & p' & M_F \end{pmatrix} \\ & \times \langle N', S', J', I', F' | T^1(\mathbf{I}) | N, S, J, I, F \rangle. \end{aligned} \quad (2.59)$$

We need to decouple I from J in order to isolate the nuclear spin basis. We therefore apply Eq. (A.10) for a tensor operator which acts on the second part of a coupled scheme $F = J + I$,

$$\begin{aligned} & \langle N', S', J', I', F' | T^1(\mathbf{I}) | N, S, J, I, F \rangle \\ &= \delta_{JJ'} (-1)^{F'+J'+I+1} \sqrt{(2F'+1)(2F+1)} \begin{Bmatrix} I & F' & J \\ F & I & 1 \end{Bmatrix} \\ & \times \langle N' S' J' | N, S, J \rangle \langle I' | T^1(\mathbf{I}) | I \rangle. \end{aligned} \quad (2.60)$$

The eigenvalues of the fully decoupled matrix elements are given by,

$$\langle I' | T^1(\mathbf{I}) | I \rangle = \delta_{I'I} \sqrt{I(I+1)(2I+1)} \quad (2.61)$$

$$\langle N' S' J' | N, S, J \rangle = \delta_{N'N} \delta_{S'S} \delta_{J'J}. \quad (2.62)$$

Finally, putting together Equations (2.59), (2.60) and (2.61), we have,

$$\begin{aligned} & \langle N', S', J', I', F', M'_F | \mathbf{B} \cdot \mathbf{I} | N, S, J, I, F, M_F \rangle \\ &= T_{-p'}^1(\mathbf{B}) (-1)^{p'} \delta_{JJ'} \delta_{NN'} \delta_{SS'} \delta_{II'} (-1)^{2F'-M'_F+J'+I+1} \\ & \times \sqrt{(2F'+1)(2F+1)I(I+1)(2I+1)} \begin{pmatrix} F' & 1 & F \\ -M'_F & p' & M_F \end{pmatrix} \begin{Bmatrix} I & F' & J \\ F & I & 1 \end{Bmatrix}. \end{aligned} \quad (2.63)$$

We see that the interaction due to the nuclear spin mixes states of different F quantum numbers. By inserting $T_0^1(\mathbf{B}) = B_Z$, this matrix element agrees with the one derived in Ref. [54].

The anisotropic electron spin Zeeman interaction

This term in the Zeeman Hamiltonian arises from the magnetic interaction between orbital angular momentum and the electron spin. The orbital angular momentum alters the effective \mathbf{B} -field to which the electron spin couples. This gives rise to an anisotropy which can be incorporated in the electronic g-tensor [53, 59] or treated as a separate term in the Hamiltonian, as we shall show here. In the $X^2\Sigma_g^+$ ground state, such orbital angular momentum arises only due to the spin-orbit mixing with higher electronic states, mainly the $A^2\Pi_u$ -state [58].

The contribution along the principal molecular axis, g_{zz} , can be incorporated in the electron orbital g -factor and is not considered here. The perpendicular components, however, must be treated separately and the Hamiltonian is given by [42],

$$H_{Z,aS} = -g_l \mu_B (B_x S_x + B_y S_y) \quad (2.64)$$

The effective g -factor, g_l , then incorporates the mixing amplitude to other electronic states as well as the spin-orbit coupling strength. *Curl* derived an approximate relation between g_l and the spin-rotation constant γ_N [53]. As mentioned in section 2.1.2, the spin-rotation constant γ_v includes higher order contributions from spin-orbit coupling. This is often the dominant contribution since the magnetic moment due to rotations is very weak, as can be seen from Table 2.2. In the limit where the spin-rotation constant γ_N consists mainly of the contribution from spin-orbit interaction, the strength of g_l is related to γ_v by [53],

$$g_l \approx -\frac{\gamma_v}{2B_e}. \quad (2.65)$$

More precise values can be obtained by ab-initio calculations as reported by *Bruna & Grein* [58] for the $^{14}\text{N}_2^+$ molecule.

In order to simplify the derivation of the matrix expressions, we begin by rewriting the Hamiltonian of Eq. (2.64) in spherical tensor form. Using Equation (2.42) we can relate the operators to their spherical tensor form,

$$B_x S_x + B_y S_y = \sum_q T_{-q}^1(\mathbf{B}) T_q^1(\mathbf{S}) - B_z S_z \quad (2.66)$$

The last term above is just the zeroth component $T_0^1(\mathbf{B}) T_0^1(\mathbf{S})$ and therefore,

$$B_x S_x + B_y S_y = \sum_{q=\pm 1} T_{-q}^1(\mathbf{B}) T_q^1(\mathbf{S}). \quad (2.67)$$

As the magnetic field \mathbf{B} is defined in our lab coordinates, we transform the coordinate system using Eq. (2.45),

$$\begin{aligned} \sum_{q=\pm 1} T_{-q}^1(\mathbf{B})T_q^1(\mathbf{S}) &= \sum_{q=\pm 1} \sum_p D_{pq}^1(\omega)^* T_p^1(\mathbf{B})T_q^1(\mathbf{S}) \\ &= B_Z \sum_{q=\pm 1} D_{0q}^1(\omega)^* T_q^1(\mathbf{S}), \end{aligned} \quad (2.68)$$

where we have once again defined the magnetic field along the Z direction, $T_{p=0}^1(\mathbf{B}) = B_Z$.

We may also rewrite this expression in the form,

$$\begin{aligned} B_Z \sum_{q=\pm 1} D_{0q}^1(\omega)^* T_q^1(\mathbf{S}) &= B_Z \sum_q D_{0q}^1(\omega) T_q^1(\mathbf{S}) - D_{00}^1(\omega)^* T_{q=0}^1(\mathbf{S}) \\ &= B_Z T_p^1(\mathbf{S}) - D_{00}^1(\omega)^* T_{q=0}^1(\mathbf{S}). \end{aligned} \quad (2.69)$$

This form of the Hamiltonian may simplify the derivation, as we have already derived an expression for the first term in Section 2.1.3. We may then simply add g_l to the effective g -factor of the electron-spin Zeeman Hamiltonian, as $g_S = g_e + g_l$, and derive an expression for the second term of Eq. (2.69) which now represents a single component, S_z , in the molecule-fixed basis. In Appendix B.4 we derive the matrix expression using the form of Eq. (2.69) by transforming our Hund's case (b) basis to the case (a) basis. This simplifies the derivation as the operator S_z naturally lends itself to be evaluated using Hund's case (a) quantum numbers.

If we also aim to evaluate the electron-spin operator $T_q^1(\mathbf{S})$ in the lab-fixed coordinates, which is more suitable for a Hund's case (b) system, we must rotate into these coordinates using another Wigner rotation matrix from Eq. (2.45),

$$B_Z \sum_{q=\pm 1} D_{0q}^1(\omega)^* T_q^1(\mathbf{S}) = B_Z \sum_{q=\pm 1} \sum_{p'} D_{0q}^1(\omega)^* D_{p'q}^1(\omega) T_{p'}^1(\mathbf{S}) \quad (2.70)$$

Now, using the conjugation relation $D_{0q}^1(\omega)^* = (-1)^{-q}D_{0,-q}^1(\omega)$ and by expressing the two consecutive rotations as a single rotation, using Eq. (A.4), we obtain,

$$D_{0,-q}^1(\omega)D_{p'q}^1(\omega) = \sum_{k=0,1,2} (2k+1) \begin{pmatrix} 1 & 1 & k \\ 0 & p' & -p' \end{pmatrix} \begin{pmatrix} 1 & 1 & k \\ -q & q & 0 \end{pmatrix} D_{-p',0}^k(\omega)^*. \quad (2.71)$$

The Hamiltonian then becomes,

$$\begin{aligned} \frac{H_{aS}}{-g_l\mu_B B_Z} &= \sum_{q=\pm 1} (-1)^q \sum_{k=0}^2 (2k+1) \begin{pmatrix} 1 & 1 & k \\ -q & q & 0 \end{pmatrix} \\ &\times \sum_{p'} \begin{pmatrix} 1 & 1 & k \\ 0 & p' & -p' \end{pmatrix} D_{-p',0}^k(\omega)^* T_p^1(S). \end{aligned} \quad (2.72)$$

By the definition from Eq. (A.2), the last sum over p' in the equation above is exactly a first order tensor product, $-(3)^{-1/2}W_0^1(D^k, T^1)$, i.e.,

$$\begin{aligned} W_0^1(D^k(\omega), T^1(S)) &= \sum_{p'} D_{p',0}^k(\omega)^* T_{-p'}^1(S) (-1)^{-k+1} \\ &\times \sqrt{3} \begin{pmatrix} 1 & 1 & k \\ 0 & p' & -p' \end{pmatrix} (-1)^{k+2}, \end{aligned} \quad (2.73)$$

where the last phase factor comes from a permutation of the 3j symbol in Eq. (A.2) to fit our Hamiltonian. Now, the Hamiltonian takes the form,

$$\frac{H_{aS}}{-g_l\mu_B B_Z} = \sum_{q=\pm 1} (-1)^{q+1} \sum_{k=0}^2 (2k+1) \begin{pmatrix} 1 & 1 & k \\ -q & q & 0 \end{pmatrix} \frac{1}{\sqrt{3}} W_0^1(D^k(\omega), T^1(S)). \quad (2.74)$$

Because of the triangle conditions of the 3j symbol, the sum over k only runs over $k = 0, 2$.

We shall now derive the matrix expressions for the anisotropic spin Hamiltonian using the Hamiltonian form in Equation (2.74), in a coupled Hund's

case $(b_{\beta,J})$ representation. We first apply the W.E. theorem to obtain the space-reduced matrix element,

$$\begin{aligned}
& \langle N'\Lambda', S', J', I', F' M'_F | H_{aS} | N\Lambda, S, J, I, F, M_F \rangle / (-g\mu_B B_Z) \\
&= \frac{1}{\sqrt{3}} \sum_q (-1)^{q+1} \sum_k (2k+1) \begin{pmatrix} 1 & 1 & k \\ -q & q & 0 \end{pmatrix} (-1)^{F'-M'_F} \\
&\times \begin{pmatrix} F' & 1 & F \\ -M'_F & 0 & M_F \end{pmatrix} \langle N'\Lambda', S', J', I', F' | W_0^1(D^k, T^1) | N\Lambda, S, J, I, F \rangle.
\end{aligned} \tag{2.75}$$

Next, we decouple the J and I quantum numbers using Eq. (A.9),

$$\begin{aligned}
& \langle N'\Lambda', S', J', I', F' | W_0^1(D^k, T^1) | N\Lambda, S, J, I, F \rangle \\
&= \delta_{II'} (1)^{F+J'+I'+1} \sqrt{(2F'+1)(2F+1)} \begin{Bmatrix} J & F & I' \\ F' & J & 1 \end{Bmatrix} \\
&\times \langle N'\Lambda', S', J' | W_0^1(D^k, T^1) | N\Lambda, S, J \rangle.
\end{aligned} \tag{2.76}$$

We may now evaluate the reduced matrix element using Eq. (A.11) which evaluates the reduced matrix elements of a tensor product in a coupled scheme. This standard result takes care of decoupling and reduction of the projection dependence of two separate coupled systems in a single Wigner 9j symbol, and we obtain,

$$\begin{aligned}
& \langle N'\Lambda', S', J' | W_0^1(D^k, T^1) | N\Lambda, S, J \rangle \\
&= \sqrt{3} \sqrt{(2J'+1)(2J+1)} \begin{Bmatrix} J' & J & 1 \\ N' & N & k \\ S' & S & 1 \end{Bmatrix} \\
&\times \langle N'\Lambda' | D_{.0}^k(\omega)^* | N\Lambda \rangle \langle S' | T^1(S) | S \rangle.
\end{aligned} \tag{2.77}$$

We evaluate the two remaining matrix elements using the eigenvalue relations from Eq. (A.7) and Eq. (A.5) and by combining the equations above we arrive at,

$$\begin{aligned}
& \langle N'\Lambda', S', J', I', F', M'_F | H_{aS} | N\Lambda, S, J, I, F, M_F \rangle \\
&= -g_I \mu_B B_Z \delta_{S'S} \delta_{I'I} (-1)^{F'-M'_F+F+J'+I'+1+N'-\Lambda'} \begin{pmatrix} F' & 1 & F \\ -M'_F & 0 & M_F \end{pmatrix} \\
&\times \sqrt{(2F'+1)(2F+1)(2J'+1)(2J+1)} \\
&\times \sqrt{(2N'+1)(2N+1)S(S+1)(2S+1)} \\
&\times \sum_q (-1)^q \sum_k (2k+1) \begin{pmatrix} 1 & 1 & k \\ -q & q & 0 \end{pmatrix} \begin{pmatrix} N' & k & N \\ -\Lambda' & 0 & \Lambda \end{pmatrix} \\
&\times \begin{Bmatrix} J & F & I' \\ F' & J & 1 \end{Bmatrix} \begin{Bmatrix} J' & J & 1 \\ N' & N & k \\ S' & S & 1 \end{Bmatrix}. \tag{2.78}
\end{aligned}$$

We also note that all terms containing q are invariant to $q = \pm 1$ and we can drop the sum to obtain,

$$\begin{aligned}
& \langle N'\Lambda', S', J', I', F', M'_F | H_{aS} | N\Lambda, S, J, I, F, M_F \rangle \\
&= -g_I \mu_B B_Z \delta_{S'S} \delta_{I'I} (-1)^{F'-M'_F+F+J'+I'+N'-\Lambda'} \begin{pmatrix} F' & 1 & F \\ -M'_F & 0 & M_F \end{pmatrix} \\
&\times \sqrt{(2F'+1)(2F+1)(2J'+1)(2J+1)} \\
&\times \sqrt{(2N'+1)(2N+1)S(S+1)(2S+1)} \\
&\times 2 \sum_k (2k+1) \begin{pmatrix} 1 & 1 & k \\ -1 & 1 & 0 \end{pmatrix} \begin{pmatrix} N' & k & N \\ -\Lambda' & 0 & \Lambda \end{pmatrix} \\
&\times \begin{Bmatrix} J & F & I' \\ F' & J & 1 \end{Bmatrix} \begin{Bmatrix} J' & J & 1 \\ N' & N & k \\ S' & S & 1 \end{Bmatrix}. \tag{2.79}
\end{aligned}$$

This matrix expression mixes states of different N , J and F quantum numbers. By evaluating the 3j symbol with $(1, 1, k)$ in the upper row analytically, we find that this matrix expression is equivalent to the one derived in Ref. [54].

2.1.4 Numerical evaluation of the effective Hamiltonian

The complete Hamiltonian given in Eq. (2.14) was diagonalized numerically to obtain the eigenvalues and eigenvectors, i.e. the energies and mixing coefficients c_i^k , of the molecular states. The numerical diagonalization yields all-order solutions that are more suitable than a perturbation approach for describing molecules which do not conform exactly to a specific Hund's case.

A basis set including 2 vibrational states ($v = 0, 1$), 3 rotational states ($N = 0, 2, 4$), 2 nuclear configurations ($I = 0, 2$) and all resulting fine-structure, hyperfine and Zeeman states was used for a total of 360 states. The built in `eig()` function in MATLAB [60] was used for diagonalization and takes ~ 4 s to complete for a single magnetic field value on a desktop computer¹⁰. The computational time is reduced by adding the selection rules and triangle conditions of the Wigner symbols as conditions before computing the matrix elements in order to avoid calculating vanishing elements. Another technique to improve the computational time is to order the basis states according to selection rules, e.g. by value of M_F which remains a good quantum number, such that the final sparse Hamiltonian matrix becomes block diagonal. Using block-diagonal solvers, the computational time is then greatly reduced [61]. Tables 2.2 and 2.3 show the parameters used in the Hamiltonian.

¹⁰CPU: Intel Core i7-8559U @ 2.70GHz, RAM 16 GB

$^{14}\text{N}_2^+$	$v = 0$	$v = 1$
$G_v - G_0$ (cm^{-1})	0	2174.746(1) [62]
B_v (cm^{-1})	1.9223897(53) [63]	1.90330(2) [64]
D_v ($\times 10^6 \text{ cm}^{-1}$)	5.9748(50) [63]	5.904(21) [64]
γ_v (MHz)	280.25(45) [65]	276.92253(13) [51]
γ_{Dv} (kHz)	0	-0.39790(23) [51]
b_{Fv} (MHz)	102.4(1.1) [65]	100.6040(15) [51]
t_v (MHz)	23.3(1.0) [65]	28.1946(13) [51]
t_{Dv} (Hz)	0 [65]	-73.5(2.7) [51]
eQq_v (MHz)	–	0.7079(60) [51]
c_{Iv} (kHz)	–	11.32(85) [51]
$g_s\mu_B$ (MHz/G)	-2.8025 [66, 67]	-2.8025 [66, 67]
$g_r\mu_B$ (Hz/G)	50.107 [67]	49.547 [67]
$g_n\mu_N$ (Hz/G)	307.92 [67]	307.92 [67]
$g_l\mu_B$ (Hz/G)	3793 [58]	3821 [58]
Q (ea_0^2)	1.86 [58]	1.89*
R_e (a_0)	2.13 [58]	2.14*
$\frac{dQ}{dR}$ (ea_0)	2.63 [58]	–

Tab. 2.2. Molecular parameters of $^{14}\text{N}_2^+$ in $v = 0$ and $v = 1$ vibrational states of the electronic ground state, $X^2\Sigma_g^+$, that was used to calculate the energy levels. The numbers in parentheses are uncertainties given in the literature. * Values are estimated from the vibrational variation of other constants as described in the text.

$^{15}\text{N}_2^+$	$v = 0$	$v = 1$
$G_v - G_0$ (cm^{-1})	–	2101.45 [67]
B_v (cm^{-1})	–	1.777794 (16) [65]
D_v ($\times 10^6 \text{ cm}^{-1}$)	–	5.299 (57) [65]
γ_v (MHz)	–	258.55708 (26) [65]
γ_{Dv} ($\times 10^4$) (MHz)	–	-3.4640 (35) [65]
$g_S\mu_B$ (MHz/G)	-2.8025 [67]	-2.8025 [67]
$g_N\mu_B$ (Hz/G)	46.748 [67]	46.328 [67]
$g_I\mu_B$ (Hz/G)	429.69 [67]	429.69 [67]

Tab. 2.3. Molecular parameters of $^{15}\text{N}_2^+$ in $v = 0$ and $v = 1$ vibrational states of the electronic ground state, $X^2\Sigma_g^+$, that was used to calculate the energy levels. The numbers in parentheses are uncertainties given in the literature.

2.1.5 Magic clock transitions and state mixing

In Table 2.4, we show the calculated mixing coefficients of three example levels in the rovibrational ground state with an external magnetic field value of $B = 10$ G. Vibrational mixing is omitted in these data for simplicity. We note that even in the absence of hyperfine interaction, $I = 0$, there is mixing of all quantum numbers except M_F . This is a result of our zero-order basis states that fail to perfectly describe our system. The effect of mixing on the energy of the quantum states is relatively small, typically below 5 kHz from N , J and F mixing with the exception of rovibrational mixing which was found to be 6 MHz in $v = 0$, $N = 2$ and is included in the centrifugal distortion constant, D_v . The mixing, however, proves important for the apparent breaking of selection rules in the electric dipole forbidden molecular spectra presented in Section 2.2. Mixing also causes deviations from linearity with respect to magnetic field of the Zeeman levels which allows for 'magic' clock transitions as described below.

State $ \psi_k\rangle_p$	$c_i \cdot \mathbf{N}, \mathbf{S}, \mathbf{J}, \mathbf{I}, \mathbf{F}, \mathbf{M}_F\rangle_i$
$N = 0, I = 0$ $F = 1/2, M_F = 1/2$	$\sim 1.0000 \cdot 0, 1/2, 1/2, 0, 1/2, 1/2\rangle$ $-1.12 \cdot 10^{-6} \cdot \mathbf{2}, 1/2, 5/2, \mathbf{2}, 1/2, 1/2\rangle$ $-9.16 \cdot 10^{-7} \cdot \mathbf{2}, 1/2, 3/2, \mathbf{2}, 1/2, 1/2\rangle$ $+2.59 \cdot 10^{-8} \cdot \mathbf{2}, 1/2, 3/2, 0, 3/2, 1/2\rangle$
$N = 0, I = 2$ $F = 5/2, M_F = 1/2$	$-0.9986 \cdot 0, 1/2, 1/2, 2, 5/2, 1/2\rangle$ $-0.052 \cdot 0, 1/2, 1/2, 2, 3/2, 1/2\rangle$ $+1.26 \cdot 10^{-4} \cdot \mathbf{2}, 1/2, 3/2, 2, 5/2, 1/2\rangle$ $+5.26 \cdot 10^{-6} \cdot \mathbf{2}, 1/2, 3/2, 2, 3/2, 1/2\rangle$
$N = 2, I = 2$ $J = 5/2, F = 3/2$ $M_F = 1/2$	$-0.9625 \cdot 2, 1/2, 5/2, 2, 3/2, 1/2\rangle$ $-0.180 \cdot 2, 1/2, 5/2, 2, 1/2, 1/2\rangle$ $-0.178 \cdot 2, 1/2, 3/2, 2, 3/2, 1/2\rangle$ $+0.095 \cdot 2, 1/2, 5/2, 2, 5/2, 1/2\rangle$

Tab. 2.4. The four leading mixing coefficients, c_i^k , for three states in the vibrational ground state. The vibrational mixing is not included. The left column shows the label for the state which dominates the mixing coefficients at $B = 0$ and the right column shows the mixing coefficients at $B = 10$ G. Bold numbers show N and I mixing. The coefficients are normalized such that $\sum_i (c_i^k)^2 = 1$

The Zeeman energy splitting of the rovibronic ground states of $I = 0$ and $I = 2$ are presented in figure 2.3a as a function of an external static magnetic field. The non-linearity is seen clearly for all but the 'stretched' states, $M_F = \pm F$, even at low magnetic field strengths. Here, the strongest mixing arises due to the Fermi-contact hyperfine interaction.

Clock transitions are transitions between two states that are insensitive to experimental noise, such as fluctuating electric and magnetic fields, and can therefore be used for precision measurements and as stable qubit states. From Figure 2.3b, we can identify several transitions where the derivative with respect to magnetic field is the same in the upper and lower levels for a given 'magic' magnetic field. Such 'magic transitions' are independent of magnetic field to first order and are therefore good candidates for clock transitions. Magic transitions have been employed in the hyperfine manifold of Ca^+ [68] and Be^+ [69] to reach qubit coherence times of several minutes. Figure 2.3a shows four magic transitions below 70 Gauss in the $\Delta F = \pm 1$ transitions between hyperfine components of the rovibrational ground state around 250 MHz.

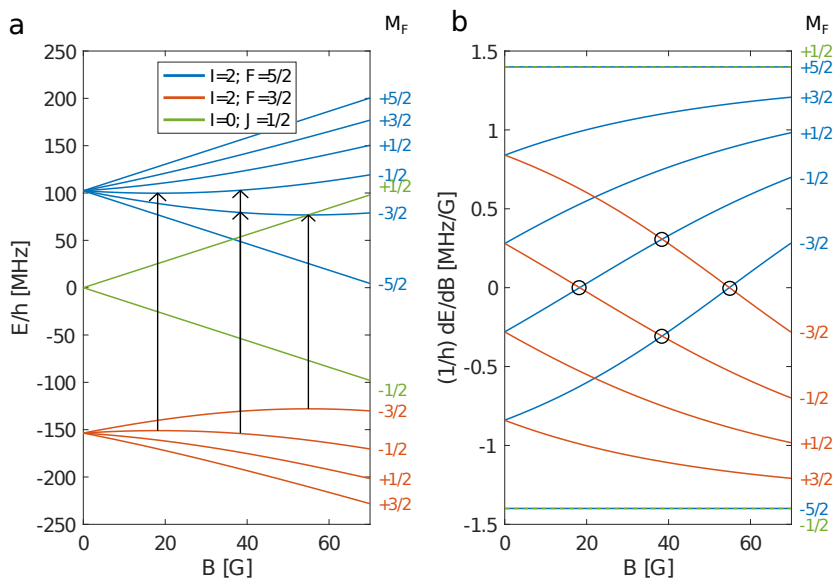


Fig. 2.3. **a)** Energies of the rovibronic ground state ($v = 0$, $N = 0$) manifold as a function of external magnetic field strength. The colors correspond to the schematic from Figure 2.1 and numbers on the right show the projection quantum number. **b)** The derivative of the energies in (a) with respect to the magnetic field. The circles indicate positions of the 'magic' magnetic field values at which the transition energy between two levels is independent of the magnetic field to first order. The corresponding transitions are indicated by the arrows in (a).

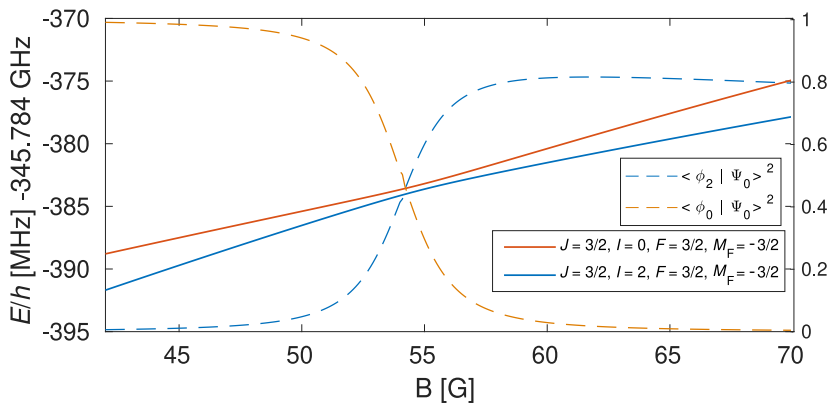


Fig. 2.4. Avoided crossing between two energy levels originating from two different nuclear spin states ($I = 0, 2$) in the $X^2\Sigma_g^+(v=0, N=2)$ state. The dashed lines show the mixing coefficients $(c_{I=0}^0)^2$ (dashed, orange) and $(c_{I=2}^0)^2$ (dashed, blue) of the state that starts out in $I = 0$ at low magnetic fields (solid, orange). Note that the sum of the squared mixing coefficients are different from unity due to mixing with other states not shown in this figure.

The mixing between the nuclear-spin states $I = 0$ and $I = 2$ through the electric-quadrupole hyperfine interaction, H_{eqQ} , allows a change in the nuclear-spin state of the molecule on demand, either by direct excitation or through a two-photon Raman process. This interaction also results in avoided crossings of energy levels originating from different spin states with the same value of hyperfine quantum number, F , and M_F . As an example, we show an avoided crossing in Figure 2.4 between the $|F = 3/2, M_F = -3/2\rangle$ states of the $I = 0$ (orange) and $I = 2$ (blue) configurations at a magnetic field of ~ 54 Gauss. The nuclear-spin states are a 50-50 mixture of $I = 0$ and $I = 2$ at the point of avoided crossing. The strength of transitions between the two nuclear configurations is thus greatly enhanced near the avoided crossing as these transitions are only allowed due to mixing in the magnetic dipole and electric quadrupole selection rules, derived in the next section.

2.2 The theory of dipole-forbidden transitions

In a homonuclear diatomic molecule, transitions within the same Born-Oppenheimer electronic state are electric-dipole (E1) forbidden. This is because the electric dipole operator, $\hat{\mu}^{E1}$, is an odd function of the position operators and can therefore only couple states of opposite parity with respect to coordinate inversion i.e. between + and – states in the molecular term notation $^{2S+1}\Lambda^{\pm}$. A homonuclear diatomic molecule has only even or odd rotational states (of the same parity) for a given nuclear-spin symmetry and therefore parity change in a Σ -state is only possible through electronic transitions¹¹. Furthermore, in the ground $X^2\Sigma_g^+$ -state of N_2^+ there is no permanent electric dipole moment that can couple to an electric field, other than a small contribution from mixing of electronic states, and E1 transitions between vibrational levels are in a sense doubly forbidden. We therefore consider only magnetic dipole (M1) and electric quadrupole (E2) transitions. We will derive general matrix expressions for these transitions and calculate their strengths.

2.2.1 Transition moments and Rabi frequencies

The line strength of a transition can be separated into an angular (A) and a radial (R) part as the operators that act on the angular wavefunctions, e.g. S, N, I , will not act upon the vibrational wavefunctions and vice versa [44]. Consider, for example, the rotational Zeeman term derived in Section 2.1.3 which can induce M1 transitions with $\Delta F = 0, \pm 1$. The Hamiltonian for this interaction is, from Eq. (2.57),

$$H_{Z,N} = -g_N(R)\mu_B \mathbf{B} \cdot \mathbf{N}. \quad (2.80)$$

Here, we have made the dependence of the rotational g -factor on the internuclear distance, R , explicit through the notation $g_N(R)$. In our basis of Eq. (2.13), the operator \mathbf{N} does not act upon the vibrational

¹¹Different vibrational states are all of even parity.

wavefunctions and in the Hund's case (b) basis approximation, the spin-rotational wavefunctions are independent of the internuclear distance R . The evaluation of this Hamiltonian can therefore be separated into an angular (A) and a radial (R) part as,

$$\sqrt{S_{kl}} = -\mu_B \langle v_k | g_N(R) | v_l \rangle \langle N', S', J', I', F', M'_F | \mathbf{B} \cdot \mathbf{N} | N, S, J, I, F, M_F \rangle. \quad (2.81)$$

Here we have introduced the line strength factor S_{kl} between states k, l as the square of the transition moment¹². For a better approximation to the real transition moments we must also include the effects of mixing between our zero-order basis states. We express the wavefunction $|\psi_k\rangle_p$ as superpositions of the zero-order basis functions $|\phi_i\rangle$ as defined in Eq. (2.10),

$$|\psi_k\rangle_p = \sum_i c_i^k |\phi_i\rangle. \quad (2.82)$$

We can therefore write the line strength factor between two states as,

$$\begin{aligned} S_{kl} &= \sum_p |\langle \psi_k | T_p^u(\hat{\mu}) | \psi_l \rangle|^2 \\ &= \sum_p \left| \sum_{i,j} c_j^{k*} c_i^l \langle \phi_j | T_p^u(\hat{\mu}) | \phi_i \rangle \right|^2 \end{aligned} \quad (2.83)$$

$$= \sum_p \left| \sum_{i,j} c_j^{k*} c_i^l A(\dots, F'_j, M'_F, F_i, M_F, p) R(v_j, v_i) \right|^2. \quad (2.84)$$

Here, $\hat{\mu}$ is the electric dipole, magnetic dipole or electric quadrupole-moment operator and $T_p^u(\hat{\mu})$ is the operator in spherical tensor notation. The spherical tensor component p represents the polarization of the radiation with respect to the quantization axis defined by the direction of the external magnetic field.

As the line strength factor has different units for M1 and E2 transitions, their relative strengths can be compared through the Einstein

¹²The line-strength factor in Eq. (2.83) is usually defined as the sum over all upper and lower Zeeman components, M'_F and M_F . As we are interested in comparing the strength between specific Zeeman states we have omitted the sum over M_F , looking instead at a single component. Since we use this convention consistently throughout this thesis no confusion should occur.

A-coefficients, A_{21} , or the Rabi frequencies. The Einstein coefficients are given by [70],

$$A_{21}^{M1} = \frac{16\pi^3 \mu_0}{3h\lambda^3} S_{21}^{M1}, \quad (2.85)$$

for M1 transitions and,

$$A_{21}^{E2} = \frac{16\pi^5}{15h\epsilon_0\lambda^5} S_{21}^{E2} \quad (2.86)$$

for E2 transitions ¹³. Here, λ is the transition wavelength, μ_0 is the vacuum permeability, ϵ_0 is the vacuum permittivity and h is the Planck constant. Note the difference in functional dependence on λ between M1 and E2 transitions. This is because the magnetic dipole interacts with the magnetic field amplitude of radiation whereas the electric quadrupole moment of the molecule interacts with an electric field 'gradient' of the radiation field [47]. This implies that with comparable line strength factors, S_{kl} , M1 transitions are naturally several orders of magnitude stronger than E2 transitions.

When interacting with a coherent source, the population transfer between two levels can be represented by a Rabi frequency, Ω_{ij} . If the limiting coherence time of the system is longer than the excitation rate, the system will oscillate between the two levels and the oscillation frequency is obtained from the transition moment by [71, 72],

$$\Omega_{ij}^{M1} = B_0 \langle i | \hat{\mu} | j \rangle / \hbar \quad (2.87)$$

$$\Omega_{ij}^{E2} = E_0 k \langle i | \hat{\mu} | j \rangle / \hbar, \quad (2.88)$$

where $k = 2\pi/\lambda$ is the laser k-vector. The field strengths, E_0 and B_0 , can be obtained from the source intensity $I = \epsilon_0 c E_0^2 / 2$ or $I = c B_0^2 / (2\mu_0)$ in terms of the electric and magnetic field respectively. A laser beam with a Gaussian beam profile has an intensity distribution given by

¹³The Einstein coefficient, A_{21} , represents the time constant for spontaneous emission of a particular state. The conventional definition of A_{21} therefore involves a sum over all the different decay channels through which this level can decay. As we are interested in comparing the excitation rate between two states for different mechanisms, M1 and E2, we will omit the sum over other decay channels. The strongest transitions we consider have lifetimes on the order of $A_{21} \approx 10^{-8}$ Hz corresponding to a lifetime of several years and spontaneous decay can therefore be neglected in this analysis.

$I(r) = 2P/(\pi r_b^2)e^{-(2r^2)/(r_b^2)}$ where P is the source power, r_b is the beam-waist radius and r is the radial distance from the center of the beam. With the molecule aligned to the center of the beam, $r = 0$, we can rewrite the Rabi frequencies as,

$$\Omega_{ij}^{(M1)} = \frac{2}{\omega} \sqrt{\frac{P\mu_0}{\pi c}} \langle i|\hat{\mu}|j\rangle/\hbar, \quad (2.89)$$

and

$$\Omega_{ij}^{(E2)} = \frac{2}{\omega} \sqrt{\frac{P}{\pi\epsilon_0 c}} k \langle i|\hat{\mu}|j\rangle/\hbar. \quad (2.90)$$

In order to estimate the Rabi frequencies, two different sources shall be considered here. The first is a coherent continuous-wave (CW) laser source at $\lambda \approx 4.6 \mu\text{m}$ with a beam waist of $r_b = 50 \mu\text{m}$ and 100 mW of power, which is used to drive vibrational transitions. The field intensity is thus 2.55 kW/cm^2 . Transitions within a vibrational state, e.g. hyperfine or rotational transitions, are within the range of phase-locked-loop-stabilized THz electronics [73]. The radiation source is therefore assumed to be a direct Radio frequency (RF) or Microwave (MW) drive applied to one electrode of the trap, as described in Section 3.1.3, with a peak voltage of $\pm 10 \text{ V}$. The field intensity at the position of the molecule $\sim 2 \text{ mm}$ away from the electrode, is then 0.16 W/cm^2 ¹⁴.

2.2.2 Magnetic dipole transitions and matrix elements

The interaction Hamiltonian for a magnetic dipole moment which couples to the radiation to induce M1 transitions takes the same form as the Zeeman Hamiltonian in Eq. (2.35). Indeed, they are treated in the same way, as a perturbation to the zero-order basis states, albeit time dependent with the substitution $\mathbf{B} \rightarrow \mathbf{B}(t)$. It comes as no surprise then that the off-diagonal elements in the derived matrix expressions of the Zeeman

¹⁴While it is relatively easy to apply an RF field of $< 1 \text{ GHz}$ to a trap electrode, it may be technically unfeasible to achieve an amplitude of $\pm 10 \text{ V}$ inside a vacuum chamber, at 345 GHz (which corresponds to the $N = 0 \rightarrow 2$ transition in N_2^+). The intensity is provided and the quoted Rabi frequency, Ω_{ij} , can be scaled by \sqrt{I} for any other source of MW radiation.

Hamiltonian, Equations (2.50) (2.57) (2.63) and (2.79), which couple different zero-order basis states also determine the selection rules obeyed by the M1 transitions of a given interaction mechanism. We will denote transitions that are induced by interaction with the electron spin, rotation and nuclear spin and residual angular momentum by $M1_S$, $M1_N$ and $M1_I$ and $M1_{aS}$ respectively. From the angular part of the transition moments, we have the following selection rules in common for all M1 transitions,

$$\begin{aligned} \Delta M_F &= 0, \pm 1, \quad \Delta F = 0, \pm 1, \\ \Delta I &= 0, \quad \Delta S = 0. \end{aligned} \quad (2.91)$$

Specifically, for each coupling mechanism we have the additional selection rules,

$$M1_S : S \neq 0, \quad \Delta N = 0, \quad (2.92)$$

$$M1_N : N \neq 0, \quad \Delta N = 0, \quad (2.93)$$

$$M1_I : I \neq 0, \quad \Delta N = 0, \quad \Delta J = 0 \quad (2.94)$$

$$M1_{aS} : S \neq 0, \quad \Delta N = 0, 2. \quad (2.95)$$

2.2.3 Electric quadrupole transitions and matrix elements

For E2 transitions, the coupling operator in spherical tensor notation is $T_p^2(\hat{Q}_{\eta\Lambda})$ where $\hat{Q}_{\eta\Lambda}$ is the electric quadrupole moment operator in a given electronic state $|\eta, \Lambda\rangle$.

The angular part of the line strength for E2 transitions within the $X^2\Sigma_g^+$ ground state is given by [74],

$$\begin{aligned} &\langle N', S', J', I', F', M'_F | T_p^2(\hat{Q}) | N, S, J, I, F, M_F \rangle \\ &= \delta_{SS'} \delta_{II'} (-1)^{S+I+J+J'+F+F'-M'_F} \\ &\times \sqrt{(2N+1)(2N'+1)(2J+1)(2J'+1)(2F+1)(2F'+1)} \\ &\times \begin{pmatrix} N' & 2 & N \\ 0 & 0 & 0 \end{pmatrix} \begin{pmatrix} F' & 2 & F \\ -M'_F & p & M_F \end{pmatrix} \begin{Bmatrix} N' & J' & S \\ J & N & 2 \end{Bmatrix} \begin{Bmatrix} J' & F' & I \\ F & J & 2 \end{Bmatrix}. \end{aligned} \quad (2.96)$$

From the angular part of the transition moment, the following selection rules are obtained for E2 transitions,

$$\Delta M_F = 0, \pm 1, \pm 2, \Delta F = 0, \pm 1, \pm 2, \Delta I = 0, \Delta S = 0. \quad (2.97)$$

Furthermore, $N = 0 \rightarrow 0$ transitions are not allowed within a Σ -state by the triangle condition of the first Wigner $3j$ symbol in Eq. (2.96).

2.2.4 Vibrational transition moments

We shall now investigate the different mechanisms that can induce vibrational transitions in our molecule. The line strength can be treated in full, according to Eq. (2.83), using the mixed rovibrational basis without the following analysis. As, however, we want to understand the mechanisms that lead to vibrational transitions we shall treat the vibrational transition moments analytically.

As we have seen from Eq. (2.83), the transition moment may be expanded in an angular part $A(\dots, F'_j, M'_F, F_i, M_F, p)$ and a radial part given by,

$$R(v', v) = \langle v' | T^u(\hat{\mu}) | v \rangle. \quad (2.98)$$

This equation implies that if the operator μ is independent of the vibrational coordinates, it may be rewritten,

$$R(v', v) = T^u(\hat{\mu}) \langle v' | v \rangle = T^u(\hat{\mu}) \delta_{v'v}.$$

Here we have assumed that the basis states are the zero-order harmonic oscillator states and therefore mutually orthogonal. Vibrational transitions between $v' \neq v$ due to a permanent magnetic or electric moment are therefore suppressed to first order¹⁵.

The transitions between different vibrational levels are therefore due to higher-order effects. We expand the radial part of the transition moment

¹⁵For transitions within a vibrational manifold, with $v' = v$, the radial part of the line strength is the expectation value of the effective magnetic dipole or electric quadrupole moment in a particular vibronic state, e.g. $R(v, v) = g_v \mu_B$

operator to first order around the equilibrium bond length ($R - R_e$) [44] as we have done with the rotational constant in Section 2.1.2,

$$\hat{\mu} \approx \mu_p + \frac{d\mu}{dR}(R - R_e) + \frac{d^2\mu}{dR^2}(R - R_e)^2 + \dots \quad (2.99)$$

Here, $\mu_p = \mu(R)\Big|_{R=R_e}$ is the permanent multipole moment and $d\mu/dR$ is its derivative as a function of internuclear distance. Once again we assume that the position operator $R - R_e$ does not operate on the electronic or spin-rotational states. We then find that the radial part of the transition moment is,

$$R(v', v) \approx \mu_p \langle \phi_{v'} | \phi_v \rangle + \frac{d\mu}{dR} \langle \phi_{v'} | (R - R_e) | \phi_v \rangle + \frac{d^2\mu}{dR^2} \langle \phi_{v'} | (R - R_e)^2 | \phi_v \rangle + \dots \quad (2.100)$$

From the equation above, we see that vibrational transitions are allowed either by the first (permanent moment) term, through an overlap between wavefunctions, or by the second term through a change in the transition moment with internuclear distance. Vibrational overtones $\Delta v = 2, 3, \dots$ can also be induced due to the higher order terms in Eq. (2.100).

A non-vanishing overlap between the wavefunctions of Eq. (2.10) in the first term of Eq. (2.100) may be caused by the rovibrational interaction presented in Section 2.1.2 which mixes different zero-order basis functions. The coupling between the ground and first excited vibrational states was estimated in Section 2.1.2 to be,

$$|\langle v' = 1, N' | H_{\text{rovib}} | v = 0, N \rangle|^2 \approx \delta_{NN'} (2N(N+1))^2 \left(\frac{B_0^3}{\omega_e} \right). \quad (2.101)$$

As we saw from Table 2.1, the opposite signs of the vibrational mixing coefficients result in a strong degree of cancellation of the sub-transition amplitudes in the line-strength formula of Eq. (2.83). In $N = 2$, the difference between $c_{v=1}^{(v=0)p}$ and $c_{v=0}^{(v=1)p}$ is on the order of $5 \times 10^{-6} \mu_B$ and the line strength S_{12} is therefore suppressed by $\sim 10^{-10}$ compared to pure rotational transitions for the same value of the angular transition moment $A(\dots, F'_j, M'_F, F_i, M_F, p)$.

The vibrational matrix element in the second term of Eq. (2.100) can be approximated in the same way as derived in Eq. (2.18) as,

$$\langle v' = 1 | R - R_e | v = 0 \rangle \approx R_e \sqrt{\frac{B_e}{\omega_e}}. \quad (2.102)$$

The derivative $d\mu/dR$ can either be calculated or obtained experimentally. The rotational magnetic moment and the anisotropic-spin correction term both change by $\sim 1\%$ between $v = 0$ and $v = 1$ (See Table 2.2). The difference in equilibrium bond lengths ΔR_e between $v = 0$ and $v = 1$ can be estimated from the difference in the rotational constants, from Eq. (2.8), by $B_1/B_0 = R_1^2/R_0^2$ with $R_0 = 2.13 \text{ a}_0$ [58] and B_v from Table 2.2. Thus, for the rotational term we have $\Delta g_N/\Delta R_e \approx 4 \cdot 10^{-5} \mu_B/a_0$ and therefore $R(v', v) \approx 2.6 \cdot 10^{-6} \mu_B$. For the anisotropic correction term, we have $\Delta g_I/\Delta R_e \approx 2 \cdot 10^{-3} \mu_B/a_0$ and therefore $R(v', v) \approx 1.3 \cdot 10^{-4} \mu_B$. The change in the electric quadrupole moment with the internuclear distance was calculated by *Bruna & Grein* [58] as $dQ/dR = 2.63 \text{ ea}_0$ and therefore $R(v', v) \approx 0.17 \text{ ea}_0^2$.

A dimensionless quantity can be formed by $\Delta_\mu^{M1} = R(v', v)/(g\mu_B)$ and $\Delta_\mu^{E2} = R(v', v)/(Q_v)$ to describe the relative R -dependence of the three mechanisms. We find $\Delta_\mu^{M1} \approx 1/14$ for the rotational term, $\Delta_\mu^{M1} \approx 1/21$ for the anisotropic correction term and $\Delta_\mu^{E2} \approx 1/11$ for the quadrupole term. The nuclear magnetic moment, g_I , will also change with vibrations due to the magnetic shielding effects of the surrounding electrons. This shift is expected to be $\sim 1 \text{ ppm}$ [67] corresponding to $\Delta_\mu^{M1} \sim 1/10^5$. This means that vibrational transitions due to the $\mathbf{B} \cdot \mathbf{I}$ -interaction are induced predominantly through vibrational mixing. The vibrational line strength for the $M1_S$ coupling mechanism is suppressed by $\sim 10^{-10}$ due to vibrational mixing which makes it a factor $\sim 10^4$ weaker than the strength of $M1_{aS}$ due to its strong R -dependence.

In Figure 2.5, we compare the strength of vibrational transitions by comparing the radial transition moment $\sum_{ij} c_i^{v'} c_j^v |R(v', v)|^2$ due to the first and second term in Eq. (2.100) as a function of rotational state N . As expected by Eq. (2.101), the vibrational mixing increases with the rotational quantum number N and thus mixing-induced transitions become stronger. Horizontal lines show the radial transition strength from the second term in Eq. (2.100) for a few different values of Δ_μ . From

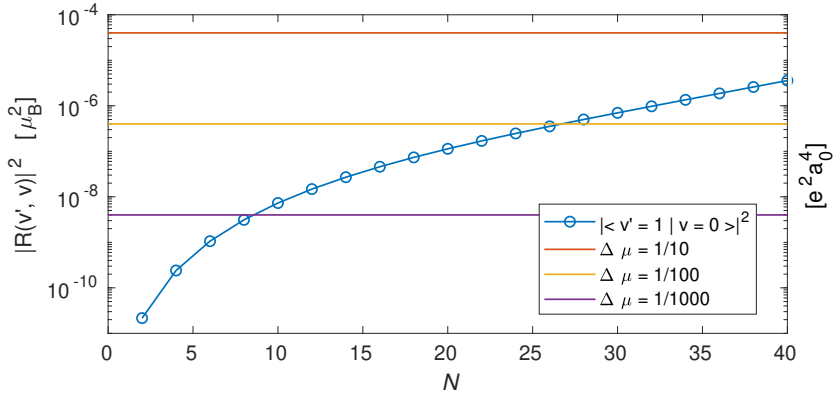


Fig. 2.5. Strength of the radial transition moment between different vibrational states due to rovibrational mixing of basis states (blue curve) and due to the vibrational state dependence of the coupling operator (horizontal lines) plotted as a function of the rotational quantum number N . The rovibrational-mixing-induced transition moment increases with N whereas the transition moment due to vibrational dependence of the coupling operator is constant. The values of Δ_μ for our coupling terms are $\Delta_\mu^{M1} = 1/14$ for the rotational coupling, $M1_N$, $\Delta_\mu^{M1} = 1/21$ for the anisotropic-spin coupling, $M1_{aS}$, $\Delta_\mu^{E2} = 1/11$ for electric quadrupole coupling, E2, and $\Delta_\mu^{M1} = 1/10^5$ for the nuclear spin coupling, $M1_I$.

our analysis above, we have seen that g_N , g_I and eQ all have $\Delta_\mu \sim 1/10$ and therefore transitions due to vibrational mixing are not relevant below $N = 40$. This figure does not take into account the angular part of the transition moment which will introduce an additional rotational-state dependence.

In Figure 2.6 we compare the rotational-state dependence of $M1_S$, $M1_N$, $M1_{aS}$ and E2 transitions, for the $\Delta N = 0$, $v = 0 \rightarrow 1$ transitions in $I = 0$ between the highest spin-rotation states $J = N + 1/2$. The E2 and $M1_N$ transitions are zero in $N = 0$ as expected from the selection rules of Eq. (2.92) and (2.97).

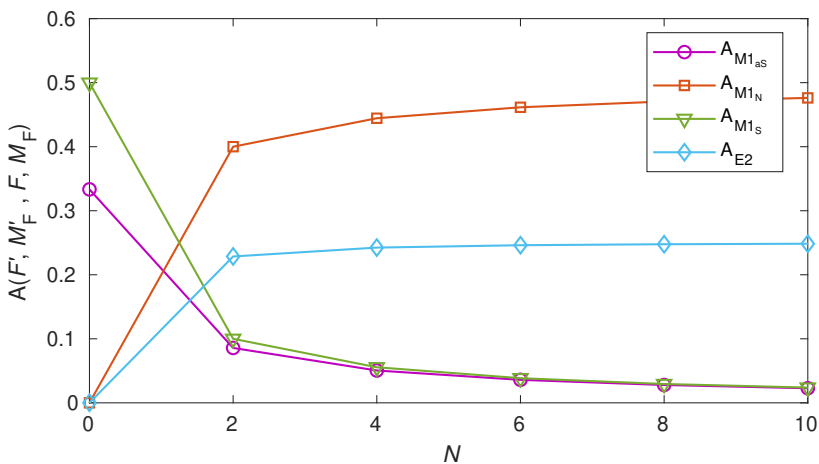


Fig. 2.6. The angular matrix elements (unitless) for M1 and E2 transitions (Equations (2.50), (2.57), (2.63), (2.79) and (2.96)) for the $I = 0$, $\Delta N = 0$ transitions of the fundamental vibrational band as a function of rotational quantum number N . The four curves represent $M1_S$ (green), $M1_N$ (red) and $M1_{aS}$ (purple) as well as E2 couplings (blue).

2.3 Clock transitions and qubits in N_2^+

In this section we have used the results of the energy levels from Section 2.1 together with the calculated transition strengths from section 2.2 to find the dominating coupling mechanisms for each class of transitions (Zeeman, hyperfine, fine-structure, rotational and vibrational). We therefore present the spectra and transitions that are of particular interest for clock transitions and as qubit states.

2.3.1 Zeeman transitions, $\Delta M_F = \pm 1$

In Figure 2.3a, we presented the energies of Zeeman components of the rovibronic ground state, $X^2\Sigma_g^+(v = 0, N = 0)$, in N_2^+ as a function of the strength of an external applied magnetic field.

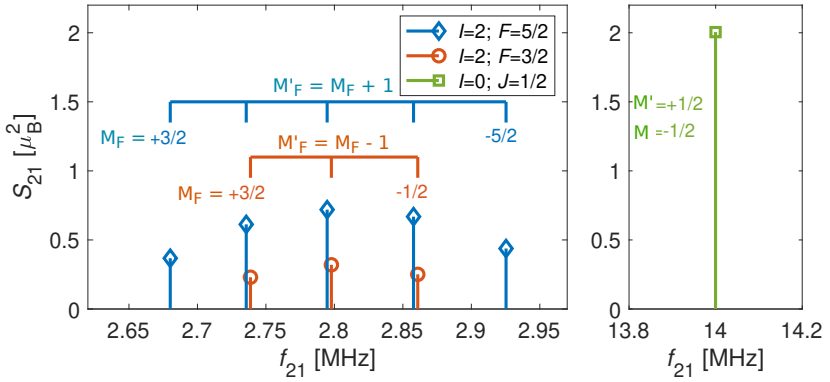


Fig. 2.7. Line strengths of transitions between Zeeman levels within the hyperfine manifolds of the rovibronic ground state, $X^2\Sigma_g^+(v=0, N=0)$ of the $I=0$ (green) and $I=2$ (blue, red) species. The abscissa indicates the transition frequencies at a magnetic field of $B=5$ G.

In the $I=0$ species, there are only two states with $F=1/2$ and $M_F = \pm 1/2$. The Zeeman splitting is similar to the ground states of alkaline earth ions, e.g. $^{88}\text{Sr}^+$, which have also been used as qubits [75]. All terms in the Hamiltonian are zero except for the electron-spin Zeeman term and the anisotropic-spin Zeeman term. The Zeeman levels are thus separated by $\sim (g_s + 2/3g_l)\mu_B \approx 2.8$ MHz/G. Transitions between the two Zeeman levels are allowed by $M1_S$ -interaction with the electron spin which dominates the spectrum. The Zeeman spectrum is presented in Figure 2.7. Measurement of these transitions are a measurement of $g_s + g_l$. The relative contributions of g_s, g_l can however not be separated in this measurement.

A magnetic field shift of 1 mG will induce a shift of 2.8 kHz in the energies corresponding to a relative shift of the transition frequency of $\Delta f/f \approx 10^{-3}$. As g_s, g_l have not previously been measured in N_2^+ , this level of precision will yield improved constants and a test of the ab-initio theory of *Bruna & Grein* [58] which predicted $g_s \approx 1.99$ and $g_l \approx 2710$ ppm in the rovibrational ground state of $X^2\Sigma_g^+$. A deviation from the free-electron value, $g_e \approx 2.0023$, is therefore on the 10^{-4} level and within reach of such a measurement with minimal averaging of ~ 100 repetitions, under 1 mG of magnetic field fluctuations.

In the $I = 2$ species, in addition to the two Zeeman terms mentioned above, the Fermi-contact hyperfine interaction, H_{b_F} from Eq. (2.31), contributes and leads to a splitting into two hyperfine manifolds with a total angular momentum of $F = 3/2$ and $F = 5/2$. The relatively low splitting of ~ 250 MHz, leads to a noticeable nonlinear Zeeman behavior at low magnetic fields of few tens of Gauss. Therefore, these transitions can be addressed individually which allows for optical pumping to any desired state and state readout as also demonstrated with CaH^+ molecules [76].

In this species, g_I will contribute to the Zeeman energies. A comparison of Zeeman transitions in both the $I = 0$ and the $I = 2$ configurations will allow the separation of contributions from $g_s + g_I$ and g_I . With 1 mG of magnetic field noise a relative uncertainty of $\Delta f/f \approx 10^{-3}$ is achieved which is sufficiently low to measure the nuclear spin Zeeman interaction, of ~ 300 Hz [67], with minimal averaging.

2.3.2 Hyperfine transitions, $\Delta F = \pm 1$

Transitions between the two hyperfine manifolds ($F = 3/2 \rightarrow F' = 5/2$) in the rovibrational ground state are allowed by $M1_S$ coupling. A simulated spectrum is presented in Figure 2.8a. In section 2.1.5, we identified transitions for which the magnetic-field dependence is equal in both the lower and upper states for specific values of the magnetic field. Due to the small hyperfine splittings in N_2^+ , these magic magnetic fields occur at small and easily accessible values. 'Magic transitions' between hyperfine levels have also been used as stable qubit states in atomic ions, such as $^9\text{Be}^+$ [69] and $^{43}\text{Ca}^+$ [68].

A second-order magnetic-field dependence persists due to the nonzero second derivative around the magic field values. We find a second derivative of ~ 16 mHz/mG² for all four magic transitions below 70 G. Under magnetic-field fluctuations of 1 mG, we then estimate a shift of 16 mHz in the transition frequencies. These transitions are therefore suited for encoding qubits with coherence times of up to $1/\Delta f \approx 60$ s [77] without the need for magnetic-field stabilization or magnetic shielding. These transitions are also suitable clock transitions with a relative (Zeeman-limited) shift of $\Delta f/f \approx 10^{-11}$. In addition to probing g_s , g_I and g_I , such

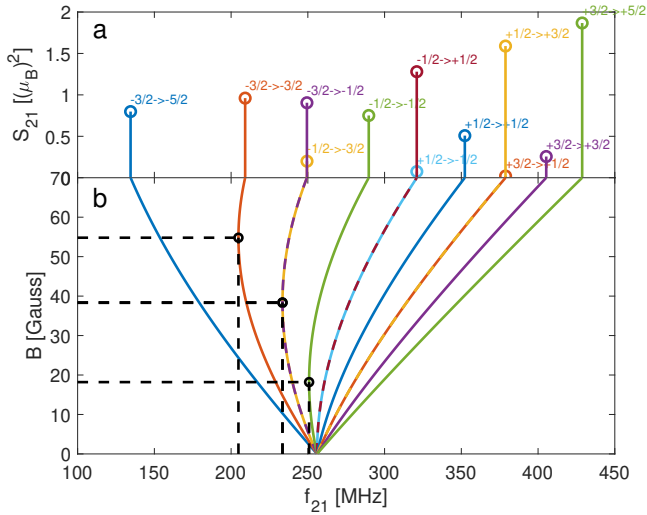


Fig. 2.8. **a)** Line strengths of hyperfine Zeeman transitions, $|F = 3/2\rangle \rightarrow |F' = 5/2\rangle$, within in the rovibronic ground state, $X^2\Sigma_g^+(v = 0, N = 0)$ of the $I = 2$ species. The abscissa indicates the transition frequencies at a magnetic field value of 70 Gauss. The Zeeman components, $M_F \rightarrow M'_F$, of each transition is indicated. **b)** Dependence of the transition frequencies on the magnetic field. Dashed lines indicate 'magic' values of the magnetic field in which the transition frequency is insensitive in first order to changes in the magnetic field.

transitions are also sensitive to the b_F hyperfine constant which has been measured to a relative uncertainty of 10^{-2} and 10^{-5} in $v = 0$ and $v = 1$, respectively (see Table 2.2).

2.3.3 Fine structure transitions, $\Delta J = \pm 1$

The energies of Zeeman components of the $N = 2$ rotationally excited state in the vibronic ground state, $X^2\Sigma_g^+(v = 0, N = 2)$, are shown in Figure 2.9. The spin rotation coupling, $\gamma_{v,N}$, splits the levels into a $J = 3/2$ and a $J = 5/2$ manifold which are separated by ~ 700 MHz.

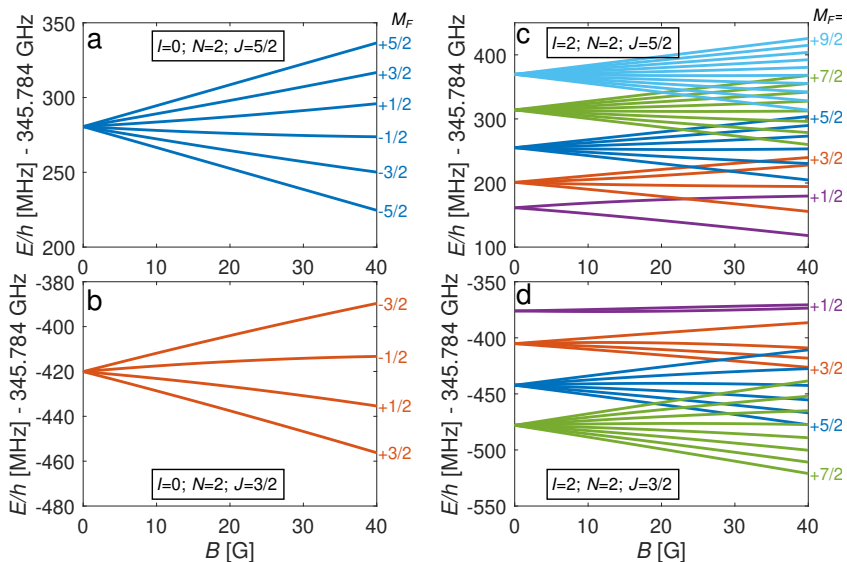


Fig. 2.9. Energies of the hyperfine Zeeman levels of the $v = 0$, $N = 2$ state as function of magnetic field strength. The $I = 0$ configuration is shown in panels (a) and (b) while the $I = 2$ configuration is shown in panels (c) and (d). Color code for the different spin-rotation quantum numbers: $F = 1/2$ in purple, $F = 3/2$ in red, $F = 5/2$ in blue, $F = 7/2$ in green and $F = 9/2$ in light blue. Colors correspond to the colors in the schematic of Figure 2.1.

In the $I = 0$ species, this coupling generates a spectrum which is similar to the spectrum of the $I = 2$ species of $N = 0$, i.e. with a total angular momentum of $F = 3/2$ and $F = 5/2$. However, because of the larger spacing between the $J = 3/2$ and $J = 5/2$ manifolds, the deviation from a linear Zeeman effect occurs at higher magnetic fields. Therefore, the first magic transition, $|F = 3/2, M_F = -1/2\rangle \rightarrow |F' = 5/2, M'_F = -1/2\rangle$ of $^{14}\text{N}_2^+$, appears at ~ 49 Gauss compared to ~ 18 Gauss in the $N = 0$ spectrum of the $I = 2$ species. In $^{15}\text{N}_2^+$, due to the different coefficients (see Table 2.3) the first magic magnetic field appears for the same transition at 46.1 Gauss, as shown in Figure 2.10. Transitions between these manifolds can be measured to $\Delta f/f \approx 10^{-11}$ under 1 mG of magnetic field noise with minimal averaging. The spin-rotation constant, $\gamma_{v,N}$, has so far been measured to a relative uncertainty of 2×10^{-3} .

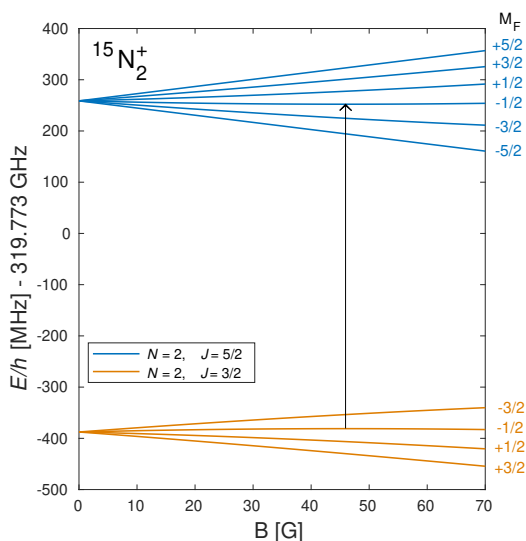


Fig. 2.10. Energies of the Zeeman levels of the $v = 1$, $N = 2$ state of $^{15}\text{N}_2^+$ as function of magnetic field strength. The vibrational energy $G_{v=1} - G_{v=0} = 2174.746 \text{ cm}^{-1}$ was subtracted for clarity. Color code for the different spin-rotation quantum numbers: $F = 5/2$ in blue, $F = 3/2$ in orange and numbers on the right show the projection quantum number. The arrow shows the position of a 'magic' transition at 46.1 Gauss.

In the $I = 2$ state of $^{14}\text{N}_2^+$, the spectrum further splits by the hyperfine interaction. Thus, the energy levels split into $F = 9/2, \dots, 1/2$ and $F = 7/2, \dots, 1/2$ for the $J = 5/2$ and $J = 3/2$ spin-rotation manifolds (Figure 2.9c and Figure 2.9d, respectively). Out of the three allowed hyperfine components, $\Delta F = \pm 1, 0$, we find the $\Delta F = +1$ are dominating as can be seen in the simulated spectrum in Figure 2.11. This propensity may be understood by the $M1_S$ coupling mechanism which flips the electron spin to change $\Delta J = +1$ and leads to $\Delta F = +1$. Any other arrangements of ΔF require additional internal rearrangements of angular momenta. Magic transitions can be found in $I = 2$ at magnetic fields as low as few Gauss such as the $|F = 5/2, M_F = +1/2\rangle \rightarrow |F' = 7/2, M'_F = -1/2\rangle$ transition at $\sim 756.3 \text{ MHz}$ and $B = 1.55 \text{ G}$, with a susceptibility of $\sim 8 \text{ mHz/mG}^2$. A partial list of magic transitions below 70 G is presented in Appendix C.

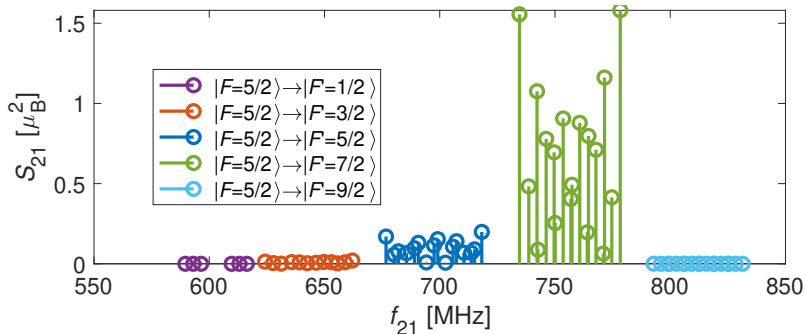


Fig. 2.11. Line strengths of transitions involving a change in the spin-rotation and hyperfine quantum numbers at a magnetic-field value of 10 Gauss. The transitions shown are of the form $|v = 0, N = 2, J = 3/2, I = 2, F = 5/2\rangle \rightarrow |v' = 0, N' = 2, J' = 5/2, I' = 2, F'\rangle$.

2.3.4 Rotational transitions, $\Delta N = \pm 2$

We now consider transitions from the rotational ground state, $N = 0$, to the second rotationally excited state, $N' = 2$, at approximately $6B_0 - 36D_0 \approx 345$ GHz. Due to the direct dependence of B_0 on the molecular bond length, these transitions are candidates for testing a possible time variation of the proton-to-electron mass ratio, as described in Section 2.4.4.

The $M1_S$ selection rules do not permit a change of rotational quantum numbers, but this mechanism must still be considered due to mixing of rotational states. The anisotropic spin term, $M1_{aS}$, allows for $\Delta N = 2$ transitions although with a smaller coupling constant $g_l/g_s \approx 10^{-3}$. The rotational mixing coefficients are between 10^{-6} and 10^{-3} for different levels (see Table 2.4) which makes the strongest, mixing-induced, $M1_S$ transitions as strong as $M1_{aS}$ transitions. We also consider the E2 electric-quadrupole transitions which also allow rotational transitions, according to Eq. (2.97). E2 transitions also allow $\Delta M_F = \pm 2$ and $\Delta F = \pm 2$ transitions which are magnetic dipole forbidden.

In Figure 2.12, we show the hyperfine rotational spectrum of the $I = 2$ state, $|N = 0, J = 1/2, F = 5/2\rangle \rightarrow |N' = 2, J' = 5/2, F'\rangle$, and $|N = 0, J = 1/2, F = 3/2\rangle \rightarrow |N' = 2, J' = 5/2, F' = 1/2\rangle$ due to different M1 and E2 contributions. The strongest $M1_S$ lines are as strong

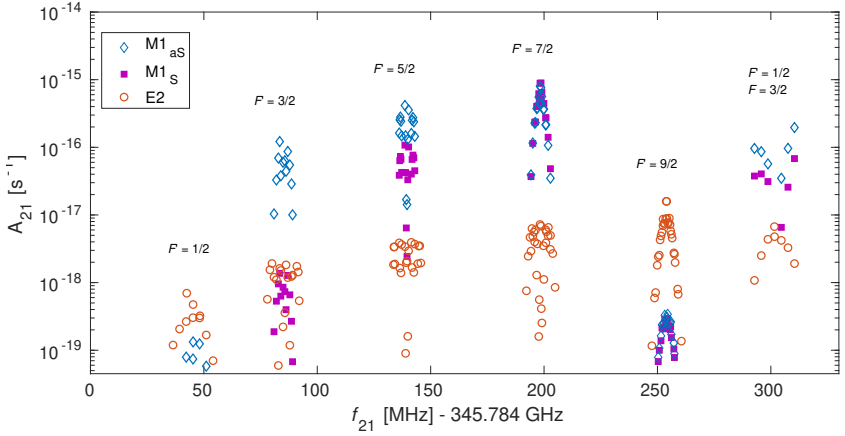


Fig. 2.12. Spectrum of the rotational transition $|N = 0, J = 1/2, F = 5/2\rangle \rightarrow |N' = 2, J' = 5/2, F'\rangle$ of the $I = 2$ state. Transitions due to $M1_S$, $M1_{aS}$ and E2 are indicated by purple squares, blue diamonds and red circles respectively. The $|N = 0, J = 1/2, F = 3/2\rangle \rightarrow |N' = 2, J' = 5/2, F' = 1/2\rangle$ transitions are also shown where indicated (rightmost points). These transitions are free from the electric quadrupole shift, as detailed in Section 2.4.3. The magnetic field was set to 5 Gauss.

as $M1_{aS}$ lines and two order of magnitude stronger than the E2 lines. However, in some cases only E2 transitions are allowed due to quadrupole selections rules such that one should consider all three mechanisms when analyzing the molecular spectrum.

The rotational spectrum of the $I = 2$ state shows magic transitions with susceptibilities as low as ~ 3 mHz/mG² corresponding to a Zeeman-limited coherence time of $1/\Delta f \approx 5$ minutes and a relative shift of $\Delta f/f \approx 10^{-14}$ under 1 mG of magnetic field noise.

The $|N = 0, J = 1/2, F = 3/2\rangle \rightarrow |N' = 2, J' = 5/2, F' = 1/2\rangle$ transitions are free from electric quadrupole shift, as detailed in Section 2.4.3. The Rabi frequency was estimated for the strongest $M1$ transitions, due to a coherent drive of 10 V on the trap electrode, and gives $\Omega \approx 0.5$ kHz. The appearance of $M1_S$ transitions in Figure 2.12 is additional proof that off-diagonal terms in the Hamiltonian, here $N' \neq N$, should not be neglected.

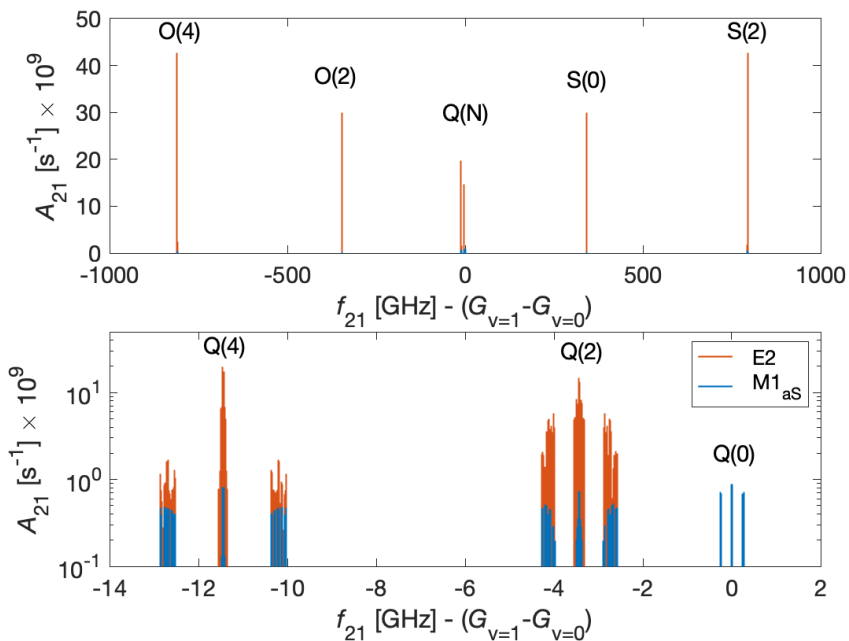


Fig. 2.13. The relative coupling strength of E2 and $M1_{aS}$ transitions in terms of the Einstein coefficient in the $O(N)$, $Q(N)$ and $S(N)$ branches of the fundamental vibrational transition $|v = 0, N = 0, 2, 4\rangle \rightarrow |v' = 1, N' = 0, 2, 4\rangle$. The bottom figure is zoomed in on the $Q(N)$ transitions. Only the E2 and $M1_{aS}$ contributions are shown as all other mechanisms are weaker.

2.3.5 Vibrational transitions, $\Delta v = 1$

As the vibrational frequencies are also sensitive to the molecular bond length, vibrational transitions are promising candidates for testing a possible variation in the proton-to-electron mass ratio. They benefit from higher transition frequencies than rotational lines and thus allow for a better relative precision [35]. Figure 2.13 shows the $O(N)$, $Q(N)$ and $S(N)$ branches of the fundamental vibrational spectrum, i.e. $|v = 0, N = 0, 2, 4\rangle \rightarrow |v' = 1, N' = 0, 2, 4\rangle$ of both the $I = 0$ and $I = 2$ configurations.

E2 selection rules forbid $\Delta N = 0$ transitions from $N = 0$. $Q(0)$ transitions, i.e., $|v = 0, N = 0\rangle \rightarrow |v' = 1, N' = 0\rangle$, are therefore E2 forbidden. The transitions induced by the anisotropic-spin Zeeman Hamiltonian, however, allow $N = 0 \rightarrow N' = 0$ transitions, according to Eq. (2.92). This term shows a considerable change with the internuclear distance and therefore induces vibrational transitions, as described in Section 2.2.4. This leads to the appearance of $Q(0)$ lines in the spectrum, although much weaker than the $Q(2)$ and $S(0)$ transitions that are E2 allowed.

Figure 2.14 shows the $Q(0)$ fundamental vibrational spectrum, i.e. $|v = 0, N = 0, J = 1/2\rangle \rightarrow |v' = 1, N' = 0, J' = 1/2\rangle$ of both $I = 0$ and $I = 2$ configurations. Transitions between the stretched states, i.e. $|J = 1/2, M_F = \pm 1/2\rangle \rightarrow |J' = 1/2, M'_F = \pm 1/2\rangle$ and $|F = 5/2, M_F = \pm 5/2\rangle \rightarrow |F' = 5/2, M'_F = \pm 5/2\rangle$ show a very small linear Zeeman dependence of $\Delta g_I/3 \approx 9.3 \text{ mHz/mG}^2$ for all magnetic fields. In the $I = 2$ species, the $Q(0)$ spectrum also exhibits magic transitions (indicated by black squares in Figure 2.14). The second-order Zeeman susceptibility of these transitions is $\sim 16 \text{ mHz/mG}^2$. Assuming a laser power of $P = 100 \text{ mW}$ with a $50 \mu\text{m}$ beam radius the Rabi frequency of these M1 transitions are estimated $\Omega \approx 5 \text{ kHz}$ for the strongest $Q(0)$ transitions.

The $S(0)$ and $Q(2)$ transitions, i.e. $|v = 0, N = 0\rangle \rightarrow |v' = 1, N' = 2\rangle$ and $|v = 0, N = 2\rangle \rightarrow |v' = 1, N' = 2\rangle$, are predicted to be ~ 30 times stronger than the $Q(0)$ spectrum, as shown in Figure 2.13, due to the allowed E2 transitions. The second largest contribution to the $S(0)$ spectrum is due to $M1_{aS}$ coupling. All other coupling mechanisms were found to be more than 5 orders of magnitude smaller.

The $S(0)$ spectrum shows magic transitions at low magnetic fields of a few Gauss with second-order Zeeman susceptibilities as low as $\sim 1 \text{ mHz/mG}^2$. With magnetic field fluctuations on the order of $\sim 1 \text{ mG}$, they can be used for encoding vibrational qubits with coherence times of up to $1/\Delta f \approx 15$ minutes. This corresponds to a relative Zeeman shift of $\Delta f/f \approx 1 \times 10^{-17}$ without active or passive magnetic field stabilization. Assuming a laser power of $P = 100 \text{ mW}$ and a $50 \mu\text{m}$ beam radius, these transitions can be driven with Rabi frequencies of $\Omega \approx 60 \text{ kHz}$. In Appendix C, we present a list of the strongest magic transitions below 70 G.

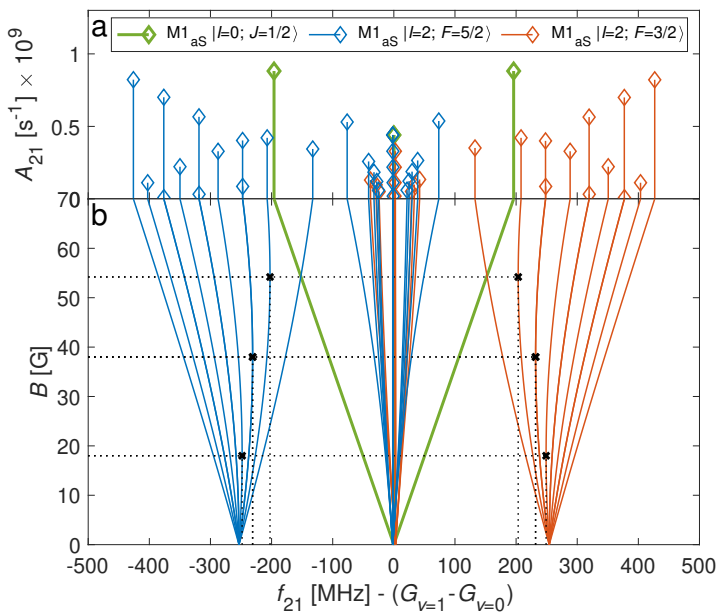


Fig. 2.14. Coupling strength (a) and line position as function of magnetic field strength (b) of the Q(0) branch of the fundamental vibrational transition $|v = 0, N = 0\rangle \rightarrow |v' = 1, N' = 0\rangle$. Only contributions from $M1_{aS}$ coupling are shown. Black squares and dotted lines indicate positions of 'magic' magnetic field transitions.

2.4 Systematic shifts and uncertainties

So far, we have considered the benefits of using $N_{\frac{1}{2}}^+$ transitions as qubit states and clock transitions in terms of the first order Zeeman interactions. In order to find good clock candidates, we must also consider other systematic shifts and uncertainties. In this section, we consider neglected Zeeman terms as well as the ac-Stark shifts induced by the ion trap, black-body radiation and the probe laser. We shall also estimate the electric quadrupole shift from the trap which affects states with an electric quadrupole moment. Finally, we will estimate the attainable statistical precision of clock candidates and explore their use for measuring a possible time variation of the proton-to-electron mass ratio. The relativistic Doppler shift is treated in Section 3.1.1 and found to be negligible for a trapped ion near the motional ground state of the trap.

2.4.1 Residual Zeeman shift

The magnetic susceptibility of the molecular-clock candidates that were presented in Section 2.2, are due to the linear Zeeman terms presented in Section 2.1.3. A residual intrinsic shift remains even for the magic transitions as the second derivative of the transition frequency with respect to magnetic field does not vanish. The residual shifts are presented in Appendix C.

Near magic transitions, Zeeman terms that were neglected will be effectively absorbed by the strong quadratic magnetic-field dependence around the magic magnetic field. Terms that are linear in \mathbf{B} will only shift the magic \mathbf{B} -field value without altering the residual magnetic susceptibility. Terms of higher order, $\propto \mathbf{B}^2$, will shift the magic field value and also alter the residual susceptibility. To test the effect of neglected terms in the Zeeman Hamiltonian, we add an additional linear Zeeman term, $\propto \mathbf{B}$, with the interaction strength of the nuclear-spin term of $\mu \approx 300$ Hz/G, to the Zeeman Hamiltonian in Eq. (2.35)¹⁶. The magic magnetic field value of the hyperfine $|N = 0, I = 2, F = 3/2, M_F = -1/2\rangle \rightarrow$

¹⁶This value is chosen somewhat arbitrarily as a relatively small Zeeman contribution for illustrative purposes.

$|N' = 0, I' = 2, F' = 5/2, M'_{F'} = -1/2\rangle$ transition at 18.286 G is then shifted by 1 mG without altering the residual shift of 16 mHz/mG². An interaction of the same strength but quadratic in the magnetic field $\propto \mathbf{B}^2$ will shift the magic field value by 35 mG and change the residual susceptibility to 20 mHz/mG². This effective 'absorption' of smaller terms works irrespective of the vibrational dependence of the coupling operator, $g(R)$. We therefore find that the magic magnetic field transitions are robust against neglected terms in the theoretical estimate of the Zeeman Hamiltonian.

For the stretched-state transitions, presented in Sections 2.3.4 and 2.3.5, any neglected terms will add or subtract to the total magnetic susceptibility. An additional linear term that does not equally contribute to the lower and upper state of the transition, i.e. with a vibrational or rotational state dependence, will change the total susceptibility. For example, a neglected Zeeman term of $\mu \approx 300$ Hz/G with a vibrational state dependence of $\Delta g_v/g \approx 3\%$ between $v = 0$ and $v = 1$ will double the susceptibility of the stretched state Q(0) transitions presented in Section 2.3.5. These transitions are therefore less forgiving of neglected interactions in the theory than magic transitions.

2.4.2 Ac-Stark shifts

The ac-Stark shift of transitions within an electronic state are suppressed as there is no transition dipole moment which couples different levels within the ground-state manifold. A higher order shift is induced by far off-resonant interaction with other electronic states. This shift may be caused by the trap RF drive, by black-body radiation (BBR) or by the probe laser.

The ac-Stark shift, ΔE_j , of the level j can be estimated from the dynamic polarizability of the molecule, $\alpha_j(\omega)$, due to interaction with higher electronic states as [35],

$$\Delta E_j = -\frac{1}{2}\alpha_j(\omega)E_0^2. \quad (2.103)$$

Here, E_0 is the electric-field amplitude of the ac electric field with frequency ω . The polarizability is a sum over all states k to which the state j can couple, given by [35],

$$\alpha_j(\omega) = \sum_k \frac{|\langle k|\mu|j\rangle|^2}{\hbar} \frac{\omega_{jk}}{\omega^2 - \omega_{jk}^2}. \quad (2.104)$$

The differential shift of the transition frequency between levels j and i is then $\Delta f_{AC} = \Delta E_j - \Delta E_i$. The transition dipole moments, $\langle k|\mu|j\rangle$, and frequencies ω_{jk} between vibrational states of different electronic states of $^{14}\text{N}_2^+$ are given in Ref. [35].

The ac-Stark shift from the trap RF drive with frequencies of $\omega \approx 2\pi \cdot 20$ MHz can be estimated in the limit where $\omega \rightarrow 0$ in Eq. (2.104). For vibrational transitions with $f \approx 65.2$ THz, we find a relative shift of $\Delta f / (f E_0^2) = 7 \cdot 10^{-24} (\text{m/V})^2$. The field vanishes along the trap axis, but will cause a relative shift of $1.26 \cdot 10^{-18}$ at a field amplitude of 300 V/m. This electric field amplitude corresponds to an excessive radial distance of 100 nm away from the RF-null line of an $^{14}\text{N}_2^+$ ion in an ion trap with secular frequencies of $\omega_r = 2\pi \cdot 1$ MHz, as described in Section 3.1. For transitions within a vibrational state, the shift becomes smaller as the spacing between the two levels decreases and the differential shift between both levels cancels to a greater extent.

BBR shifts can also be estimated in the limit of $\omega \rightarrow 0$ since the spectral-density maximum of a 300 K black-body radiator occurs at 31 THz, which is small compared to the frequencies of electronic transitions from the vibrational ground state. The time-averaged value of the quadratic electric field from a 300 K radiator is $\langle E_0^2 \rangle \approx 831.9 (\text{V/m})^2$ [78] and we obtain a relative shift of $\Delta f / f = 1.0 \cdot 10^{-17}$ for the vibrational transitions. Transitions within a vibrational state will have smaller shifts due to cancellation between the upper and lower states. The N_2^+ molecular clock is therefore suitable for operation in a room-temperature environment.

Ac-Stark shifts from the probe laser can be eliminated by using the Hyper-Ramsey method of spectroscopy or through a balanced Raman scheme [35]. In a conventional Rabi- or Ramsey-type clock experiment, the laser power is reduced in order to minimize power broadening. In order to obtain a Rabi π -time of ~ 1 Hz on the strongest S(0) vibrational transitions, as presented in Section 2.3.5, we need 1 nW of laser power

focused to a beam radius of $50 \mu\text{m}$. The intensity is thus $I = 0.26 \text{ W/m}^2$ corresponding to an electric field of 13.9 V/m . The ac-Stark shift obtained from Equations (2.103) and (2.104) is then $\Delta f/f = 8.9 \cdot 10^{-22}$. With a laser power more suitable for driving qubits of $\sim 100 \text{ mW}$, the intensity is $I = 2.55 \cdot 10^7 \text{ W/m}^2$ and we obtain a stark shift of 5.8 Hz or $\Delta f/f = 8.9 \cdot 10^{-14}$. This stark shift can be taken into account by calibrating the transition frequency for different laser intensities and stabilizing the laser power.

2.4.3 Electric quadrupole shifts

Electric quadrupole shifts were estimated for rovibrational transitions in N_2^+ in Ref. [35, 67]. Here, we will extend the analysis to transitions within a vibrational state. The electric quadrupole shift is significant for molecular ions with an electric quadrupole moment interacting with the confining quadrupole field from a trap [79, 80]. The shift is proportional to the electric quadrupole moment $Q_{v\Lambda}$ of level v and the electric field E_0 as [81]¹⁷,

$$\Delta\nu \propto \frac{dE_0}{dZ} Q_{v\Lambda} (3M_F^2 - F(F+1)), \quad (2.105)$$

where the field is assumed along the lab-fixed Z -direction. The differential shift is then $\Delta E_{eq} = \Delta\nu_i - \Delta\nu_j$.

We see that the quadrupole shift vanishes for states with $F = 0, 1/2$. Eq. (2.105) also implies that for states with $\Delta N = \Delta J = \Delta F = \Delta M_F = 0$, the shift is the same in both upper and lower states and the differential shift is given by the difference between the molecular quadrupole moment between the upper and lower states, $\Delta Q = Q_{v'\Lambda} - Q_{v\Lambda}$. This vanishes in the case, $\Delta v = 0$, and was estimated to be of order $\Delta Q/Q \approx 1\%$ for transitions between $v = 0$ and $v = 1$. We shall now treat this shift in more detail.

¹⁷The factor $(3M_F^2 - F(F+1))$ results from the Wigner-Eckart theorem for the zeroth component of a second rank spherical tensor operator, such as the electric quadrupole moment, $T_0^{(2)}(\mathbf{Q})$.

In Section 2.2.3, we presented the matrix expression for the electric quadrupole moment operator evaluated in a Hund's case (b_{β_j}) basis. This was derived in Ref. [39] for estimating the coupling of the molecular quadrupole moment with electromagnetic radiation, which induces E2 transitions. The same interaction Hamiltonian, $H_Q = T^2(\nabla\mathbf{E}) \cdot T^2(\mathbf{Q})$, is responsible for the electric quadrupole shift from the trap. This time, the molecular quadrupole moment is interacting with a static field gradient, $E_0(t) \rightarrow E_0$, assumed to be along the ($p = 0$) Z -direction. To find the energy shift of a specific level, this Hamiltonian can be added to the total Hamiltonian and diagonalized with the other terms, or treated as a perturbation to the energies. The first-order energy correction in perturbation theory is the matrix element of the operator between the zero order basis functions, given by [81],

$$\Delta E_j = -\frac{1}{2} \frac{dE}{dz} \langle \phi_j | T^{(2)}(\hat{Q}_{\eta\Lambda}) | \phi_j \rangle. \quad (2.106)$$

We recall the matrix element of the quadrupole operator from Eq. (2.96),

$$\begin{aligned} & \langle v, N', S', J', I', F', M'_F | T_p^2(\hat{Q}_{\eta\Lambda}) | v, N, S, J, I, F, M_F \rangle \\ &= \delta_{SS'} \delta_{II'} (-1)^{S+I+J+J'+F+F'-M'_F} \\ & \times \sqrt{(2N+1)(2N'+1)(2J+1)(2J'+1)(2F+1)(2F'+1)} \\ & \times \begin{pmatrix} N' & 2 & N \\ 0 & 0 & 0 \end{pmatrix} \begin{pmatrix} F' & 2 & F \\ -M'_F & 0 & M_F \end{pmatrix} \begin{Bmatrix} N' & J' & S \\ J & N & 2 \end{Bmatrix} \begin{Bmatrix} J' & F' & I \\ F & J & 2 \end{Bmatrix} R(v, v), \end{aligned} \quad (2.107)$$

to which we have added the radial part of the matrix element $R(0,0) \approx 1.86 ea_0^2$ for $v = 0$ and $R(1,1) \approx 1.89 ea_0^2$ for $v = 1$ [58], with $p = 0$ to describe a static field along the Z -direction¹⁸.

The selection rules for E2 transitions now give the non-vanishing elements of the electric quadrupole shift, with the modification that only $\Delta M_F = 0$ is allowed for a static field gradient along $p = 0$. By the first Wigner 3j symbol in the equation above, we find that the shift is exactly zero for all transitions within the $N = 0$ state of the electronic ground state. By the sum rule of the second Wigner 3j symbol in Eq. (2.107) we also find

¹⁸Here, we have used the definition of the electric quadrupole moment $T_0^{(2)}(\mathbf{Q}) = -e \sum_j (3z_j^2 - r_j^2)$ from Ref. [81].

that the shift vanishes for $F = 0, 1/2$ states, as we have seen from Eq. (2.105).

For other states in $v = 0, 1$ with $N = 0, 2, 4$, the matrix element ranges between $10^{-3} - 10^{-1}R(v, v)$. The electric field gradient in a trap with secular frequencies of $\omega_z \sim 2\pi \cdot 1$ MHz, can be estimated by [82] $dE_0/dz = \omega_z^2 m/e$ where m is the mass of the ion and e the elementary charge. We then estimate a field gradient of $\sim 10^7$ V/m² for $^{14}\text{N}_2^+$ and a quadrupole shift (absolute value) between 0.21 – 14.4 Hz in the different levels. The difference between Q_0 and Q_1 is $\sim 1.4\%$ and the differential quadrupole shifts are between 10 – 660 mHz for vibrational transitions with $\Delta N = \Delta J = \Delta F = \Delta M_F = 0$.

All the Zeeman and hyperfine transitions in the rotational ground state are therefore immune to the electric quadrupole shift. Rotational $N = 0 \rightarrow (N' = 2, F' = 1/2)$ transitions, where we have identified several magic transitions, are also free from the shift. Likewise, Q(0) vibrational transitions are free from the quadrupole shift. The Q(0) transitions with $I = 0$, presented in Section 2.3.5, are therefore especially suitable for clock operation as they are free from the quadrupole shift and allow the use of stretched-state transitions which have a low susceptibility for all values of the applied magnetic field. The Q(2) transitions can also be chosen with $F = F' = 1/2$ such that the shift cancels. For S(0) transitions, the shift vanishes in the lower states S(0) and the upper state can be chosen as $F' = 1/2$.

The differential shift of the fine-structure transitions with $\Delta J = 1$ in the $N = 2$ manifold was calculated in first order perturbation theory for the magic transitions listed in Appendix C. The differential shift ΔE_{eq} ranges between 1.13 – 5.65 Hz for the magic transitions with the exception of the $|J = 3/2, I = 2, F = 7/2, M_F = -1/2\rangle \rightarrow |J' = 5/2, I' = 2, F' = 9/2, M'_F = -3/2\rangle$ magic transition where an accidental cancellation leads to a vanishing shift. We therefore find clock transitions with low magnetic field susceptibility and vanishing quadrupole shifts in every class of transitions.

2.4.4 Statistical uncertainty

For testing a possible time variation of the proton-to-electron mass ratio, $\mu_m = m_p/m_e$, we are interested in the center frequency of a transition and the precision with which it can be determined. Through repeated measurements, the center of a clock transition can be determined to a precision of several orders of magnitude better than the spectroscopic linewidth.

The uncertainty in determining the line center in a spectroscopic measurement is given by [83],

$$\Delta\nu = \frac{\Gamma}{\sqrt{M}(S/\delta S)}, \quad (2.108)$$

where Γ is the spectroscopic linewidth, M is the number of measurements preformed and $S/\delta S$ is the signal-to-noise ratio. In a Ramsey-type coherent spectroscopic measurement, the noise can be reduced to the quantum projection noise $S/\delta S = \sqrt{N}$ [84], where $N = 1$ is the number of ions probed at the same time. Thus for a spectroscopic linewidth of $\Gamma = 1$ kHz and an interrogation time dominated by the probe pulse, of 100 ms, the uncertainty in the line center is $\Delta\nu \approx 1$ Hz after 1 hour of continuous repeated measurements.

The variation of the proton-to-electron mass ratio that can be deduced from an experiment depends on the functional dependence of the transition frequency on μ_m . The relative precision of the mass ratio is given by [85],

$$\begin{aligned} \frac{\Delta\mu_m}{\mu_m} &= \frac{1}{\mu_m} \frac{\partial\mu_m}{\partial\nu} \Delta\nu \\ &= \frac{\partial(\log \mu_m)}{\partial\nu} \Delta\nu = \kappa^{-1} \Delta\nu, \end{aligned} \quad (2.109)$$

where κ is called the sensitivity coefficient. For rotational and vibrational transitions, they are $\kappa \approx 1$ and $\kappa \approx 1/2$ respectively.

As an example, consider the magic transitions mentioned in Section 2.3.5 on rovibrational transitions. With a laser-linewidth-limited spectral linewidth on the $v = 0 \rightarrow 1$ transition of $\Gamma = 10$ Hz and an interrogation time of 100 ms, we attain a precision of $\Delta\nu = 0.01$ Hz and a relative

uncertainty $\Delta\nu/\nu \approx 1.5 \times 10^{-16}$ in 24 hours of measurements. Therefore $\Delta\mu_m/\mu_m \approx 3 \times 10^{-16}$.

In comparison, a rotational transition with a spectral linewidth of $\Gamma = 2\pi \cdot 1$ Hz limited by a phase-locked-loop THz source with an interrogation time of 1 s can achieve $\Delta\nu = 3$ mHz and a relative uncertainty of $\Delta\nu/\nu \approx 1 \times 10^{-14}$ and therefore $\Delta\mu_m/\mu_m \approx 1 \times 10^{-14}$ in 24 hours of averaging.

2.5 Summary

We have explored the ground state manifold of N_2^+ to find suitable molecular clock and qubit transitions. We have also shown that the theory of energy levels, transition strengths and systematic shifts in a molecule can be treated in a single, consistent framework. By considering the breakdown of our approximations for the basis states, we have seen that off-diagonal terms in the effective Hamiltonian should not be neglected and will give rise to 'magic' transitions and even invalidate certain selection rules in an observed spectrum.

In Table 2.5 we have compiled a summary of the results from each class of transitions. Transitions were found, spanning 6 orders of magnitude in frequency, that are suitable as molecular qubits with expected coherence times of up to 10's of minutes without the need for a cryogenic environment or magnetic field stabilization. Clock transitions were identified which can be measured to a relative uncertainty of 10^{-17} , free from electric-quadrupole shifts, in a room temperature environment. The picture is thus painted of the homonuclear diatomic molecule as a versatile and stable system for encoding quantum information and for high-precision measurements. While this analysis focuses on N_2^+ many of the desirable features that are presented here are expected to extend to other homonuclear diatomic species.

Transition type	Frequency f	Zeeman shift	$\Delta f/f,^a$	$\Delta E_{eq},^b$	$\Omega_0,^c$ [kHz]
Zeeman					
$\Delta M_F = \pm 1$					
$N = 0, I = 0$	1 – 100 MHz	2.8 kHz/mG	10^{-3}	0	800
$N = 0, I = 2$	1 – 100 MHz	1 kHz/mG	10^{-3}	0	800
Hyperfine					
$\Delta F = \pm 1$					
$N = 0, I = 2$	200 – 300 MHz	16 mHz/mG	10^{-11}	0	700
Fine-structure					
$\Delta J = \pm 1$					
$N = 2$	600 – 900 MHz	6 mHz/mG	10^{-11}	0-6 Hz	700
Rotational					
$\Delta N = \pm 2$					
$M1_S$	345 GHz	10 mHz/mG	10^{-14}	0-15 Hz	0.5
$M1_{a,S}$	345 GHz	10 mHz/mG	10^{-14}	0-15 Hz	0.5
$E2 \Delta F = \pm 2$	345 GHz	10 mHz/mG	10^{-14}	0-15 Hz	0.1
Rovibrational					
$\Delta v = \pm 1$					
$M1_{a,S} Q(0)$	64.9 THz	10 mHz/mG	10^{-17}	0	5
$E2 Q(N) N \neq 0$	64.9 THz	5 mHz/mG	10^{-17}	0-15 Hz	60
$E2 S(0)$	65.2 THz	5 mHz/mG	10^{-17}	0-15 Hz	60

Tab. 2.5. A summary of the results from Section 2.3 and 2.4. The columns shows (from left to right) the different classes of transitions and their coupling mechanisms, transition frequencies f , residual Zeeman shifts for the least susceptible transitions, the relative uncertainty due to the residual Zeeman susceptibility $\Delta f/f$ under 1 mG of field fluctuations, the electric quadrupole shift ΔE_{eq} and finally the Rabi frequencies Ω_0 . ^aThe Zeeman-limited relative line shift with 1 mG of magnetic field noise. ^b The electric quadrupole shift as described in Section 2.4.3 ^c Two radiation sources were assumed as described in Section 2.2.4

Building a Molecular Clock Experiment for N_2^+

” *Inexplicably working is barely better than
inexplicably not working.*

— Georg Holderied

In this chapter we present the experimental implementation of a high-precision single-molecule experiment for N_2^+ with particular emphasis on the design of the ion trap, laser stabilization and the electronics required for stable operation. Another important part of the experimental apparatus is the molecular-beam machine and accompanying laser systems that are used to produce rovibrationally selected molecular N_2^+ ions. This setup was described in Ref. [86, 87]. For the experiments presented in this thesis, the probe laser for vibrational transitions in N_2^+ , at $4.6 \mu\text{m}$, was not used and is therefore only briefly mentioned in the context of stabilization schemes. Complementary details on the experimental setup may be found in Ref. [88, 47].

We begin, in Section 3.1, by briefly reviewing the physics of ion traps and then proceed to describe the design and manufacturing of a new trap for single molecule operation. In Section 3.2, we describe the electronic circuits that were built to drive the trap and in Section 3.3, we describe several methods for laser stabilization, including a Pound-Drever-Hall lock to a cavity and a lock to a spectroscopic reference. We end this chapter, in Section 3.4, by describing some specifics of the experimental apparatus such as the control electronics and the magnetic-field coils.

3.1 A new trap for single molecule manipulations

A molecular-clock experiment for a trapped homonuclear diatomic molecule has different requirements from many other trapped-ion experiments. We have seen in Chapter 2 that the molecular qubits and clock states encoded in the electronic ground state of N_2^+ are extremely long-lived, even at ambient temperatures, and possess a low sensitivity to stray electromagnetic fields. There is, therefore, no need for a cryogenic setup or active field compensation. In order to reach the frequency precision of state-of-the-art clock experiments, long probe times, $\propto 1/\Delta f$, are required in order to avoid broadening of the line profile [77]. The experimental duty cycle is then dominated by this probe time and a low heating rate takes priority over the fast cooling and short gate times that are sought in quantum-information experiments [89]. A miniaturized trap, with ion-electrode distances of $r_0 \approx 100 \mu\text{m}$, is therefore not required and we may instead implement a millimeter-scale trap which will reduce the anomalous heating rate of the ion motion [90], simplify manufacturing and increase access to the trap center by the molecular beam and lasers. We begin by briefly reviewing the motional dynamics of an ion in a linear Paul trap.

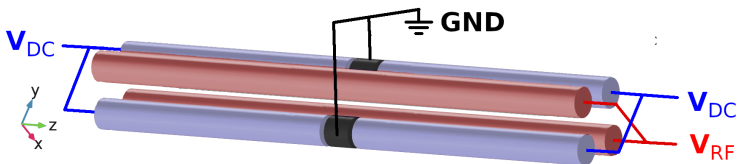


Fig. 3.1. A linear Paul trap in the 'single-phase' configuration with two solid RF electrodes and two segmented DC electrodes.

3.1.1 The linear Paul trap

A linear Paul trap is shown schematically in Figure 3.1. It consists of four cylindrical rods, two of which are segmented. We apply a radio-frequency (RF) potential on the two solid electrodes to generate a trapping potential along the radial (x, y) axes. On the segmented rods, the central segments are held at ground potential. The remaining four 'endcap' segments have applied static (DC) potentials to produce confinement along the 'axial' z -direction. The trapping conditions and motional dynamics of ions in a linear Paul-trap have been extensively described in Ref. [91, 92, 93, 94]. Here we will use these results for designing and characterizing a new trap.

The secular motion

In the absence of stray electric fields and assuming that the RF and endcap electrodes produce harmonic potentials, the equations of motion for an ion in such a trap takes the form of Mathieu equations,

$$\frac{d^2u}{d\tau^2} + [a_u - 2q_u \cos(2\tau)]u = 0, \quad (3.1)$$

with $u = x, y, z$ describing the coordinates. The trap parameters a_u and q_u and τ are defined by,

$$\tau = \frac{\Omega_{RF}t}{2}, \quad q_x = -q_y = 2 \frac{eV_{RF}}{m\gamma_0^2\Omega_{RF}^2}, \quad a_x = a_y = -\frac{1}{2}a_z = -\kappa \frac{4eV_{DC}}{mz_0^2\Omega_{RF}^2}, \quad (3.2)$$

where e and m is the charge and mass of the trapped ion. The radial distance from the symmetry axis of the trap to the RF electrodes is denoted r_0 and the axial distance between the endcap electrodes is $2z_0$. Ω_{RF} is the frequency of the RF drive with amplitude V_{RF} . The voltage on the endcap electrodes is V_{DC} and κ is a geometric factor which depends on the specific trap design and can be simulated or measured experimentally.

In the limit of $|a|, |q| \ll 1$, the solutions to Eq. (3.1) describe two superimposed ion trajectories separated into a 'secular' harmonic oscillator

motion with frequency ω_r and a faster superimposed 'micromotion' at the drive frequency Ω_{RF} ,

$$u(t) = u_0 \left[1 - \frac{q_u}{2} \cos(\Omega_{RF}t) \right] \cos \omega_r t. \quad (3.3)$$

The secular harmonic frequency for a single ion is given by,

$$\omega_u \approx \frac{\Omega_{RF}}{2} \sqrt{\frac{q_u^2}{2} + a_u}. \quad (3.4)$$

The axial confinement is due to the static field only, with $q_z = 0$, and the axial secular frequency is therefore,

$$\omega_z \approx \frac{\Omega_{RF}}{2} \sqrt{a_z}. \quad (3.5)$$

By the mass dependence of the a_u and q_u parameters, we note that a lighter ion will experience a deeper potential in the trap.

A two-ion string along the trap axis has two motional modes in the trap, given by [95],

$$\omega_{\mp}^2 = \frac{\omega_z}{m_1} \left(1 + \frac{1}{M_{12}} \mp \sqrt{1 + \frac{1}{M_{12}^2} - \frac{1}{M_{12}}} \right), \quad (3.6)$$

where ω_z is the axial frequency of the ion with higher mass, m_1 , and $M_{12} = m_1/m_2$ is the mass ratio of the two ions. The slower frequency ω_- is an in-phase motion resembling the center-of-mass (COM) motion of two ions with equal masses. This mode will be denoted ω_{COM} . The faster frequency ω_+ is an out-of-phase motion resembling a stretch (STR) mode and will be denoted ω_{STR} .

The micromotion

The properties of micromotion in a linear Paul trap have been extensively described in Ref. [96, 97]. In an ideal trap free from misalignment, stray electric fields and a phase mismatch between the RF electrodes, the micromotion vanishes on a line along the trap axis, the 'RF null line'.

Close to the trap axis, the kinetic energy of the ion motion in the radial directions is dominated by the micromotion energy, given by,

$$E_k = \frac{1}{2}m\omega_r^2x^2. \quad (3.7)$$

The effective electric field amplitude at a radial distance x away from this axis is then,

$$E_0^{MM} = \frac{m\omega_r^2x}{e}. \quad (3.8)$$

Under the influence of this RF field, the micromotion of the ion will produce spectral sidebands at integer multiples of the drive frequency, Ω_{RF} . In the limit of low modulation the strength of these micromotion sidebands are given by the ratio of two Bessel functions of the first kind, J_i [96],

$$\frac{I_{MM}}{I_{Car.}} \approx \left(\frac{J_1(\beta)}{J_0(\beta)} \right)^2. \quad (3.9)$$

Here, I_{MM} and $I_{Car.}$ represent the line intensities on the first micromotion sideband and carrier transition respectively. For a low modulation index, β , we have,

$$\frac{J_1(\beta)}{J_0(\beta)} \approx \beta/2. \quad (3.10)$$

In the absence of a phase mismatch in the RF potentials, β is related to the radial distance, x , and laser wave-vector, k , by,

$$\beta \approx \frac{1}{2}kqx. \quad (3.11)$$

A small, unavoidable micromotion component appears on the trap axis due to the finite extent of the ion wavefunction. The extent of an ion wavefunction in the motional ground state of a harmonic potential is given by,

$$x_0 = \sqrt{\frac{\hbar}{2m\omega_r}}. \quad (3.12)$$

The quantity $\eta = kx_0$ is called the Lamb-Dicke parameter and represents the ratio between the wavelength of incoming radiation, $k = 2\pi/\lambda$, and the extent of the wavefunction of the ion in the secular ground state of the trap, $n = 0$. With a radial secular frequency of $\omega_r \approx 2\pi \times 1$ MHz and the mass of a $^{14}\text{N}_2^+$ ion, we find that in the trap ground state the ion has a spatial extent of $x_0 \approx 13$ nm. According to Eq. (3.8), the ion therefore experiences a maximum RF field of $E_0^{MM} \approx 0.15$ V/m.

In the Lamb-Dicke regime, defined as $\eta^2(2\bar{n} + 1) \ll 1$, where \bar{n} represents the average motional quantum number in the trap, the first-order Doppler shift vanishes and the ion spectrum shows sidebands at multiples of the trapping frequency rather than broadening. A second-order Doppler shift is induced by the relativistic time dilation of the ion with a relative shift of [96],

$$\frac{\Delta\nu}{\nu} = -\frac{E_k}{mc^2}. \quad (3.13)$$

In the limit of $q \ll 1$, the kinetic energy, E_k , is dominated by the kinetic energy due to micromotion. Thus, according to Eq. (3.7), the relativistic Doppler shift of the N_2^+ ion due to the finite extent of the wavefunction in $n = 0$ is then $\Delta\nu/\nu \approx 1 \times 10^{-20}$. The modulation index measured with a laser of $k = 2\pi/729$ nm is $\beta = 0.006$ corresponding to a sideband-to-carrier intensity ratio of 1×10^{-5} . A clock transition in a properly compensated N_2^+ -ion near the trap ground state is therefore not limited by the first or second order Doppler shifts.

3.1.2 Axial RF gradients

The ion trap described in Ref. [98] was implemented in several molecular ion experiments [87, 99, 39] by using a string of molecular N_2^+ ions embedded in a Coulomb crystal of Ca^+ for sympathetic cooling. Such crystals reached a temperature of ~ 20 mK, with a corresponding Doppler linewidth of ~ 1 MHz [47]. The Doppler cooling limit on the $(4s)^2\text{S}_{1/2} \rightarrow (3d)^2\text{P}_{1/2}$ transition in Ca^+ is 0.5 mK [100]. The discrepancy is because away from the RF null line, the ions experience significant micromotion which causes heating of the crystal. We therefore consider using a string of ions along the trap axis rather than a 3D Coulomb crystal.

In order to reduce the Doppler shift, we shall aim for the Lamb-Dicke regime, $\eta^2(2\bar{n}+1) \ll 1$, where the first-order Doppler shift vanishes [91]. A secular frequency of $\omega_z \approx 2\pi \cdot 0.64$ MHz and a temperature after Doppler cooling of 0.5 mK corresponds to an average motional state of $\bar{n} \approx 16$ and $\eta^2(2\bar{n}+1) = 0.41$. We must therefore cool the $2\bar{n}$ motion to near the trap ground state, $n = 0$, in order to properly fulfill the Lamb-Dicke condition and remove the first-order Doppler shift.

Different segments of the trap have different capacitance to ground which may cause a phase shift or amplitude shift between the RF potentials. The old trap [98] had all four rods segmented. In order to reduce unwanted pickup or phase mismatch, the RF potential was only applied to the middle segments of two opposing rods while the other segments were capacitively grounded. In this configuration, however, an additional RF field appears along the z -direction due to the short middle segment of the trap, as shown in Figure 3.2a.

The small r_0/z_0 ratio of this trap, $r_0/z_0 \approx 0.8$, introduces a steep RF-quadrupole potential in the z -direction which causes micromotion along the trap axis¹. Figure 3.2b shows the measured intensity ratio between the first micromotion sideband and the carrier transition, $I_{MM}/I_{Car.}$, as a function of the ion position along the axial z -direction. This was measured by electron-shelving spectroscopy [91] on the $(4s)^2S_{1/2}(m_J = -1/2) \rightarrow (3d)^2D_{5/2}(m_J = -5/2)$ transition² of a single $^{40}\text{Ca}^+$.

The micromotion amplitude is low, $\beta \approx 0.01$, near the axial center, $z = 0$, and as strong as the carrier, $\beta \approx 2$, only $1 \mu\text{m}$ away. The RF null line is thus only an RF null point. In a single-ion experiment, this axial micromotion can be compensated, as with radial micromotion [96], by placing the ion in the center of the RF potential using static compensation fields. For a two-ion string along the axis this is no longer possible. In this case only one ion can be compensated. The lighter ion will experience a deeper potential (see Eq. (3.4)) and is therefore more likely to take the compensated center position.

¹This axial potential could in principle be used to confine ions axially without an applied endcap voltage.

²The lowest energy states in Ca^+ , e.g. $(4s)^2S_{1/2}$, $(3d)^2D_{5/2}$ and $(4p)^2P_{3/2}$ will henceforth be denoted simply by the shorthand notation $S_{1/2}$, $D_{5/2}$ and $P_{3/2}$.

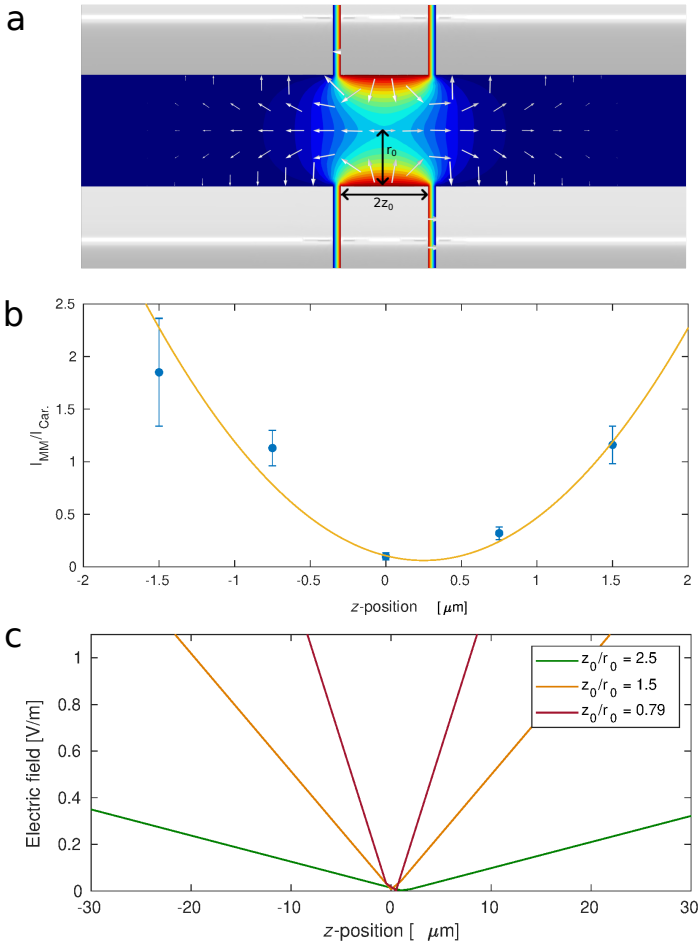


Fig. 3.2. **a)** The simulated potential from an old version of the RF trap with $r_0/z_0 = 0.786$ with RF potentials applied to the central segments showing the axial RF potential when the DC electrodes are held at ground potential. The colors show the potential (arb. u.) and white arrows show the direction of the electric field. **b)** The measured intensity ratio between the first micromotion sideband and the carrier transition, $I_{MM}/I_{Car.}$, as a function of the ion position along the axial z -direction. Electron-shelving was performed on the $S_{1/2}(m_J = -1/2) \rightarrow D_{5/2}(m_J = -5/2)$ transition of a $^{40}\text{Ca}^+$ ion and the ion position was moved using static voltages on the endcap electrodes. Error bars represent 1σ statistical uncertainties. In the limit of low modulation, we expect a quadratic dependence on the ion position (orange line), as described in the text. **c)** The simulated electric field strength along the z -axis for three different r_0/z_0 -ratios with 1 V applied to the central segments. All simulations were performed in COMSOL [101].

Figure 3.2c shows the electric field amplitude along the trap axis with 1 V applied to the central segments, simulated by a finite-element method in COMSOL [101]. With a two-ion distance of $10 \mu\text{m}$ and an RF amplitude of 1000 V, the ions experience a field of up to 600 V/m in the lowest ratio $z_0/r_0 = 0.79$. A r_0/z_0 -ratio of at least 2.5 is necessary in order to obtain a negligible RF potential along the axis below 15 V/m for both ions. A more conventional solution is to use long, unsegmented RF electrodes, like those shown in Figure 3.1. In this configuration, the DC electrodes can be segmented with any value of z_0 without introducing an axial RF potential³.

3.1.3 Trap design

A new trap was designed to achieve radial frequencies of $\omega_r \approx 2\pi \cdot 1 \text{ MHz}$ for Ca^+ and a low $q \approx 0.1$, without axial RF potentials and with a low heating rate. First we consider the effect of changing the electrode radius, r_e , on the trapping fields and the geometric access to the trap center.

Electrode radius

Anharmonic RF trapping potentials will couple different motional degrees of freedom and may therefore cause heating of a ground-state-cooled axial mode by the radial modes [102]. The ratio of the ion-electrode distance, r_0 , to electrode radius, r_e , that produces the most harmonic potential is $r_0/r_e \approx 1$ [103]. This ratio, however, limits access to the trap center by a molecular beam and reduces the effective numerical aperture. The simulations presented in Figure 3.3 show the effect of reducing the electrode radius, r_e , while keeping the ion-electrode distance fixed to $r_0 = 1.75 \text{ mm}$.

The gain in numerical aperture between $r_e = 2 \text{ mm}$ and $r_e = 0.25 \text{ mm}$ is nearly a factor of 2. Figure 3.3b shows the simulated RF potential along the radial x -axis for four different electrode radii. We find that the trap electrodes can be reduced to thin wires without introducing any

³The endcap electrodes will then require voltages a factor of 2 higher than if all rods were segmented.

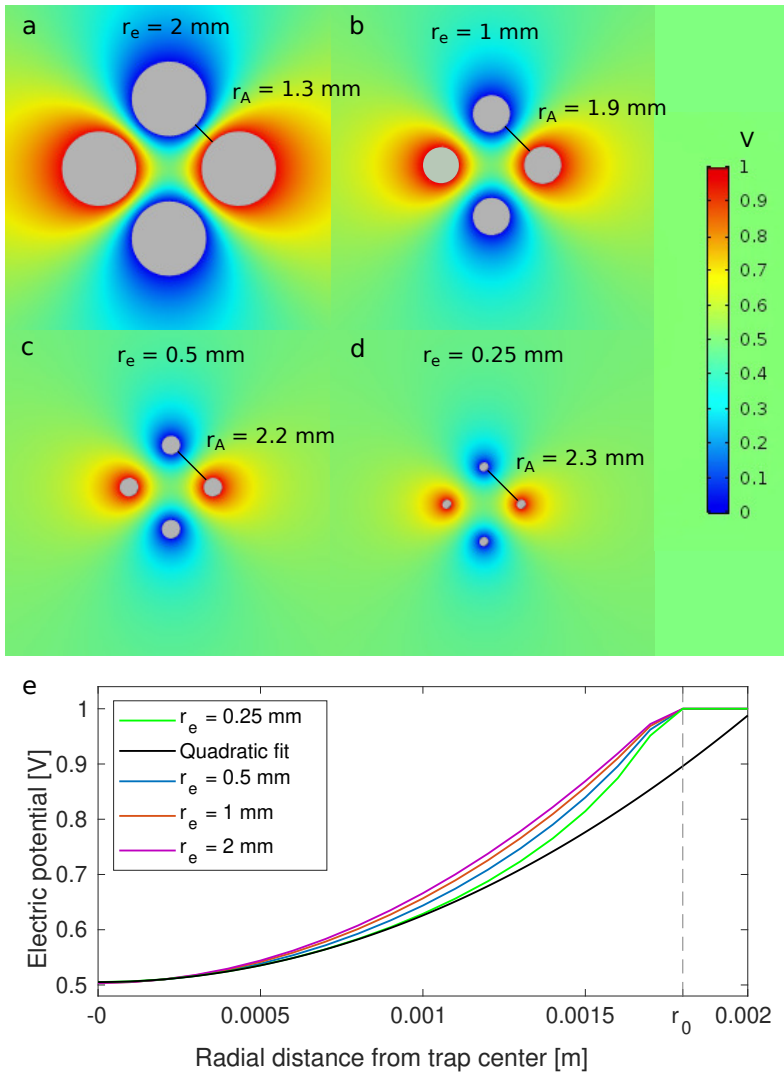


Fig. 3.3. **a-d)** Four traps with different electrode radii, $r_e = 2, 1, 0.5, 0.25$ mm, simulated in COMSOL [101] with $r_0 = 1.75$ mm. The radial distance between electrodes is denoted r_A **e)** The simulated potential along the radial x -direction for the different configurations shown in **(a-d)**. A quadratic fit to the curve of $r_e = 0.25$ mm near $x = 0$ (black curve) shows a deviation of 1% from harmonicity at $x = 750 \mu\text{m}$ from the trap center.

significant anharmonicity close to the trap axis. The thinnest configuration, $r_e = 0.25$ mm, shows a 1% deviation from harmonicity above ~ 750 μm from the trap center. This distance corresponds to a secular temperature of above 10^4 K and will not be accessible to the ions. The thinner electrodes also reduce the effective solid angle covered by the trap electrodes as seen by the ion. This leads to a lower heating by black-body radiation (BBR) from the electrodes, which are typically hotter than their environment.

In a segmented design, $r_e \approx 1.5$ mm is the lower practical limit to build a mechanically robust and self-supporting segmented electrode. One could instead use a pair of ring electrodes or additional rods as endcap electrodes in a wire trap to achieve the same effect.

Compensation electrodes

Next, we consider the addition of compensation electrodes outside the trap in order to apply auxiliary fields to the trapping region. These will be useful for compensation of micromotion [96] and for coherent motional excitation of the motional modes [104]. The field strength that can be applied to the ions from a trap electrode is shown in Figure 3.4a. The value of the electric field on the trap axis is $E_0 = 20$ V/m in the y -direction (the plane of the DC electrodes) for a potential of 1 V applied on the middle segment. Such an offset field can not be applied in the x -direction without a mixing of RF and DC voltages on the RF electrodes which may introduce additional noise in the trapping potentials. Instead, we investigate the effect of adding compensation electrodes to the outside of the trap as shown in Figure 3.4b.

Due to the electric shielding from the trap electrodes, the field from one compensation electrode is a factor of 10^{-2} smaller than from a trap electrode with the same applied voltage. By adding the compensation electrodes in the horizontal plane of the chamber, we avoid restricting the numerical aperture in the vertical direction which is used for photon counting and imaging. The placement of these electrodes in the horizontal plane also serves to shield the trap electrodes from being coated by the Ca-oven or molecular beam, while also blocking stray light from the lasers from directly hitting the trap electrodes.

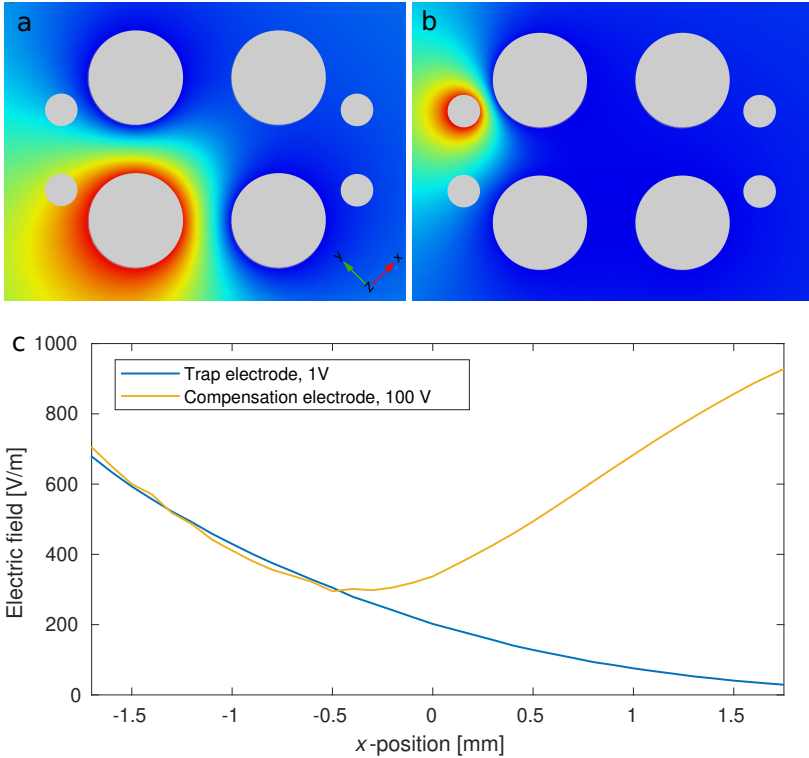


Fig. 3.4. **a-b)** The radial potential (arb. u.) induced by applying **(a)** 1 V on a trap electrode and **(b)** a compensation electrode, simulated in COMSOL [101]. **c)** The electric-field amplitude as a function of radial distance along the x -direction. To reach the same amplitude in the trap center as 1 V on the trap electrode (blue curve), a potential of ~ 60 V must be applied to the compensation electrode (orange curve).

3.1.4 Trap manufacturing

The millimeter-sized trap design presented here allows the trap to be manufactured through CNC machining, without the special manufacturing techniques or electrode coatings used for miniaturized traps [105]. The size and shape allows for stainless steel rods to act as trap electrodes. These can be polished to remove surface roughness and coating the electrodes with, e.g., gold will not be necessary as the ion-electrode distance is large. We have seen in Chapter 2 that the lack of a dipole moment in N_2^+ means that the heating of electrodes will not limit the lifetime of the rovibrational states. Heat dissipation is therefore not as important as in traps made for polar species, or for cryogenic setups.

Figure 3.5a-c shows the trap assembly including a stainless steel holder. We chose a segmented, self-supporting electrode design and we therefore need a mechanically robust insulator to act as a spacer and to hold the middle segments in place. Between the commercial machinable ceramics, Shapal Hi-M Soft has a bending strength 3 times that of Macor (300 MPa vs. 96 MPa) and better heat conductivity (90 W/(m K) vs. 1.46 W/(m K))⁴.

Figure 3.5d shows a cross section of the trap assembly and in-vacuum lens system. A 2-inch lens assembly below the trap is used for collecting fluorescence photons from the ions on a PMT outside the chamber for detection of the Ca^+ state⁵. Two 1 inch lenses placed 80 mm from either side of the trap center are used to achieve a narrow focus of the lasers along the trap axis. The finished trap assembly mounted inside the vacuum chamber is shown in Figure 3.6.

⁴Precision Ceramics, Shapal Hi-M Soft

⁵The lens assembly was designed by Z. Meir

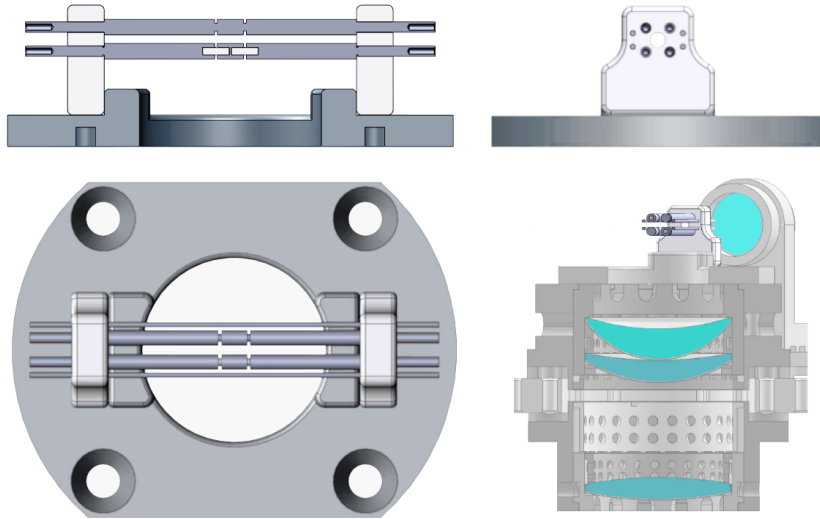


Fig. 3.5. The final trap design with $r_0 = 1.75$ mm, $r_e = 1.5$ mm $z_0 = 2.5$ mm and four compensation electrodes outside the trap. Two 1 inch lenses are placed along the axis 80 mm from the trap center and a 2 inch lens system is placed below the trap to capture fluorescence from Ca⁺ and focus it on a photomultiplier tube outside of the trap chamber.

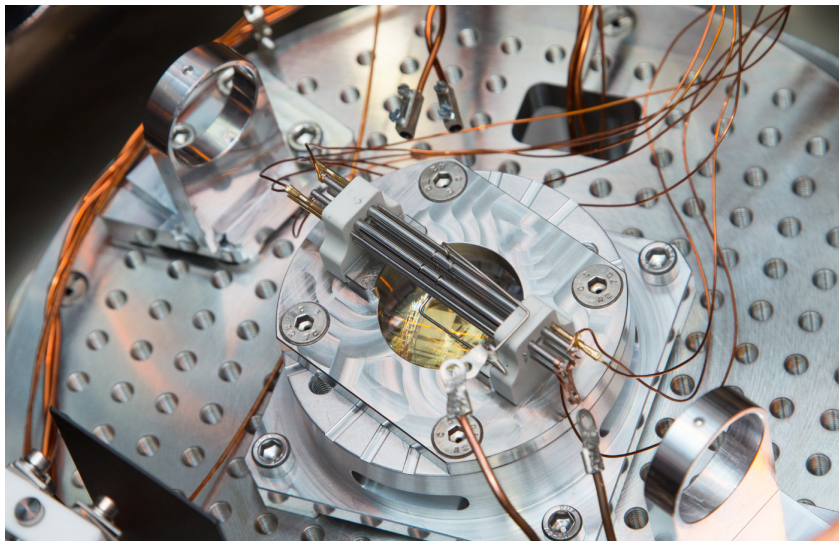


Fig. 3.6. The assembled trap in the center of the vacuum chamber. Picture by *P. Eberle*

3.2 Trap electronics

In this section, we describe the electronics that were built to drive the trap with stable RF and DC voltages. A schematic overview of the trap circuit is shown in Figure 3.7. This includes a helical-resonator circuit for the RF potentials, a voltage supply for the endcap and compensation voltages as well as filters to stabilize the DC voltages. We have also added an auxiliary RF source⁶ on one compensation electrode for coherent excitation of the motional modes [104]. These circuits are described in more detail below.

⁶StemLab 125-14 'Red Pitaya'

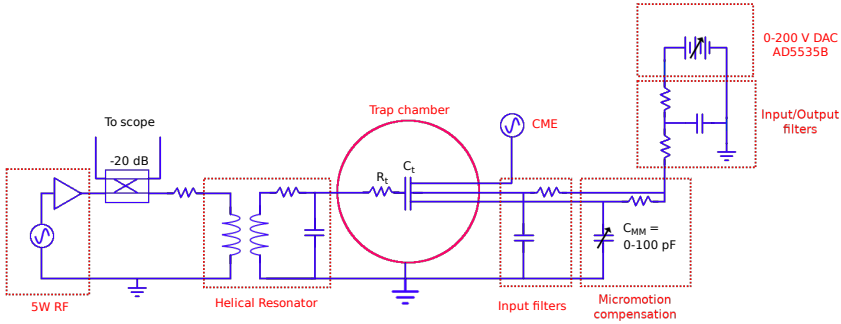


Fig. 3.7. A simplified equivalent circuit for a stable trap drive. The circuit includes (from left to right) the RF source and amplifier, marked '5W RF', a -20 dB directional coupler and the helical resonator connected to the trap. An additional RF source is connected to a compensation electrode for coherent motional excitation (CME) [104]. Input filters are placed on the DC vacuum feedthrough with a variable capacitor on one endcap channel for axial micromotion compensation. Input/Output filters are also placed at the output of the voltage supply, here marked '0-200 V DAC'.

3.2.1 Helical resonator design and characterisation

The preferred method for achieving a stable and high-voltage RF potential on the trap is through a helical resonator circuit. The helical resonator acts as a resonant amplifier with an inductive coupling between the trap and the RF source. The design and characterization of the helical resonator has been extensively described in Ref. [106]. This circuit achieves a higher output voltage compared to a direct drive for the same values of input power, as it allows precise impedance matching of the amplifier to the trap. The resonator also acts as a narrow notch filter to remove unwanted frequency components coming from the RF synthesizer or amplifier. Finally, the ground connection to which the RF potentials are referenced can be decoupled from the source and amplifier grounds which may be noisy and may cause ground loops.

We treat the resonator circuit, theoretically, as a series LCR oscillating circuit with resonance frequency ω_0 , where L is the total inductance, R

the total resistance and C the total capacitance of the circuit. The peak voltage on the trap can be estimated by [106],

$$V_p = \kappa \sqrt{2PQ}. \quad (3.14)$$

Here κ is a function of the inductance and capacitance of the combined resonator and trap circuit with $\kappa = (L/C)^{1/4}$, P is the forward power and Q is the quality factor of the resonator circuit describing the energy stored in the circuit, or equivalently, the time constant for damping of the oscillations, with,

$$Q = \frac{1}{R} \sqrt{\frac{L}{C}}. \quad (3.15)$$

In terms of the resonance frequency, $\omega_0 = 1/\sqrt{LC}$, we can rewrite the above equation as,

$$Q = \frac{1}{\omega_0 RC}. \quad (3.16)$$

A high quality factor is therefore dependent on having a low RF resistance from the coil to the trap. A low resistance is achieved by using highly conductive materials (copper, silver) with large diameter and well soldered connections between the coil, the vacuum feedthrough and the trap. We also note that the Q factor scales with the inverse of the frequency and capacitance. It is therefore easier to achieve a high-Q circuit with lower trap frequencies and a low capacitance to ground in the resonator, vacuum feedthrough and on the trap. This circuit is therefore not useful for traps with high capacitance to ground where a direct drive may be necessary.

In our trap design, we aim for radial frequencies of $\omega_r \approx 2\pi \cdot 1$ MHz, axial frequencies of $\omega_z > 2\pi \cdot 0.5$ MHz and $q \approx 0.1$ for a Ca^+ ion. By inserting $q = 0.1$ and $r_0 = 1.75$ mm and a maximum practical voltage level of $V_{RF} = 1000$ V into Eq. (3.4), we find that we need $\Omega_{RF} \approx 2\pi \cdot 20$ MHz in order to achieve the desired radial frequencies.

The capacitance to ground of the trap and feedthrough was measured as ~ 15 pF each, for a total of 30 pF. The RF resistance between the helical coil and the trap is frequency dependent and can not be measured without

a network analyzer. Assuming that the leads are thick and the connections are well soldered, we expect $R_t < 1 \Omega$. From Eq. (3.16), we therefore find that we can achieve $Q \approx 265$ at $\Omega_{RF} \approx 2\pi \cdot 20$ MHz. According to Eq. (3.15) we need a coil inductance of $L \approx 2.1 \mu\text{H}$ and we can reach our desired peak voltage with 3.6 W of RF power.

The resonator was therefore built for a frequency of $\Omega_{RF} \approx 2\pi \cdot 20$ MHz and an inductance of $L_C \approx 2.1 \mu\text{H}$. A copper tube with outer diameter of 100 mm and a wall thickness of 3 mm was cut to a height of 150 mm to form the outer shield of the resonator. The resonator coil was made by winding a copper wire 9 turns with a winding pitch of 6 mm around a cylinder of diameter 50 mm. The diameter of the coil wire is 3 mm. The coil height is then 54 mm. One end of the coil was attached to the resonator shield and the other end was connected to the vacuum feedthrough via copper wire, 2 mm in diameter. The antenna coil was made from 1 mm-diameter silver-coated copper wires and is held in place above the main coil by a copper cap that was fitted to the outer shield. The antenna coil was not grounded to the resonator shield in order to decouple the grounds between the electrical mains and the resonator which was grounded to the trap chamber.

With the RF source⁷ and helical resonator in place, using a -20 dB directional coupler⁸, we measure a resonance frequency of 16.86 MHz and by measuring the width of the resonance a Q-factor of 300 was inferred. This corresponds to a coil inductance of $L_C = 3.0 \mu\text{H}$. We can therefore reach ~ 1000 V on the trap with 2.6 W of power⁹ and $q \approx 0.14$. These moderate power levels are not expected to lead to significant heating of the trap electrodes.

3.2.2 Trap voltage supply

The static voltages required for obtaining axial radial frequencies of $\omega_z > 2\pi \cdot 0.5$ MHz on a single $^{40}\text{Ca}^+$ were estimated, using Eq. (3.4),

⁷Keithley 3390 Arbitrary Waveform Generator

⁸MiniCircuits ZFBDC20-61HP+

⁹By improving the connections or by using thicker-gauge wire to reduce the resistance to $R_t = 0.5$ Ohm the Q-factor would increase to $Q = 600$ and we would reach the same voltage on the trap with half the power.

to be below 200 V. We therefore base the source of static DC voltages around the AD5535B evaluation board^{10,11}. A stable 5 V input reference allows 32 individually tunable voltages in the range 0-200 V with a 14 bit resolution. These outputs were filtered using two cascaded first order RC input-output filters to produce a second-order filter to the outputs and to protect the board from spurious voltages picked up near the trap. Using $R = 15 \text{ k}\Omega$ and $C = 10 \text{ }\mu\text{F}$, these filters have a -3 dB corner frequency of 0.6 Hz and a steep 40 dB/decade slope thus effectively filtering any 50 Hz noise components with -83 dB suppression.

Shielded cables carry the voltages to a filtering box placed as close as possible to the vacuum feedthrough where the voltages are once again filtered to remove any noise picked up along the way. With $R = 20 \text{ k}\Omega$ and $C = 10 \text{ }\mu\text{F}$, these first-order RC filters have a corner frequency of 0.8 Hz. The capacitors in this filter box also serve to ground the DC electrodes from RF potentials picked up on the trap. Such a capacitive grounding is best preformed inside the chamber close to the trap in order to reduce the amount of residual RF voltage pick-up on the endcap electrodes. Due to the varying capacitance between different trap electrodes, some spurious RF field along the trap axis is, nonetheless, expected and can be compensated by the method presented in the next section. For this method it is beneficial not to ground all electrodes in vacuum to allow tuning of the RF pickup on some electrodes.

3.2.3 Axial micromotion compensation circuit

Axial micromotion, as a result of trap misalignment or RF pick-up on endcap electrodes, can not be compensated using DC fields [96]. There are several methods for active micromotion compensation, e.g. by driving an additional RF potential on an auxiliary electrode out of phase with the trapping field to cancel the axial field component [107]. Another method is the modulation of the laser frequency in phase with the RF drive as shown in Ref. [108]. Here, we employ a passive method of compensation which relies on tuning the RF pickup on the endcap electrodes selectively by changing the capacitors in the filter box. This ensures that the phase,

¹⁰Analog Devices EVAL-AD5535BSDZ

¹¹The voltage supply was designed and built by *G. Hegi*

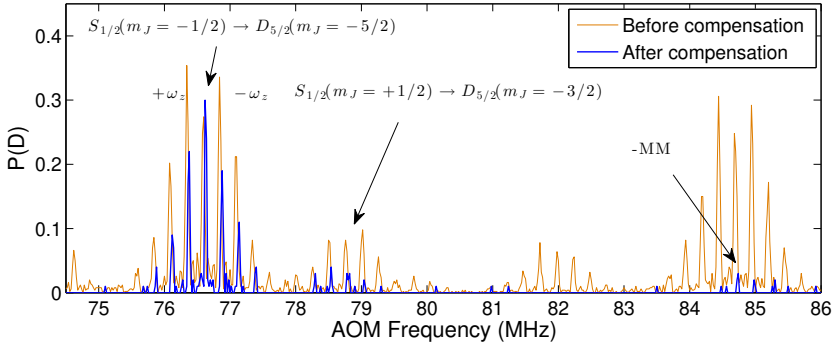


Fig. 3.8. The $S_{1/2}(m_J = -1/2) \rightarrow D_{5/2}(m_J = -5/2)$ carrier transition in Ca^+ and its first micromotion sideband (MM), measured by electron-shelving spectroscopy, before and after axial micromotion compensation. Each carrier is accompanied by motional sidebands at multiples of the secular frequency ω_z . Small contributions from the $S_{1/2}(m_J = +1/2) \rightarrow D_{5/2}(m_J = -3/2)$ transition also appear in the spectrum due to imperfect state preparation. The frequency axis shows the measured AOM frequency which is $-2\times$ the real frequency shift and is added to the transition frequency of $f_0 \approx 411.042$ THz.

frequency and voltage of the RF compensation field always matches the RF drive.

A single capacitor in the filter box was replaced with a variable capacitor, with $C_{MM} = 0 - 100$ pF, on one endcap channel, as shown schematically in Figure 3.7. By reducing the capacitance of this electrode successively, the RF pickup is increased until it cancels the spurious field. The filtering properties of the low-pass filter can be restored by changing the resistor on this channel.

Figure 3.8 shows the $S_{1/2}(m_J = -1/2) \rightarrow D_{5/2}(m_J = -5/2)$ carrier transition in Ca^+ and its first micromotion sideband, measured by electron shelving, before and after axial micromotion compensation. The measured modulation was reduced from $\beta \approx 2$ to $\beta \approx 0.1$. The measured modulation index does not change significantly over a distance of $\pm 100 \mu\text{m}$ along the trap axis. A more precise compensation can be achieved by using an additional variable capacitor with a finer tuning.

3.3 Laser stabilisation for precision spectroscopy

In this section, we will give an overview of a few different techniques used for laser stabilization. We begin with the Pound-Drever-Hall technique for locking a laser to a high-finesse cavity and present a method for estimating the linewidth of the locked laser. We then present three additional methods for stabilizing a laser for molecular spectroscopy.

The energy levels and lasers involved in the $\text{Ca}^+ - \text{N}_2^+$ experiment are presented schematically in Figure 3.9. Two continuous wave (CW) external cavity diode lasers (ECDL), at 423 nm and 387 nm, are used for isotope-selective ionization of Ca^+ [109]. Another two pulsed dye-lasers, at 202 nm and 375 nm, are used for rovibrationally selective ionization of N_2^+ in the electronic ground state from a molecular beam of neutral N_2 [86]. The Doppler cooling of Ca^+ requires two lasers, 397 nm and 866 nm, one for fast repeated excitation on the $S_{1/2} \rightarrow P_{1/2}$ transition and the other to repump any population trapped in the $D_{3/2}$ state back to the $P_{1/2}$ state [98].

Sympathetic sideband-cooling [110, 111] of the shared motional modes of the $\text{Ca}^+ - \text{N}_2^+$ string proceeds on the narrow electric quadrupole $S_{1/2} \rightarrow D_{5/2}$ line at ~ 729 nm or ~ 411.042 THz. A laser at 854 nm is used for repumping the population from the $D_{5/2}$ state to the $P_{3/2}$ state which subsequently decays back to $S_{1/2}$. All coherent manipulations in Ca^+ such as state preparation, shelving spectroscopy and sideband thermometry [92] are performed using the 729 nm laser. This laser therefore has high requirements in terms of absolute frequency stability and narrow linewidth. We will show how this stability can be achieved using a Pound-Drever-Hall lock to a high-finesse cavity in Section 3.3.1.

In addition, a state-readout laser is added close to a resonance with the molecular $X^2\Sigma_g^+(v=0) \rightarrow A^2\Pi_u(v=2)$ transition at ~ 789 nm to map the internal state of the molecule onto the shared motional modes of the $\text{Ca}^+ - \text{N}_2^+$ string. This mapping relies on the state-dependent force exerted on the N_2^+ by the near-resonant 789 nm laser through the optical dipole-force. This readout scheme is described in Chapter 5. The entanglement of the internal state of the molecule with the motional modes of the Ca^+ can

also be preformed with the probe-laser by driving motional sidebands of a transition in a quantum-logic type scheme [112]. As the strength of motional sidebands scale with the Lamb-Dicke parameter, $\eta = kx_0$, the Rabi frequency on the sidebands are 2 orders of magnitude weaker than the carrier transitions at $4.6 \mu\text{m}$, with $\eta \approx 0.02$, and even weaker for microwave (MW) probes. In order to increase the Lamb-Dicke parameter, a scheme to lower the trap frequency adiabatically was implemented in Ref. [113].

The mid-IR or MW source that is used to probe the molecular states has even higher requirements in order to reach the precision of state-of-the-art clock experiments. A mid-IR laser, e.g. a quantum cascade laser (QCL) at $\sim 4.6 \mu\text{m}$, can be used to probe the Q(0) and S(0) clock transitions, as described in Chapter 2. This type of laser has been stabilized with a $\sim \text{Hz}$ linewidth (1s integration time) by locking it to a frequency-comb or ULE-cavity in Refs. [114, 115]. To provide an overview of additional techniques for stabilizing a probe laser, we describe three possible methods in Sections 3.3.3, 3.3.4 and 3.3.5, based on a lock to a frequency comb, a lock to a spectroscopic reference or through single-laser Raman excitation.

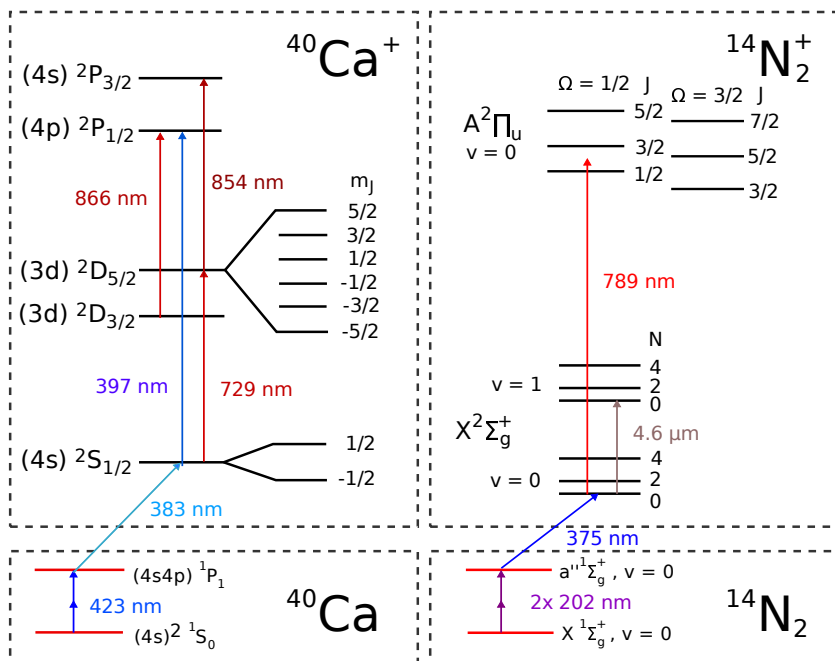


Fig. 3.9. A simplified energy-level diagram of the relevant levels in Ca^+ and N_2^+ (not to scale). The arrows represent the lasers that are used to manipulate the states. The ionization steps from the neutral species are presented at the bottom of the figure. The wavelengths are approximate.

3.3.1 Pound-Drever-Hall locking to a cavity

A high-finesse optical cavity provides short-term optical stability through rejection of frequencies outside of a narrow frequency band of typically $\Delta f \sim 10$ kHz. A stable error signal can be obtained from the high-finesse cavity by using a Pound-Drever-Hall locking-scheme [116], as presented schematically in Figure 3.10. Here we employ this technique for the stabilization of the 729 nm laser used for coherent state manipulations of Ca^+ on the $S_{1/2} \rightarrow D_{5/2}$ transition.

The Pound-Drever-Hall technique relies on a fast modulation of the laser frequency to extract the sign of frequency excursions around the top of the cavity resonance profile. The error signal is obtained by interfering the reflected power from the cavity with the incoming beam and demodulating the signal. In this way, the laser can be locked to the derivative of the reflected intensity at the top of the cavity resonance¹². This error signal is therefore, to first order, independent of fluctuations in the laser intensity.

The quality factor of an optical cavity can be characterized by its finesse \mathcal{F} which is analogous to the Q-factor of the helical resonator presented in Section 3.2.1. It is related to the decay time τ and cavity length L by,

$$\mathcal{F} = \tau \frac{c\pi}{L} = 2\pi \cdot \tau \cdot \nu_{FSR}. \quad (3.17)$$

Here $\nu_{FSR} = c/L$ is the free spectral range of the cavity and represents the frequency spacing between the fundamental spectral modes of the cavity. The finesse can be measured through a ring-down measurement which measures the lifetime, τ , of the laser power stored in the cavity. The light leaking out of the cavity is recorded on a fast photodiode as a function of time when the incoming light is blocked. Figure 3.11a shows the results of such a measurement on the 729 nm cavity¹³. To ensure that the measured decay constant is not limited by the decay time of the photodiode, the reverse-bias voltage of the photodiode was successively increased until no reduction in the ringdown time was observed. The decay constant was

¹²A Topical PDD110 module provides the error signal and a Topica FALC110 is used for a fast servo lock.

¹³ATF-6020-4, $L = 100$ mm notched ULE plano-convex Fabry-Perot cavity. AR coated for 745 nm.

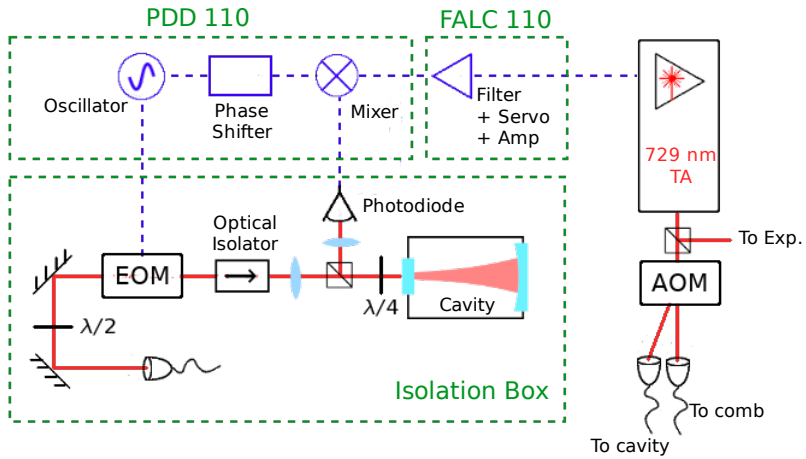


Fig. 3.10. A simplified schematic of the experimental setup for Pound-Drever-Hall locking of a 729 nm diode laser to a high-finesse Cavity as described in the text. AOM and EOM denotes an acousto-optic modulator and electro-optic modulator respectively. $\lambda/2$ and $\lambda/4$ refers to laser phase shifters in the form of a half-wave and quarter-wave plates, respectively.

measured to be $\tau = 29.6 \mu\text{s}$ corresponding to a finesse of $\mathcal{F} \approx 270000$. The linewidth of the cavity is therefore $\nu_{FSR}/\mathcal{F} = 8 \text{ kHz}$.

In order to stabilize the cavity length, it is mounted on a block of ultra-low expansion (ULE) glass which has a vanishing first-order thermal expansion coefficient at some zero-crossing temperature, T_0 . By monitoring the laser frequency of the locked laser as a function of the cavity temperature on a stable reference, the zero-crossing temperature can be measured. We monitor the beat-note frequency between the locked 729 nm laser and a frequency comb, as described in Section 3.3.3, to record the frequency of the laser while changing the cavity temperature. The results are shown in Fig 3.11b. A quadratic fit to the data shows a zero-crossing temperature of $T_0 = 26.83 \text{ }^\circ\text{C}$.

The cavity ULE block is placed on a Zerodur spacer¹⁴ inside a vacuum can in order to reduce thermal fluctuations and acoustic noise. A small ion

¹⁴Stable-Laser-Systems HC-6020-1-mntz1

pump¹⁵ is mounted on the can and reaches a pressure of $< 3 \times 10^{-6}$ mBar. The ULE block has no contact with the vacuum can and is placed on the Zerodur spacer on four small Viton pads. Therefore, heat exchange proceeds predominantly through radiation and a temperature change takes up to 10 hours to settle near the final values. This is a desirable feature which decreases the susceptibility of the cavity to temperature fluctuations in the environment. The temperature is maintained at the zero-crossing temperature using resistive heaters placed around the vacuum can. Unlike Peltier elements, which can be used to heat or cool, these resistive heaters do not permit cooling. Therefore, an ordinary Proportional-Integral (PI) servo loop will cause temperature oscillations as shown in Figure 3.11c. By operating the PI-controller¹⁶ without an integrator and with a slightly too low P-setting, a steady state can be reached where the heater is always on. The temperature will stabilize, although with an offset, to a set value. Using this trick, we achieve an acceptable temperature stability of a few mK over the course of a day.

The PDH setup was placed on a passive vibrational-damping breadboard resting on an airpad¹⁷. This platform has a low resonance frequency, of ~ 1 Hz, and therefore effectively dampens vibrations from the laser table and floors. Acoustic, electric-field and optical noise can also enter the setup through free space and a box was built to minimize outside interference. Figure 3.11d shows the displacements of the breadboard measured by an accelerometer with and without a simple cardboard box on top of the setup. The root-mean-squared displacements reduce by nearly a factor 2 with the box. A heavy isolation box was therefore built using 10 mm thick MDF board for a low resonance frequency. A layer of 30 mm thick sound-isolation foam padded the complete inside of the box. The box was also painted with electrically conducting paint which forms a Faraday cage when grounded in order to minimize stray electromagnetic fields which may interfere with the signals. Extra care was also taken to avoid ground loops in the stabilization circuit [117].

¹⁵Agilent 2 l/s Ion Pump

¹⁶Thorlabs TED200C

¹⁷Newport BenchTop vibration isolation system

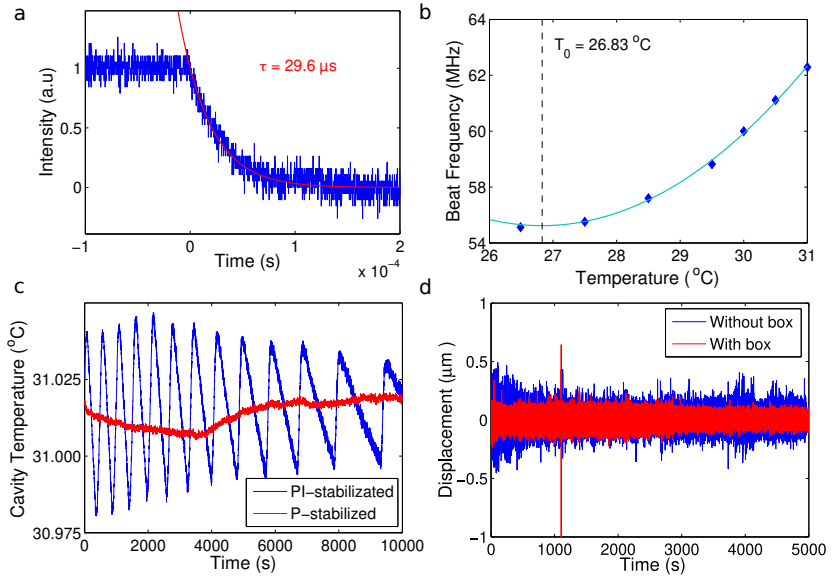


Fig. 3.11. **a)** A cavity ring-down experiment measured by a photodiode placed behind the cavity when the lock is turned off. An exponential fit to the data reveals a time constant of $\tau = 29.6 \mu\text{s}$ corresponding to a cavity finesse of ~ 270000 . **b)** The beat-note frequency between a frequency comb and the PDH-locked 729 nm laser, measured on a stable counter, as a function of cavity temperature (blue dots). The zero-crossing temperature is found by a quadratic fit to the data (blue curve) as $T_0 = 26.83^{\circ}\text{C}$. **c)** The temperature stability of the vacuum can that houses the cavity as a function of time with two different PI-servo settings, as described in the text. **d)** The measured displacements of an accelerometer placed on the vibrational damping pad as a function of time with (red) and without (blue) an ordinary cardboard box on top of the setup.

3.3.2 Linewidth characterisation using the in-loop error signal

The in-loop PDH error signal can be used to optimize the lock. It can also be used to estimate the laser linewidth using the method described in Ref. [118]. The relation between the measured frequency-noise spectrum and the Lorentzian linewidth is not exact but is nevertheless useful when there is no auxiliary narrow reference with which to compare the locked laser. A self-heterodyne measurement of a laser with a 1 kHz linewidth would require a delay line of ~ 100 km in order to lose coherence between the two beam paths [77].

A PDH error signal, obtained while scanning the laser frequency over the cavity resonance, is shown in Figure 3.12a. The modulation sidebands from the EOM¹⁸ have a frequency spacing of 20 MHz and a transfer function of $0.114 \mu\text{V}/\text{Hz}$ is inferred from the slope of the error signal (see inset). This function is used to relate the voltage fluctuations in the error signal of the locked laser to the real frequency fluctuations of the laser and hence to the laser linewidth.

The power spectral density (PSD) was obtained by recording the in-loop error signal for 1 s on a fast oscilloscope¹⁹ and taking its Fourier transform. In Figure 3.12b we show the PSD of the in-loop error signal with Fourier-frequency components up to 1.5 MHz. A large servo bump at 1.1 MHz represents the electronic bandwidth of the lock. The power spectrum (in dBm) was converted to a linear scale (W) and multiplied by the measurement impedance to obtain the units of V^2 . This is normalized to the resolution bandwidth of the measurement to obtain the Power Spectral Density in units of V^2/Hz . Using the transfer function, $1.14 \cdot 10^{-7} \text{ V}/\text{Hz}$, the PSD is converted to a noise spectral density (NSD) by dividing the PSD by the square of the transfer function to obtain the units of Hz^2/Hz . Figure 3.12c shows the noise spectral density (NSD) of the in-loop error signal of the PDH-locked 729 nm laser.

Two different regimes can be identified separated by the β -separation line given by $\beta = 8(\ln 2)f/\pi^2$. Frequency components above the β -line will contribute to the linewidth of the laser whereas frequency components

¹⁸Thorlabs EO-PM Phase Modulator EO-PM-NR-C1

¹⁹Teledyne Lecroy Wavesurfer 104MXs-B

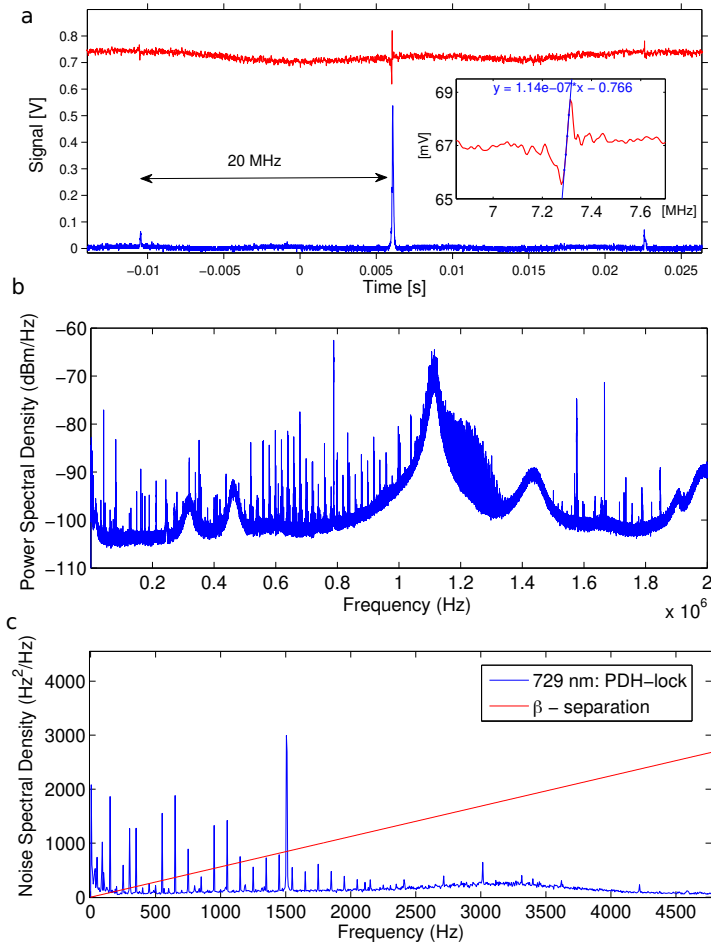


Fig. 3.12. **a)** The Pound-Drever-Hall error signal measured while scanning the laser frequency over the cavity resonance (red). The error signal is scaled and offset from the real value for visibility. The transmitted power behind the cavity is shown in blue. The inset shows the error signal as a function of frequency. A transfer function of $1.14 \cdot 10^{-7}$ V/Hz is inferred. **b)** The power spectral density of the in-loop error signal of the locked laser, obtained through a Fourier transform of the error signal measured on a fast oscilloscope for 1 s. The largest peak corresponds to the bandwidth of the lock at ~ 1.1 MHz while smaller peaks are due to the servo bandwidth of individual integrators. **c)** The noise spectral density describing the real in-loop frequency fluctuations of the laser. The line shows the β -separation line and the point where the two curves meet, around 150 Hz, is the separation frequency. The area under the curve between 1 Hz and 150 Hz determines the laser linewidth.

below the line are too small as compared to their frequency to significantly contribute to the linewidth²⁰. The latter may instead add to the 'wings' of the spectral profile. Individual peaks that appear above the separation line at higher frequencies are then likely to cause sidebands in the line profile. The Lorentzian linewidth $\Delta\nu$ is estimated from the area under the curve, A , by $\Delta\nu \approx \sqrt{8(\ln 2)A}$. We integrated from 1 Hz to 500 Hz²¹, and a (1 s integration) linewidth of 1 kHz was inferred. A more precise estimate of the laser line shape can be obtained by an in-depth analysis of the NSD, taking into account all the peaks that cross the β -line at higher frequencies using the method in Ref. [119].

With the above analysis, the laser lock can be optimized while monitoring the noise spectrum of the in-loop error signal. The most important noise contributions are those below the β -separation frequency and sacrifices can be made in higher frequencies in order to obtain a lower laser linewidth. The analysis presented in Ref. [118], and used here, is only valid as long as the laser frequency is the dominant source of voltage fluctuations of the error signal. This is usually the case with a PDH error signal, which is insensitive to power fluctuations to first order [116]. If there are large fluctuations in the cavity modes, e.g. by thermal or pressure effects, then the measured NSD does not describe the absolute laser linewidth but will nevertheless serve as a useful measure of the performance of the lock.

3.3.3 The frequency comb

While the PDH lock provides a narrow linewidth, the cavity will slowly deform over time and does not serve as a stable absolute frequency reference. A frequency comb can transfer the stability of an RF or MW clock into the optical domain by referencing its repetition rate and carrier envelope offset (CEO) to this clock. We can therefore utilize the stability of a commercial atomic clock²² to allow an absolute frequency determination on

²⁰As apparent to by the notation, β is analogous to the modulation index of micromotion and also the Lamb-Dicke parameter η . They describe the separation into regions where modulations either cause broadening or sidebands on the spectral profile.

²¹As can be seen in Fig 3.12c, many peaks appear in the region between 100 Hz and 1.5 kHz and the choice of integrating up to 500 Hz is somewhat arbitrary.

²²Stanford Research FS725m Rubidium frequency standard

the 10^{-11} level (100 s integration time). The clock can also be disciplined to GPS time which provides one order of magnitude better long-term stability. To achieve a better stability, a laser can be referenced to a primary or secondary frequency standard by interfering the two sources in a beat note, or by using a frequency comb as a mediator, as described below. The $S_{1/2} \rightarrow D_{5/2}$ transition in Ca^+ has been measured to a relative accuracy of 10^{-15} in an ion trap [120] and could potentially be used as a stable reference frequency within the same experimental setup.

We measured the frequency of the PDH-locked 729 nm laser through an optical beat note with a commercial frequency comb²³. By overlapping both sources with matching polarization and spatial modes on a fast photodiode, the optical interference between the 729 nm laser and the closest comb tooth produces an interference signal at the difference frequency of the two lasers. The repetition rate of the comb, $R_r \approx 250$ MHz, and higher frequency components are filtered out from the signal. After amplification, the difference frequency is sent to a counter which is referenced to the atomic clock.

Figure 3.13a shows a beat-note signal at 60 MHz measured by the counter over several hours. The observed drift is 65 mHz/s or 234 Hz/hour. This drift was also measured on the $S_{1/2} \rightarrow D_{5/2}$ transition in Ca^+ as shown in Figure 3.13b. The measurements were taken two years apart and a discrepancy in the absolute value between the two measured drifts are expected. As the stability of the comb teeth and the counter are both derived from the clock, and better than 10^{-11} for 100s integration time, the observed drift in the beat-note frequency of $10^{-7}/(100\text{s})$ is due to the CW laser and reflects a drift of the cavity modes²⁴.

The short-term frequency fluctuations of the comb teeth are proportional to the comb tooth number N by $\Delta\nu \approx N \cdot \Delta R_e$, such that the small fluctuations of the fundamental repetition rate of $\Delta R_e \approx 0.02$ Hz translates into a linewidth of 300 kHz at 411.042 THz, with $N \approx 1644000$. In order to narrow the comb teeth further, the repetition rate of the comb can be locked to the beat note with the 729 nm laser to transfer its short term stability to the comb, while monitoring the long-term drifts using the

²³Menlo Systems GmbH, M-Comb FC1500-250-WG, Carrier wavelength: 1560 nm.

²⁴By design, the counter can not measure the drift of the repetition rate as they are both referenced to the same clock. We therefore rely on the values specified from the manufacturer.

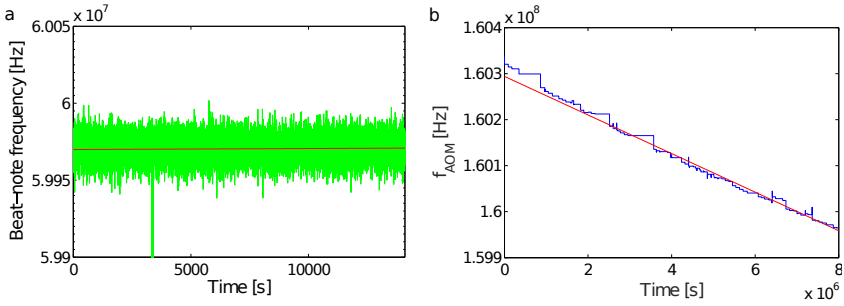


Fig. 3.13. **a)** The measured frequency of an optical beat note between the PDH-locked 729 nm laser and the frequency comb referenced to the atomic clock. A linear fit to the data (red line) shows a drift of 65 mHz/s or ~ 230 Hz/hour. The sign of the drift measured by the beat note depends on the detuning of the closest comb tooth and does not necessarily correspond to the real sign of the drift. **b)** A frequency drift was measured spectroscopically on the Ca^+ $S_{1/2}(m_J = -1/2) \rightarrow D_{5/2}(m_J = -5/2)$ transition over the course of several days. Assuming the experimental conditions were stable this reflects a drift in the cavity. A linear fit (red line) shows a drift of 42 mHz/s.

clock-referenced counter. The measured cavity drift can be compensated, e.g., on the AOM leading to the cavity and any laser that is subsequently referenced to the comb will therefore inherit the narrow linewidth of the PDH-lock and the long-term stability of the atomic clock. Figure 3.14 shows a proposed setup for transferring the short-term stability of a high-finesse cavity and the long-term frequency stability of an atomic clock to a probe laser at $4.6 \mu\text{m}$ using a frequency comb.

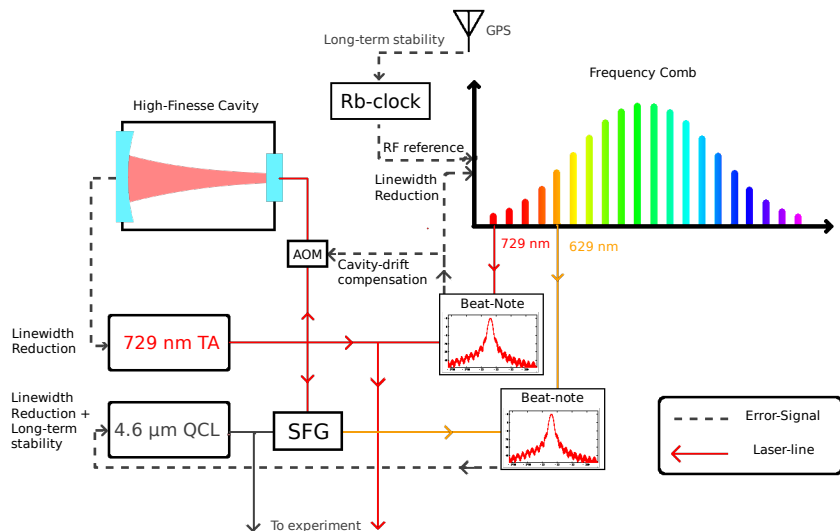


Fig. 3.14. A simplified schematic diagram of a proposed setup for transferring the short-term frequency stability of a high-finesse cavity and long-term stability of an atomic clock to the molecular probe laser at $4.6 \mu\text{m}$. The cavity narrows the linewidth of the 729 nm laser that is used for state manipulation in Ca^+ which in turn narrows the linewidth of the comb by locking the comb to an optical beat-note frequency. The comb derives its long-term stability from the optical clock and the slow drift of the cavity will be measured by the counter and compensated on the AOM leading to the cavity. Any laser that is subsequently locked to the comb, e.g. by sum-frequency generation (SFG), will inherit the narrow linewidth and long-term stability of the comb.

3.3.4 Locking and characterising a QCL using a gas cell

Just like the atomic clock, the molecular probe laser can also be referenced directly to a spectral line that serves as a stable frequency reference. The slope of an absorption feature may serve as an error signal to achieve linewidth reduction as well as long term stability. A suitable medium can be found for many optical and mid-IR wavelengths. Figure 3.15a shows a test setup that was used for narrowing and stabilizing a $7.9 \mu\text{m}$ QCL²⁵ to a gas cell of N_2O .

The rovibrational lines in N_2O , specifically the rotational components fundamental branch of the symmetric stretch mode $v = 0 \rightarrow v' = 1$, provide absorption features with a linewidth of ~ 11 MHz at a pressure of 2 mBar [121]. The FWHM point of maximum slope of a line shows a nearly linear transfer function of 3.9×10^{-9} V/Hz for locking, as shown in Figure 3.15b. At the slope of a spectral feature, intensity fluctuations in the laser are indistinguishable from frequency fluctuations and the laser will be locked to both of these sources of noise.

The intensity fluctuations can be measured on a flat region of the spectrum, away from the spectral feature, where frequency fluctuations do not cause voltage fluctuations on the photodiode. In order to compare the measured intensity fluctuations with the frequency fluctuations, the laser power should be adjusted to a similar voltage level on the photodiode in both measurements. If the PSD of the intensity noise is low compared to the frequency noise, the linewidth can once again be estimated using the method in Ref. [118].

In the test setup presented schematically in Figure 3.15a, two photodiodes²⁶ were used in a differential measurement between two beam paths in order to cancel the influence of intensity fluctuations on the error signal. One beam passes through the gas cell and another is measured directly from the source. The intensity noise therefore does not contribute to the quality of the lock and we achieve an in-loop NSD lower than the intensity

²⁵Alpes Lasers $7.9 \mu\text{m}$ DFB QCL

²⁶Vigo PVI-4TE-08

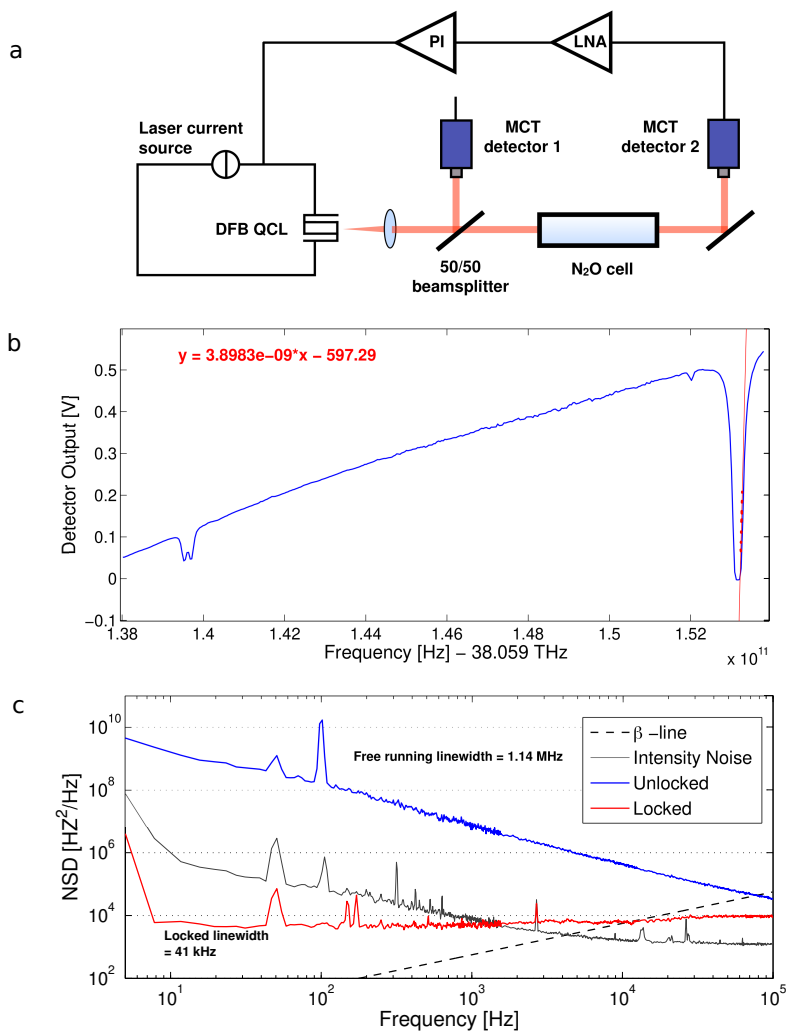


Fig. 3.15. **a)** The test setup for stabilizing of a quantum cascade laser to a gas cell. Two photodiodes were used in a differential measurement in order to cancel the influence from intensity fluctuations of the laser. The gas cell of length 100 mm contains N₂O with a pressure of 2 mBar. **b)** The measured absorption features in a gas cell of N₂O as a function of the QCL frequency. The strongest line has a nearly linear frequency dependence close to 0.1 V. This was used for locking the QCL and estimating the linewidth. **c)** The noise spectral density (NSD) of the locked and unlocked QCL. The power spectral density was measured by a spectrum analyzer and converted to NSD using the transfer function obtained in (b). A locked linewidth of 40 kHz was inferred.

noise. The side-of-fringe error signal was sent to a PI servo and fed back to the current controller²⁷ of the laser.

The linewidth was again estimated by using the measured transfer function from Figure 3.15b to relate the PSD measured by spectrum analyzer²⁸ to the Noise Spectral Density (NSD) of the in-loop error signal. Integrating from 4 Hz to the β -crossing at 10 kHz, we obtain a (250 ms integration time) linewidth of 40 kHz. For a narrower linewidth, a better transfer function can be obtained through Doppler-free spectroscopy e.g. using a saturated-absorption-spectroscopy technique [123].

3.3.5 Single-laser Raman transitions

Near-resonant Raman transitions use the proximity of an auxiliary state to drive transitions at the difference frequency of two laser beams [124]. For driving sub-THz transitions, such as the Zeeman, hyperfine or rotational transitions presented in Chapter 2, these two beams can be derived from the same source. A difference frequency is then obtained by modulating one or both beams in an AOM or EOM as shown in Figure 3.16a. If the laser lines are shorter than the coherence length of the laser source, the two beams maintain phase coherence. This resembles a homodyne interference, where common-mode frequency and phase noise cancels and a high spectroscopic resolution can be obtained without active linewidth stabilization. This technique has been used for sideband cooling in Ref. [125].

Figure 3.16b shows the Zeeman transition $D_{5/2}(m_J = -3/2) \rightarrow D_{5/2}(m_J = -5/2)$ in Ca^+ at ~ 7.7 MHz driven by two Raman beams derived from our optical lattice beams at 789 nm and shifted by 8 MHz from one another by AOMs²⁹. The ECDL has an intrinsic linewidth of ~ 1 MHz (1s integration time) yet the obtained spectroscopic linewidth is 12 kHz. Rabi flopping between the two states was preformed with a coherence time of 250 μs (see inset). The coherence length of a laser with a linewidth of 1 MHz and a Lorentzian line profile is $L = c/(\pi\Delta f)$ or close to 100 m. The limit to the measured coherence time is then most likely

²⁷The current controller and the QCL are described in detail in Ref. [122]

²⁸Stanford Research System SR770

²⁹This optical setup was designed and built by *G. Hegi and Z. Meir*

power fluctuations which were not stabilized in this setup. This method therefore allows coherent state manipulations and a narrow linewidth to be achieved without a narrow frequency reference such as a high-finesse cavity or frequency comb.

Vibrational or electronic transitions are difficult to drive with a single laser source as the frequency difference is typically too large for EOMs and AOMs. A frequency comb could instead be used, as it has a wide spectrum of different frequencies that maintain some level of phase coherence [82].

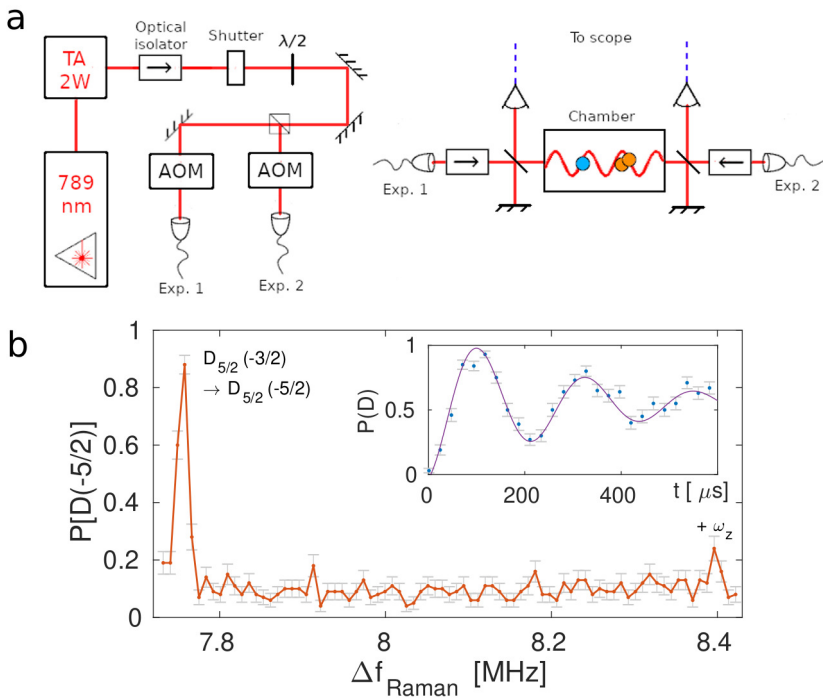


Fig. 3.16. **a)** A simplified schematic overview of the optical lattice setup for our 789 nm state-readout laser. Two beam paths derived from the same laser source are shifted in frequency from one another by acousto-optic modulators (AOMs). The two beams are overlapped with the ions in the trap center, with matching polarizations, where they interfere to form an optical lattice. The two beam paths maintain phase coherence and can therefore also be used to measure narrow spectral features via Raman transitions without the need for a narrow laser linewidth. **b)** The measured Raman spectrum of Ca^+ in the Zeeman transition $D_{5/2}(m_J = -3/2) \rightarrow D_{5/2}(m_J = -5/2)$ driven by two Raman beams derived from our optical lattice laser at 789 nm and shifted by 8 MHz from one another by AOM's. The obtained spectroscopic linewidth is 12 kHz. The inset shows Rabi oscillations on the Raman transition with a coherence time of 250 μs .

3.4 Experiment peripherals

3.4.1 Control electronics

The experiment requires fast and reproducible $\sim \mu\text{s}$ pulses of several lasers in order to perform robust, coherent manipulations on both Ca^+ and N_2^+ . The 729 nm, 397 nm, 789 nm and the molecular-probe lasers all require fast frequency switching between the pulses with precise $\sim\text{Hz}$ frequency control. Figure 3.17 shows a schematic overview of the pulse electronics that is used to run a spectroscopy experiment on Ca^+ with a repetition rate of up to 1 kHz, limited by the state detection time for a single Ca^+ ion of ~ 1 ms.

A Pulseblaster³⁰ serves as the main pulse sequencer. It also drives two acousto-optic modulators (AOMs), the 729 nm and 397 nm laser controls, which have the highest requirements for fast frequency switching. An FPGA board from National Instruments³¹ is used to switch the AOMs that drive the 854 nm re-pump laser and the 789 nm lattice laser on and off based on a real-time 4-bit TTL instruction from the Pulseblaster. The 789 nm laser is driven by a home made DDS driver³² with built in amplitude and frequency registers. A mechanical shutter is used for extra protection against stray light leaking through the AOM of the 789 nm laser. The 866 nm laser remains on for most applications.

The FPGA board also acts as a counter for the short (~ 4 ns) photon signals from the PMT. The state detection on the $S_{1/2}$ and $D_{5/2}$ levels in Ca^+ takes ~ 1 ms to discriminate between the states with a low error rate. The power of the 729 nm laser is actively stabilized by measuring its power during the Doppler-cooling pulse (~ 1 ms) on a photodiode. The photodiode signal is averaged by the FPGA which adjusts the RF power of the 729 nm control AOM in a feed-forward servo loop.

An auxiliary pulse sequencer³³ handles pulse timings for the molecular beam and ionization lasers for N_2^+ ionization. The Ca^+ ionization lasers

³⁰PulseBlaster DDS-II-300-AWG, 50 MHz sub-ppm temperature stabilized oscillator. Minimum pulse duration: 67 ns. Pulse resolution: 13 ns. Frequency resolution: 0.3 Hz

³¹National Instruments, PXI Multifunction I/O module, PXI-7846R

³²Based on Analog Devices AD9959 chip. Built by G. Hegi.

³³Quantum Composers Pulse Generator 9520

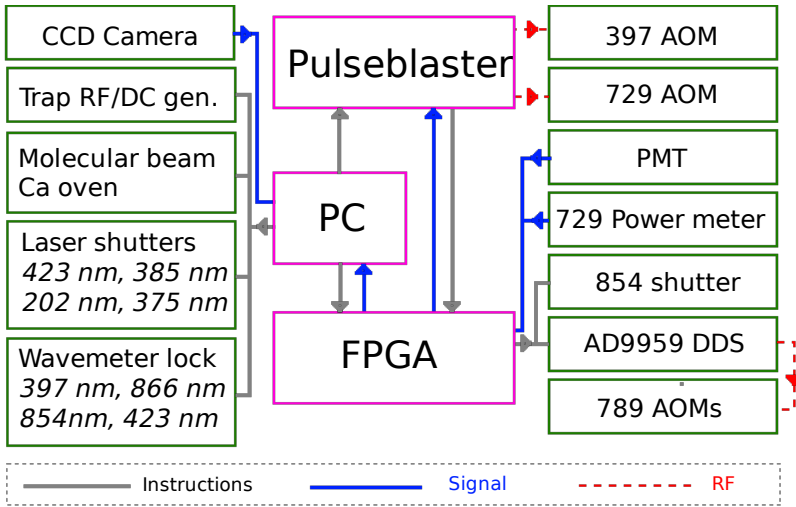


Fig. 3.17. A block diagram over the control electronics that is used to produce short pulses of the lasers, to drive the trap electronics and to capture the ion signals. The blue lines refer to signals that are continually sent during an experiment whereas the grey lines are instructions that are typically sent once in the beginning of an experiment.

have lower timing requirements and are controlled directly from the PC by Arduino-driven, mechanical shutters. The PC also monitors the wavemeters³⁴ and records the camera image from the CCD³⁵. All the instructions for an experiment are sent using GUI programs written in LABVIEW³⁶.

3.4.2 Chamber layout

Figure 3.18 shows the layout of the trap chamber and the direction of the lasers that pass through the trap center. All lasers are operated with linear polarizations. The lasers are overlapped using dichroic mirrors. The 729 nm laser is introduced along several axes for measuring the micromotion in the radial directions.

³⁴HighFinesse WS6-200

³⁵Andor Luca R EMCCD

³⁶LABVIEW National Instruments

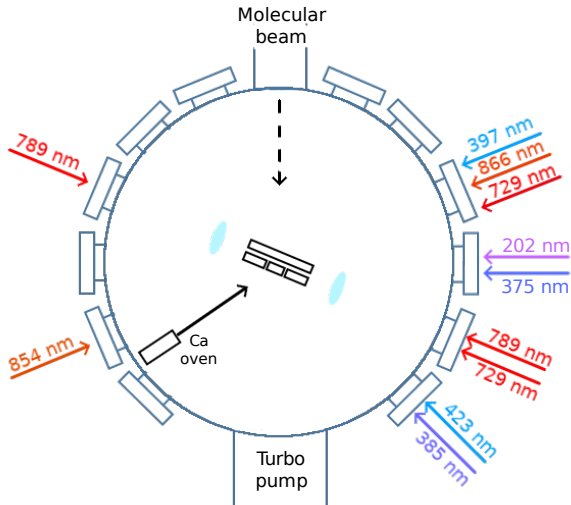


Fig. 3.18. A schematic layout of the vacuum chamber and the directions of the lasers that are used in the experiment.

3.4.3 Magnetic field coils

An applied magnetic field is required in order to achieve a closed cycle in the transitions used for sideband cooling. Two Helmholtz coils were made with 50-pin ribbon cables with the connectors shifted by 1 pin to form a coil. A laboratory power supply with a specified root-mean-square jitter of < 1 mV drives the two coils³⁷. The resistance of each coil is 25Ω and the current jitter is thus expected to be below $< 40 \mu\text{A}$. A current of 0.8 A runs through each coil to produce a field of 4.6 G at the position of the ions. The transfer function is therefore ~ 2.9 mG/ μA .

Figure 3.19 shows the frequency jitter of two transitions in Ca^+ with equal magnitude but opposite signs of magnetic susceptibility, ± 2.8 kHz/mG, measured as a function of time. Each data point takes several seconds to obtain and higher frequency noise will therefore not contribute to the measured fluctuations. The observed frequency fluctuations are anti-correlated which suggests that the jitter is caused by fluctuations in the magnetic field. The standard deviation of ~ 2 kHz corresponds to

³⁷Aim-TTi EL302RT

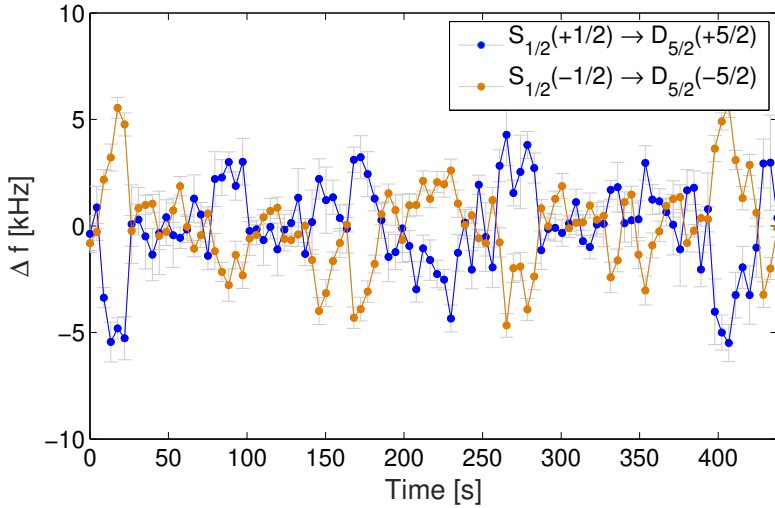


Fig. 3.19. Frequency fluctuations of two $S_{1/2}(m_J = \pm 1/2) \rightarrow D_{5/2}(m_J = \pm 5/2)$ transitions in Ca^+ with opposite susceptibility to magnetic field ± 2.8 kHz/mG. The anti-correlated fluctuations with a standard deviation of 2 kHz suggest magnetic field fluctuations on the ~ 1 mG level.

magnetic-field fluctuations of ~ 1 mG. To produce the observed magnetic field noise, the equivalent current noise is ~ 0.3 mA and therefore significantly above the specifications of the power supply. The measured magnetic field noise may therefore be caused by stray fields in the trap chamber rather than by the output of the power supply. As we have seen in Chapter 2, this noise level of ~ 1 mG will not limit the spectroscopic resolution of clock transitions in N_2^+ .

3.5 Summary

In this chapter we have presented an experimental apparatus for the implementation of a molecular clock experiment for a single homonuclear diatomic molecule. This implementation results in a significant experimental overhead in terms of stable laser sources, i.e., many lasers are

required as the molecule can not be cooled directly and the molecular state can not be read out by fluorescence methods. On the other hand, due to the beneficial field-insensitive properties of the rovibrational molecular levels, the requirements for a suitable ion trap and accompanying electronic circuits are significantly reduced as we do not require cryogenic cooling or compensation of stray fields in the chamber. The experimental procedure and a characterization of the new ion trap is presented in the next chapter.

Motional State Dynamics of N_2^+ in an Ion Trap

” *The nitrogen in our DNA, the calcium in our teeth, the iron in our blood, the carbon in our apple pies were made in the interiors of collapsing stars. We are made of starstuff.*

— Carl Sagan

In this chapter, we describe the techniques that are used for cooling the translational motion of N_2^+ from temperatures of ~ 1000 K to the motional ground state of the trap with a temperature of ~ 10 μ K, a temperature reduction spanning 8 orders of magnitude. The N_2^+ ion cannot be laser cooled without a great effort as it lacks anything resembling a closed cycling transition [22]. We must instead use an auxiliary ion, such as Ca^+ , as a coolant ion which interacts with N_2^+ in the trap through the Coulomb interaction.

The initial cooling from the temperature at ionization to the Doppler-cooling limit of ~ 0.5 mK using a crystal of Ca^+ ions is described in Section 4.1. A technique was developed to subsequently reduce the number of Ca^+ ions in the trap to a single ion and is described in Section 4.2. The sympathetic sideband cooling of the two ion $Ca^+ - N_2^+$ string to the motional ground state of the trap is described in Section 4.3. In this section, we shall also present the heating rates of the ground-state-cooled modes (Section 4.3.3) and the limits to the coherence time for state manipulation (in Section 4.3.4).

4.1 From ionization to the Doppler limit

The N_2^+ ions are produced from a molecular beam of neutral N_2 by a $[2 + 1']$, three photon, resonantly enhanced multi-photon ionization scheme (REMPI) as described in Ref. [86]. The molecular beam produces a packet of internally cold neutral N_2 , with rotational temperature $T_{\text{rot}} \sim 10$ K, through a supersonic expansion into vacuum from a pulsed valve with a backing pressure of 2 bar. After expansion into vacuum, the molecules reach a final velocity of ~ 780 m/s [99] corresponding to a kinetic energy of 1300 K. This kinetic energy must be removed within minutes of ionization for experiments to be feasible as the lifetime of N_2^+ is on the order of 5 minutes in a vacuum of 10^{-11} mbar. This initial cooling step can be avoided in experiments where the molecule is produced in the trap [22]. If the N_2 is not ionized in the trap center it also acquires an additional kinetic energy from the trap potential.

The ionization lasers and the molecular beam both overlap in the trap center. The lasers, at 202 nm and 375 nm, are co-propagating and focused to a diameter of ~ 100 μm from the outside of the trap chamber. The Rayleigh length, $l = \pi r_b^2 / \lambda$ [77], therefore spans tens of millimeters and ionization can occur with a high probability at any position in the trap within the molecular beam. The diameter of the molecular beam at the center of the trap is measured to be ~ 0.6 mm, as expected by the aperture of the last skimmer, of 0.5 mm. Therefore, there is an uncertainty in the ionization position of up to 0.3 mm. The N_2^+ loading is preformed at the lowest possible trap frequencies, where the Ca^+ ions are stable, in order to reduce the energy that N_2^+ acquires from ionizing off-axis. With a radial frequency of $\omega_r = 2\pi \cdot 100$ kHz, using Eq. 3.8, we find that loading off-center by 300 μm radially imparts the N_2^+ ion with an additional 100 K of kinetic energy. This is small compared to the initial kinetic energy of the molecular beam.

In order to reach the Lamb-Dicke regime, we use a string consisting of a single Ca^+ and a single N_2^+ along the trap axis and cool their motional modes to the ground state of the trap, as described in Section 4.3. Cooling an N_2^+ ion from a temperature of over 1000 K to the mK-range, where the ion crystallizes [126], using a single Ca^+ ion takes an exceedingly long time. The trajectory of a translationally hot N_2^+ ion does not necessarily

cross the trap center to interact with the Ca^+ ion and sympathetic cooling times of up to 1 hour were observed in our setup, longer than the lifetime of N_2^+ .

In order to overcome this limitation, we start the initial cooling of N_2^+ with a crystal of 10-30 Ca^+ ions in a string or a 3D Coulomb crystal. This reduces the initial cooling time down to, typically, between 10 s and 2 minutes before the N_2^+ appears in the crystal as a dark ion as seen by the microscope image. An example is shown in Figure 4.1b. The time constant for this initial cooling step decreases linearly with the number of Ca^+ ions in the crystal [127], at the cost of an increased uncertainty in the number of ionized N_2^+ ions. In a string of Ca^+ , the dark ion appears as a hole in the string and can be detected with negligible uncertainty. In a 3D crystal, however, the dark ion may be outside the camera plane and is therefore hard to discern and an uncertainty is associated with the number of ionized N_2^+ ions. Once the N_2^+ appears in the crystal we successively reduce the number of Ca^+ ions in the trap, until only a single Ca^+ ion remains. The technique that was developed for reduction of Ca^+ ions in the trap is described in the following section.

4.2 Reduction of Ca^+ from the trap

Figure 4.1a shows the stability diagram for N_2^+ and Ca^+ in terms of their a and q parameters, calculated according to Eq. 3.2. $^{14}\text{N}_2^+$ has a lighter mass than $^{40}\text{Ca}^+$ and, therefore, experiences a deeper potential from the ion trap. We may therefore reduce the trap depth to the edge of the stability region for Ca^+ with no risk of losing the N_2^+ ion. At the edge of stability, the ion trajectories are semi-stable such that loss of Ca^+ from the trap proceeds slowly and reproducibly with the time constant for the rate of loss, Γ , within experimentally accessible values, of ~ 1 Hz. To reach the edge of stability, we may either lower the RF potentials to decrease q or increase the DC potentials to increase a . All the experimental data shown in this section was obtained using the latter method. We utilize this effect to reduce the number of Ca^+ from 10 – 30 ions to a single Ca^+ , as shown in Figure 4.1b.

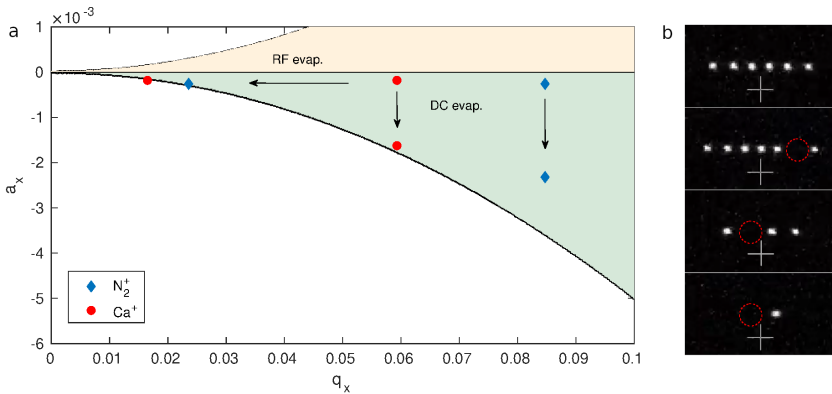


Fig. 4.1. **a)** Single-ion stability diagram. Red dots and blue diamonds represent Ca^+ and $^{14}\text{N}_2^+$ respectively. The starting position corresponds to the a and q parameters that are used for loading of Ca^+ and N_2^+ into the trap. By lowering the RF amplitude or increasing the endcap voltages the Ca^+ can be shifted to the edge of the stability region (blue shaded area) while the N_2^+ is well confined. **b)** Fluorescence images obtained from the CCD camera showing (from top to bottom) the initial loading of six Ca^+ -ions cooled to the Doppler-cooling limit, the loading and initial cooling of a single N_2^+ as apparent by the appearance of a dark ion in the string (red circle), the reduction of the number of Ca^+ achieved by increasing the endcap voltage in two steps until a single Ca^+ and a single N_2^+ ion remains.

The Ca^+ ions are lost from the trap while formally inside the single-ion stability region, i.e. the radial trap frequencies are positive and the trap depth is larger than the initial kinetic energy of the ions. The trap depth for $^{40}\text{Ca}^+$ at a radial frequency of $\omega_r = 2\pi \cdot 100$ kHz at the edge of stability, where ion loss is observed, is > 2000 K. The physical mechanism for ion loss is then either nonlinear resonances for Ca^+ that are not adequately described by the first-order pseudo-potential approximation [94] or through RF heating of the ion motion to kinetic energies above the trap depth in an evaporation process [128]. We shall characterize the loss of ions in order to determine the loss mechanism.

4.2.1 Characterizing ion decay

The ions are moved to the edge of stability for a short time $t = t_{\text{red}} + t_0$, where t_0 is the time it takes to change the trap potentials and t_{red} is the effective time spent at the edge of stability. The potentials are then returned to a stable region of a and q and the number of ions lost in the reduction step is recorded by the microscope image. The ion loss is well described by an exponential decay $P_N = P_0 e^{-\Gamma \cdot t}$ where Γ is the decay constant. Figure 4.2a shows the measured ion decay as a function of reduction time, t , in terms of the quantity $\Gamma \cdot t = \log(N_f/N_i)$ where N_i and N_f are the number of ions before and after the reduction pulse. $\Gamma \cdot t$ is linear in time and the ion number therefore closely resembles an exponential decay for any duration t . In this experiment, the edge of stability was reached by increasing the axial potentials and the large $t_0 \approx 7$ s comes from the low-pass filtering properties of the DC circuit as described in Chapter 3.

We now measure the width of this semi-stability region. Figure 4.2b shows the measured decay rate constant, Γ , as a function of the radial trap frequency, and thus the proximity to the edge of stability, for a fixed reduction time constant, t . As the axial potential is increased, the radial trap depth decreases and the decay rate, Γ , increases smoothly. This suggests that the mechanism for loss is not nonlinear resonances which occur for specific values of a and q with widths of $\Delta a/a, \Delta q/q \approx 10^{-3}$ [94]. For careful Ca^+ reduction we adjust the radial confinement to keep

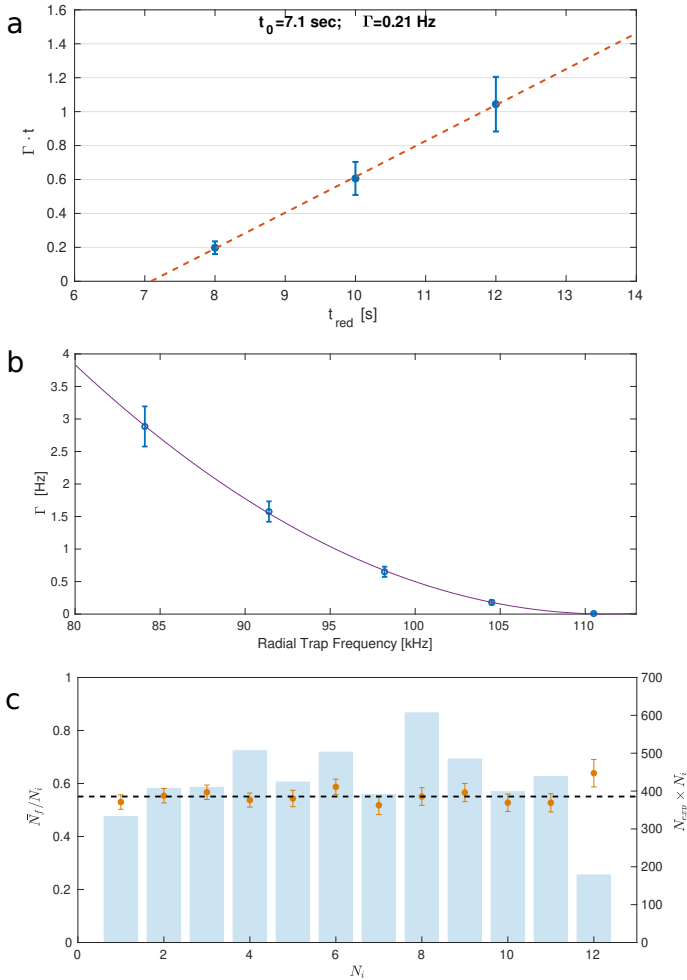


Fig. 4.2. **a**) The measured decay ratio $\Gamma \cdot t$ (unitless) of Ca^+ ions from the trap as a function of time. t_0 is the time it takes to reach the final DC potentials due to the low pass filters. The dashed line shows the linear behaviour of the ratio with time as expected by an exponential decay, with a decay constant of $\Gamma = 0.21 \text{ Hz}$. **b**) The decay constant, Γ , measured as a function of the radial confinement which is lowered by increasing the endcap voltages. The endcap voltages that were used for the radial deconfinement were (from left to right) $V_{DC} = 92, 91, 90, 89, 88 \text{ V}$. The purple line shows a quadratic fit to the data. **c**) The loss ratio N_f/N_i as a function of the number of Ca^+ in the trap (orange points). The variance is proportional to the number of probed ions N_i and the number of averaged experiments N_{exp} and thus the product $N_i \times N_{exp}$ represents the statistical power of each measurement (blue bars). All error bars represent the 1σ binomial uncertainties.

the probability of loss below 0.5 in each reduction step in order to reduce the risk of losing all the Ca^+ in the reduction step.

Instabilities or heating of the ion trajectories may be dependent on the number of ions in the trap as the Coulomb potential between ions modify the effective potentials and hence the trajectories of the ions. We therefore measure the decay rate, Γ , as a function of the number of ions, N_i , in the trap. The results are presented in Figure 4.2c. The decay is independent of the number of ions up to $N = 12$ and ion-ion interactions are therefore not significantly contributing to the decay mechanism.

4.2.2 Heating mechanism

We now consider different mechanisms that can lead to motional heating and evaporation from the trap. The observed exponential decay and high decay rate, ~ 1 Hz, suggests that ion loss is not due to collisions with background gas. With a trap depth of ~ 2000 K, collisions with a background gas of 300 K are unlikely to cause the observed evaporation as the tail of the Boltzmann distribution is small at the trap-depth temperature. The time between Langevin collisions in a vacuum pressure of 10^{-11} mBar is expected to be ~ 1 minute [129] and the observed time constants for ion decay are too high to be caused by collisions. The purely exponential decay also rules out several subsequent collisions as the source of heating as, in this case, the temperature is expected to increase linearly with the number of collisions and thus with time. Figure 4.3(a-d) shows the result of four experiments performed to test the decay rate as a function of collisions and initial ion temperature.

Figure 4.3a shows the decay rate with the Doppler-cooling lasers, at 397 nm and 866 nm, turned on or off during the reduction step. The decay rate is significantly slower when the cooling lasers remain on during the reduction step. In Figure 4.3b we displace the ions from the trap center to impart them with an initial kinetic energy between 10 – 1000 K due to micromotion. The decay rate Γ increases with the initial ion temperature. These results suggest that the decay mechanism is indeed evaporation from the trap due to heating.

We test the influence of collisions on the evaporation by measuring the decay rate with the Ca oven and molecular beam passing through the trap center. The results are presented in Figures 4.3(c-d). The influence of collisions with the molecular beam of ~ 1300 K or the neutral Ca from the oven with ~ 600 K is not significant on the measured decay rate. This could be either due to the low densities from both of these sources or that the collisional heating is insignificant compared to another source of heating.

We therefore conclude that the most likely decay mechanism at the edge of stability is evaporation from the trap due to heating of the ions. The most likely heating mechanism is then RF heating through the micromotion. In order to test this hypothesis an experiment can be preformed to compare the decay rate using different values of the RF potentials but with the same trap depth. The radial frequencies, ω_r , and thus the trap depth depend on both the RF voltage and DC voltage and can be kept constant by increasing both the RF potential and DC potentials to achieve a similar trap depth but with a higher RF drive. The micromotion heating is thus separated from other heating mechanisms and the decay rate measurement, as shown in Figure 4.2b, will thus prove or exclude micromotion as the dominant source of heating.

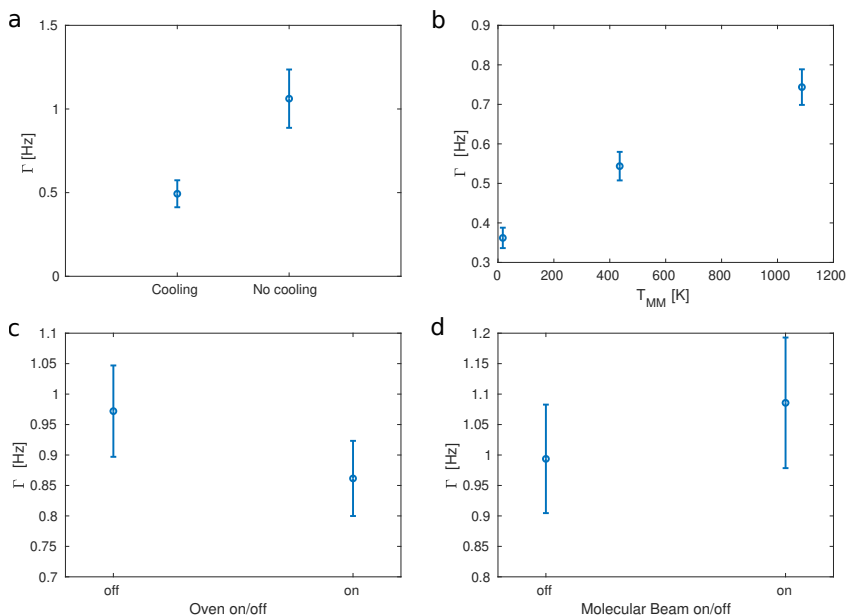


Fig. 4.3. Four evaporation experiments performed to test the influence of ion temperature and collisions on the measured decay rate. **a)** The decay rate constant measured with and without the Doppler-cooling lasers active during Ca^+ reduction. **b)** The decay rate constant measured as a function of the initial ion energy. The energy was adjusted by shifting the ion away from the trap axis radially into a region of high micromotion. **c)** The measured decay rate constant with and without the Ca-oven (~ 600 K) passing through the trap center during the reduction. **d)** The decay rate constant with and without the molecular beam (10 Hz repetition rate) passing through the trap center during Ca^+ reduction. All error bars represent 1σ binomial uncertainties.

4.3 Sympathetic sideband cooling

For efficient sympathetic cooling, the molecule and the coolant ion should be of similar masses [100]. The $^{40}\text{Ca}^+$ ion serves as a suitable coolant for $^{14}\text{N}_2^+$. Here we describe the experimental implementation of sympathetic sideband cooling from Doppler-cooling temperatures of ~ 0.5 mK to the ground state of the trap.

4.3.1 The N_2^+ motional modes

The motional modes along the axis of a two-ion string were presented in Section 3.1.1. Two motional modes appear along the trap axis which are denoted the center-of-mass mode (COM) and the stretch mode (STR). The sideband spectrum of the axial motional modes after Doppler cooling of a two-ion $\text{Ca}^+ - \text{N}_2^+$ string is presented in Figure 4.4.

The obtained frequencies are $\omega_{COM} = 725$ kHz and $\omega_{STR} = 1215$ kHz for the COM and STR modes using $V_{RF} = 1000$ V and $V_{DC} = 190$ V in the trap described in the previous chapter. The motional Lamb-Dicke parameter for these modes are 0.113 and 0.088 respectively. The mean motional occupation for the two modes are therefore $\bar{n} = 16$ and $\bar{n} = 10$ after Doppler cooling, assuming a thermal distribution.

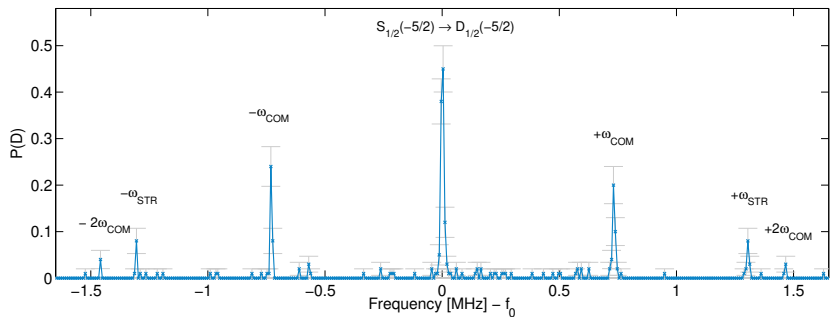


Fig. 4.4. A sideband spectrum measured by electron-shelving spectroscopy on the $S_{1/2}(m_J = -1/2) \rightarrow D_{5/2}(m_J = -5/2)$ transition in Ca^+ , along the trap axis of a two-ion $\text{Ca}^+ - \text{N}_2^+$ string. The spectrum is taken immediately after Doppler cooling with a temperature of ~ 0.5 mK. The axial frequencies are $\omega_{COM} = 725$ kHz and $\omega_{STR} = 1215$ kHz for the COM and STR modes respectively. Error bars represent 1σ statistical uncertainties. The frequency axis is offset from the carrier frequency by $f_0 \approx 411.042$ THz.

4.3.2 Sideband-cooling sequence

Sideband cooling can be performed in a continuous or a pulsed mode, i.e., either with alternating red sideband and repump pulses (pulsed mode) or with both lasers on at the same time (continuous mode). A combination of both methods are typically used as the continuous cooling is faster and avoids population trapping whereas the pulsed method can be fine-tuned in the last stages of cooling to reduce off-resonant scattering and thus reach a higher ground state occupation probability [130, 110]. As we lack full control over the frequency and power of the 854 nm laser, the pulsed method was employed. Several sideband-cooling sequences were simulated in order to avoid population trapping, as described in Appendix D.

A typical pulse sequence after Doppler cooling is presented in Table 4.1. Each pulse consist of a 729 nm pulse on a red sideband followed by a short re-pump pulse of the 854 nm laser of $5 \mu\text{s}$. By incrementally changing the pulse length in several steps, we avoid population trapping, as discussed in Appendix D. The laser power is lowered in the last stages of cooling to reduce off-resonant scattering on the carrier transition and blue sidebands.

Step No.	Transition type	Amplitude [Arb. units]	Pulse length [μs]	Repetitions
1	OP	0.7	16	11
2	$-2\omega_z$	0.7	20	30
3	OP	0.7	15	5
4	$-2\omega_z$	0.7	30	30
5	OP	0.7	15	5
6	$-2\omega_z$	0.7	45	30
7	OP	0.7	15	5
8	$-\omega_z$	0.7	20	30
9	OP	0.5	22	5
10	$-\omega_z$	0.5	45	30
11	OP	0.5	22	5
12	$-\omega_z$	0.5	70	30
13	OP	0.5	22	5

Tab. 4.1. A typical sequence for sideband cooling of a single axial mode of a Ca^+ or a two-ion $\text{Ca}^+ - \text{N}_2^+$ string. The pulse length and amplitude are controlled by the 729 nm control-AOM with a maximum amplitude of 1.0 corresponding to 2W of RF power. Each pulse is followed by pulse of the 854 nm laser of $5 \mu\text{s}$ to pump the population back to the $S_{1/2}$ state via the $P_{3/2}$ -state. OP refers to the optical pumping transition $S_{1/2}(m_J = +1/2) \rightarrow D_{5/2}(m_J = -3/2)$ which is used to collect the population in the $S_{1/2}(m_J = -1/2)$ state and $-\omega_z$ and $-2\omega_z$ refer to the first and second red sideband of the $S_{1/2}(m_J = -1/2) \rightarrow D_{5/2}(m_J = -5/2)$ transition, respectively.

The complete sequence takes ~ 9 ms. Shorter pulse sequences of ~ 5 ms have also been employed with an equally good ground-state occupation probability but were found to be more susceptible to imperfections in the Doppler cooling due to drifts in the frequency and power of the Doppler-cooling lasers over the course of a day.

In the lowest motional states, the average motional occupation, \bar{n} , can be estimated by [91],

$$\bar{n} = \frac{p_{RSB}}{p_{BSB} - p_{RSB}}, \quad (4.1)$$

where p_{RSB} and p_{BSB} are the measured intensities on the first red and blue sidebands, respectively. This method of establishing the temperature

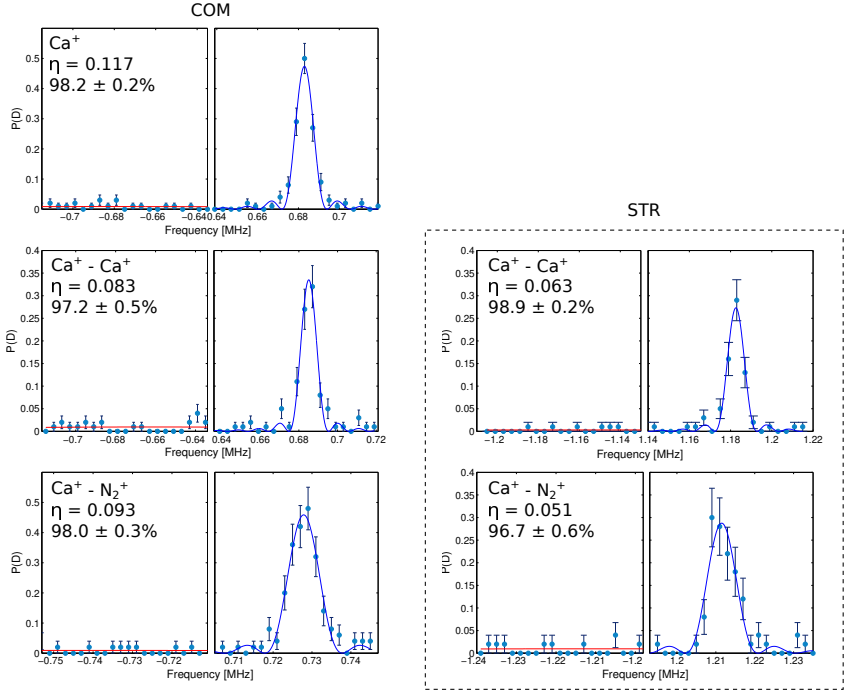


Fig. 4.5. The first blue and red sidebands measured directly after sideband cooling of (top to bottom) a single Ca^+ ion, a two-ion $\text{Ca}^+ - \text{Ca}^+$ string and a $\text{Ca}^+ - \text{N}_2^+$ string. The error bars represent 1σ statistical uncertainties. The blue and red lines are fits to the experimental data fitted with Rabi *sinc*-functions [131]. Inset numbers are the Lamb-Dicke parameter, η , and the ground-state occupation probability according to the estimate in Eq. (4.1). The equivalent temperatures of the residual kinetic energies range from 8 – 15 μK .

is denoted 'sideband thermometry' in the following¹. Figure 4.5 shows the measured intensity on the red and blue sidebands after sideband cooling of a single Ca^+ -ion, a two-ion $\text{Ca}^+ - \text{Ca}^+$ string and a $\text{Ca}^+ - \text{N}_2^+$ string.

The sympathetic sideband cooling of N_2^+ proceeds with the same sequence as the single- Ca^+ -ion cooling sequence, as shown in Table 4.1. The difference in the frequencies, ω_{COM} and ω_{STR} , means that the frequencies have to be adjusted. We typically reach a ground-state occupation probability of $97 \pm 2\%$ in a mode using the sequence described above. The

¹Not to be confused with Rabi sideband thermometry which uses measured Rabi oscillations on a sideband to obtain the motional state distributions.

kinetic energy of the ions immediately after sideband cooling is then, $E_k \approx 1/2k_B T$ or $\sim 10 \mu\text{K}$. Cooling of both the COM and STR modes takes twice as long as cooling of a single mode. However, as we shall see in the next section, for many applications the cooling of a single axial mode is sufficient.

4.3.3 Heating rates

The heating rate of the motional modes after sideband cooling may limit the achievable contrast in a state detection scheme which relies on motional excitation, such as quantum-logic readout [92, 132]. The increase in temperature may also cause thermal decoherence which limits the number of coherent operations that can be preformed on the molecule. Figure 4.6 shows the average motional occupation, \bar{n} , measured through sideband thermometry with a variable delay inserted between sideband cooling and the temperature determination.

On the COM mode of the $\text{Ca}^+ - \text{N}_2^+$ string, with an axial frequency of 725 kHz, a heating rate of 4 n/s is measured corresponding to an average increase of 1 phonon every 250 ms. The STR mode at 1215 kHz heats up more slowly, by 3 n/s , as expected from the approximate ω^{-1} scaling law for anomalous heating [133]. This heating rate is among the lowest absolute rates reported [134] and approximately conforms to the expected $(r_0)^4$ scaling when compared to two mm-scale traps from Refs. [135] and [136]. Thus, a single quantum of motional excitation may be detected with a good contrast in a quantum-logic detection using a probe time of 100 ms, corresponding to a Fourier-limited linewidth of 10 Hz.

4.3.4 Coherence times

The decoherence of the ground-state-cooled system can be measured by observing the population inversion or 'Rabi oscillations' between two states under the influence of a narrow laser source. Figure 4.7a shows the coherent population transfer as a function of pulse length on the $S_{1/2}(m_J = -1/2) \rightarrow D_{5/2}(m_J = -5/2)$ transition in Ca^+ . The measured coherence time in the single- Ca^+ experiment is 1.5 ms. This coherence

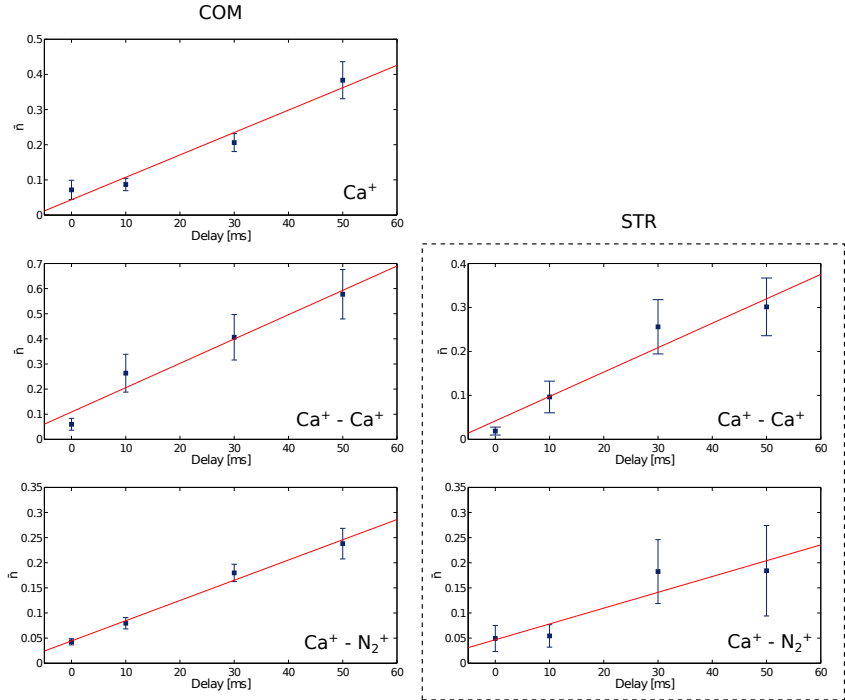


Fig. 4.6. The heating rate of the motional modes measured using sideband thermometry with a variable delay after sideband cooling on (top to bottom) a single Ca^+ -ion, a two-ion $\text{Ca}^+ - \text{Ca}^+$ string, a $\text{Ca}^+ - \text{N}_2^+$ string. The blue data points are measured using the ratio of the red and blue sidebands and the error bars represent the statistical 1σ uncertainties. The red line is a linear fit to the data and the heating rate in n/ms is obtained from the slope. The measured heating rates are (top to bottom) for a single Ca^+ -ion, COM: 6.4 n/s , for a two-ion $\text{Ca}^+ - \text{Ca}^+$ string, COM: 9.7 n/s STR: 5.6 n/s , for a $\text{Ca}^+ - \text{N}_2^+$ string, COM: 4.0 n/s STR: 3.1 n/s .

time is therefore not limited by the motional decoherence due to heating². The limit to the coherence is then either due to the magnetic-field fluctuations described in Section 3.4.3 or the coherence of the laser source as described in Section 3.3.2. Figure 4.7b shows the coherent population transfer on the $S_{1/2}(m_J = -1/2) \rightarrow D_{5/2}(m_J = -5/2)$ transition in Ca^+ , in a $\text{Ca}^+ - \text{N}_2^+$ string with only the COM-mode cooled to the ground state. The measured coherence time, of ~ 0.25 ms, is not limited by heating but due to the initial temperature of the STR-mode. By assuming a thermal distribution of motional states, each with a Rabi frequency given by Eq. (D.2) in Appendix D, we find an effective ion temperature of $\sim 90 \mu\text{K}$.

The measured coherence time is long compared to the Rabi frequencies of rovibrational qubits, estimated as > 1 kHz in Chapter 1. Therefore a sequence of coherent manipulations can be preformed with only the COM mode cooled to the ground state. For precision measurements, the observed decoherence limits the (coherent) probe time to < 0.1 ms corresponding to a Fourier-limited linewidth of 10 kHz. A longer coherence time, similar to the one shown above for a single Ca^+ , is obtained by cooling both axial modes to the ground state.

²Coupling between the axial and radial modes would also manifest as a heating of the axial modes and can therefore be ruled out as the observed source of decoherence.

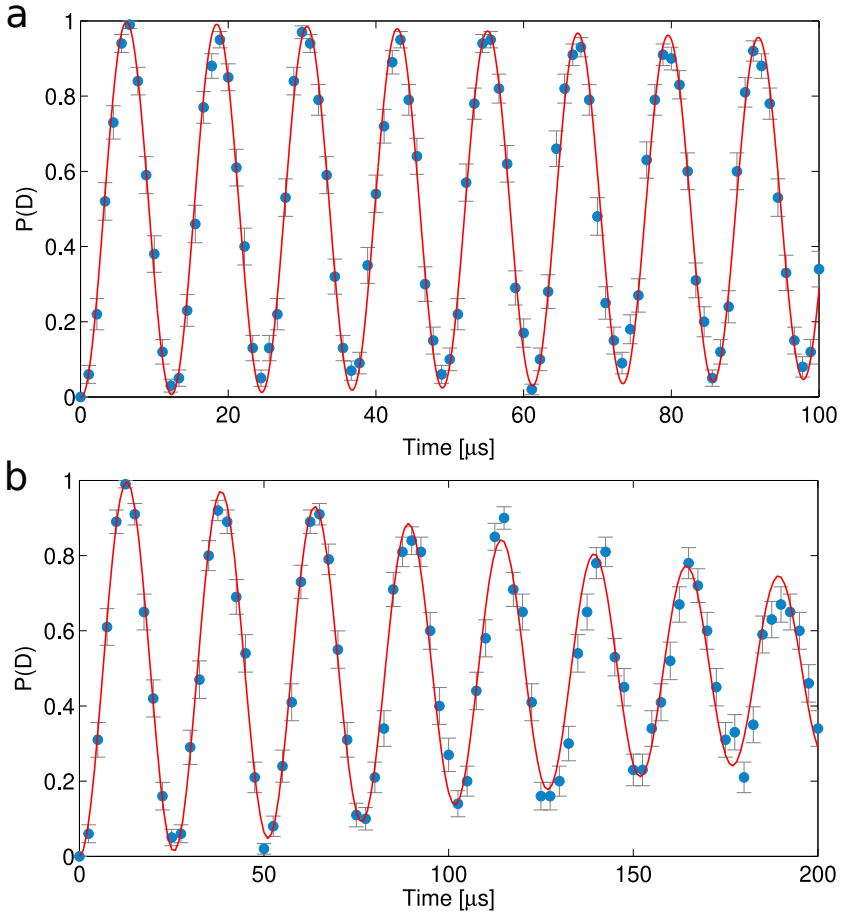


Fig. 4.7. Coherent population transfer on the $S_{1/2}(m_J = -1/2) \rightarrow D_{5/2}(m_J = -5/2)$ transition in Ca^+ as a function of the pulse length of the 729 nm laser. **a)** A single Ca^+ mode at $\omega = 680$ kHz, and $\eta = 0.117$, cooled to the motional ground state. Blue points are experimental data and the error bars are 1σ statistical uncertainties. The red line is a fitted sinusoid convoluted with an exponential decay with a time constant of 1.5 ms. **b)** The COM mode of a $\text{Ca}^+ - \text{N}_2^+$ string with frequency $\omega = 725$ kHz, and $\eta = 0.113$, cooled to the motional ground state. Blue dots are the measured data and the error bars are 1σ statistical uncertainties. The red line is fitted with a thermal distribution of convoluted Rabi frequencies for each motional state (Eq. (D.2)) with an effective temperature $89 \mu\text{K}$. The equivalent decay constant is 0.25 ms. Note that figures **a)** and **b)** were measured at different laser powers.

4.4 Summary

In this chapter we have described the trapping and sympathetic cooling of N_2^+ to the ground state of the trap. The initial cooling of the kinetic energy, acquired from supersonic expansion in the molecular beam machine, adds a significant amount of time to the experimental duty-cycle. To reduce the sympathetic cooling time it is reasonable to consider mixing the neutral N_2 with a heavier seed gas in the beam machine in order to reduce its initial kinetic energy. Alternatively, a suitable stopping field can be applied to the trap electrodes at the time of ionization in order to decelerate the kinetic energy of the ionized molecule using an electric field. These improvements may eliminate the need for multiple Ca^+ for sympathetic cooling and the subsequent Ca^+ -evaporation sequence.

The trap described in Chapter 3 and characterized in this chapter shows a low heating rate and a good coherence time. The sympathetic ground-state cooling of the N_2^+ is straightforward once the Doppler cooling and sideband cooling of a single Ca^+ is optimized. In the next chapter, Chapter 5, we will present a new method for the readout of the molecular state of N_2^+ .

Non-destructive Molecular State Detection

” *Stability can only be attained by inactive matter.*

— **Marie Curie**
nobel lecture

The methods for detecting the internal state of molecules have typically relied on destructive action-spectroscopic techniques such as dissociation [137, 138, 139] or chemical reactions [140, 86, 141]. Such methods are not suitable for a single-molecule clock experiment as it would require a constant supply of new molecules. This would slow down the experimental repetition rate and therefore reduce the statistical precision of the experiment. In this chapter, we present a new method for quantum-non-demolition detection [142] of the molecular state. The internal state is conserved after the measurement and the experiment can be repeated in fast succession for an enhanced statistical precision compared to previous destructive readout techniques [143, 100].

Non-destructive readout schemes typically rely on entanglement between the internal molecular state and the motional state of the crystal [24, 25], e.g. by applying a state-dependent force to the molecule [144, 145]. By modulating this force at the secular frequency of the trap, motion is excited which can subsequently be read out with high sensitivity on the atomic ion. This type of readout has been demonstrated experimentally with MgH^+ in Ref. [144] and with CaH^+ in Ref. [76]

Even in the simplest molecules, the force induced on the molecule may be of similar strength for several internal states such that they cannot be

distinguished from the measured motional excitation amplitude. This is especially the case when considering hyperfine or Zeeman structure in which the non-degenerate states couple differently to the force-generating field. For more complex molecules, a prior knowledge of transition strengths may not be available and a prediction of the expected force is therefore not possible.

The method presented in this chapter relies on the interference between the state-dependent force on the molecule and a reference force on the atomic ion to extract additional information about the molecular state. In addition to the amplitude of the force exerted on the molecule, we also obtain the phase or 'direction' of the force, i.e. whether the internal molecular state is low- or high-field seeking.

Using this method, we have demonstrated a number of single-molecule experiments on N_2^+ . We will show the unambiguous identification of specific spin-rotational states in different rotational states of the molecule. As the internal states are conserved in the measurement, this identification also constitutes a probabilistic state preparation. We will also show the ability to track changes in the state during chemical or scattering processes. Further, we show a partial state readout that can be used to exclude a large subset of states in a molecule even when the transition strengths are unknown.

We begin, in Section 5.1, by describing the optical lattice setup which is used for state detection. In Section 5.2, we derive and estimate the ac-Stark shift on both the molecular and atomic ions induced by the optical lattice. In Section 5.3, we describe the numerical and quantum simulations of the expected N_2^+ signal and present the method that is used for phase-sensitive state detection. Finally, in Section 5.4 we present the results of several single-molecule experiments implemented in N_2^+ .

5.1 The optical lattice

The optical lattice setup was presented schematically in Figure 3.16a in the context of laser-stabilization methods, where the two lattice beams were used to drive Raman transitions in Ca^+ . Here, we will present the optical lattice as a useful tool for molecular quantum non-demolition spectroscopy and state detection.

The optical lattice consists of two counter-propagating Gaussian laser beams of wavelength $\lambda = 789 \text{ nm}$, along the trap axis, each with $\sim 10 \text{ mW}$ of laser power and a $25 \mu\text{m}$ beam-waist radius. The two beam paths have matching polarizations, parallel to the magnetic field. The beams therefore form a 1D optical lattice with an intensity-modulated pattern with a period of $\lambda/2$.

The optical lattice induces an ac-Stark shift in both the N_2^+ and Ca^+ ions which exerts a force on the ions depending on their internal states. Figure 5.1 shows two vibronic components of the $X^2\Sigma_g^+ \rightarrow A^2\Pi_u$, 'Meinel' band of N_2^+ as a function of rotational quantum number of the lower state, N . The wavelength of the lattice beams, $\lambda = 789 \text{ nm}$, is closely detuned from the $X^2\Sigma_g^+(v=0) \rightarrow A^2\Pi_u^+(v=2)$ transition of N_2^+ and can therefore be used to non-destructively detect its internal state by inducing a state-dependent optical dipole force (ODF) on both the molecular and atomic ions.

The resulting ODF is modulated at the trap frequency, ω_z , by applying a frequency difference, $\Delta f = \omega_z$, between the two lattice beams to form a running-wave lattice. The modulated ODF will then excite coherent motion, $|\alpha\rangle$, in a motional mode of the two ion string [146]. After the ODF pulse, the internal state of the molecule is entangled with the motion of the ions and can be read out with a high sensitivity on the atomic ion through Rabi sideband thermometry [91].

To detect the motional excitation, Rabi oscillations are excited on a sideband of the $S_{1/2}(m_J = -1/2) \rightarrow D_{5/2}(m_J = -5/2)$ transition in Ca^+ using the 729 nm laser. The frequency and contrast of the observed signal depends on the motional-state distribution through Eq. (D.3) in Appendix D. If no motion is excited, the ions remain in the motional ground state and no Rabi oscillations are observed on a red sideband transition.

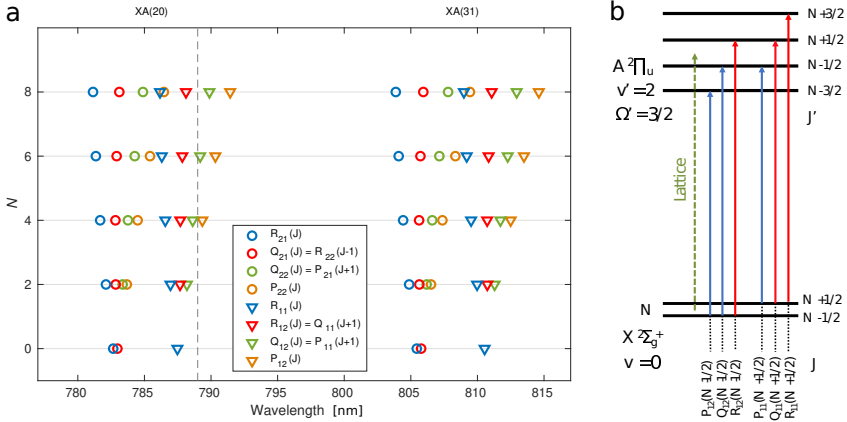


Fig. 5.1. **a**) Wavelengths of the $X^2\Sigma_g^+ \rightarrow A^2\Pi_u$, ($v = 0$) \rightarrow ($v' = 2$) (labeled XA(20)) and ($v = 1$) \rightarrow ($v' = 3$) (labeled XA(31)) bands in N_2^+ originating from the rotational levels $N = 0, 2, 4, 6$ and 8 . Several transitions are overlapping as indicated in the legend. The dashed gray line shows the approximate position of the lattice laser at ~ 789 nm. **b**) Simplified energy-level diagram (not to scale) of the XA(20) band of N_2^+ . Solid arrows indicate the possible transitions from a single rotational level (split into two spin-rotation components) of the ground vibronic state. Red (blue) arrows indicates red (blue) detuning of the lattice frequency (dashed green) with respect to the relevant transitions.

5.2 The ac-Stark shift

The amplitude of motional excitation, $|\alpha\rangle$, after the ODF pulse depends on the sign and amplitude of the ac-Stark shift on both ions. The force on the atomic ion can be adjusted by changing its internal electronic and Zeeman state, as shown in Figure 5.2. For some applications, such as the force-amplitude-spectroscopy presented in Section 5.4.3, a negligible ac-Stark shift, $\pm|\Delta E_a|$, is desirable on the atomic ion. This can be achieved by shelving the Ca^+ to the $D_{5/2}(m_J = -5/2)$ state, which has a low Stark shift for a linear polarization parallel to the magnetic field. As we will show in Section 5.4.1, for molecular-state determination in a complex region of the spectrum, a weak but significant force on the atom proves helpful for resolving the molecular states.

In the molecular ion, the sign and amplitude of the ac-Stark shift depends on the specific rovibronic, hyperfine and Zeeman state, as shown in Figure 5.1b, and can therefore be used to distinguish between different internal states. The sign of the shift, $\pm|\Delta E_m|$, also depends on the detuning from the dominant resonance. In Figure 5.2, we show the ac-Stark shift of the $N = 0$ state of the $I = 0$ species of the vibronic ground state near 787 nm. As we cross the resonance with the lattice wavelength, the sign of the induced ac-Stark shift changes and the molecule changes from low-field seeking (red detuned) to high-field seeking (blue detuned). The force on the Ca^+ ion, derived in the next section, stays constant over this range of wavelengths and the interference between the two forces can be used to extract the sign of the Stark shift in N_2^+ . In the following two sections, we will estimate the shifts induced in the N_2^+ and Ca^+ theoretically.

5.2.1 Ac-Stark shift of N_2^+

The ac-Stark shift of the molecular energies was presented in Section 2.4.2 where it was used to estimate the systematic energy shift of clock transitions due to the trapping potentials, from blackbody radiation and from a Mid-IR probe laser. In these estimates, the oscillating fields were far detuned from any dipole-allowed molecular transitions. Therefore a simplified 'rotationless' transition moment was used in the calculation which neglects the spin-rotational, hyperfine and Zeeman structure of

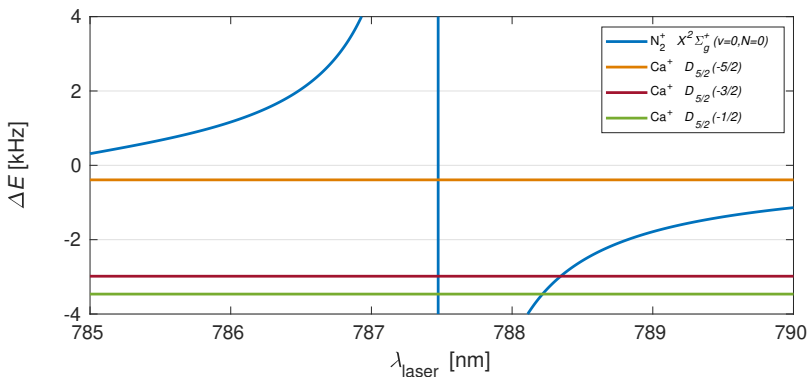


Fig. 5.2. The theoretically calculated ac-Stark shift experienced by Ca^+ , ΔE_a , in the $D_{5/2}(m = -5/2)$ (orange), $D_{5/2}(m = -3/2)$ (red), $D_{5/2}(m = -1/2)$ (green) states as a function of lattice wavelength using typical lattice parameters as described in the text. The blue curve shows the shift on the molecule, ΔE_m , due to the $R_{11}(J = 1/2)$ resonance of N_2^+ in the $X^2\Sigma_g^+(v = 0, N = 0)$ state. The ac-Stark shift changes sign when changing from negative to positive detuning across a molecular resonance while the ac-Stark shift experienced by the AI remains constant in this wavelength range as there is no resonance in Ca^+ nearby.

the transitions. As the lattice laser is close to resonance with dipole-allowed electronic transitions, we now include rotational, fine-structure and hyperfine-structure effects in the dynamic polarizability that is used to estimate the ac-Stark shift.

We recall the ac-Stark shift formula from Section 2.4.2,

$$\Delta E_j = -\frac{1}{2}\alpha_j(\omega)E_0^2, \quad (5.1)$$

where E_0 is the electric-field amplitude of the ac electric field with frequency ω and $\alpha_j(\omega)$ is the dynamic polarizability of the molecule given by,

$$\alpha_j(\omega) = \sum_k \frac{|\langle k|\mu|j\rangle|^2}{\hbar} \frac{\omega_{jk}}{\omega^2 - \omega_{jk}^2}. \quad (5.2)$$

The sum runs over all states, k , to which the state j can couple. In the literature, the line strength for vibronic lines is often cited in terms of the vibronic Einstein A_{jk} coefficients. The Einstein A coefficients for an electric dipole allowed transition is [70],

$$A_{jk}^{E1} = \frac{\omega_{jk}^3}{3\pi\epsilon_0\hbar c^3} S_{jk}^{E1}. \quad (5.3)$$

The dynamic polarizability can therefore be rewritten as,

$$\alpha_j(\omega) = \sum_k \frac{3\pi\epsilon_0 c^3}{\omega_{jk}^2(\omega^2 - \omega_{jk}^2)} c_{jk} A_{jk}^{\text{vib.}}. \quad (5.4)$$

Here, we have once again separated the transition strength, S_{jk}^{E1} , into a 'radial' rotationless moment, $A_{jk}^{\text{vib.}}$, and an angular 'Hönl-London' factor, c_{jk} , as shown in Section 2.2. For the radial part of the transition moment we use the rotationless Einstein coefficients for vibronic transitions in the Meinel-band from Ref. [147]. The angular transition frequencies, ω_{jk} , are taken from Ref. [63]. The angular matrix elements, c_{jk} , are derived in Appendix B.5 by treating the lower $X^2\Sigma_g^+$ state in a Hund's case ($b_{\beta J}$)

basis and the upper state, $A^2\Pi_u$, in a Hund's case ($a_{\beta,J}$) basis. The derived matrix elements are given by Eq. (B.37) as,

$$\begin{aligned}
 c_{jk} = & (2F' + 1)(2F + 1)(2J' + 1)(2J + 1)(2N + 1) \\
 & \times \begin{pmatrix} F' & 1 & F \\ -M'_F & 0 & M_F \end{pmatrix}^2 \left\{ \begin{matrix} J & F & I \\ F' & J & 1 \end{matrix} \right\}^2 \begin{pmatrix} J' & 1 & J \\ -\Omega' & 1 & \Omega \end{pmatrix}^2 \\
 & \times \left[\begin{pmatrix} J & 1/2 & N \\ \Omega & 1/2 & 0 \end{pmatrix} + \begin{pmatrix} J & 1/2 & N \\ \Omega & -1/2 & 0 \end{pmatrix} \right]^2. \tag{5.5}
 \end{aligned}$$

An additional off-resonant contribution to the ac-Stark shift comes from the core electrons in N_2^+ . The core polarizability is nearly the same for both upper and lower states and therefore cancels in the measured transition frequency. It will, however, add to the ac-Stark shift induced by the lattice lasers on the molecule and must therefore be included in the calculation. This contribution was estimated by *P. Straňák* using Gaussian 09 [148], as the polarizability of the doubly charged species N_2^{2+} . The calculated polarizability was found to be $\alpha^{N_2^+, \text{core}} \approx \alpha^{N_2^{2+}} = 7.23$ a.u. corresponding to an ac-Stark shift of -390 Hz with our optical lattice parameters.

Figure 5.3 shows the calculated ac-Stark shift of rotational states, $N = 0, 2, 4, 6, 8$, in the vibrational ground state of the $X^2\Sigma_g^+$ -state near 789 nm. The thicker lines show the components of the $I = 0$ state and the thinner lines of the $I = 2$ state. With this figure, we wish to show that even in a relatively simple diatomic molecule such as N_2^+ , the presence of vibrational, rotational, fine-structure, hyperfine-structure and Zeeman terms in the Hamiltonian give rise to a beautiful complexity in the ac-Stark shift spectrum which makes distinguishing different rotational states using the ODF a challenging task.

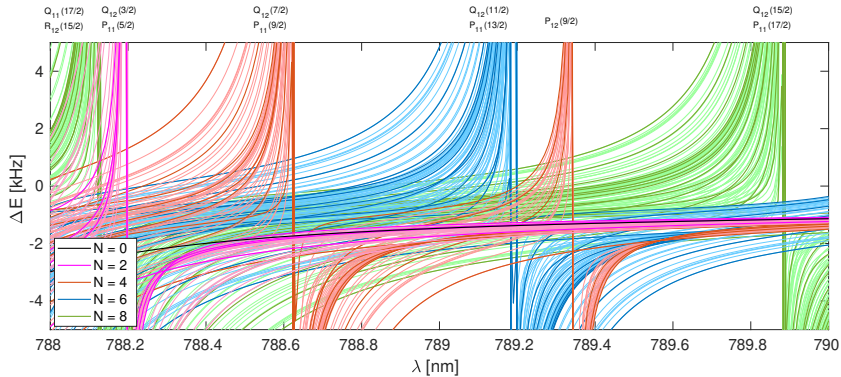


Fig. 5.3. Theoretically determined ac-Stark shift of N_2^+ on the XA(20) band in rotational states $N = 0, 2 \dots 8$ (color-coded as shown in legend) around 789 nm from a lattice beam with 10 mW of power and $25 \mu\text{m}$ beam waist radius. Q(J), P(J) and R(J) transitions are indicated above each resonance. Bold lines correspond to $I = 0$ state and thin lines show $I = 2$ states including the effects of hyperfine structure. The magnetic field is here assumed small but finite such that the Zeeman levels are not degenerate but with a negligible effect on the position of the resonances.

5.2.2 Ac-Stark shift of Ca^+

The ac-Stark shift in Ca^+ is estimated in the same manner as in N_2^+ , by summing over all levels, k , to which the level j couples using Equations (5.1) and (5.2). The radial transition moments are once again obtained as the 'reduced' matrix elements from the Einstein coefficients A_{jk} . The polarizability, $\alpha_j(\omega)$, is then,

$$\alpha_j(\omega) = - \sum_k \frac{3\pi\epsilon_0 c^3}{\omega_{jk}^2 (\omega_{jk}^2 - \omega^2)} A_{jk} c_{jk}. \quad (5.6)$$

The angular factor, c_{jk} , is given by the Wigner-Eckart theorem as [93],

$$c_{jk} = (2J_k + 1) \left| \sum_{p=-1}^1 \begin{pmatrix} J_k & 1 & J_j \\ -m_k & p & m_j \end{pmatrix} \bar{c}^{(q)} \bar{\epsilon} \right|^2. \quad (5.7)$$

Here, we have included the degeneracy of the state k as $g_k = (2J_k + 1)$ in the angular factor. The coefficients $\bar{c}^{(q)}$ are the normalized basis functions

of a first order spherical tensor defined in Eq. (2.45). The laser polarization vector, $\bar{\epsilon}$, is defined in the space-fixed frame of reference where $\bar{\epsilon} = (0, 0, 1)$ corresponds to the $p = 0$ component of the polarization and couples $\Delta m = 0$ states.

We use the transition frequencies and oscillator strengths from Ref. [149]. By the above equation, we find that the $(4s) \ ^2S_{1/2}$ state of Ca^+ has $\alpha^S(\omega) = 97.5$ a.u. for a lattice with linear polarization, parallel to the magnetic field, at ~ 789.0 nm. This corresponds to a shift of -5.4 kHz with our lattice parameters.

With linear polarization parallel to the magnetic field, the $D_{5/2}(m_J = -5/2)$ state of Ca^+ does not interact with the $P_{3/2}$ states since $\Delta m = 0$ transitions are not possible. This state therefore only interacts with higher-lying electronic states. We sum up the contributions from higher-lying states, (nf) , up to $n = 10$ to obtain $\Delta E_a = -0.2$ kHz, -2.8 kHz, and -3.0 kHz in the $D_{5/2}(m_J = -5/2)$, $D_{5/2}(m_J = -3/2)$ and $D_{5/2}(m_J = -1/2)$ levels respectively, as shown in Figure 5.2.

The core contribution of Ca^+ is nearly the same in both electronic states, $S_{1/2}$ and $D_{5/2}$, and does not contribute to the spectroscopically measured shift. It does, however, add to the ODF from the lattice and can not be neglected when compared to the small shift in the $D_{5/2}(m_J = -5/2)$ state. The core polarization is $\alpha^{S,\text{core}} = 3.134$ a.u. [149] corresponding to -405 Hz for our lattice parameters.

The ac-Stark shift induced by the lattice lasers are readily measured on the Ca^+ spectroscopically as exemplified in Figure 5.4a. We employ electron-shelving spectroscopy with and without a single lattice beam on during the shelving pulse. From these measurements, the intensity of the lattice laser is calibrated.

The polarization dependence of the ac-Stark shift can also be measured experimentally. In Figure 5.4b, we compare the ratio of ac-Stark shifts, $\Delta E_i/\Delta E_j$, between several transition frequencies in the $S_{1/2} \rightarrow D_{5/2}$ manifold for different lattice polarizations. The ratio of two ac-Stark shifts is free from the influence of the laser power. We see that the states involving $D_{5/2}(m_J = -5/2)$ show a discrepancy with the theoretical predictions of up to 15% while the other states agree well with the theory. This discrepancy may be due to spurious polarization of the lattice beams.

For the internal state detection of N_2^+ , we perform calibration experiments in the $S_{1/2}(m_J = -1/2)$ -state and measure the shifts on Ca^+ directly. The observed discrepancy therefore does not impact the N_2^+ state detection.

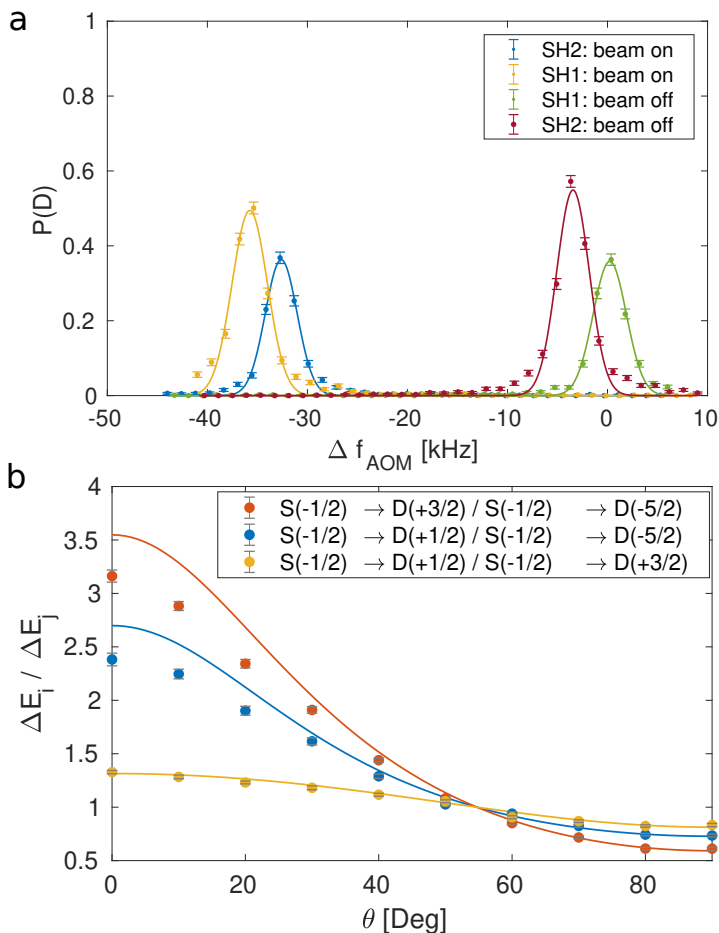


Fig. 5.4. **a)** The ac-Stark shift of Ca^+ measured by electron-shelving spectroscopy under the influence of the lattice lasers on the $S_{1/2}(m = -1/2) \rightarrow D_{5/2}(m = -5/2)$ (SH1, yellow and green) and $S_{1/2}(m = 1/2) \rightarrow D_{5/2}(m = 5/2)$ (SH1, blue and red) transitions. The measured shift was obtained with both lattice beams at full power, ~ 15 mW per beam, and corresponds to the combined shift in both the lower and upper states of the transition. **b)** The ratio of the ac-Stark shift between three transitions in Ca^+ (dots, see legend) compared to the theoretical prediction (lines) as a function of linear lattice polarization, θ . The polarization $\theta = 0$ corresponds to linear polarization parallel to the magnetic field. The error bars represent the 1σ statistical uncertainties.

5.3 Motional excitation by the optical lattice

We now consider the effect of the ac-Stark shifts, modulated on resonance with one of the motional modes, on the motional excitation amplitude of the two-ion $\text{Ca}^+ - \text{N}_2^+$ -string. A two-ion crystal exhibits two normal modes along the trap axis, as described in Section 3.1.1. Here we will consider the influence of the ODF modulated on resonance with the ground-state cooled COM mode, with frequency ω_z .

The running-wave optical lattice leads to a modulated ac-Stark shift on each ion given by [150],

$$\Delta E_i = 2\Delta E_i^0 (1 + \cos(2kq_i - \Delta\omega t + \phi_i^0)), \quad (5.8)$$

where ΔE_i^0 is the ac-Stark shift induced by a single lattice beam on the ion with index i . $\Delta\omega$ is the angular modulation frequency of the lattice and $k = 2\pi/\lambda$ is the lattice-laser wavenumber. The phase, $\phi_i^0 = 2kx_i^0$, depends on both the equilibrium positions of the ions and the sign of the ac-Stark shift, $\pm|\Delta E_i^0|$. The sign of the ac-Stark shift, in turn, depends on the detuning of the lattice-laser frequency from the dominant resonance at the lattice-laser wavelength, $\lambda \approx 789$ nm.

The relative phase of the lattice intensity gradient experienced by the two ions can be tuned continuously by changing the two-ion equilibrium distance, d , in the trap. If the distance between the ions corresponds to an integer number of lattice sites, $d = n\lambda/2$, the phase between the two ions, $\phi_2^0 - \phi_1^0 = 2\pi n$, is such that the intensity gradient has the same phase (SP) for both ions. If the two-ion distance corresponds to $d = n\lambda/2 + \lambda/4$ then the particles experience opposite phases (OP) of the intensity gradient of the lattice.

We can estimate the force acting on both the atomic and molecular ions by expanding Eq. 5.8 in a Taylor series around the equilibrium positions, q , and taking the gradient of the ac-Stark shift potential,

$$\frac{d\Delta E_i}{dq_i} = F_i \approx -4k\Delta E_i^0 \sin(\Delta\omega t - \phi_i^0). \quad (5.9)$$

In this approximation, the lattice exerts an oscillating spatially homogeneous force with an amplitude $F_i = 4k\Delta E_i^0$ on ion i . In the case of a single ion, this force will cause coherent excitation of motion in the trap. The impact of such a force applied to both ions will be simulated in the next section.

5.3.1 Numerical simulation of the motional excitation

In order to estimate the motional excitation amplitude of the two-ion crystal due to the modulated ODF, including higher-order effects which couple different motional modes, we perform a classical simulation of the two-ion system in 1D¹. We solve the equations of motion for the two ions under the influence of a harmonic trapping potential, their mutual Coulomb repulsion and the ODF on each ion.

The trap potential is approximated as a harmonic potential with a 'spring constant' $k_0 = \omega_i^2 m_i$ which is readily measured on a single ion. By measuring the axial frequency of a single Ca⁺ ion we find $\omega_i = \sqrt{k_0/m_i} \approx 642$ kHz and thus $k_0 \approx 1 \times 10^{-12}$ N/m. The mutual Coulomb repulsion between two singly charged ions is $F_c = -e^2/(4\pi\epsilon_0 r_{12}^2)$, where r_{12} is the instantaneous distance between the two ions and e is the elementary charge. The force due to the optical lattice is given by Eq. (5.9).

The equations of motion to be solved for two ions are then given by four ordinary differential equations,

$$\begin{aligned} \dot{x}_i &= v_i \\ m_i \dot{v}_i &= -k_0 x_i + (-1)^i \frac{e^2}{4\pi\epsilon_0 r_{12}^2} - 4k\Delta E_i \sin(\omega_i t + \phi). \end{aligned} \quad (5.10)$$

These equations are solved using the numerical RK4 method [151] with a time step of ~ 1 ns. The ions start near their equilibrium positions, $x_i^0 = \pm (e^2/(4\pi\epsilon_0 k_0 4))^{1/3}$, in the trap ground state, $v_i^0 = 0$, with the trapping potentials obtained on a single Ca⁺ ion from the experiment

¹The simulation was implemented in MATLAB [60] by Ziv Meir.

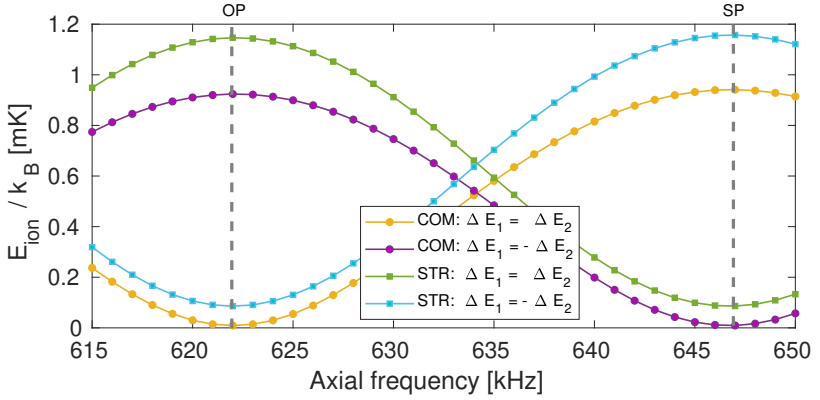


Fig. 5.5. The simulated motional energy of a two-ion $\text{Ca}^+ - \text{N}_2^+$ -string after a 3 ms long ODF pulse modulated at the COM (circles) and STR (squares) frequencies as a function of the single Ca^+ ion trap frequency. Green and orange points correspond to an ac-Stark shift of +1 kHz on both ions and blue and purple points represent the case where the ions have opposite signs of the stark shift ± 1 kHz. The excitation energy (in mK) depends on the two-ion distance in the trap as well as their relative sign of the ac-Stark shift. The SP and OP frequencies (indicated by the dashed grey lines) represent the limiting cases where the forces on both ions are in phase and π -shifted respectively.

of $\omega_z = 641$ kHz. The initial phase, ϕ , is randomized in the beginning of each simulation. We record the total ion energies as a function of time for a total ODF pulse of $t = 3$ ms. In Figure 5.5, we present the simulated energy of the COM and STR modes as a function of axial trap frequency and hence of the two-ion separation. Stark shifts of equal magnitude, ± 1 kHz, are applied to both ions with both equal (orange and green points) and opposite signs (blue and purple points) with a lattice frequency difference matching the COM mode, $\Delta f = \omega_{COM}$ (circles), and the STR mode, $\Delta f = \omega_{STR}$ (squares).

When the two ions have equal detuning and magnitude of the ac-Stark shift, $-|\Delta E_a| = -|\Delta E_m|$, there is a cancellation of the forces at 620 kHz corresponding to the two-ion distance where the ions experience opposite phases (OP) of the optical lattice. In this configuration, the STR-mode is instead excited. At 645 kHz, the ions experience the same phase (SP) of the optical lattice and the forces interfere constructively to enhance the excitation of the COM mode. The opposite is true in the case of

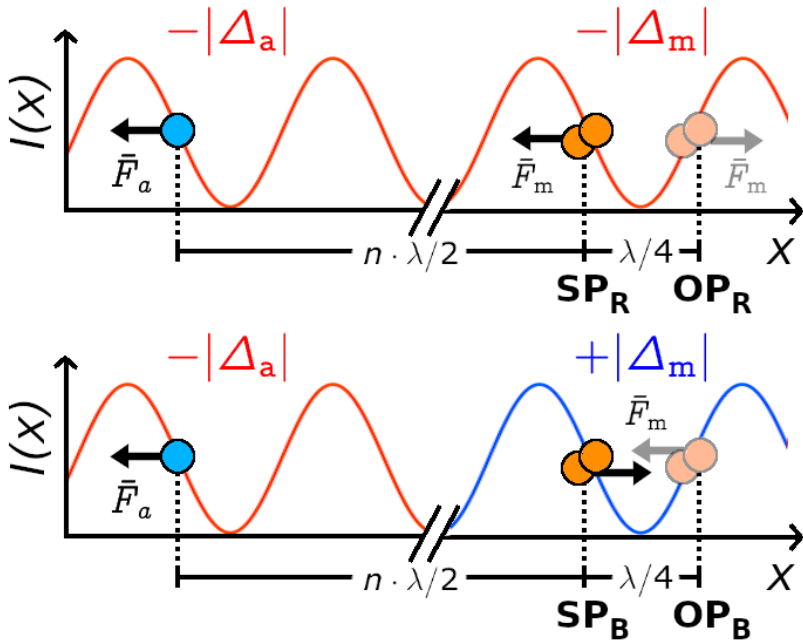


Fig. 5.6. Four possible configurations ($SP_{R/B}$, $OP_{R/B}$) of the lattice containing the atomic ion (AI, blue circle) and the molecular ion (MI, orange circles). The direction of the force on the MI (AI) ($F_{m(a)}$) depends on the frequency detuning $\pm|\Delta_{m(a)}|$ of the lattice laser beams from resonance and the relative positions of the particles in the lattice field. The AI and the MI have either the same signs of detuning (top) or opposite signs (bottom). For a MI at positions SP_R and SP_B in the lattice, the distance between the two ions is such that they experience the same phase (SP), while at positions OP_R and OP_B the ions experience opposite phases (OP) of the lattice intensity gradient.

opposite detuning, $-|\Delta E_a| = +|\Delta E_m|$, where the heating of the COM mode is enhanced in the OP configuration and nearly cancels in the SP configuration. These four scenarios are illustrated schematically in Figure 5.6. We therefore find constructive or destructive interference between the forces on both ions to form an effective force which depends on the detuning with respect to the dominant resonance of the ions and their axial distance. By measuring both SP and OP configurations, we may therefore obtain both the amplitude and phase of the force on the molecular ion if the force on the atomic ion is known.

In this simulation, by assuming harmonic trapping potentials and perfect ground-state occupation of both motional modes, the resulting motional-state distribution after the ODF resembles a coherent state. However, due to experimental imperfections, such as imperfect ground-state cooling, spurious lattice polarizations or anharmonic potentials, the shape of the motional-state distribution is not assumed in the data analysis and we instead calibrate the forces directly in a 'quantum simulation' experiment described in the next section.

5.3.2 'Quantum simulation' using N_2H^+

The state detection of N_2^+ relies on the accurate determination of the final motional 'Fock state' distribution by Rabi sideband thermometry on a red sideband of the $\text{S}_{1/2} (m_J = -1/2) \rightarrow \text{D}_{5/2} (m_J = -5/2)$ transition in Ca^+ , or equivalently, when performing the experiment in the $\text{D}_{5/2}$ state, on a blue sideband of the $\text{D}_{5/2} (m_J = -5/2) \rightarrow \text{S}_{1/2} (m_J = -1/2)$ transition. As we have seen in Appendix D, the sideband transitions are sensitive to the motional state distribution of the crystal. If no excitation occurred during the ODF pulse, the COM mode remains in the motional ground state and no Rabi oscillations are observed on a red sideband transition. In order to relate the observed Rabi-oscillations to the ac-Stark shift experienced by the molecular ion, we simulate the expected signal on a two-ion $\text{Ca}^+ - \text{N}_2\text{H}^+$ string with a well defined ac-Stark shift applied on the Ca^+ ion. In this manner, we may associate an oscillation signal with a well-determined shift which includes contributions from many experimental imperfections which are not captured by the numerical simulation presented in the previous section.

The ac-Stark shift is determined experimentally by electron-shelving spectroscopy on the $\text{S}_{1/2} (m_J = -1/2) \rightarrow \text{D}_{5/2} (m_J = -5/2)$ transition, as described in Section 5.2.2, and the shift is varied by changing the power of the lattice laser. As the simulations are performed in the $\text{S}_{1/2} (m_J = -1/2)$ state, the contribution to the measured shift from the $\text{D}_{5/2} (m_J = -5/2)$ state is subtracted. For example, with a lattice power of ~ 10 mW per beam, the measured Stark shift from a single lattice beam on the $\text{S}_{1/2} (m_J = -1/2) \rightarrow \text{D}_{5/2} (m_J = -5/2)$ transition is ~ 5 kHz. The theoretical contribution from the $\text{D}_{5/2} (m_J = -5/2)$ state amounts to a shift

of -405 Hz (see Figure 5.2) and we find the shift of the $S_{1/2} (m_J = -1/2)$ state to be -5.4 kHz.

Lattice-excitation simulations were performed with six different laser powers, corresponding to ac-Stark shifts between $0.8 - 4.6$ kHz, in which the ODF was applied for 3 ms and a Rabi-oscillation signal was obtained for each ac-Stark shift as presented in Figure 5.7. To fit an arbitrary shift between these simulated points, a fitting-function was implemented to interpolate between the calibration points.

First, the Rabi-oscillations are each fitted with three parameters in the Rabi-oscillation formula from Eq. (D.4) assuming a coherent distribution of motional states, $P_n(\alpha)$, with an additional source of decoherence. The three fit parameters correspond to the average motional occupation of a coherent state, $\langle n \rangle$, the detuning from resonance, δ , and an additional decoherence mechanism characterized by the time constant T_2 . While these parameters have physical meaning, we treat them phenomenologically as a way to interpolate between the measured calibration points.

A global fitting-function was constructed to interpolate between the fitted values of these three parameters for any Stark shift, ΔE , by fitting linear (T_2 and δ) and quadratic ($\langle n \rangle$) functions to the calibrated points as presented in Figure 5.8. An arbitrary Rabi-oscillation curve can then be reconstructed using Eq. (D.4) for any value of ΔE by interpolating between these three parameters.

An N_2H^+ was used in the calibration as it is far detuned from any resonance at $\lambda = 789$ nm and therefore only experiences a small force from the lattice. It also benefits from a longer lifetime in our trap of ~ 1 hour compared to ~ 5 minutes for N_2^+ . The residual contribution of N_2H^+ to the effective force was included through an iterative calibration as described below. The mass difference of 1 u between N_2H^+ and N_2^+ only amounts to a small correction ($< 2\%$) to the calibration compared to other experimental errors

As the ac-Stark shift on N_2H^+ , $\Delta E_{N_2H^+}$ is expected to be small compared to the shift on Ca^+ in the $S_{1/2} (m = -1/2)$ state, it was neglected to first order. This zero-order fit function, obtained from the calibration described above, was used to measure the ac-Stark shift of N_2H^+ from an SP/OP measurement as the difference between the SP and OP configurations

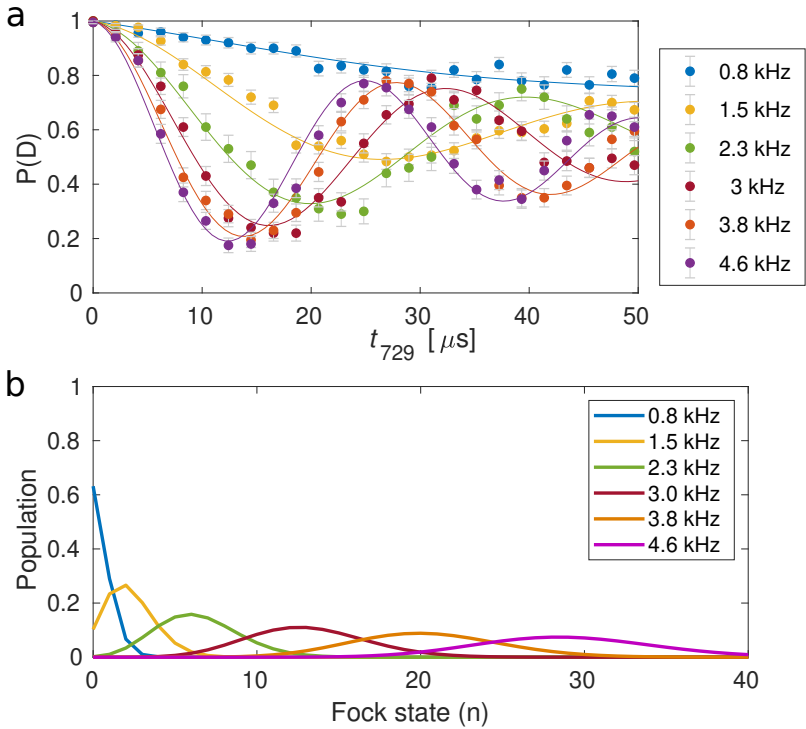


Fig. 5.7. Calibration measurements: **a)** Rabi-oscillation data from a two-ion Ca^+ - N_2H^+ string with six different ac-Stark shifts applied to Ca^+ . The Ca^+ ion was prepared in the $S_{1/2}(m = -1/2)$ state. The contribution of N_2H^+ to the excitation signal is corrected iteratively (see text). The legend shows the second-iteration results for the ac-Stark shift including the contribution from N_2H^+ . Error bars represent 1σ binomial uncertainties. **b)** The coherent state populations that were fitted to the calibration data presented in **a)** as a function of motional state n . The fitted motional state distributions are used to interpolate between the calibration points.

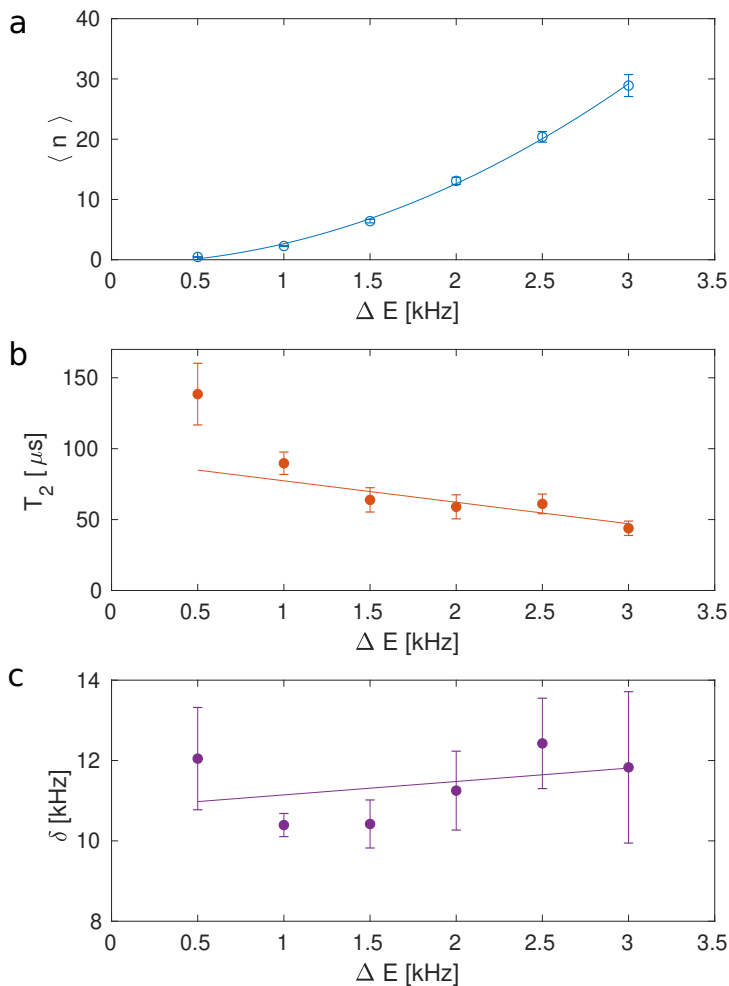


Fig. 5.8. Three parameters fitted to the calibration points from Figure 5.7 as a function of the ac-Stark shifts applied to a two-ion $\text{Ca}^+ - \text{N}_2\text{H}^+$ -string. These functions are used to interpolate between the calibration points. **a)** The fitted values of the average motional state occupation, $\langle n \rangle$, for a coherent state after an ODF of 3 ms. A second order polynomial (blue line) was fitted to the data. **b)** The fitted values of the decoherence time, T_2 , of an exponential decay. A first order polynomial (orange line) was fitted to the data. **c)** The fitted values of the detuning of the 729 nm laser from resonance, δ , on the first red sideband of the $S_{1/2} (m = -1/2) \rightarrow D_{5/2} (m = -5/2)$ transition. A first-order polynomial (purple line) was used to fit the data. All error bars represent 1σ confidence intervals of the fits to the Rabi-oscillation data.

(see e.g. Figure 5.9). An approximate shift of $\Delta E_{\text{N}_2\text{H}^+} = -0.81$ kHz was obtained which corresponds to $\sim 15.8\%$ of $\Delta E_{\text{Ca}^+} = 5.41$ kHz for the same laser power. As the SP configuration was observed to be stronger than the OP configuration, the shift on the N_2H^+ is negative, like the shift in Ca^+ , and the forces interfere constructively. This shift was then added to the calibration data for a more realistic calibration which includes the total shift from both Ca^+ and N_2H^+ interfering constructively to excite the COM mode.

This procedure was iterated for a first-order estimate of the ac-Stark shift of N_2H^+ . The first iteration changes the measured shift to $\Delta E_{\text{N}_2\text{H}^+} = -0.93$ kHz corresponding to $\sim 18.1\%$ of ΔE_{Ca^+} . The second iteration yields $\Delta E_{\text{N}_2\text{H}^+} = -0.99$ kHz corresponding to $\sim 18.5\%$ of ΔE_{Ca^+} . Any residual error in the fitting function after the second iteration was therefore neglected. In Figure 5.7a, we present the results of the calibration experiments including the effect of N_2H^+ excitation. We also present the coherent-state distributions that were fitted to these calibration data for illustrative purposes in Figure 5.7b.

5.3.3 Example signal

For determination of the internal molecular state, the force on the atomic ion is chosen such that it is small but not negligible. After sympathetic ground-state cooling of the COM mode of the $\text{Ca}^+ - \text{N}_2^+$ -string, the lattice lasers are turned on for a pulse duration of 3 ms and the motional excitation is subsequently read out on Ca^+ as described in the previous section. As the internal state of the molecule is undisturbed by the detection scheme, the process of sideband cooling, ODF pulse and state detection can be repeated until sufficient statistics are obtained so that the Rabi oscillations can be fitted.

The measurement of a Rabi-oscillation signal does not by itself yield information about the sign of the detuning, since the ac-Stark shift varies greatly between different states, as was shown in Figure 5.3, such that a priori the strength of the signal cannot be predicted. In order to disentangle the strength and sign of the ac-Stark shift, the Rabi-oscillation signal is taken twice with two different two-ion distances. Once with an ion distance of $d = n\lambda/2$ where $n = 19$ and $\lambda \approx 789$ nm corresponding to the

SP configuration ($f_{\text{IP}}^{\text{SP}} = 695$ kHz) and once with the ion distance shifted by $\Delta d = +\lambda/4$ corresponding to the OP configuration ($f_{\text{IP}}^{\text{OP}} = 668$ kHz). The configuration is changed by adjusting the voltages on the ion trap endcap electrodes between ~ 180 V and ~ 160 V for the SP and OP configurations, respectively.

Figure 5.9 shows two different molecular states of N_2^+ measured using this method. The sideband pulse duration, t_{729} , was scanned and averaged 20 times for each data point to retrieve two Rabi-oscillation signals in each experiment, one for the SP (blue) and the other one for the OP (purple) configurations.

In Figure 5.9a, the frequency and contrast of the Rabi signals are higher for the SP configuration compared to the OP configuration implying that the motional excitation, and thus the effective ODF, is stronger for the SP configuration. This indicates that the detuning of the lattice frequency from a molecular resonance is the same as in Ca^+ , i.e., red detuned. The resulting Rabi oscillations were fitted to extract the amplitude of the ac-Stark shift. By comparing the obtained ac-Stark shift and phase to the theory presented in Section 5.2.1, the molecular state was unambiguously identified as $N = 6$, $J = 11/2$.

In Figure 5.9b, the opposite situation occurred for the same settings of the lattice-laser beams. Here, the observed frequency and contrast of the Rabi signals are higher in the OP configuration. This implies that the lattice frequency is oppositely detuned compared to the Ca^+ from the closest molecular resonance, i.e., blue detuned. In Section 5.4.5 we show how, based on this observation, without knowledge of the ac-Stark shifts in the molecule, all molecular states with $N \leq 4$ can be excluded.

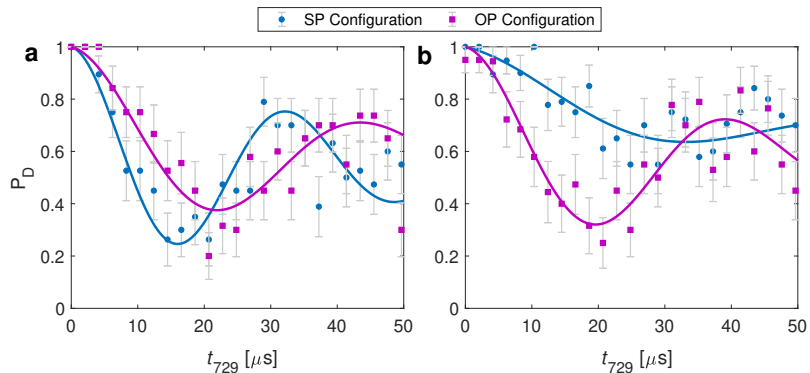


Fig. 5.9. Rabi thermometry on a $\text{Ca}^+ - \text{N}_2^+$ two-ion string. Rabi oscillation signals for the SP (blue) and OP (purple) lattice configurations after an ODF pulse for two different molecular states (panel (a) and panel (b)). Each data point is an average of 20 ODF excitations. Error bars represent 1σ binomial uncertainties. The solid curves represent fits to the data as described in Section 5.3.3 from which the ac-Stark shifts were extracted. **a)** The stronger SP signal (larger frequency and amplitude of the Rabi oscillation) suggest that the lattice laser ($\lambda = 789.71$ nm, in both experiments) was red detuned from the closest molecular transition. By comparing the measured amplitude and sign of the ac-Stark shift with theory, the molecular state could unambiguously be identified as $N = 6, J = 11/2$. **b)** The stronger OP signal suggests that the lattice laser was blue detuned from the closest molecular transition. Therefore, all rotational states $N \leq 4$ can be excluded as described in Section 5.4.5

5.4 Single-molecule experiments

In this section, we present the results of several proof-of-principle experiments with N_2^+ using the detection method described in the previous sections. We shall prove the usefulness of this method for determining the internal state of the molecule out of hundreds of possible states, and the ability to measure dipole-allowed transitions, both while preserving the original state. We shall also show the ability to trace state-sensitive reaction and scattering events in a single molecule. Finally we present a scheme to simultaneously exclude hundreds of initial states in a partial state-determination scheme.

5.4.1 Identifying molecular states

The phase-sensitive detection scheme, described in Section 5.3, is useful for positively identifying molecular states out of several possible initial states. The additional information that is gained by extracting the phase of the ODF in addition to its magnitude allows us to distinguish between states of the same magnitude, but opposite sign of the ac-Stark shift. This scenario is typical for different rotational states where the ac-Stark shifts of a given rotational state, N , show a broad range of values for different hyperfine and Zeeman components whereas the detuning from a resonance remains the same². The different rotational states are then readily distinguished using the sign of the shift instead of the magnitude.

This method was used to identify specific spin-rotation, hyperfine and Zeeman levels in the electronic and vibrational ground state of N_2^+ as presented in Figure 5.10. In these experiments, the N_2^+ ion was generated primarily in rotational states with $N \leq 8$ in the vibronic ground state by a rotationally unselective photoionization scheme. In each experiment, the molecule was therefore initialized in one of 540 possible hyperfine Zeeman states.

²In order to keep the scattering rate from the lattice lasers low we typically work with detunings > 10 GHz which is large compared to the typical hyperfine splitting of ~ 100 MHz in N_2^+ .

Using the phase-sensitive detection method, the rotational and fine-structure states of molecules after ionization were successfully identified. A few illustrative data points are presented in Figure 5.10 overlaid with the theoretical ac-Stark shift. Near 789 nm, the detection is sensitive to initial states in the $N = 4$, $J = 7/2$ spin-rotation manifold which experience a significant ac-Stark shift through the $Q_{12}(7/2)$ transition at 788.624 nm. In these states, the lattice laser is red detuned (higher wavelength) with respect to the resonance. At the same wavelength, the detection is also sensitive to initial states in the $N = 6$, $J = 11/2$ spin-rotation manifold. These states experience a significant ac-Stark shift from the $Q_{12}(11/2)$ transition at 789.1872 nm where the lattice laser is blue detuned (lower wavelength) with respect to the resonance. At this lattice wavelength, other rotational states, $N = 0, 2, 8$, are further detuned and therefore not distinguishable.

For the experiments labelled 1-3 in Figure 5.10, the measured shift was large enough to determine whether the molecule was in the $N = 6$, $J = 11/2$ or the $N = 4$, $J = 7/2$ spin-rotational states. The additional information gained by the sign of the ac-Stark shift enables us to distinguish between these two spin-rotation manifolds (blue and red triangles respectively). The black square represents an experiment in which the sign information is missing and, therefore, an unambiguous identification of the molecular rotational state is not possible. In many experiments, the signal was very low, indicating that the state of the molecule was indistinguishable at this lattice-laser wavelength, as exemplified by the red triangles in the bottom of Figure 5.10. The possible Zeeman and Hyperfine components of the detected internal state in the experiments labelled 1-4 are presented in Table 5.1.

5.4.2 State preparation

The initialization of the molecule into a specific internal state which interacts with a probe laser is key to a useful clock experiment performed on a single ion. In the single-molecule experiments demonstrated on polar molecules, this initialization was aided by a reshuffling of the internal states due to coupling with black-body radiation (BBR) [152, 144, 76]. As we have seen in Section 2.4.2, in homonuclear diatomic molecules

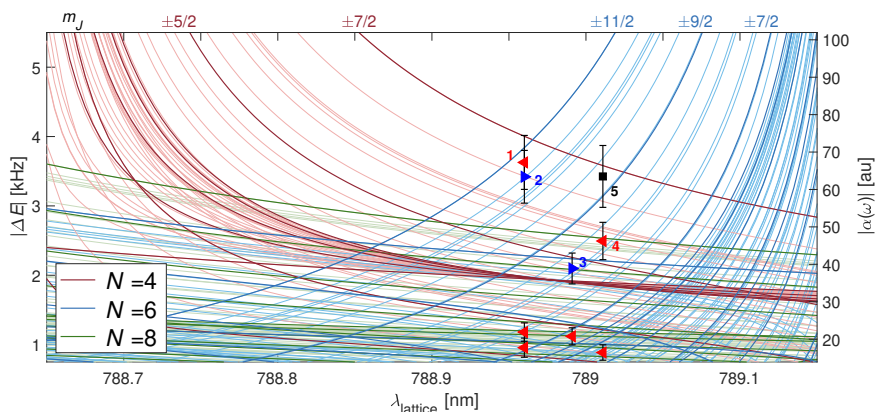


Fig. 5.10. Molecular state identification. Absolute magnitude of the ac-Stark shifts (left ordinate) and the molecular dynamic polarizability (right ordinate) for molecules in the $N = 4, 6, 8$ rotational states (red, blue and green lines) at a lattice-laser wavelength around 789 nm. Thick lines correspond to the ac-Stark shift of Zeeman components of the $I = 0$ nuclear-spin isomer without hyperfine structure (labeled by their magnetic quantum numbers M_J on top of the figure) while thin lines correspond to the hyperfine Zeeman components of the $I = 2$ state. Blue (red) triangles represent experiments in which the measured ac-Stark shifts were stronger in the OP (SP) configuration corresponding to a lattice blue (red) detuned from the transition. The black square represents an experiment without the phase information. Error bars are the combined 1σ uncertainties of the fit to the data and the uncertainty of the lattice laser power ($\sim 10\%$). The ac-Stark shifts originating from the $N = 0, 2$ rotational levels are lower than the ones for the $N = 8$ state in this wavelength range and were omitted for clarity.

Experiment No.	Agreement	N	J	I	F	$M_{J/F}$
1	$< 1\sigma$	4	7/2	0		$\pm 7/2$
				2	11/2	$\pm 11/2$
	2			9/2	$\pm 9/2$	
	2			11/2	$\pm 9/2$	
	2			7/2	$\pm 7/2$	
	2			3/2	$\pm 3/2$	
2	$< 1\sigma$	6	11/2	2	13/2	$\pm 13/2$
				2	11/2	$\pm 11/2$
	2			7/2	$\pm 7/2$	
	0				$\pm 11/2$	
	2			15/2	$\pm 15/2$	
	2			9/2	$\pm 9/2$	
3	$< 1\sigma$	6	11/2	2	15/2	$\pm 11/2$
	$< 2\sigma$			2	9/2	$\pm 7/2$
				2	11/2	$\pm 9/2$
4	$< 1\sigma$	4	7/2	2	11/2	$\pm 9/2$
				2	9/2	$\pm 7/2$
				2	7/2	$\pm 7/2$
				2	5/2	$\pm 5/2$
				2	3/2	$\pm 3/2$
		8	17/2	0		$\pm 17/2$
				2	21/2	$\pm 21/2$
				2	19/2	$\pm 19/2$
				2	17/2	$\pm 17/2$
				2	15/2	$\pm 15/2$
0	13/2	$\pm 13/2$				

Tab. 5.1. Molecular state identification. The numbers in the first column correspond to the labels shown in Figure 5.10. The second column indicates the level of agreement between experiment and theory for the given state (for experiment 4, only states within 1σ agreement are given; an additional 20×2 states within 2σ agreement are omitted). N , J , I , F and $M_{J/F}$ stand for the rotational, spin-rotational, nuclear-spin, hyperfine and magnetic quantum numbers of N_2^+ in the electronic and vibrational ground state.

such as N_2^+ the rovibrational states are largely unaffected by BBR and alternative methods of state preparation are required [86].

The state determination presented in the previous section also constitutes a probabilistic preparation of specific hyperfine and Zeeman levels. As the internal state of the molecule is detected non-destructively, the molecule is automatically initialized in the detected state. Any molecule which is not in the desired state may then be discarded. Alternatively, the molecular states can be reshuffled by additional Raman, RF or microwave fields to mix different states in, e.g., the $v = 0$ manifold. The ODF detection will then project the molecule into one of the coupled states and by repeating the process of mixing and ODF detection, the desired state will be found eventually and the molecule is initialized.

5.4.3 Molecular dipole-allowed spectroscopy

The strength of the ODF depends on the detuning of the lattice laser from a resonance in the dipole-allowed spectrum, as shown in Figure 5.3. The wavelength of the lattice laser can therefore be scanned while measuring the strength of the Rabi-oscillation signal after the ODF pulse to measure the spectral lines. As the molecular state is unperturbed by the lattice laser, the signal can be obtained to the desired statistical precision limited by the state or chemical lifetime of the molecule ³.

In Ref. [145], we used the ODF detection scheme without the sign information to perform spectroscopy on the $R_{11}(1/2)$ line of the $X^2\Sigma_g^+(v = 0) \rightarrow A^2\Pi_u(v = 2)$ transition from the rotational ground state ⁴. The internal state of the molecule was prepared by rotationally selective ionization in the $N = 0$ state where the difference in the ac-Stark shift and detuning between different Zeeman and Hyperfine states can be neglected. The lattice detuning was chosen such that the $N = 0$ state could be detected with $> 99\%$ fidelity. The wavelength was tuned across the resonance and a center frequency of $f_0 = 380.7011(2)$ THz was inferred.

³Close to resonance the scattering lifetime due to the state-readout laser will be shorter and may limit the achievable spectral resolution. An alternative spectroscopic signal can then be obtained by measuring the average scattering lifetime as a function of the wavelength of the lattice laser.

⁴The main authors of this work are *Mudit Sinhal* and *Ziv Meir*.

5.4.4 Tracing reactions and inelastic scattering events

Another useful application of the phase-sensitive state detection method is to trace state-sensitive chemical reactions and scattering events on the single molecule level. As we have seen in Section 5.4.1, the phase-detection method can distinguish many initial states in a single measurement. A reaction experiment can therefore be simultaneously sensitive to several initial states at once. With a carefully chosen lattice wavelength, the final states can also, in principle, be determined. This allows state-to-state sensitive single-molecule reactions at ultra-cold temperatures.

As an example, we implement a reaction experiment to observe an N_2^+ molecule in a determined state react with H_2 background gas to form N_2H^+ . The result of such an experiment is presented in Figure 5.11a-b. An N_2^+ molecule was identified in the $N = 4$, $J = 7/2$ spin-rotational state. The molecule reacted with background gas and turned into N_2H^+ . The change of the Rabi-oscillation signal indicated a possible change of the chemical composition of the molecule which was then verified by mass spectrometry. In order to obtain the ac-Stark shift from the product, N_2H^+ , the frequency difference between the lattice beams, Δf , was adjusted to match the new COM frequency $f_{COM}^{SP}(N_2H^+) = 690$ kHz.

The energy-level structure of N_2H^+ is not sufficiently well known to identify the molecular quantum state in the reaction product. However, the phase information indicates that the lattice beams were red detuned from the dominant resonance. This experiment exemplifies the possibility to perform state-to-state chemical reaction experiments involving diatomic and polyatomic species using this method⁵.

In a similar manner, inelastic scattering events, e.g. due to collisions or photon scattering, can also be traced state-selectively in a single molecule. Figure 5.11c-d shows the results of such an experiment. An N_2^+ ion was identified in the $N = 6$, $J = 11/2$ spin-rotational state. The molecule then experienced a quantum jump to a different rotational state as is apparent by the change in the amplitude and phase of the Rabi-oscillation signal. The change of state could be caused either by an inelastic collision with a

⁵This experiment also represents, to the best of our knowledge, the first experiment on a single trapped polyatomic molecule cooled to the ground state of an ion trap.

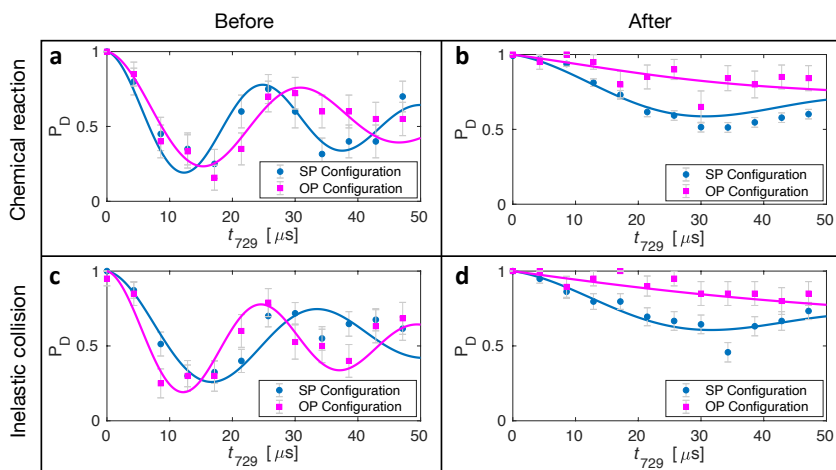


Fig. 5.11. Tracing molecular states during inelastic processes. State dynamics of two molecules (experiment No. “1” and “2” in Figure 5.10) probed by the present SP/OP protocol under a chemical reaction (a \rightarrow b) and a quantum jump (c \rightarrow d). **a \rightarrow b):** An N_2^+ molecule in the $N = 4, J = 7/2$ state reacts with a background gas H_2 molecule and converts into N_2H^+ . **c \rightarrow d)** An N_2^+ molecule in $N = 6, J = 11/2$ changes its state due to an inelastic collision or photon scattering. Error bars represent 1σ binomial uncertainties.

background-gas molecule or by the scattering of a photon from the lattice laser. The sign of the ac-Stark shift is flipped after the scattering which suggests that the molecule underwent a rotational-state change.

In the experiments presented thus far, the sequence of cooling and detection took ~ 15 ms, dominated by the sideband-cooling sequence, and was typically scanned with 10 different Rabi-times, t_{729} , and repeated 20 times for statistics. The interrogation time for a high-fidelity state identification is therefore on the order of a few seconds. In the homonuclear diatomic molecule where all states in the electronic ground state are long-lived this relatively long interrogation time poses no problem. This detection time could, however, limit the usefulness of this method for polar molecules where rovibrational states typically have shorter radiative lifetimes. This can also pose a problem in a state-to-state sensitive reaction experiment in which the product states are short lived or if interaction with black-body radiation shuffles the state populations. The interrogation time can be reduced by carefully choosing the lattice parameters to maximize the signal and reduce the averaging time. The sideband-cooling sequence can also be shortened, as described in Chapter 4. Moving the experiment to a cryogenic environment would increase the interrogation time for systems limited by BBR reshuffling.

5.4.5 Partial state readout

All the experiments presented thus far rely on a prior knowledge of the strengths and positions of the molecular transitions to positively identify specific states of a molecule by comparing the experimentally obtained ac-Stark shift to theory. In some molecules, however, this information is not available or sufficiently accurate for state determination. Here we propose and demonstrate here an adaption of the detection method for a partial state readout [153] for the common situation in which only the frequencies of the transitions are known, e.g., from a prediction based on known spectroscopic constants. We will show how this method can be used to simultaneously exclude a large subset of molecular states and provide a nondestructive spectroscopic signal, e.g., for vibrational spectroscopy from a range of different rotational states.

An example of this method is given for N_2^+ . In Figure 5.12 we show the positions of all spectral lines which belong to the $X^2\Sigma_g^+(v=0) \rightarrow A^2\Pi_u(v'=2)$ transitions up to $N=6$. A lattice-laser wavelength larger than 789.4 nm (dashed line) is red detuned with respect to all transitions with $N \leq 4$. Therefore, detecting a blue detuning in the SP/OP experiment at this wavelength excludes this entire manifold regardless of its substructure or strengths. Figure 5.9b shows a demonstration this partial state readout. Here, a lattice wavelength of 789.71 nm was used and a stronger OP than SP signal was detected which implies that the lattice was blue detuned of the molecular resonance. In this molecule we can therefore exclude all states with rotational quantum number $N \leq 4$.

This protocol can also be used as a non-destructive readout of spectroscopic excitations when exciting from a partially known initial state, e.g., $N \leq 4$ ($v=0$) to a long-lived excited state with a known detuning with respect to the lattice such as the $X^2\Sigma_g^+(v'=1)$ ground state. At 789.7 nm, with respect to the valence electron, the lattice laser is blue detuned from the closest transitions in ($v'=1$) and one can detect a successful spectroscopic excitation from any state $N \leq 4$ as a change in the detuning (i.e. the sign of the ac-Stark shift) even with no available information about the hyperfine or Zeeman structure of either upper or lower states or the transition strengths ⁶.

In this detection scheme only the sign information is used for state detection and therefore the amplitude information encoded in the frequency and contrast of the Rabi-oscillation signal can be disregarded. Therefore, by choosing a suitable pulse length for the Ca^+ probe laser, t_{729} , the detection time can be reduced to a fraction of the detection time for the state determination described in Section 5.4.1, as we need only find the strongest of the SP and OP configurations. We typically use 10-20 different probe times to obtain a full Rabi-oscillation signal and the state-detection time, which is on the order of 1 s, can thus be reduced by an order of magnitude.

⁶In this estimation, as a simplification to illustrate the method, we have neglected the core polarizability of N_2^+ which, when included, will shift the lattice laser wavelength which distinguishes the lower and upper states. Including the core contribution, the lattice laser wavelength which distinguishes the $v=0$ and $v=1$ occurs at around 804 nm.

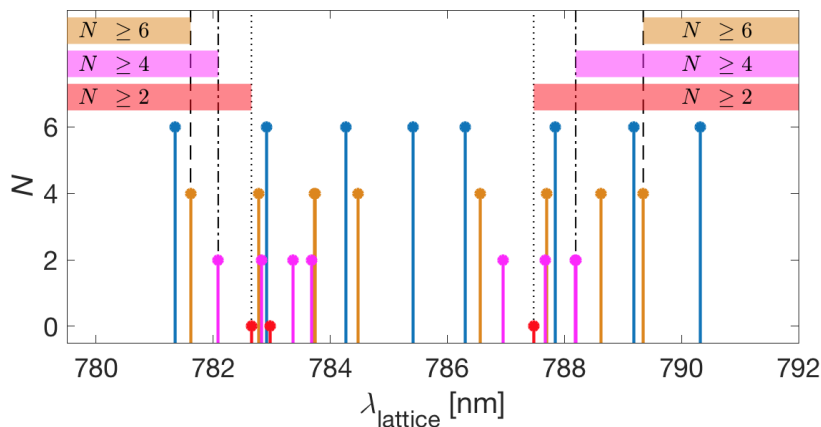


Fig. 5.12. Stick spectrum showing the positions of the allowed P, Q, and R transitions of the $X^2\Sigma_g^+(v=0) \rightarrow A^2\Pi_u(v'=2)$ band of N_2^+ originating from the rotational levels $N = 0, 2, 4, 6$. A subset of these states can be excluded by determining the effective detuning at specific lattice wavelengths using an SP/OP experiment. The dotted, dash-dotted and dashed lines show the lattice wavelengths that enable the exclusion of rotational states $N = 0$, $N \leq 2$ and $N \leq 4$ respectively. The detuning can be chosen either blue of the transitions (782.6, 782.1 and 781.6 nm to exclude $N = 0$, $N \leq 2$ and $N \leq 4$ respectively) or red (787.5, 788.2, and 789.4 nm to exclude $N = 0$, $N \leq 2$ and $N \leq 4$). By choosing the detuning opposite to the detuning of an excited state of interest, the initial and final states are easily distinguishable in an SP/OP test with no available information about the hyperfine or Zeeman structure of either upper or lower states or the specific transition strengths.

5.5 Summary

In this chapter we have described a new method for detecting the state of a single molecule in a long-lived internal state. The ac-Stark shift induced on the atomic and molecular ions were estimated theoretically. The shift on N_2^+ shows great complexity and state determination based on the amplitude of the induced coherent motion alone is unfeasible in most cases. By using Ca^+ as a reference, the phase of the force on the molecule is obtained in an interferometric measurement.

This method was simulated numerically by solving the equations of motions and the optimum two-ion distance for phase determination was determined. The optical dipole force was calibrated through a 'quantum simulation' in a two-ion $Ca^+-N_2H^+$ experiment. We have verified experimentally how this method can be used to distinguish between spin-rotational levels in a complex region of the spectrum non-destructively. We have also shown the usefulness of the present method for dipole-allowed non-demolition spectroscopy and for tracing the states involved in reactions and inelastic scattering events. Finally, we have presented a method for 'partial state readout', which can be used for detecting spectroscopic excitation, which relies only on the transition frequencies and not on the strength of the induced force.

Conclusions and Outlook

” *We came whirling out of nothingness
scattering stars like dust*

— Rumi

In this thesis, we have described the theory and experimental implementation of a single-molecule experiment for a homonuclear diatomic molecule, N_2^+ . Theoretically, we found N_2^+ to be a suitable system for a test of a possible time variation of the proton-to-electron mass ratio, for a noise-insensitive clock-standard in a wide range of frequencies and for a stable qubit. The implementation of such experiments are in development. In this thesis several new techniques were introduced to reach these goals. The detection of the internal states of a ground-state-cooled single N_2^+ molecule in Chapter 5, indicates that all the prerequisites listed in Chapter 1 for coherent control of a single molecule have been accomplished. We will now briefly discuss each of these prerequisites.

- **State initialization:** We may initialize the molecule in a specific hyperfine and Zeeman state through rotational state-selective ionization in combination with the projective or probabilistic state preparation described in Section 5.4.2. In practice, however, as the loading, initial cooling of N_2^+ and subsequent reduction of Ca^+ from the trap takes 1 minute or more, the probabilistic loading into a specific Zeeman state is likely associated with a low duty cycle. The interrogation time may be limited by inelastic collisions with background gas, chemical reactions or a leakage into an inaccessible state by off-resonant scattering. Therefore, in order to reach the precision of state-of-the-art clock experiments, a reduced chamber pressure is desirable for a longer chemical and collisional lifetime. A faster

initialization can be achieved by hyperfine and Zeeman-selective ionization using narrow-linewidth ionization lasers. Alternatively, in order to reduce the number of possible initial states, the $^{15}\text{N}_2^+$ isotope may be used as it is free from hyperfine structure.

- **Cooling:** The sympathetic ground-state cooling of a single N_2^+ ion using a single Ca^+ ion was shown, in Section 4.3, to be straightforward once the ground-state cooling of a single Ca^+ ion was implemented. The length of the sideband-cooling sequence, while short in comparison with a probe pulse designed for precision measurements, adds up to a significant amount of time after many repetitions of cooling and ODF detection to obtain statistics. This time can be reduced by an initial continuous sideband-cooling pulse or an initial sub-Doppler-cooling sequence, e.g. by sympathetic EIT cooling [154]. Using the new mm-scale trap, we found a low heating rate suitable for long probe times, as presented in Section 4.3.3.
- **Probe laser:** While the addition of a probe laser is no more challenging for the molecular ion than in the atomic case, the molecule may scatter to many more states outside the bandwidth of this source. The state-readout laser may be used to reshuffle, e.g., Zeeman and hyperfine levels but not vibrational levels, as discussed in Section 3.3.5. The initialization of a new molecule adds significant time to the duty cycle and should be avoided where possible. We therefore find that the addition of two Raman beams derived from a frequency comb, while adding significant experimental overhead, may be worthwhile as it serves as a stable multi-purpose molecular drive for both vibrations and rotations. Such a system can be used for a controlled initialization, probe pulse and as an auxiliary detection pulse in the molecular ion [82].
- **State detection:** The state-detection scheme, described in Chapter 5, is suitable for detecting states with a long lifetime such as the rovibrational lines of a homonuclear diatomic molecule. We have shown that the pulse time of this detection, which takes on the order of seconds for the data presented in Section 5.4, can be reduced by an order of magnitude by carefully choosing the pulse time of the ODF pulse as well as the Rabi-thermometry pulse. The detection time is then insignificant compared to the probe pulse.

Thus we find that the remaining challenges in the present implementation of a single-molecule precision experiment are the duty cycle and the leakage of the molecular state into dark states. With the increased availability of stable frequency combs, these challenges are expected to be overcome in the foreseeable future and the single-molecule experiments may become an indispensable tool for fundamental and applied physics.

In the field of quantum computing, a good duty cycle and coherence time has been shown with atomic ions with significantly less experimental overhead than required by the present single-molecule experiment. It is therefore likely that for most applications in quantum computing the molecules will not play a prominent role with a possible exception for certain quantum simulations which utilize the full complexity of the rovibrational manifold.

Standard Results from Spherical Tensor Algebra

In this appendix we list some of the useful results from spherical tensor algebra from *Brown & Carrington* [42] and *R. Zare*[43]. We refer the reader to these great texts for the derivation of these results and for further details.

An irreducible spherical tensor of rank k is denoted, $T_p^k(\mathbf{x})$, where p specifies a specific tensor component $-k \leq p \leq k$. The spherical tensor can be defined by its transformation properties under a generalized rotation,

$$T_p^k(\mathbf{x}) = \sum_p D_{p'p}^{(k)}(\omega) T_{p'}^k(\mathbf{x}), \quad (\text{A.1})$$

where $D_{p'p}^{(k)}(\omega)$ is an irreducible representation of the rotation group or 'rotation matrix element' of rank k . Here, ω represents the Euler angles which in three dimensions are $\omega = (\phi, \theta, \chi)$. This equation can therefore be used to transform between the space-fixed (subscript index p) and molecule fixed (subscript index q) coordinate systems when the origin of both systems are at the center of mass of the molecule.

The tensor product of two such tensors $T_{p_1}^{k_1}(\mathbf{x}) \times T_{p_2}^{k_2}(\mathbf{y})$ is defined as,

$$W_{p_{12}}^{k_{12}}(k_1, k_2) = \sum_{p_1} T_{p_1}^{k_1}(\mathbf{x}) T_{p_{12}-p_1}^{k_2}(\mathbf{y}) (-1)^{-k_1+k_2-p_{12}} \\ \times (2k_{12} + 1)^{1/2} \begin{pmatrix} k_1 & k_2 & k_{12} \\ p_1 & p_{12} - p_1 & -p_{12} \end{pmatrix}, \quad (\text{A.2})$$

and produces another tensor of rank $|k_1 - k_2| \leq k_{12} \leq |k_1 + k_2|$. A scalar quantity can be produced by two tensors of the same rank $k_1 = k_2$ by choosing $k_{12} = p_{12} = 0$ in the tensor product,

$$T^{k_1}(\mathbf{x}) \cdot T^{k_2}(\mathbf{y}) = \sum_p (-1)^p T_p^{k_1}(\mathbf{x}) T_{-p}^{k_2}(\mathbf{y}). \quad (\text{A.3})$$

The product of two first-rank rotation matrices may be written as a single rotation by,

$$D_{p'_1 p_1}^{k_1}(\omega) D_{p'_2 p_2}^{k_2}(\omega) = \sum_{k_{12}} (2k_{12} + 1) \begin{pmatrix} k_1 & k_2 & k_{12} \\ p'_1 & p'_2 & p'_{12} \end{pmatrix} \begin{pmatrix} k_1 & k_2 & k_{12} \\ p_1 & p_2 & p_{12} \end{pmatrix} D_{p'_{12} p_{12}}^{k_{12}}(\omega)^*. \quad (\text{A.4})$$

A rotation matrix operator acting on the reduced rotational basis states $|N, \Lambda\rangle$ leads to,

$$\begin{aligned} \langle N', \Lambda' | D_{q \Lambda}^k(\omega) | N, \Lambda \rangle &= \\ (-1)^{N' - \Lambda'} \begin{pmatrix} N' & k & N \\ -\Lambda' & q & \Lambda \end{pmatrix} \sqrt{(2N' + 1)(2N + 1)}. \end{aligned} \quad (\text{A.5})$$

For the evaluation of spherical tensor operators acting upon a general angular-momentum state $|J, M_J\rangle$ with quantum number J and projection M_J , we present here a list of useful standard results. The Wigner-Eckart (W.E.) theorem allows us to reduce the dependence on projection quantum-numbers,

$$\begin{aligned} \langle J', M'_J | T_p^k(\mathbf{x}) | J, M_J \rangle &= \\ (-1)^{J' - M'_J} \begin{pmatrix} J' & k & J \\ -M'_J & p & M_J \end{pmatrix} \langle J' | T_{\dot{p}}^k | J \rangle. \end{aligned} \quad (\text{A.6})$$

Here, the subscript dot in $T_{\dot{p}}^k$ suggests that the tensor operator no longer depends on the space projection, p .

A first rank spherical tensor operator associated with the eigenvalue J acting on the pure basis states $|J\rangle$ gives,

$$\langle J' | T^1(\mathbf{J}) | J \rangle = \delta_{J' J} \sqrt{J(J+1)(2J+1)}, \quad (\text{A.7})$$

where the $\delta_{J',J}$ appears due to the orthogonality of the zero-order basis-states $\langle J'|J \rangle$. When two angular momenta couple to form a total angular momentum $J_1 + J_2 = J$ the basis-states can be written in a coupled representation given by,

$$\begin{aligned} |J, M_J\rangle &= \sum_{M_1, M_2} (-1)^{M_1 - M_2 + M_J} \sqrt{2J + 1} \\ &\times \begin{pmatrix} J_1 & J_2 & J \\ M_1 & M_2 & -M_J \end{pmatrix} |J_1, M_1\rangle |J_2, M_2\rangle. \end{aligned} \quad (\text{A.8})$$

A standard result allows us to evaluate a spherical tensor operator $T^1(\mathbf{J}_1)$ that only acts on the first part of a coupled scheme, $J_1 + J_2 = J$, without manually decoupling them and reducing their projection quantum numbers,

$$\begin{aligned} \langle J'_1, J'_2, J' || T^k(\mathbf{J}_1) || J_1, J_2, J \rangle &= \delta_{J'_2 J_2} (-1)^{J + J'_1 + J'_2 + k} \\ &\times \sqrt{(2J' + 1)(2J + 1)} \begin{Bmatrix} J_1 & J & J_2 \\ J' & J'_1 & k \end{Bmatrix} \langle J'_1 || T^k(\mathbf{J}_1) || J_1 \rangle. \end{aligned} \quad (\text{A.9})$$

When the operator $T^1(\mathbf{J}_2)$ is instead acting on the second part of the coupled system $J_1 + J_2 = J$, we have,

$$\begin{aligned} \langle J'_1, J'_2, J' || T^k(\mathbf{J}_2) || J_1, J_2, J \rangle &= \delta_{J'_1 J_1} (-1)^{J' + J'_1 + J_2 + k} \\ &\times \sqrt{(2J' + 1)(2J + 1)} \begin{Bmatrix} J_2 & J & J'_1 \\ J' & J'_2 & k \end{Bmatrix} \langle J'_2 || T^k(\mathbf{J}_2) || J_2 \rangle. \end{aligned} \quad (\text{A.10})$$

A tensor-product $W^k(k_1, k_2) = T_1^{k_1}(\mathbf{J}_1) \times T_2^{k_2}(\mathbf{J}_2)$ that acts on both parts of the coupled system produces,

$$\begin{aligned} \langle J'_1, J'_2, J' || W^k(k_1, k_2) || J_1, J_2, J \rangle &= \\ &\sqrt{(2J' + 1)(2J + 1)(2k + 1)} \\ &\times \begin{Bmatrix} J' & J & k \\ J'_1 & J_1 & k_1 \\ J'_2 & J_2 & k_2 \end{Bmatrix} \langle J'_1 || T^{k_1}(\mathbf{J}_1) || J_1 \rangle \langle J'_2 || T^{k_2}(\mathbf{J}_2) || J_2 \rangle. \end{aligned} \quad (\text{A.11})$$

It is sometimes useful to write the Hund's case (*b*) basis-states as a superposition of Hund's case (*a*) bases using the relation,

$$|N\Lambda, S, J\rangle = \sum_{\Sigma=-S}^{\Sigma=+S} (-1)^{N-S+\Omega} \sqrt{2N+1} \\ \times \begin{pmatrix} J & S & N \\ \Omega & -\Sigma & -\Lambda \end{pmatrix} |S\Sigma; J\Omega\Lambda\rangle. \quad (\text{A.12})$$

A Wigner 6j symbol can be written as a product of four Wigner 3j symbols,

$$\left\{ \begin{matrix} a & b & e \\ d & c & f \end{matrix} \right\} = \sum_{\alpha\beta\gamma\delta\epsilon\phi} (-1)^{d+c+f+\delta+\gamma+\phi} \\ \times \begin{pmatrix} a & b & e \\ \alpha & \beta & \epsilon \end{pmatrix} \begin{pmatrix} a & c & f \\ \alpha & \gamma & -\phi \end{pmatrix} \begin{pmatrix} d & b & f \\ -\delta & \beta & \phi \end{pmatrix} \begin{pmatrix} d & c & e \\ \delta & -\gamma & \epsilon \end{pmatrix}. \quad (\text{A.13})$$

By multiplying the equation above by a Wigner 3j symbol on the left side we obtain another useful relation,

$$\begin{pmatrix} a & b & e \\ \alpha & \beta & \epsilon \end{pmatrix} \left\{ \begin{matrix} a & b & e \\ d & c & f \end{matrix} \right\} = \sum_{\alpha\beta\gamma\delta\epsilon\phi} (-1)^{d+c+f+\delta+\gamma+\phi} \\ \times \begin{pmatrix} a & c & f \\ \alpha & \gamma & -\phi \end{pmatrix} \begin{pmatrix} d & b & f \\ -\delta & \beta & \phi \end{pmatrix} \begin{pmatrix} d & c & e \\ \delta & -\gamma & \epsilon \end{pmatrix}. \quad (\text{A.14})$$

Alternative Derivations of Matrix Expressions

B.1 The spin-Zeeman interaction in Hund's case (a).

Here, we will derive the matrix element of the electron-spin Zeeman interaction in a Hund's case (a_{β_J}) basis which is a useful basis when the electron spin couples strongly to the molecular axis, e.g., by spin-orbit coupling as in the $A^2\Pi_u$ state of $^{14}\text{N}_2^+$. The Hund's case (a_{β_J}) basis states are labelled $|\eta, \Lambda, S, \Sigma, J, \Omega, I, F, M_F\rangle$. The electron spin S is now coupled to the internuclear axis with projection quantum number Σ and is therefore readily evaluated in the molecule-fixed coordinates.

We begin as we did before by writing the operator in spherical-tensor notation $\mathbf{B} \cdot \mathbf{S} = T^1(\mathbf{B})T^1(\mathbf{S})$ and make use of the Wigner-Eckart theorem of Eq. (A.6) to reduce the space-projection quantum number from the matrix element,

$$\begin{aligned} \langle \eta, \Lambda, S', \Sigma', J', \Omega', I', F', M'_F | \mathbf{B} \cdot \mathbf{S} | \eta, \Lambda, S, \Sigma, J, \Omega, I, F, M_F \rangle = \\ T_{-p'}^1(\mathbf{B})(-1)^{-p'}(-1)^{F'-M'_F} \begin{pmatrix} F' & 1 & F' \\ -M'_F & p' & M_F \end{pmatrix} \\ \langle \eta, \Lambda, S', \Sigma', J', \Omega', I', F' | T_{p'}^1(\mathbf{S}) | \eta, \Lambda, S, \Sigma, J, \Omega, I, F \rangle. \end{aligned} \quad (\text{B.1})$$

We need to decouple the wavefunction from the nuclear spin, i.e., from the total angular momentum F using Eq. (A.9),

$$\begin{aligned} \langle \eta, \Lambda, S', \Sigma', J', \Omega', I', F' | T_{p'}^1(\mathbf{S}) | \eta, \Lambda, S, \Sigma, J, \Omega, I, F \rangle = \\ \delta_{II'} (-1)^{F+J'+I'+1} \sqrt{(2F'+1)(2F+1)} \begin{Bmatrix} J' & F' & I \\ F & J & 1 \end{Bmatrix} \\ \langle \eta, \Lambda, S', \Sigma', J', \Omega' | T^1(\mathbf{S}) | \eta, \Lambda, S, \Sigma, J, \Omega \rangle. \end{aligned} \quad (\text{B.2})$$

The rotation between our two coordinate systems depends on the physical coordinates of the molecule and the Wigner rotation matrix $D_{pq}^1(\omega)$ therefore acts on the rotational wavefunction of the molecule. It must therefore be introduced before we can proceed. The transformation between the space- and molecule-fixed coordinates in spherical tensor formalism is straightforward and the transformation is simply given by Eq. (A.1),

$$T^1(S) = \sum_q D_{.q}^1(\omega) T_q^1(S). \quad (\text{B.3})$$

Indeed, this is the very definition of a spherical tensor i.e. tensors with these transformation properties under rotations. We can now apply the rotation operator to our rotational basis functions using another standard result from spherical tensor algebra. Using Eq. (A.5) we obtain,

$$\begin{aligned} \langle \eta, \Lambda, S', \Sigma', J', \Omega' | T^1(\mathbf{S}) | \eta, \Lambda, S, \Sigma, J, \Omega \rangle = \\ \sum_q (-1)^{J'-\Omega'} \sqrt{(2J'+1)(2J+1)} \begin{pmatrix} J' & 1 & J \\ -\Omega' & q & \Omega \end{pmatrix} \\ \langle S', \Sigma' | T_q^1(\mathbf{S}) | S, \Sigma \rangle. \end{aligned} \quad (\text{B.4})$$

We apply the Wigner-Eckart theorem once more to reduce the projection quantum number Σ ,

$$\begin{aligned} \langle S', \Sigma' | T_q^1(\mathbf{S}) | S, \Sigma \rangle \\ = (-1)^{S'-\Sigma'} \begin{pmatrix} S' & 1 & S \\ -\Sigma' & q & \Sigma \end{pmatrix} \langle S' | T^1(\mathbf{S}) | S \rangle. \end{aligned} \quad (\text{B.5})$$

Finally putting together Equations (B.1), (B.2), (B.4) and (B.5) with $p' = 0$ we obtain,

$$\begin{aligned}
& \langle \eta, \Lambda, S', \Sigma', J', \Omega', I', F', M'_F | \mathbf{B} \cdot \mathbf{S} | \eta, \Lambda, S, \Sigma, J, \Omega, I, F, M_F \rangle = \\
& \quad B_Z \delta_{SS'} \delta_{II'} (-1)^{F'+F-M'_F+2J'+I-\Omega'+S'-\Sigma'+1} \\
& \quad \times \sqrt{(2F'+1)(2F+1)(2J'+1)(2J+1)S(S+1)(2S+1)} \\
& \quad \times \begin{pmatrix} F' & 1 & F \\ -M'_F & 0 & M_F \end{pmatrix} \begin{Bmatrix} J' & F' & I \\ F & J & 1 \end{Bmatrix} \sum_q \begin{pmatrix} J' & 1 & J \\ -\Omega' & q & \Omega \end{pmatrix} \begin{pmatrix} S' & 1 & S \\ -\Sigma' & q & \Sigma \end{pmatrix}
\end{aligned} \tag{B.6}$$

This expression has nonzero elements for $J' = J$ and $F' = F$ and confirms the expression derived in Ref. [42].

B.2 The spin-Zeeman interaction in a case (b) \rightarrow (a) transformation

Sometimes, when an interaction is more naturally described in different quantum numbers it can be useful to transform between Hund's case (a) and (b) bases for deriving the Hamiltonian matrix elements. This may be the case for an electronic state best described in an intermediate Hund's case (a) and (b) basis. We now illustrate this technique by expressing the Hund's case (b) basis as a superposition of Hund's case (a) bases and re-derive the electron-spin Zeeman term and show that this is expression is equivalent to the one derived in Section 2.1.3.

The transformation between a Hund's case (a) and (b) basis is given by Eq. (A.12) as,

$$|N\Lambda, S, J\rangle = \sum_{\Sigma=-S}^{\Sigma=+S} (-1)^{N-S+\Omega} \sqrt{2N+1} \begin{pmatrix} J & S & N \\ \Omega & -\Sigma & -\Lambda \end{pmatrix} |S\Sigma; \Lambda J\Omega\rangle. \tag{B.7}$$

By applying this transformation for both our bra and ket, we can write the electron spin-Zeeman interaction as,

$$\begin{aligned}
& \langle v', N', S', J', I', F', M'_F | \mathbf{B} \cdot \mathbf{S} | v, N, S, J, I, F, M_F \rangle \\
&= T_{-p'}^1(\mathbf{B}) (-1)^{p'} (-1)^{F'-M'_F} \begin{pmatrix} F' & 1 & F \\ -M'_F & p' & M_F \end{pmatrix} \\
&\times (-1)^{N+N'-S-S'} \sqrt{(2N'+1)(2N+1)} \\
&\times \sum_{\Sigma'=-S'}^{+S'} \sum_{\Sigma=-S}^{+S} (-1)^{\Omega+\Omega'} \begin{pmatrix} J' & S' & N' \\ \Omega' & -\Sigma' & -\Lambda' \end{pmatrix} \begin{pmatrix} J & S & N \\ \Omega & -\Sigma & -\Lambda \end{pmatrix} \\
&\times \langle S' \Sigma' \Lambda' J' \Omega' I' F' | \sum_q D_{\cdot q}^1(\omega)^* T_q^1(S) | S \Sigma \Lambda J \Omega I' F' \rangle, \quad (\text{B.8})
\end{aligned}$$

Here, we have once again applied the W.E. theorem as apparent by the subscript dot in $D_{\cdot q}^1(\omega)$ which suggests that the matrix element is reduced with respect to the space projection p' . As before, we need to decouple the nuclear spin quantum number I from the angular momentum J using Eq. (A.9) and we obtain,

$$\begin{aligned}
& \langle S' \Sigma' \Lambda' J' \Omega' I' F' | \sum_q D_{\cdot q}^1(\omega)^* T_q^1(\mathbf{S}) | S \Sigma \Lambda J \Omega I' F' \rangle = \\
& \delta_{I'I} (-1)^{F+J'+I'+1} \begin{Bmatrix} J & F & I' \\ F' & J' & 1 \end{Bmatrix} \\
& \times \sum_q \langle \Lambda' J' \Omega' | D_{\cdot q}^1(\omega)^* | \Lambda J \Omega \rangle \langle S' \Sigma' | T_q^1(\mathbf{S}) | S, \Sigma \rangle \quad (\text{B.9})
\end{aligned}$$

The uncoupled matrix elements above are given by,

$$\begin{aligned}
& \langle J' \Omega' | D_{\cdot q}^1(\omega)^* | J \Omega \rangle = \quad (\text{B.10}) \\
& (-1)^{J'-\Omega'} \sqrt{(2J'+1)(2J+1)} \begin{pmatrix} J' & 1 & J \\ -\Omega' & q & \Omega \end{pmatrix},
\end{aligned}$$

for the rotational part and the spin part is given as before by,

$$\langle S', \Sigma' | T_q^1(\mathbf{S}) | S, \Sigma \rangle = \delta_{SS'} (-1)^{S-\Sigma'} \begin{pmatrix} S & 1 & S \\ -\Sigma' & q & \Sigma \end{pmatrix} \sqrt{S(S+1)(2S+1)}. \quad (\text{B.11})$$

We put together Equations (B.8), (B.2), (B.10) and (B.11) to form,

$$\begin{aligned}
& \langle N', S', J', I', F', M'_F | \mathbf{B} \cdot \mathbf{S} | N, S, J, I, F, M_F \rangle \\
&= T_{-p'}^1(\mathbf{B}) \delta_{I'I} \delta_{S'S} (-1)^{p'} (-1)^{F' - M'_F + F + 2J' + S' + I' + 1} \\
&\times \sqrt{(2F' + 1)(2F + 1)(2J' + 1)(2J + 1)S(S + 1)(2S + 1)} \\
&\times \begin{pmatrix} F' & 1 & F \\ -M'_F & p' & M_F \end{pmatrix} \begin{Bmatrix} J & F & I' \\ F' & J' & 1 \end{Bmatrix} \\
&\times \sum_{\Sigma' = -S'}^{+S'} \sum_{\Sigma = -S}^{+S} (-1)^{N+N' - S - S' + \Omega + \Omega'} \sqrt{(2N' + 1)(2N + 1)} \\
&\times \begin{pmatrix} J' & S' & N' \\ \Omega' & -\Sigma' & -\Lambda' \end{pmatrix} \begin{pmatrix} J & S & N \\ \Omega & -\Sigma & -\Lambda \end{pmatrix} \begin{pmatrix} J' & 1 & J \\ -\Omega' & q & \Omega \end{pmatrix} \begin{pmatrix} S & 1 & S' \\ -\Sigma' & q & \Sigma \end{pmatrix} \\
& \hspace{15em} \text{(B.12)}
\end{aligned}$$

This expression is different from Eq. (B.6) by the two Wigner 3j symbols containing J, S, N . The equivalence with the expression derived in Hund's case ($b_{\beta, \gamma}$) (Eq. (2.50)) can be shown by relating the four Wigner 3j symbols to a Wigner 6j symbol using the relation from Eq. (A.13),

$$\begin{aligned}
& \delta_{N'N} \begin{Bmatrix} J' & S' & N' \\ S' & J & 1 \end{Bmatrix} \\
&= \sum_{\Sigma' = -S'}^{+S'} \sum_{\Sigma = -S}^{+S} (2N + 1) (-1)^{J' + S' - N' + S + J + 1 - \Omega - \Sigma} \\
&\times \begin{pmatrix} J' & S' & N' \\ \Omega' & -\Sigma' & -\Lambda' \end{pmatrix} \begin{pmatrix} J & S & N \\ \Omega & \Sigma & \Lambda \end{pmatrix} \begin{pmatrix} J' & 1 & J \\ -\Omega' & q & \Omega \end{pmatrix} \begin{pmatrix} S' & 1 & S' \\ -\Sigma' & q & \Sigma \end{pmatrix}. \\
& \hspace{15em} \text{(B.13)}
\end{aligned}$$

The equivalence of the phase factors between Eq. (2.50) and Eq. (B.12) is shown below by noting that $(-1)^{2i} = 1$ for integer i and $(-1)^{2i} = (-1)^{-2i}$ for half integer i 's and thus we have,

$$\begin{aligned}
(-1)^{J' + S' - N' + S + J + 1 - \Omega - \Sigma} &= (-1)^{-\Omega - \Sigma + J' - S' + J - S + 2\Lambda + 1} \\
(-1)^{S' - N' + S} &= (-1)^{-S' - S} \\
(-1)^{2S - N'} &= (-1)^{-2S}. \\
& \hspace{15em} \text{(B.14)}
\end{aligned}$$

Thus we find the phase factor $(-1)^N$ which completes the equivalence with Eq. (2.50). This exercise shall prove useful for evaluating the anisotropic spin-Zeeman term which is more readily evaluated in a Hund's case (a) basis.

B.3 The rotational Zeeman interaction in the uncoupled basis

Here, we shall derive the matrix expressions for the Hamiltonian describing the interaction of the rotational magnetic moment coupling to an external magnetic field. To do so, we shall use the uncoupled basis sets $|N, M_N\rangle|S, M_S\rangle$ in which the projection quantum numbers of each interaction is separately defined. Such a form is useful in a strong magnetic field where each magnetic moment aligns with the external field. We recall the relation between the coupled and the uncoupled basis states from Eq. (A.8),

$$|N, S, J, I, F, M_F\rangle = \sum_{M_J, M_I} (-1)^{J-I+M_F} \sqrt{2F+1} \begin{pmatrix} J & I & F \\ M_J & M_I & -M_F \end{pmatrix} |N, S, J, M_J\rangle |I, M_I\rangle \quad (\text{B.15})$$

We can further decouple the angular momentum $|J, M_J\rangle$ in terms of its components $|N, M_N\rangle|S, M_S\rangle$,

$$|N, S, J, M_J\rangle = \sum_{M_N, M_S} (-1)^{N-S+M_J} \sqrt{2J+1} \begin{pmatrix} N & S & J \\ M_N & M_S & -M_J \end{pmatrix} \times |N, M_N\rangle |S, M_S\rangle. \quad (\text{B.16})$$

Our Hamiltonian expression to evaluate is then,

$$\begin{aligned}
& \langle N', S', J', I', F', M'_F | \mathbf{B} \cdot \mathbf{N} | N, S, J, I, F, M_F \rangle \\
&= B_Z \sum_{M'_J, M'_I, M_J, M_I} (-1)^{J'+J-I'-I+M'_F+M_F} \sqrt{(2F'+1)(2F+1)} \\
&\times \begin{pmatrix} J' & I' & F' \\ M'_J & M'_I & -M'_F \end{pmatrix} \begin{pmatrix} J & I & F \\ M_J & M_I & -M_F \end{pmatrix} \\
&\times \langle N', S', J', M'_J | T^1(\mathbf{N}) | N, S, J, M_J \rangle \langle I' M'_I | I M_I \rangle. \tag{B.17}
\end{aligned}$$

The overlap of the nuclear-spin bases $\langle I' M'_I | I M_I \rangle$ lead to the conditions $\delta_{I'I}$ and $\delta_{M'_I, M_I}$. We proceed to write the angular momentum state $|J, M_J\rangle$ in terms of its components $|N, M_N\rangle |S, M_S\rangle$ which produces,

$$\begin{aligned}
& \langle N', S', J', M'_J | T^1(\mathbf{N}) | N, S, J, M_J \rangle \\
&= \sum_{M'_N, M'_S, M_N, M_S} (-1)^{N'+N-S'-S+M'_J+M_J} \sqrt{(2J'+1)(2J+1)} \\
&\times \begin{pmatrix} N' & S' & J' \\ M'_N & M'_S & -M'_J \end{pmatrix} \begin{pmatrix} N & S & J \\ M_N & M_S & -M_J \end{pmatrix} \\
&\times \langle N', M'_N | T^1_p(\mathbf{N}) | N, M_N \rangle \langle S', M'_S | S, M_S \rangle. \tag{B.18}
\end{aligned}$$

The overlap of the spin bases $\langle S', M'_S | S, M_S \rangle$ lead to the selection rules $\delta_{S'S} \delta_{M'_S, M_S}$ and the rotational matrix element is evaluated using the Wigner Eckart theorem of Eq. (A.6) and the eigenvalue relation of Eq. (A.7) as,

$$\begin{aligned}
\langle N', M'_N | T^1_p(\mathbf{N}) | N, M_N \rangle &= (-1)^{N'-M'_N} \begin{pmatrix} N' & 1 & N \\ -M'_N & 0 & M_N \end{pmatrix} \\
&\times \delta_{N'N} \sqrt{N(N+1)(2N+1)}. \tag{B.19}
\end{aligned}$$

Finally, putting together Equations (B.17), (B.18) and (B.19) we obtain,

$$\begin{aligned}
& \langle N', S', J', I', F', M'_F | \mathbf{B} \cdot \mathbf{N} | N, S, J, I, F, M_F \rangle \\
&= B_Z \delta_{S'S} \delta_{I'I} \delta_{N'N} (-1)^{J'+J-2I+N'+N-2S+J+J'+N'+N+1} \\
&\times \sqrt{(2F'+1)(2F+1)(2J'+1)(2J+1)N(N+1)(2N+1)} \\
&\times \sum_{M'_J, M_J, M'_I, M_I} \delta_{M_I M'_I} (-1)^{M'_F+M_F+M'_J+M_J} \\
&\times \begin{pmatrix} J' & I' & F' \\ M'_J & M'_I & -M'_F \end{pmatrix} \begin{pmatrix} J & I & F \\ M_J & M_I & -M_F \end{pmatrix} \\
&\times \sum_{M'_N, M_S, M'_N, M_S} \delta_{M'_S M_S} (-1)^{M'_N} \\
&\times \begin{pmatrix} N' & S' & J' \\ M'_N & M'_S & -M'_J \end{pmatrix} \begin{pmatrix} N & S & J \\ M_N & M_S & -M_N \end{pmatrix} \begin{pmatrix} N' & N & 1 \\ -M'_N & M_N & 0 \end{pmatrix}.
\end{aligned} \tag{B.20}$$

We show the equivalence of Eq. (B.20) with the expression derived in the coupled basis (Eq. (2.57)) by using a relation between the Wigner 3j and Wigner 6j symbols. First, we use the relation Eq. (A.14) to write the sum over the last three 3j symbols as the product of a 3j and 6j symbol,

$$\begin{aligned}
& \sum_{\text{all } M_i M'_i} (-1)^{J'+J+N'+N-S'+S-M'_J-M_N} \\
&\times \begin{pmatrix} N' & S' & J' \\ M'_N & M'_S & -M'_J \end{pmatrix} \begin{pmatrix} N & S & J \\ M_N & M_S & -M_N \end{pmatrix} \begin{pmatrix} N' & N & 1 \\ -M'_N & M_N & 0 \end{pmatrix} \\
&= \begin{pmatrix} J' & 1 & J \\ -M'_J & 0 & M_J \end{pmatrix} \left\{ \begin{matrix} J' & N' & S' \\ N & J & 1 \end{matrix} \right\}.
\end{aligned} \tag{B.21}$$

Plugging this relation in to the matrix element of Eq. (B.20) gives,

$$\begin{aligned}
& \langle N', S', J', I', F', M'_F | \mathbf{B} \cdot \mathbf{N} | N, S, J, I, F, M_F \rangle = \\
& = B_Z \delta_{S'S} \delta_{I'I} \delta_{N'N} (-1)^{J'+J-2I+N'+N-2S+J+J'+N'+N+1} \\
& \times \sqrt{(2F'+1)(2F+1)(2J'+1)(2J+1)N(N+1)(2N+1)} \\
& \times \sum_{M'_J, M'_I, M'_F} \delta_{M_I M'_I} (-1)^{M'_F + M_F + M'_J + M_J} \\
& \times \begin{pmatrix} J' & I' & F' \\ M'_J & M'_I & -M'_F \end{pmatrix} \begin{pmatrix} J & I & F \\ M_J & M_I & -M_F \end{pmatrix} \\
& \times (-1)^{M'_N} \begin{pmatrix} J' & 1 & J \\ -M'_J & 0 & M_J \end{pmatrix} \begin{Bmatrix} J' & N' & S' \\ N & J & 1 \end{Bmatrix}. \tag{B.22}
\end{aligned}$$

We use the relation from Eq. (A.14) again to show that the remaining three 3j symbols can also be written as the product of a 3j and a 6j symbol using,

$$\begin{aligned}
& \sum_{\text{all } M_i M'_i} (-1)^{F'+F+J'+J-I'+I-M'_F-M_J} \\
& \times \begin{pmatrix} J' & I' & F' \\ M'_J & M'_I & -M'_F \end{pmatrix} \begin{pmatrix} J & I & F \\ M_J & M_I & -M_F \end{pmatrix} \begin{pmatrix} J' & J & 1 \\ -M'_J & M_J & 1 \end{pmatrix} \\
& = (-1)^{J'+J+1} \begin{pmatrix} F' & 1 & F \\ -M'_F & 0 & M_F \end{pmatrix} \begin{Bmatrix} F' & J' & I' \\ J & F & 1 \end{Bmatrix}. \tag{B.23}
\end{aligned}$$

Plugging the above relation into the equation from Eq. B.22 gives,

$$\begin{aligned}
& \langle N', S', J', I', F', M'_F | \mathbf{B} \cdot \mathbf{N} | N, S, J, I, F, M_F \rangle \\
& = \delta_{S'S} \delta_{I'I} \delta_{N'N} (-1)^{J'+J-2I+N'+N-2S+J+J'+N'+N+1} \\
& \times \sqrt{(2F'+1)(2F+1)(2J'+1)(2J+1)N(N+1)(2N+1)} \\
& \times (-1)^{J'+J+1} \begin{pmatrix} F' & 1 & F \\ -M'_F & 0 & M_F \end{pmatrix} \begin{Bmatrix} F' & J' & I' \\ J & F & 1 \end{Bmatrix} \cdot \begin{Bmatrix} J' & N' & S' \\ N & J & 1 \end{Bmatrix}. \tag{B.24}
\end{aligned}$$

The resulting expression is exactly Eq. (2.57).

B.4 The anisotropic spin-Zeeman Hamiltonian in Hund's case (*a*)

Here, we shall use the Hamiltonian form of Eq. (2.69) to find the matrix expression by transforming into a Hund's case (*a*) basis. As this interaction originates from unquenched electronic angular momentum, this term is better suited for a basis where the projection of the electron spin along the molecular axis, Σ , is defined. Using the Hamiltonian form Eq. (2.69), we need only to derive half of the expression, $D_{00}^1(\omega)^* T_{q=0}^1(\mathbf{S})$, with the other half already derived in Eq. (2.50).

We begin by transforming into the Hund's case (*a*) basis using Eq. (A.12),

$$\begin{aligned}
 & \langle N', S', J', I', F, M'_F | D_{00}^1(\omega)^* T_{q=0}^1(\mathbf{S}) | N, S, J, I, F, M_F \rangle \\
 &= (-1)^{F' - M'_F} \begin{pmatrix} F' & 1 & F \\ -M'_F & 0 & M_F \end{pmatrix} \\
 & \times \sum_{q=\pm 1} (-1)^{N+N'-S-S'} \sqrt{(2N'+1)(2N+1)} \\
 & \times \sum_{\Sigma'=-S'}^{+S'} \sum_{\Sigma=-S}^{+S} (-1)^{\Omega+\Omega'} \begin{pmatrix} J' & S' & N' \\ \Omega' & -\Sigma' & -\Lambda' \end{pmatrix} \begin{pmatrix} J & S & N \\ \Omega & -\Sigma & -\Lambda \end{pmatrix} \\
 & \times \langle S', \Sigma'; \Lambda', J', \Omega', I', F' | D_{00}^1(\omega)^* T_0^1(\mathbf{S}) | S, \Sigma; \Lambda, J, \Omega, I, F \rangle. \quad (\text{B.25})
 \end{aligned}$$

We apply Eq. (A.9) to decouple J from I ,

$$\begin{aligned}
 & \langle S', \Sigma'; \Lambda', J', \Omega', I', F' | D_{00}^1(\omega)^* T_0^1(\mathbf{S}) | S, \Sigma; \Lambda, J, \Omega, I, F \rangle \\
 &= \delta_{I'I} (-1)^{F+J'+I'+1} \sqrt{(2F'+1)(2F+1)} \begin{Bmatrix} J & F & I' \\ F' & J & 1 \end{Bmatrix} \\
 & \langle \Lambda', J', \Omega' | D_{00}^1(\omega)^* | \Lambda, J, \Omega \rangle \langle S', \Sigma' | T_0^1(\mathbf{S}) | S, \Sigma \rangle. \quad (\text{B.26})
 \end{aligned}$$

The spin part is then evaluated using the eigenvalue relation, $S_z |S, \Sigma\rangle = \Sigma |S, \Sigma\rangle$,

$$\langle S', \Sigma' | T_0^1(\mathbf{S}) | S, \Sigma \rangle = \langle S', \Sigma' | S_z | S, \Sigma \rangle = \delta_{S'S'} \delta_{\Sigma'\Sigma} \Sigma, \quad (\text{B.27})$$

and the rotational part is evaluated using Eq. (A.5)

$$\begin{aligned} & \langle J'\Omega' | D_{1,0}^1(\omega)^* | J, \Omega \rangle = \\ & (-1)^{J'-\Omega'} \sqrt{(2J'+1)(2J+1)} \begin{pmatrix} J' & 1 & J \\ -\Omega' & 0 & \Omega \end{pmatrix}. \end{aligned} \quad (\text{B.28})$$

By combining the equations (B.25), (B.26), (B.27) and (B.28) we obtain,

$$\begin{aligned} & \langle N', S', J', I', F, M'_F | D_{00}^1(\omega)^* T_{q=0}^1(\mathbf{S}) | N, S, J, I, F, M_F \rangle \\ & = \delta_{I'I} \delta_{S'S} (-1)^{F'-M'_F+F+J'+I'+N+N'-S-S'+1} \\ & \times \sqrt{(2F'+1)(2F+1)(2J'+1)(2J+1)(2N'+1)(2N+1)} \\ & \times \begin{pmatrix} F' & 1 & F \\ -M'_F & 0 & M_F \end{pmatrix} \begin{Bmatrix} J & F & I' \\ F' & J & 1 \end{Bmatrix} \\ & \times \sum_{\Sigma=-S}^{+S} \delta_{\Sigma'\Sigma} (-1)^\Omega \begin{pmatrix} J' & S' & N' \\ \Omega' & -\Sigma' & -\Lambda' \end{pmatrix} \\ & \times \begin{pmatrix} J & S & N \\ \Omega & -\Sigma & -\Lambda \end{pmatrix} \begin{pmatrix} J' & 1 & J \\ -\Omega' & 0 & \Omega \end{pmatrix} \Sigma. \end{aligned} \quad (\text{B.29})$$

B.5 The E1 operator in a combined Hund's case (a) and (b) basis.

Here, we will derive the matrix expression for the electric dipole (E1) operator between the $X^2\Sigma_g^+$ and $A^2\Pi_u$ states in N_2^+1 . This expression will prove useful for estimating the ac-Stark shift induced by the lattice laser at 789 nm. We express the excited $A^2\Pi_u$ state in Hund's case (a_{β_J}) basis-states and the ground $X^2\Sigma_g^+$ state, as before, in a Hund's case (b_{β_J}) basis. The overlap is evaluated by expressing the Hund's case (b) basis in a superposition of Hund's case (a) bases, as we have seen in Sections B.2 and B.4.

As before, we begin by expressing the electric-dipole operator in the spherical-tensor notation, as $T^1(\mu^{(E1)})$. As the laser polarization is defined

¹Here, we follow the derivation by *Mudit Sinhal*.

in the space-fixed axis, the space-fixed operator (subscript p) must be rotated into the molecular frame where the electric dipole moment of the molecule (in the $A^2\Pi_u$ state) is defined. The expression to evaluate is then,

$$\begin{aligned} &\langle \eta', v', \Lambda', S', \Sigma', J', \Omega', I', F', M'_F | T_p^1(\mu) | \eta, v, \Lambda, N, S, J, I, F, M_F \rangle = \\ &\quad (-1)^{F'-M'_F} \begin{pmatrix} F' & 1 & F \\ -M'_F & p & M_F \end{pmatrix} \\ &\quad \times \langle \eta', v', \Lambda', S', \Sigma', J', \Omega', I', F' | T^1(\mu) | \eta, v, \Lambda, N, S, J, I, F \rangle. \end{aligned} \quad (\text{B.30})$$

In this first step, we have applied the Wigner-Eckart theorem from Eq. (A.6). The projection-reduced matrix element in the above equation is further simplified by using Eq. (A.9) for a tensor operator acting on the first part of a coupled system, $J + I = F$,

$$\begin{aligned} &\langle \eta', v', \Lambda', S', \Sigma', J', \Omega', I', F' | T^1(\mu) | \eta, v, \Lambda, N, S, J, I, F \rangle = \\ &\quad \delta_{I'I} (-1)^{F'+J'+I'+1} \sqrt{(2F'+1)(2F+1)} \begin{Bmatrix} J & F & I \\ F' & J' & 1 \end{Bmatrix} \\ &\quad \times \langle \eta', v', \Lambda', S', \Sigma', J', \Omega' | T^1(\mu) | \eta, v, \Lambda, N, S, J \rangle. \end{aligned} \quad (\text{B.31})$$

We now express the $X^2\Sigma_g^+$ ground-state Hund's case (b)-basis in Hund's case (a)-bases using Eq. (A.12) and we obtain,

$$\begin{aligned} &\langle \eta', v', \Lambda', S', \Sigma', J', \Omega' | T^1(\mu) | \eta, v, \Lambda, N, S, J \rangle = \\ &\quad \sum_{\Sigma=-S}^{\Sigma=+S} (-1)^{J-S+\Lambda} \sqrt{2N+1} \begin{pmatrix} J & S & N \\ \Omega & -\Sigma & -\Lambda \end{pmatrix} \\ &\quad \times \langle \eta', v', \Lambda', S', \Sigma', J', \Omega' | T^1(\mu) | \eta, v, \Lambda, S, \Sigma, J, \Omega \rangle \end{aligned} \quad (\text{B.32})$$

We may now rotate the tensor operator into the molecule-fixed reference-frame by using,

$$T^1(\mu) = \sum_q D_{.q}^1(\omega) T_q^1(\mu). \quad (\text{B.33})$$

The remaining matrix expression from Eq. (B.32) is then separated into its angular and radial parts as,

$$\begin{aligned} & \langle \eta', v', \Lambda', S', \Sigma', J', \Omega' | T^1(\mu) | \eta, v, \Lambda, S, \Sigma, J, \Omega \rangle = \\ & \sum_q \langle S', \Sigma' | S, \Sigma \rangle \langle \Lambda', J', \Omega' | D_{.q}^1(\omega) | \Lambda, J, \Omega \rangle \langle \eta', v' | T_q^1(\mu) | \eta, v \rangle. \end{aligned} \quad (\text{B.34})$$

The overlap of the electron-spin basis functions leads to the Kronecker-delta conditions $\delta_{S'S} \delta_{\Sigma'\Sigma}$ and the Wigner rotation matrix is readily evaluated using Eq. (A.5) as,

$$\begin{aligned} & \langle \Lambda', J', \Omega' | D_{.q}^1(\omega) | \Lambda, J, \Omega \rangle \\ & = (-1)^{J'-\Omega'} \begin{pmatrix} J' & 1 & J \\ -\Omega' & q & \Omega \end{pmatrix} \sqrt{(2J'+1)(2J+1)}. \end{aligned} \quad (\text{B.35})$$

Finally, putting together Equations (B.30), (B.31), (B.32), (B.34) and (B.35), we obtain,

$$\begin{aligned} & \langle \eta', v', \Lambda', S', \Sigma', J', \Omega', I', F', M'_F | T_p^1(\mu) | \eta, v, \Lambda, N, S, J, I, F, M_F \rangle \\ & = \delta_{I'I} \delta_{S'S} (-1)^{F'-M'_F+F+2J'+I'+1-S-J'} \\ & \times \sqrt{(2F'+1)(2F+1)(2J'+1)(2J+1)(2N+1)} \\ & \times \begin{pmatrix} F' & 1 & F \\ -M'_F & p & M_F \end{pmatrix} \begin{Bmatrix} J & F & I \\ F' & J' & 1 \end{Bmatrix} \\ & \times \sum_{\Sigma=-S}^{\Sigma=+S} \delta_{\Sigma'\Sigma} \sum_q (-1)^{\Lambda-\Omega'} \begin{pmatrix} J & S & N \\ \Omega & -\Sigma & -\Lambda \end{pmatrix} \begin{pmatrix} J' & 1 & J \\ -\Omega' & q & \Omega \end{pmatrix} \\ & \times \langle \eta', v' | T_q^1(\mu) | \eta, v \rangle. \end{aligned} \quad (\text{B.36})$$

The square of Eq. (B.36) (not including the radial part) appears in the Einstein coefficients as the 'Hönl-London factor' and is given by,

$$\begin{aligned} c_{jk} & = (2F'+1)(2F+1)(2J'+1)(2J+1)(2N+1) \\ & \times \begin{pmatrix} F' & 1 & F \\ -M'_F & 0 & M_F \end{pmatrix}^2 \begin{Bmatrix} J & F & I \\ F' & J & 1 \end{Bmatrix}^2 \begin{pmatrix} J' & 1 & J \\ -\Omega' & 1 & \Omega \end{pmatrix}^2 \\ & \times \left[\begin{pmatrix} J & 1/2 & N \\ \Omega & 1/2 & 0 \end{pmatrix} + \begin{pmatrix} J & 1/2 & N \\ \Omega & -1/2 & 0 \end{pmatrix} \right]^2, \end{aligned} \quad (\text{B.37})$$

where we have used $\Lambda = 0$ and $q = 1$, $S = S' = 1/2$ and $\Sigma = \pm 1/2$. The phase factors cancel in the squared expression. We have also assumed a linear polarization parallel with the magnetic field, $p = 0$.

In the $N = 0$ lower state, these expressions confirm the matrix-elements derived in Ref. [155]. Mixing effects were neglected in this analysis which leads to a discrepancy between the two expressions at higher rotational states due to a breakdown of the Hund's case approximations.

Table of Magic Transitions

Tab. C.1. Partial list of the strongest magic magnetic-field insensitive transitions of the hyperfine, fine, rotational and vibrational manifolds below 70 G. The quantum numbers, $|v, N, S, J, I, F, M_F\rangle$, that label the states are those with the biggest overlap with the Hamiltonian eigenstate. For each transition we state the 'magic' magnetic field value, the Einstein A-coefficient, the transition frequency and the second-order Zeeman dependence of the transition, a . The dominant coupling mechanism ($M1_S$, $M1_{aS}$ or E2) is also listed for each type of transition. The transition frequency is given with respect to the zero-transition frequency, f_0 , which is defined as follows: $f_0 = 0$ for hyperfine transitions, $f_0 = B_0 \times 6 - D_0 \times 6^2 \approx 345'784.31$ MHz for rotational transitions, $f_0 = G_1 - G_0 \approx 65'197'244.88$ MHz for Q(0) rovibrational transitions, and $f_0 = G_1 - G_0 + B_1 \times 6 - D_1 \times 6^2 \approx 65'539'595.50$ MHz for S(0) rovibrational transitions.

Hyperfine transitions: $M1_S$	$ v = 0, N = 0\rangle \rightarrow v' = 0, N' = 0\rangle$	B [G]	A [s^{-1}]	$f-f_0$ [MHz]	a [mHz/ mG^2]
$I = 2:$					
	$ J = 1/2, F = 3/2, m = -3/2\rangle \rightarrow J = 1/2, F = 5/2, m = -3/2\rangle$	54.85	8.6×10^{-18}	204.80	19.1
	$ J = 1/2, F = 3/2, m = -1/2\rangle \rightarrow J = 1/2, F = 5/2, m = -3/2\rangle$	38.40	6.1×10^{-18}	233.51	16.1
	$ J = 1/2, F = 3/2, m = -3/2\rangle \rightarrow J = 1/2, F = 5/2, m = -1/2\rangle$	38.42	6.1×10^{-18}	233.48	16.1
	$ J = 1/2, F = 3/2, m = -1/2\rangle \rightarrow J = 1/2, F = 5/2, m = -1/2\rangle$	18.28	1.6×10^{-17}	250.83	15.6
Fine-structure transitions: $M1_S$	$ v = 0, N = 2\rangle \rightarrow v' = 0, N' = 2\rangle$	B [G]	A [s^{-1}]	$f-f_0$ [MHz]	a [mHz/ mG^2]
$I = 0:$					
	$ J = 3/2, F = 3/2, m = -1/2\rangle \rightarrow J = 5/2, F = 5/2, m = -1/2\rangle$	49.20	3.1×10^{-16}	686.52	8.9
$I = 2:$					
	$ J = 3/2, F = 3/2, m = -1/2\rangle \rightarrow J = 5/2, F = 5/2, m = -1/2\rangle$	17.15	2.2×10^{-16}	656.74	12.0
	$ J = 3/2, F = 3/2, m = +1/2\rangle \rightarrow J = 5/2, F = 5/2, m = -1/2\rangle$	3.81	1.0×10^{-16}	660.16	10.5
	$ J = 3/2, F = 5/2, m = -1/2\rangle \rightarrow J = 5/2, F = 7/2, m = -3/2\rangle$	48.30	1.9×10^{-16}	738.06	8.0
	$ J = 3/2, F = 5/2, m = -3/2\rangle \rightarrow J = 5/2, F = 7/2, m = -1/2\rangle$	48.72	1.6×10^{-16}	739.40	7.0
	$ J = 3/2, F = 5/2, m = -1/2\rangle \rightarrow J = 5/2, F = 7/2, m = -1/2\rangle$	22.31	3.9×10^{-16}	752.31	8.2
	$ J = 3/2, F = 5/2, m = +1/2\rangle \rightarrow J = 5/2, F = 7/2, m = -1/2\rangle$	1.55	1.9×10^{-16}	756.33	7.9
	$ J = 3/2, F = 7/2, m = -1/2\rangle \rightarrow J = 5/2, F = 9/2, m = -3/2\rangle$	49.84	2.8×10^{-16}	832.14	6.3
	$ J = 3/2, F = 7/2, m = -3/2\rangle \rightarrow J = 5/2, F = 9/2, m = -1/2\rangle$	49.39	2.7×10^{-16}	832.67	6.2
	$ J = 3/2, F = 7/2, m = -1/2\rangle \rightarrow J = 5/2, F = 9/2, m = -1/2\rangle$	24.06	5.9×10^{-16}	843.94	6.3

Rotational transitions: $M1_{\alpha S}$	$ v = 0, N = 0\rangle \rightarrow v' = 0, N' = 2\rangle$	B [G]	A [s^{-1}]	$f-f_0$ [MHz]	a [mHz/ mG^2]
$I = 2:$					
$ J = 1/2, F = 3/2, m = -3/2\rangle \rightarrow J = 3/2, F = 1/2, m = -1/2\rangle$		45.57	2.2×10^{-15}	-244.08	9.4
$ J = 1/2, F = 3/2, m = -1/2\rangle \rightarrow J = 3/2, F = 1/2, m = -1/2\rangle$		15.80	9.3×10^{-15}	-225.74	12.3
$ J = 1/2, F = 3/2, m = -1/2\rangle \rightarrow J = 3/2, F = 1/2, m = +1/2\rangle$		9.37	2.7×10^{-15}	-223.57	9.3
$ J = 1/2, F = 3/2, m = -3/2\rangle \rightarrow J = 3/2, F = 3/2, m = -3/2\rangle$		29.85	9.8×10^{-15}	-257.50	7.3
$ J = 1/2, F = 3/2, m = -1/2\rangle \rightarrow J = 3/2, F = 3/2, m = -1/2\rangle$		36.99	1.2×10^{-15}	-254.73	3.8
$ J = 1/2, F = 5/2, m = -3/2\rangle \rightarrow J = 3/2, F = 3/2, m = -1/2\rangle$		38.86	1.4×10^{-15}	-488.22	-12.1
$ J = 1/2, F = 5/2, m = -1/2\rangle \rightarrow J = 3/2, F = 3/2, m = -1/2\rangle$		15.30	1.9×10^{-15}	-504.42	-14.9
$ J = 1/2, F = 3/2, m = -1/2\rangle \rightarrow J = 3/2, F = 3/2, m = +1/2\rangle$		48.51	7.4×10^{-15}	-264.22	5.3
$ J = 1/2, F = 3/2, m = +1/2\rangle \rightarrow J = 3/2, F = 3/2, m = +3/2\rangle$		17.64	5.9×10^{-15}	-253.71	5.4
$ J = 1/2, F = 3/2, m = -3/2\rangle \rightarrow J = 3/2, F = 5/2, m = -3/2\rangle$		44.15	7.7×10^{-15}	-297.86	5.9
$ J = 1/2, F = 5/2, m = -3/2\rangle \rightarrow J = 3/2, F = 5/2, m = -3/2\rangle$		60.07	1.9×10^{-15}	-501.62	-12.6
$ J = 1/2, F = 5/2, m = -1/2\rangle \rightarrow J = 3/2, F = 5/2, m = -3/2\rangle$		35.38	5.4×10^{-15}	-531.06	-10.9
$ J = 1/2, F = 3/2, m = -1/2\rangle \rightarrow J = 3/2, F = 5/2, m = -1/2\rangle$		16.71	7.1×10^{-15}	-289.93	3.4
$ J = 1/2, F = 5/2, m = -3/2\rangle \rightarrow J = 3/2, F = 5/2, m = -1/2\rangle$		43.39	7.8×10^{-15}	-521.55	-13.8
$ J = 1/2, F = 3/2, m = -1/2\rangle \rightarrow J = 3/2, F = 5/2, m = +1/2\rangle$		60.74	6.2×10^{-15}	-302.52	3.2
$ J = 1/2, F = 5/2, m = -1/2\rangle \rightarrow J = 3/2, F = 5/2, m = +1/2\rangle$		4.82	6.8×10^{-15}	-544.71	-11.7
$ J = 1/2, F = 3/2, m = +1/2\rangle \rightarrow J = 3/2, F = 5/2, m = +3/2\rangle$		30.76	7.5×10^{-15}	-292.22	3.0
$ J = 1/2, F = 5/2, m = -3/2\rangle \rightarrow J = 3/2, F = 7/2, m = -3/2\rangle$		58.94	1.4×10^{-14}	-539.71	-12.8
$ J = 1/2, F = 5/2, m = -1/2\rangle \rightarrow J = 3/2, F = 7/2, m = -3/2\rangle$		33.79	9.0×10^{-15}	-568.41	-10.6
$ J = 1/2, F = 5/2, m = -3/2\rangle \rightarrow J = 3/2, F = 7/2, m = -1/2\rangle$		46.34	6.2×10^{-15}	-556.10	-12.8
$ J = 1/2, F = 5/2, m = -1/2\rangle \rightarrow J = 3/2, F = 7/2, m = -1/2\rangle$		19.49	1.4×10^{-14}	-576.51	-11.1
$ J = 1/2, F = 5/2, m = -1/2\rangle \rightarrow J = 3/2, F = 7/2, m = +1/2\rangle$		6.12	7.4×10^{-15}	-580.31	-10.9

Rovibrational transitions: $M1_{\alpha S}$	$ v = 0, N = 0\rangle \rightarrow v' = 1, N' = 0\rangle$	B [G]	A [s^{-1}]	$f-f_0$ [MHz]	a [mHz/ mG^2]
$I = 2:$					
$ J = 1/2, F = 5/2, m = -3/2\rangle \rightarrow J = 1/2, F = 3/2, m = -3/2\rangle$		54.37	4.4×10^{-10}	-202.56	-19.3
$ J = 1/2, F = 5/2, m = -1/2\rangle \rightarrow J = 1/2, F = 3/2, m = -3/2\rangle$		38.05	2.1×10^{-10}	-230.99	-16.3
$ J = 1/2, F = 5/2, m = -3/2\rangle \rightarrow J = 1/2, F = 3/2, m = -1/2\rangle$		38.10	2.1×10^{-10}	-231.01	-16.2
$ J = 1/2, F = 5/2, m = -1/2\rangle \rightarrow J = 1/2, F = 3/2, m = -1/2\rangle$		18.12	4.4×10^{-10}	-248.18	-15.8
$ J = 1/2, F = 3/2, m = -3/2\rangle \rightarrow J = 1/2, F = 5/2, m = -3/2\rangle$		54.37	4.4×10^{-10}	203.45	19.3
$ J = 1/2, F = 3/2, m = -1/2\rangle \rightarrow J = 1/2, F = 5/2, m = -3/2\rangle$		38.03	2.1×10^{-10}	231.91	16.3
$ J = 1/2, F = 3/2, m = -3/2\rangle \rightarrow J = 1/2, F = 5/2, m = -1/2\rangle$		38.12	2.1×10^{-10}	231.88	16.2
$ J = 1/2, F = 3/2, m = -1/2\rangle \rightarrow J = 1/2, F = 5/2, m = -1/2\rangle$		18.12	4.4×10^{-10}	249.07	15.8

Rovibrational transitions: E2	$ v = 0, N = 0\rangle \rightarrow v' = 1, N' = 2\rangle$	B [G]	A [s^{-1}]	$f-f_0$ [MHz]	a [mHz/ mG^2]
$I = 2:$					
$ J = 1/2, F = 5/2, m = -1/2\rangle \rightarrow J = 3/2, F = 1/2, m = -1/2\rangle$		30.06	5.8×10^{-9}	-480.97	-5.2
$ J = 1/2, F = 5/2, m = -1/2\rangle \rightarrow J = 3/2, F = 3/2, m = -3/2\rangle$		47.64	8.5×10^{-9}	-491.42	-8.0
$ J = 1/2, F = 5/2, m = +1/2\rangle \rightarrow J = 3/2, F = 3/2, m = -3/2\rangle$		14.87	3.8×10^{-9}	-508.36	-6.7
$ J = 1/2, F = 3/2, m = -1/2\rangle \rightarrow J = 3/2, F = 3/2, m = -1/2\rangle$		36.60	1.8×10^{-9}	-257.19	3.9
$ J = 1/2, F = 5/2, m = -3/2\rangle \rightarrow J = 3/2, F = 3/2, m = -1/2\rangle$		39.07	6.7×10^{-9}	-490.68	-11.5
$ J = 1/2, F = 3/2, m = -1/2\rangle \rightarrow J = 3/2, F = 3/2, m = +1/2\rangle$		46.75	4.2×10^{-9}	-265.99	5.6
$ J = 1/2, F = 5/2, m = -3/2\rangle \rightarrow J = 3/2, F = 3/2, m = +1/2\rangle$		33.59	3.3×10^{-9}	-498.86	-9.9
$ J = 1/2, F = 5/2, m = -1/2\rangle \rightarrow J = 3/2, F = 3/2, m = +1/2\rangle$		4.28	5.6×10^{-9}	-509.68	-13.1
$ J = 1/2, F = 3/2, m = -1/2\rangle \rightarrow J = 3/2, F = 3/2, m = +3/2\rangle$		61.63	1.1×10^{-9}	-275.92	4.3
$ J = 1/2, F = 3/2, m = +1/2\rangle \rightarrow J = 3/2, F = 3/2, m = +3/2\rangle$		16.85	5.0×10^{-9}	-255.67	5.6
$ J = 1/2, F = 5/2, m = -1/2\rangle \rightarrow J = 3/2, F = 5/2, m = -5/2\rangle$		64.93	8.9×10^{-9}	-506.02	-7.5
$ J = 1/2, F = 3/2, m = -3/2\rangle \rightarrow J = 3/2, F = 5/2, m = -3/2\rangle$		44.62	3.2×10^{-9}	-294.67	6.0
$ J = 1/2, F = 5/2, m = -3/2\rangle \rightarrow J = 3/2, F = 5/2, m = -3/2\rangle$		59.97	6.0×10^{-9}	-498.49	-12.5
$ J = 1/2, F = 5/2, m = +1/2\rangle \rightarrow J = 3/2, F = 5/2, m = -3/2\rangle$		10.74	5.4×10^{-9}	-540.42	-10.3
$ J = 1/2, F = 5/2, m = -1/2\rangle \rightarrow J = 3/2, F = 5/2, m = -1/2\rangle$		18.34	3.8×10^{-9}	-537.47	-12.5
$ J = 1/2, F = 5/2, m = -3/2\rangle \rightarrow J = 3/2, F = 5/2, m = +1/2\rangle$		31.36	6.0×10^{-9}	-530.66	-11.9
$ J = 1/2, F = 3/2, m = +1/2\rangle \rightarrow J = 3/2, F = 5/2, m = +5/2\rangle$		65.10	5.2×10^{-9}	-300.92	2.3
$ J = 1/2, F = 3/2, m = -3/2\rangle \rightarrow J = 3/2, F = 7/2, m = -5/2\rangle$		14.88	1.5×10^{-8}	-314.32	4.0
$ J = 1/2, F = 5/2, m = -1/2\rangle \rightarrow J = 3/2, F = 7/2, m = -5/2\rangle$		51.30	3.5×10^{-9}	-543.57	-9.2
$ J = 1/2, F = 3/2, m = -3/2\rangle \rightarrow J = 3/2, F = 7/2, m = -3/2\rangle$		48.10	1.3×10^{-8}	-324.81	6.1
$ J = 1/2, F = 5/2, m = -1/2\rangle \rightarrow J = 3/2, F = 7/2, m = -3/2\rangle$		33.18	2.0×10^{-9}	-557.44	-10.9
$ J = 1/2, F = 5/2, m = +1/2\rangle \rightarrow J = 3/2, F = 7/2, m = -3/2\rangle$		8.04	2.2×10^{-9}	-568.88	-10.1

$ J = 1/2, F = 3/2, m = -1/2\rangle \rightarrow J = 3/2, F = 7/2, m = -1/2\rangle$	16.21	1.3×10^{-8}	-314.63	4.2
$ J = 1/2, F = 5/2, m = -3/2\rangle \rightarrow J = 3/2, F = 7/2, m = -1/2\rangle$	45.32	1.8×10^{-9}	-545.49	-13.1
$ J = 1/2, F = 3/2, m = -1/2\rangle \rightarrow J = 3/2, F = 7/2, m = +1/2\rangle$	54.89	1.4×10^{-8}	-324.78	2.9
$ J = 1/2, F = 5/2, m = -3/2\rangle \rightarrow J = 3/2, F = 7/2, m = +1/2\rangle$	33.85	2.3×10^{-9}	-557.16	-12.0
$ J = 1/2, F = 5/2, m = -1/2\rangle \rightarrow J = 3/2, F = 7/2, m = +1/2\rangle$	5.95	1.7×10^{-9}	-569.15	-11.1
$ J = 1/2, F = 3/2, m = +1/2\rangle \rightarrow J = 3/2, F = 7/2, m = +3/2\rangle$	22.93	1.5×10^{-8}	-315.33	2.9
$ J = 1/2, F = 3/2, m = +3/2\rangle \rightarrow J = 3/2, F = 7/2, m = +7/2\rangle$	41.67	2.7×10^{-8}	-316.98	1.3
$ J = 1/2, F = 3/2, m = -3/2\rangle \rightarrow J = 5/2, F = 3/2, m = -1/2\rangle$	56.95	4.7×10^{-9}	322.93	10.7
$ J = 1/2, F = 3/2, m = -1/2\rangle \rightarrow J = 5/2, F = 3/2, m = -1/2\rangle$	25.65	8.1×10^{-9}	348.66	9.7
$ J = 1/2, F = 3/2, m = -3/2\rangle \rightarrow J = 5/2, F = 3/2, m = +1/2\rangle$	16.17	1.1×10^{-8}	352.02	15.4
$ J = 1/2, F = 5/2, m = +1/2\rangle \rightarrow J = 5/2, F = 3/2, m = +3/2\rangle$	52.04	2.0×10^{-9}	117.76	-4.6
$ J = 1/2, F = 5/2, m = +3/2\rangle \rightarrow J = 5/2, F = 3/2, m = +3/2\rangle$	16.39	4.2×10^{-9}	101.77	-5.8
$ J = 1/2, F = 3/2, m = -1/2\rangle \rightarrow J = 5/2, F = 5/2, m = -3/2\rangle$	48.87	3.3×10^{-9}	383.90	9.3
$ J = 1/2, F = 3/2, m = +1/2\rangle \rightarrow J = 5/2, F = 5/2, m = -3/2\rangle$	23.68	5.3×10^{-9}	403.02	8.8
$ J = 1/2, F = 3/2, m = -3/2\rangle \rightarrow J = 5/2, F = 5/2, m = -1/2\rangle$	44.96	8.3×10^{-9}	382.72	13.3
$ J = 1/2, F = 5/2, m = -1/2\rangle \rightarrow J = 5/2, F = 5/2, m = -1/2\rangle$	6.98	4.1×10^{-9}	152.46	-2.4
$ J = 1/2, F = 3/2, m = -3/2\rangle \rightarrow J = 5/2, F = 5/2, m = +1/2\rangle$	25.75	4.0×10^{-9}	400.41	12.9
$ J = 1/2, F = 3/2, m = -1/2\rangle \rightarrow J = 5/2, F = 5/2, m = +1/2\rangle$	1.26	4.8×10^{-9}	408.33	12.7
$ J = 1/2, F = 5/2, m = +3/2\rangle \rightarrow J = 5/2, F = 5/2, m = +5/2\rangle$	60.47	8.4×10^{-9}	162.26	-1.8
$ J = 1/2, F = 3/2, m = -1/2\rangle \rightarrow J = 5/2, F = 7/2, m = -5/2\rangle$	67.42	3.0×10^{-9}	423.69	7.8
$ J = 1/2, F = 3/2, m = -3/2\rangle \rightarrow J = 5/2, F = 7/2, m = -3/2\rangle$	63.13	2.9×10^{-9}	416.02	12.8
$ J = 1/2, F = 3/2, m = -1/2\rangle \rightarrow J = 5/2, F = 7/2, m = -3/2\rangle$	39.26	3.8×10^{-9}	447.47	10.6
$ J = 1/2, F = 5/2, m = -3/2\rangle \rightarrow J = 5/2, F = 7/2, m = -3/2\rangle$	36.74	5.9×10^{-9}	213.99	-5.3
$ J = 1/2, F = 3/2, m = -1/2\rangle \rightarrow J = 5/2, F = 7/2, m = -1/2\rangle$	20.54	3.3×10^{-9}	459.46	11.7
$ J = 1/2, F = 3/2, m = -1/2\rangle \rightarrow J = 5/2, F = 7/2, m = +1/2\rangle$	3.88	2.1×10^{-9}	464.18	11.3
$ J = 1/2, F = 5/2, m = -1/2\rangle \rightarrow J = 5/2, F = 7/2, m = +1/2\rangle$	67.69	4.6×10^{-9}	222.96	-2.0
$ J = 1/2, F = 5/2, m = +3/2\rangle \rightarrow J = 5/2, F = 7/2, m = +5/2\rangle$	31.84	1.5×10^{-9}	210.01	-1.0
$ J = 1/2, F = 5/2, m = -3/2\rangle \rightarrow J = 5/2, F = 9/2, m = -5/2\rangle$	9.72	1.7×10^{-8}	259.28	-3.7
$ J = 1/2, F = 5/2, m = -3/2\rangle \rightarrow J = 5/2, F = 9/2, m = -3/2\rangle$	43.36	1.3×10^{-8}	268.40	-6.2
$ J = 1/2, F = 5/2, m = -3/2\rangle \rightarrow J = 5/2, F = 9/2, m = -1/2\rangle$	68.91	7.8×10^{-9}	286.49	-6.1
$ J = 1/2, F = 5/2, m = -1/2\rangle \rightarrow J = 5/2, F = 9/2, m = -1/2\rangle$	13.68	1.5×10^{-8}	259.82	-4.7
$ J = 1/2, F = 5/2, m = -1/2\rangle \rightarrow J = 5/2, F = 9/2, m = +1/2\rangle$	47.59	1.2×10^{-8}	269.15	-3.9
$ J = 1/2, F = 5/2, m = +1/2\rangle \rightarrow J = 5/2, F = 9/2, m = +3/2\rangle$	23.35	1.5×10^{-8}	261.01	-3.3

Sideband Cooling Simulations

In order to optimize sideband cooling and avoid population trapping, the sideband cooling from Doppler temperatures of ~ 0.5 mK and $\bar{n} \approx 16$ to the trap ground state was simulated using the theory of Ref. [111] as described in the Appendix of Ref. [156].

The population transferred by each pulse on resonance with a spectral sideband is given by,

$$y_e(t) = \sin^2 \left(\frac{\Omega_{n,n+s} t}{2} \right), \quad (\text{D.1})$$

where t is the pulse length and $\Omega_{n,n+s}$ is the Rabi frequency on the sideband. s describes the sideband order, e.g. $s = -1$ for the first red sideband and $s = 1$ for the first blue sideband. With a carrier Rabi frequency Ω_0 , the sideband strength is given by,

$$\Omega_{n,n+s} = \Omega_0 e^{-\eta/2} \eta^{|s|} \sqrt{\frac{n_{>}!}{n_{<}!}} L_{n_{<}}^{|s|}(\eta^2), \quad (\text{D.2})$$

where $L_{n_{<}}^{|s|}(\eta^2)$ are generalized Laguerre polynomials and $n_{<}$ and $n_{>}$ refer to the lesser and greater of n and $n + s$ respectively.

A general Rabi-oscillation signal on a motional sideband with a detuning, δ , can be obtained from the convolution of the contributions from each motional state as [92],

$$y(t_{729}) = \sum_{n,n+s} P_n \frac{\Omega_{n,n+s}}{\Omega_{n,n+s} + \delta^2} \sin^2 \left(\sqrt{\Omega_{n,n+s}^2 + \delta^2} \cdot t_{729}/2 \right). \quad (\text{D.3})$$

Other sources of decoherence can be added phenomenologically through an additional exponential decay factor with time constant, T_2 . With this contribution included, the Rabi-oscillation data is given by,

$$P_{\uparrow}(t_{729}) = y(t_{729})e^{-t_{729}/T_2} + (1 + e^{-t_{729}/T_2})/2 \quad (\text{D.4})$$

We start the sideband cooling simulation by choosing an initial motional state distribution $P_n^{(0)}$, such as a Boltzmann distribution at 0.5 mK. For each pulse iteration we calculate the population that leaves the motional state, n , i.e. the excitation probability $p_e(n)$, and the population that enters the state from neighboring levels, $p_e(n - s)$, using Eq. (D.1). The population in the new distribution after the first iteration is then,

$$P_n^{(1)} = P_n^{(0)}(1 - p_e(n) + p_e(n - s)). \quad (\text{D.5})$$

An additional heating rate can be added to this equation to simulate heating and off-resonant scattering on blue sidebands, but were not used for the simulations presented below. We then iterate this procedure for any number of pulses on any desired sideband.

Figure D.1a shows the results of a simulation using two different types of pulses. First 200 pulses are applied on resonance with the second red sideband with pulse length $t = 6\pi/\Omega_0$ followed by 200 pulses on the first red sideband with $t = 4\pi/\Omega_0$. Here we used $\eta \approx 0.1$. The excitation probabilities as a function of motional state with these pulse lengths are shown as the solid curves in Figure D.1. The simulation shows that with only two different pulse lengths, a part of the distribution gets trapped as the excitation probability vanishes for certain values of n .

Figure D.1b shows the excitation probability for different pulse lengths, on the first red sideband, as a function of the motional state, n . With the shortest pulses the excitation probability does not vanish for any motional state. Therefore, if the pulse length is incrementally increased in several steps, we can efficiently transfer the population to the ground state without population trapping. This method was employed in the experimental sideband-cooling sequence and the results are presented in Section 4.3.

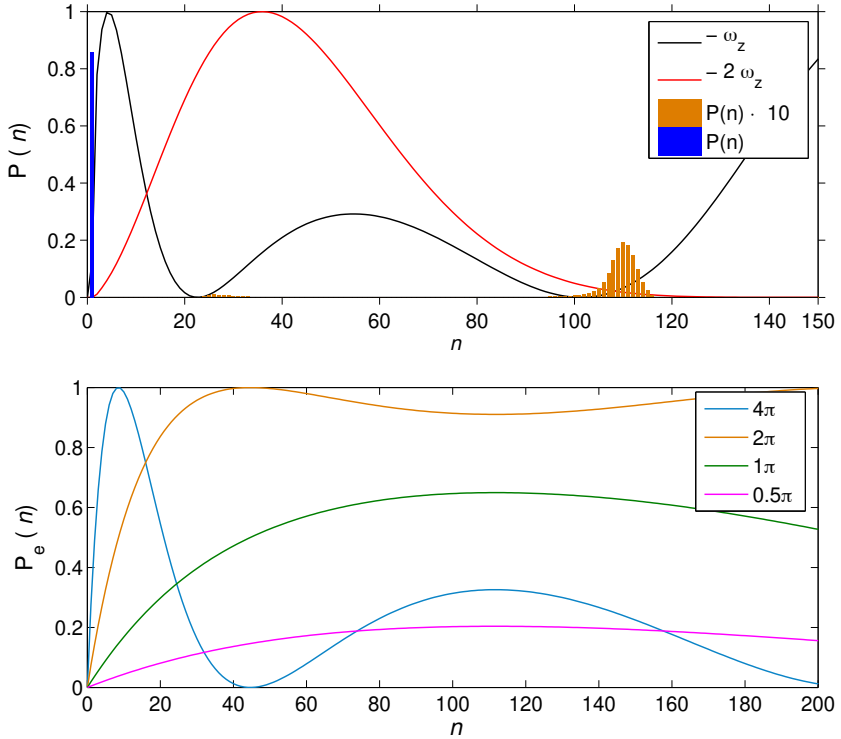


Fig. D.1. **a)** Simulated motional state distribution after sideband cooling. The simulation included 200 pulses on the second red sideband, with pulse length $t = 6\pi/\Omega_0$, followed by 200 pulses on the first red sideband of length $t = 4\pi/\Omega_0$ (blue bars). The trapped state population (orange bars) are scaled up by a factor 10 for visibility. The sequence achieves 85 % ground-state occupation with no heating or off-resonant scattering included in the simulation. The black and red curves show the coupling strength on the first and second sideband, respectively, as a function of the motional state n . The Lamb-Dicke parameter was set to $\eta = 0.1$ **b)** The coupling strength for different pulse lengths on the first red sideband as a function of motional state n .

Bibliography

- [1]S. G. Karshenboim and E. Peik. *Astrophysics, Clocks and Fundamental Constants*. Vol. 648. Lecture Notes in Physics, Springer, 2004 (cit. on p. 1).
- [2]M. S. Safronova, D. Budker, D. DeMille, et al. “Search for new physics with atoms and molecules”. In: *Rev. Mod. Phys.* 90 (2018), p. 025008 (cit. on pp. 2, 5).
- [3]D. DeMille, J. M. Doyle, and A. O. Sushkov. “Probing the frontiers of particle physics with tabletop-scale experiments”. In: *Science* 357.6355 (2017), pp. 990–994 (cit. on p. 2).
- [4]B. P. Abbott and et al. “Observation of Gravitational Waves from a Binary Black Hole Merger”. In: *Phys. Rev. Lett* 116 (2016), p. 061102 (cit. on p. 2).
- [5](ATLAS Collaboration) G. Aad et al. “Observation of a new particle in the search for the Standard Model Higgs boson with the ATLAS detector at the LHC”. In: *Phys. Lett. B* 716 (2012), pp. 1–29 (cit. on p. 2).
- [6](CMS Collaboration) S. Chatrchyan et al. “Observation of a new boson at a mass of 125 GeV with the CMS experiment at the LHC”. In: *Phys. Lett. B* 716 (2012), pp. 30–61 (cit. on p. 2).
- [7]S. M. Brewer, J.-S. Chen, A. M. Hankin, et al. “An $^{28}\text{Al}^+$ quantum-logic clock with systematic uncertainty below 10^{-18} ”. In: *Phys. Rev. Lett.* 123.3 (2019), p. 033201 (cit. on p. 3).
- [8]N. Huntemann, C. Sanner, B. Lipphardt, C. Tamm, and E. Peik. “Single-Ion Atomic Clock with 3×10^{-18} Systematic Uncertainty”. In: *Phys. Rev. Lett.* 116 (2016), p. 063001 (cit. on p. 3).
- [9]R. M. Godun, P. B. R. Nisbet-Jones, J. M. Jones, et al. “Frequency Ratio of Two Optical Clock Transitions in $^{171}\text{Yb}^+$ and Constraints on the Time Variation of Fundamental Constants”. In: *Phys. Rev. Lett.* 113 (2014), p. 210801 (cit. on pp. 3, 5).

- [10]S. Bize, S. A. Diddams, U. Tanaka, et al. “Testing stability of fundamental constants with the $^{199}\text{Hg}^+$ single ion optical clock”. In: *Phys. Rev. Lett.* 90 (2003), p. 150802 (cit. on p. 3).
- [11]N. Huntemann, B. Lipphardt, C. Tamm, et al. “Improved Limit on a Temporal Variation of m_p/m_e from Comparisons of Yb^+ and Cs Atomic Clocks”. In: *Phys. Rev. Lett.* 113 (2014), p. 210802 (cit. on p. 3).
- [12]A. D. Ludlow, M. M. Boyd, J. Ye, E. Peik, and P. O. Schmidt. “Optical Atomic Clocks”. In: *Rev. Mod. Phys.* 87 (2015), p. 637 (cit. on p. 3).
- [13]M. Kajita. *Measuring Time, Frequency measurements and related developments in physics*. IOP Publishing Ltd, 2018 (cit. on pp. 3, 5).
- [14](The Event Horizon Telescope Collaboration) K. Akiyama et al. “First M87 Event Horizon Telescope Results. IV. Imaging the Central Supermassive Black Hole”. In: *The Astrophysical Journal Letters* 875 (2019), p. L4 (cit. on p. 3).
- [15]K. Wright, K. M. Beck, S. Debnath, et al. “Benchmarking an 11-qubit quantum computer”. In: *Nat. Comm.* 10.1 (2019), pp. 1–6 (cit. on p. 3).
- [16]N. Friis, O. Marty, C. Maier, et al. “Observation of entangled states of a fully controlled 20-qubit system”. In: *Phys. Rev. X* 8.2 (2018), p. 021012 (cit. on p. 3).
- [17]F. Arute, K. Arya, R. Babbush, et al. “Quantum supremacy using a programmable superconducting processor”. In: *Nature* 574.7779 (2019), pp. 505–510 (cit. on p. 3).
- [18]J. I. Cirac and P. Zoller. “Quantum computation with cold trapped ions”. In: *Phys. Rev. Lett.* 74 (1995), p. 4091 (cit. on p. 3).
- [19]R. Blatt and C. Roos. “Quantum simulations with trapped ions”. In: *Nat. Phys.* 8 (2012), pp. 277–284 (cit. on p. 3).
- [20]I. Kassal, J. D. Whitfield, A. Perdomo-Ortiz, M.-H. Yung, and A. Aspuru-Guzik. “Simulating Chemistry Using Quantum Computers”. In: *Ann. Rev. Phys. Chem.* 62 (2011), pp. 185–207 (cit. on p. 3).
- [21]S. Schiller, D. Bakalov, and V. I. Korobov. “Simplest Molecules as Candidates for Precise Optical Clocks”. In: *Phys. Rev. Lett.* 113 (2014), p. 023004 (cit. on pp. 4, 5).
- [22]L. D. Carr, D. DeMille, R. V. Krems, and J. Ye. “Cold and ultracold molecules: Science, technology and applications”. In: *New J. Phys.* 11 (2009), p. 055049 (cit. on pp. 4, 127, 128).

- [23]J. Mur-Petit, J. Pérez-Ri'os, J. Campos-Marti'nez, et al. "Temperature-independent quantum logic for molecular spectroscopy". In: *Phys. Rev. A* 85 (2012), p. 022308 (cit. on pp. 4, 18, 36).
- [24]D. Leibfried. "Quantum state preparation and control of single molecular ions". In: *New J. Phys.* 14 (2012), p. 023029 (cit. on pp. 4, 145).
- [25]S. Ding and D. N. Matsukevich. "Quantum logic for control and manipulation of molecular ions using a frequency comb". In: *New J. Phys.* 14 (2012), p. 023028 (cit. on pp. 4, 145).
- [26]J. Biesheuvel, J.-P. Karr, L. Hilico, et al. "Probing QED and fundamental constants through laser spectroscopy of vibrational transitions in HD^+ ". In: *Nat. Commun.* 7 (2016), p. 10385 (cit. on p. 4).
- [27]E. S. Shuman, J. F. Barry, and D. DeMille. "Laser cooling of a diatomic molecule". In: *Nature* 467 (2010), p. 820 (cit. on p. 4).
- [28]S. Truppe, H. J. Williams, M. Hambach, et al. "Molecules cooled below the Doppler limit". In: *Nat. Phys.* 13 (2017), pp. 1173–1176 (cit. on p. 4).
- [29]L. Anderegg, B. L. Augenbraun, Y. Bao, et al. "Laser cooling of optically trapped molecules". In: *Nat. Phys.* 14 (2018), p. 890 (cit. on p. 4).
- [30]B. E. Sauer, H. T. Ashworth, J. J. Hudson, M. R. Tarbutt, and E. A. Hinds. "Probing the Electron EDM with Cold Molecules". In: *AIP Conference Proceedings*. Ed. by C. Roos, H. Häffner, and R. Blatt. Vol. CP869. American Institute of Physics, 2006, p. 44 (cit. on p. 4).
- [31]K. Beloy, M. G. Kozlov, A. Borschevsky, et al. "Rotational spectrum of the molecular ion NH^+ as a probe for α and m_e/m_p variation". In: *Phys. Rev. A* 83 (2011), p. 062514 (cit. on p. 4).
- [32]S. Schiller and V. Korobov. "Tests of time independence of the electron and nuclear masses with ultracold molecules". In: *Phys. Rev. A* 71 (2005), p. 032505 (cit. on p. 5).
- [33]V. V. Flambaum and M. G. Kozlov. "Enhanced sensitivity to the time variation of the fine-structure constant and m_p/m_e in diatomic molecules". In: *Phys. Rev. Lett.* 99.15 (2007), p. 150801 (cit. on p. 5).
- [34]P. Jansen, H. L. Bethlem, and W. Ubachs. "Tipping the scales: Search for drifting constants from molecular spectra". In: *J. Chem. Phys.* 140 (2014), p. 010901 (cit. on p. 5).

- [35]M. Kajita, G. Gopakumar, M. Abe, M. Hada, and M. Keller. “Test of m_p/m_e changes using vibrational transitions in N_2^+ ”. In: *Phys. Rev. A* 89 (2014), p. 032509 (cit. on pp. 5, 70, 74–76).
- [36]M. Kajita. “Evaluation of variation in m_p/m_e from the frequency difference between the $^{15}N_2^+$ and ^{87}Sr transitions”. In: *Appl. Phys. B* 122 (2016), p. 203 (cit. on p. 5).
- [37]J. Bagdonaite, M. Daprà, P. Jansen, et al. “Robust Constraint on a Drifting Proton-to-Electron Mass Ratio at $z=0.89$ from Methanol Observation at Three Radio Telescopes”. In: *Phys. Rev. Lett.* 111 (2013), p. 231101 (cit. on p. 5).
- [38]A. Shelkovich, R. J. Butcher, C. Chardonnet, and A. Amy-Klein. “Stability of the Proton-to-Electron Mass Ratio”. In: *Phys. Rev. Lett.* 100 (2008), p. 150801 (cit. on p. 5).
- [39]M. Germann, X. Tong, and S. Willitsch. “Observation of electric-dipole-forbidden infrared transitions in cold molecular ions”. In: *Nat. Phys.* 10 (2014), p. 820 (cit. on pp. 5, 77, 88).
- [40]J.-P. Karr. “ H_2^+ and HD^+ : candidates for a molecular clock”. In: *J. Mol. Spec.* 300 (2014), p. 37 (cit. on p. 5).
- [41]D. DeMille. “Quantum computation with trapped polar molecules”. In: *Phys. Rev. Lett.* 88 (2002), p. 067901 (cit. on p. 5).
- [42]J. M. Brown and A. Carrington. *Rotational Spectroscopy of Diatomic Molecules*. Cambridge University Press, 2003 (cit. on pp. 9, 11, 15, 18, 20, 25, 28, 31, 33, 37, 41, 183, 189).
- [43]R. N. Zare. *Angular Momentum*. New York: John Wiley & Sons, 1988 (cit. on pp. 9, 28, 34, 35, 183).
- [44]D. Papoušek. “Forbidden transitions in molecular vibrational-rotational spectroscopy”. In: *Collection of Czechoslovak chemical communications* 54.10 (1989), pp. 2555–2630 (cit. on pp. 9, 53, 59).
- [45]P. W. Atkins. *Phys. Chem*. Fifth Edition. Oxford University Press, 1994 (cit. on pp. 9, 12, 26).
- [46]J. T. Hougen. “The calculation of rotational energy levels and rotational line intensities in diatomic molecules”. In: *National Bureau of Standards Monograph* 115 (1970) (cit. on p. 9).
- [47]M. Germann. “Dipole-Forbidden Vibrational Transitions in Molecular Ions”. PhD thesis. University of Basel, 2016 (cit. on pp. 9, 55, 83, 88).

- [48]J. L. Dunham. “The energy levels of a rotating vibrator”. In: *Phys. Rev.* 41 (1932), p. 721 (cit. on p. 13).
- [49]J. H. van Vleck. “On σ -Type Doubling and Electron Spin in the Spectra of Diatomic Molecules”. In: *Phys. Rev.* 33 (1929), p. 467 (cit. on p. 15).
- [50]R. A. Frosch and H. M. Foley. “Magnetic hyperfine structure in diatomic molecules”. In: *Phys. Rev.* 88 (1952), p. 1337 (cit. on p. 17).
- [51]N. B. Mansour, C. Kurtz, T. C. Steimle, et al. “Laser-rf double-resonance study of N_2^+ ”. In: *Phys. Rev. A* 44.7 (1991), p. 4418 (cit. on pp. 18, 24, 25, 27, 47).
- [52]T. K. Balasubramanian, V. P. Bellary, and K. N. Rao. “Branch intensities in the magnetic dipole rotation–vibration spectrum of the oxygen molecule”. In: *Can. J. Phys.* 72.11-12 (1994), pp. 971–978 (cit. on p. 21).
- [53]R. C. Jr. “The relationship between electron spin rotation coupling constants and g -tensor components”. In: *Mol. Phys.* 9:6 (1965), pp. 585–598 (cit. on pp. 25, 40, 41).
- [54]I. C. Bowater, B. J. M, and C. A. “Microwave spectroscopy of nonlinear free radicals - I. General theory and application to the Zeeman effect in HCO”. In: *Proc. R. Soc. London A* 333 (1973), p. 265 (cit. on pp. 26, 28, 32, 36, 38–40, 45).
- [55]L. I. Schiff and H. Snyder. “Theory of the quadratic Zeeman effect”. In: *Phys. Rev.* 55.1 (1939), p. 59 (cit. on p. 28).
- [56]J. M. Brown. “Remarks on the signs of g factors in atomic and molecular Zeeman spectroscopy”. In: *Mol. Phys.* 98.20 (2000), pp. 1597–1601 (cit. on p. 29).
- [57]J. M. Brown, M. Kaise, C. M. L. Kerr, and D. J. Milton. “A determination of fundamental Zeeman parameters for the OH radical”. In: *Mol. Phys.* 36.2 (1978), pp. 553–582 (cit. on p. 31).
- [58]P. J. Bruna and F. Grein. “The $X^2\Sigma_g^+$ and $B^2\Sigma_u^+$ states of N_2^+ : hyperfine and nuclear quadrupole coupling constants; electric quadrupole moments; and electron-spin g -factors. A theoretical study”. In: *J. Mol. Spec.* 227 (2004), p. 67 (cit. on pp. 31, 40, 41, 47, 60, 63, 77).
- [59]D. Jayatilaka. “Electron spin resonance g tensors from general Hartree–Fock calculations”. In: *J. Chem. Phys.* 108 (1998), p. 7587 (cit. on p. 40).
- [60]MATLAB. *version 7.10.0 (R2018b)*. Natick, Massachusetts: The Math-Works Inc., 2018 (cit. on pp. 46, 158).

- [61]A. A. Ramos and J. T. Bueno. “Theory and modeling of the Zeeman and Paschen-Back effects in molecular lines”. In: *The Astrophysical Journal* 636 (2006), pp. 548–563 (cit. on p. 46).
- [62]F. Michaud, F. Roux, S. P. Davis, A.-D. Nguyen, and C. O. Laux. “High-Resolution Fourier Spectrometry of the $^{14}\text{N}_2^+$ Ion”. In: *J. Mol. Spec.* 203.1 (2000), pp. 1–8 (cit. on p. 47).
- [63]Y.-D. Wu, J.-W. Ben, L. Li, et al. “Study of (2, 0) Band of $A^2\Pi_u-X^2\Sigma_g^+$ System of N_2^+ by Optical Heterodyne Detected Velocity Modulation Spectroscopy”. In: *Chinese J. Chem. Phys.* 20 (2007), p. 285 (cit. on pp. 47, 151).
- [64]D. Collet, J.-L. Destombes, I. H. Bachir, and T. R. Huet. “Rotational analysis of the vibrational hot bands of N_2^+ ($A^2\Pi_u-X^2\Sigma_g^+$) in the near-infrared region using velocity modulation spectroscopy”. In: *Chem. Phys. Lett.* 286.3-4 (1998), pp. 311–316 (cit. on p. 47).
- [65]T. J. Scholl, R. A. Holt, and S. D. Rosner. “Fine and Hyperfine Structure in $^{14}\text{N}_2^+$: The B-X (0; 0) Band”. In: *J. Mol. Spec.* 192 (1998), p. 424 (cit. on p. 47).
- [66]E. Tiesinga, P. J. Mohr, D. B. Newell, and B. N. Taylor. *The 2018 CODATA Recommended Values of the Fundamental Physical Constants (Web Version 8.1)*. 2020 (cit. on p. 47).
- [67]M. Kajita. “ N_2^+ quadrupole transitions with small Zeeman shift”. In: *Phys. Rev. A* 92 (2015), p. 043423 (cit. on pp. 47, 60, 64, 76).
- [68]T. P. Harty, D. T. C. Allcock, C. J. Ballance, et al. “High-Fidelity Preparation; Gates; Memory; and Readout of a Trapped-Ion Quantum Bit”. In: *Phys. Rev. Lett.* 113 (2014), p. 220501 (cit. on pp. 49, 64).
- [69]C. Langer, R. Ozeri, J. D. Jost, et al. “Long-Lived Qubit Memory Using Atomic Ions”. In: *Phys. Rev. Lett.* 95 (2005), p. 060502 (cit. on pp. 49, 64).
- [70]G. W. F. Drake. *Springer Handbook of Atomic, Molecular and Optical Physics*. Springer, 2006, p. 192 (cit. on pp. 55, 151).
- [71]S. R. Williams, A. Jayakumar, M. R. Hoffman, B. B. Blinov, and E. N. Fortson. “Method for measuring the $6S_{1/2} \rightleftharpoons 5D_{3/2}$ magnetic-dipole-transition moment in Ba^+ ”. In: *Phys. Rev. A* 88 (2013), p. 012515 (cit. on p. 55).

- [72]A. G. Radnaev, C. J. Campbell, and A. Kuzmich. “Observation of the 717-nm electric quadrupole transition in triply charged thorium”. In: *Phys. Rev. A* 86 (2012), p. 060501 (cit. on p. 55).
- [73]S. Schiller, B. Roth, F. Lewen, O. Ricken, and M. C. Wiedner. “Ultra-narrow-linewidth continuous-wave THz sources based on multiplier chains”. In: *Appl. Phys. B* 95 (2008), pp. 55–61 (cit. on p. 56).
- [74]M. Germann and S. Willitsch. “Line strengths for fine- and hyperfine-resolved electric-quadrupole rotation–vibration transitions in Hund’s case b molecules”. In: *Mol. Phys.* 114 (2016), p. 769 (cit. on p. 57).
- [75]A. Keselman, Y. Glickman, N. Akerman, S. Kotler, and R. Ozeri. “High-fidelity state detection and tomography of a single-ion Zeeman qubit”. In: *New J. Phys.* 13.7 (2011), p. 073027 (cit. on p. 63).
- [76]C. W. Chou, C. Kurz, D. B. Hume, et al. “Preparation and coherent manipulation of pure quantum states of a single molecular ion”. In: *Nature* 545 (2017), p. 203 (cit. on pp. 64, 145, 169).
- [77]B. E. A. Saleh and M. C. Teich. *Fundamentals of photonics, 2 Ed.* Wiley Series in Pure and Applied Optics, 2007 (cit. on pp. 64, 84, 110, 128).
- [78]F. Riehle. *Frequency Standards, Basics and Applications.* WILEY-VCH Verlag GmbH, 2005 (cit. on p. 75).
- [79]D. Bakalov and S. Schiller. “The electric quadrupole moment of molecular hydrogen ions and their potential for a molecular ion clock”. In: *App. Phys. B* 114.1-2 (2014), pp. 213–230 (cit. on p. 76).
- [80]F. L. K. et al. “Enhancement of the quadrupole interaction of an atom with the guided light of an ultrathin optical fiber”. In: *Phys. Rev. A* 97 (2018), p. 013821 (cit. on p. 76).
- [81]W. M. Itano. “External-Field Shifts of the $^{199}\text{Hg}^+$ Optical Frequency Standard”. In: *J. Res. Natl. Inst. Stand. Technol.* 105.6 (2000), pp. 829–837 (cit. on pp. 76, 77).
- [82]S. Meyer. “Frequency Comb Driven Raman Transitions in the THz Range: High Precision Isotope Shift Measurements in Ca^+ ”. PhD thesis. Aarhus University, 2017 (cit. on pp. 78, 119, 180).
- [83]D. Hanneke, R. A. Carollo, and D. A. Lane. “High sensitivity to variation in the proton-to-electron mass ratio in O_2^+ ”. In: *Phys. Rev. A* 94.5 (2016), p. 050101 (cit. on p. 79).

- [84]W. M. I. et al. “Quantum projection noise: Population fluctuations in two-level systems”. In: *Phys. Rev. A* 47.5 (1993), p. 3554 (cit. on p. 79).
- [85]R. Carollo, A. Frenett, and D. Hanneke. “Two-Photon Vibrational Transitions in $^{16}\text{O}_2^+$ as Probes of Variation of the Proton-to-Electron Mass Ratio”. In: *Atoms* 7.1 (2019), p. 1 (cit. on p. 79).
- [86]X. Tong, A. H. Winney, and S. Willitsch. “Sympathetic cooling of molecular ions in selected rotational and vibrational states produced by threshold photoionization”. In: *Phys. Rev. Lett.* 105 (2010), p. 143001 (cit. on pp. 83, 103, 128, 145, 172).
- [87]X. Tong, D. Wild, and S. Willitsch. “Collisional and radiative effects in the state-selective preparation of translationally cold molecular ions in ion traps”. In: *Phys. Rev. A* 83 (2011), p. 023415 (cit. on pp. 83, 88).
- [88]Z. Meir, G. Hegi, K. Najafian, M. Sinhal, and S. Willitsch. “State-selective coherent motional excitation as a new approach for the manipulation, spectroscopy and state-to-state chemistry of single molecular ions”. In: *Faraday Discuss.* 217 (2019), pp. 561–583 (cit. on p. 83).
- [89]J. J. Garcia-Ripol, P. Zoller, and J. I. Cirac. “Speed Optimized Two-Qubit Gates with Laser Coherent Control Techniques for Ion Trap Quantum Computing”. In: *Phys. Rev. Lett.* 91(15) (2003), p. 157901 (cit. on p. 84).
- [90]W. Brownnutt, G. Wilpers, R. C. Thompson, and A. G. Sinclair. “Monolithic microfabricated ion trap chip design for scaleable quantum processors”. In: *New J. Phys.* 8 (2006), p. 232 (cit. on p. 84).
- [91]D. Leibfried, R. Blatt, C. Monroe, and D. J. Wineland. “Quantum dynamics of single trapped ions”. In: *Rev. Mod. Phys.* 75 (2003), p. 281 (cit. on pp. 85, 89, 138, 147).
- [92]D. J. Wineland, C. Monroe, W. M. Itano, et al. “Experimental issues in coherent quantum-state manipulation of trapped atomic ions”. In: *J. Res. Natl. Inst. Stan.* 103 (1998), p. 259 (cit. on pp. 85, 103, 140, 205).
- [93]D. F. V. James. “Quantum dynamics of cold trapped ions with application to quantum computation”. In: *Appl. Phys. B* 66 (1998), p. 181 (cit. on pp. 85, 153).
- [94]A. Drakoudis, M. Söllner, and G. Werth. “Instabilities of ion motion in a linear Paul trap”. In: *Int. J. Mass Spectrom.* 252 (2006), p. 61 (cit. on pp. 85, 131).

- [95]G. Morigi and H. Walther. “Two-species Coulomb chains for quantum information”. In: *Eur. Phys. J. D* 13 (2001), p. 261 (cit. on p. 86).
- [96]D. J. Berkeland, J. D. Miller, J. C. Bergquist, W. M. Itano, and D. J. Wineland. “Minimization of micromotion in a Paul trap”. In: *J. Appl. Phys.* 83 (1998), p. 5025 (cit. on pp. 86–89, 93, 101).
- [97]J. Keller, H. L. Partner, T. Burgermeister, and T. E. Mehlstäubler. “Precise determination of micromotion for trapped-ion optical clocks”. In: *J. Appl. Phys.* 118 (2015), p. 104501 (cit. on p. 86).
- [98]S. Willitsch, M. T. Bell, A. D. Gingell, and T. P. Softley. “Chemical applications of laser- and sympathetically-cooled ions in ion traps”. In: *Phys. Chem. Chem. Phys.* 10 (2008), pp. 7200–7210 (cit. on pp. 88, 89, 103).
- [99]X. Tong, T. Nagy, J. Yosa Reyes, et al. “State-selected ion-molecule reactions with Coulomb-crystallized molecular ions in traps”. In: *Chem. Phys. Lett.* 547 (2012), pp. 1–8 (cit. on pp. 88, 128).
- [100]S. Willitsch. “Coulomb-crystallised molecular ions in traps: methods; applications; prospects”. In: *Int. Rev. Phys. Chem.* 31 (2012), p. 175 (cit. on pp. 88, 136, 145).
- [101]COMSOL *Multiphysics version 3.5a and 4.3a*. www.comsol.com (cit. on pp. 90–92, 94).
- [102]J. P. Home, D. Hanneke, J. D. Jost, D. Leibfried, and D. J. Wineland. “Normal modes of trapped ions in the presence of anharmonic trap potentials”. In: *New J. Phys.* 13 (2011), p. 073026 (cit. on p. 91).
- [103]F. Hall. “Cold ion-neutral reactions”. PhD thesis. University of Basel, 2013 (cit. on p. 91).
- [104]H. G. Dehmelt. “Radiofrequency spectroscopy of stored ions II: Spectroscopy”. In: *Advances in Atomic and Molecular Physics* 5 (1969), pp. 109–154 (cit. on pp. 93, 97, 98).
- [105]M. D. Hughes, B. Lekitsch, J. A. Broersma, and W. K. Hensinger. “Microfabricated ion traps”. In: *Contemp. Phys.* 52 (2011), pp. 505–529 (cit. on p. 95).
- [106]J. D. Siverns, L. R. Simkins, S. Weidt, and W. K. Hensinger. “On the application of radio frequency voltages to ion traps via helical resonators”. In: *Appl. Phys. B* 107 (2012), pp. 921–934 (cit. on pp. 98, 99).

- [107]Z. Meir. “Dynamics of a single, ground-state cooled and trapped ion colliding with ultracold atoms: A micromotion tale.” PhD thesis. Weizmann Institute of Science, 2016 (cit. on p. 101).
- [108]T. Chen, W. Wu, Y. Xie, et al. “Controlling the rf phase error induced micromotion in Paul trap”. In: *Phys. Rev. Lett.* 126 (2020), p. 102 (cit. on p. 101).
- [109]D. M. Lucas, A. Ramos, J. P. Home, et al. “Photoionization for Ca ion trapping”. In: *Phys. Rev. A* 69 (2004), p. 012711 (cit. on p. 103).
- [110]G. Morigi, J. Eschner, J. I. Cirac, and P. Zoller. “Laser cooling of two trapped ions: Sideband cooling beyond the Lamb-Dicke limit”. In: *Phys. Rev. A* 59:5 (1999), p. 3797 (cit. on pp. 103, 137).
- [111]S. Stenholm. “Semiclassical theory of laser cooling”. In: *Rev. Mod. Phys.* 58 (1986), p. 699 (cit. on pp. 103, 205).
- [112]P. O. Schmidt, T. Rosenband, C. Langer, et al. “Spectroscopy Using Quantum Logic”. In: *Science* 309 (2005), p. 749 (cit. on p. 104).
- [113]K. Fisher. “Adiabatic Cooling for Rovibrational Spectroscopy of Molecular Ions”. PhD thesis. Aarhus University, 2017 (cit. on p. 104).
- [114]B. Argence, B. Chanteau, O. Lopez, et al. “Quantum cascade laser frequency stabilization at the sub-Hz level”. In: *Nat. Phot.* 9 (2015), p. 456 (cit. on p. 104).
- [115]M. G. Hansen, E. Magoulakis, Q.-F. Chen, I. Ernsting, and S. Schiller. “Quantum cascade laser-based mid-IR frequency metrology system with ultra-narrow linewidth and 1×10^{-13} -level frequency instability”. In: *Optics Letters* 40(10) (2015), p. 2289 (cit. on p. 104).
- [116]E. D. Black. “An introduction to Pound-Drever-Hall laser frequency stabilization”. In: *American Journal of Physics* 69 (2001), p. 79 (cit. on pp. 106, 112).
- [117]B. Whitlock. “Understanding, finding, & eliminating ground loops”. In: *Handout for Courses A14T and B50T, CEDIA* (2003) (cit. on p. 108).
- [118]G. D. Domenico, S. Schilt, and P. Thomann. “Simple approach to the relation between laser frequency noise and laser line shape”. In: *Applied Optics* 49 (2010), pp. 4801–4807 (cit. on pp. 110, 112, 116).

- [119]N. Bucalovic, V. Dolgovskiy, C. Schori, et al. “Experimental validation of a simple approximation to determine the linewidth of a laser from its frequency noise spectrum”. In: *Applied Optics* 51:20 (2012), pp. 4582–4588 (cit. on p. 112).
- [120]M. Chwalla, J. Benhelm, K. Kim, et al. “Absolute Frequency Measurement of the $^{40}\text{Ca}^+$ $S_{1/2}$ - $D_{5/2}$ Clock Transition”. In: *Phys. Rev. Lett.* 102 (2009), p. 023002 (cit. on p. 113).
- [121]R. et al. “The HITRAN 2008 Molecular Spectroscopic Database.” In: *Journal of Quantitative Spectroscopy and Radiative Transfer* 110(9-10) (2009), pp. 533–572 (cit. on p. 116).
- [122]I. Sergachev. “High Power and Narrow Linewidth optimizations of mid-infrared Quantum Cascade Lasers”. PhD thesis. University of Basel, 2017 (cit. on p. 118).
- [123]M. S. Sorem and A. L. Schawlow. “Saturation spectroscopy in molecular iodine by intermodulated fluorescence”. In: *Optics Comm.* 5:3 (1972), pp. 148–151 (cit. on p. 118).
- [124]R. Han, H. Khooon Ng, and B.-G. Englert. “Raman transitions without adiabatic elimination: a simple and accurate treatment”. In: *Journal of Modern Optics* 60:4 (2013), pp. 255–265 (cit. on p. 118).
- [125]C. Monroe, D. M. Meekhof, B. E. King, et al. “Resolved-sideband Raman cooling of a bound atom to the 3D zero-point energy”. In: *Phys. Rev. Lett.* 75 (1995), p. 4011 (cit. on p. 118).
- [126]M. Drewsen, A. Mortensen, R. Martinussen, P. Staunum, and J. L. Sørensen. “Nondestructive identification of cold and extremely localized single molecular ions”. In: *Phys. Rev. Lett.* 93 (2004), p. 243201 (cit. on p. 128).
- [127]M. Guggemos, D. Heinrich, O. A. Herrera-Sancho, R. Blatt, and C. F. Roos. “Sympathetic cooling and detection of a hot trapped ion by a cold one”. In: *New J. Phys.* 17 (2015), p. 103001 (cit. on p. 129).
- [128]J. Mikosch, F. U., S. Trippel, et al. “Evaporation of trapped anions studied with a 22-pole ion trap in tandem time-of-flight configuration”. In: *Phys. Rev. A* 78 (2008), p. 023402 (cit. on p. 131).
- [129]A. M. Hankin, E. R. Clements, Y. Huang, et al. “Systematic uncertainty due to background-gas collisions in trapped-ion optical clocks”. In: *Phys. Rev. A* 100 (2019), p. 033419 (cit. on p. 133).

- [130]Y. Wan, F. Gebert, F. Wolf, and P. O. Schmidt. “Efficient sympathetic motional-ground-state cooling of a molecular ion”. In: *Phys. Rev. A* 91 (2015), p. 043245 (cit. on p. 137).
- [131]A. M. Kaufmann, B. J. Lester, and C. A. Regal. “Cooling a Single Atom in an Optical Tweezer to Its Quantum Ground State”. In: *Phys. Rev. X* 2 (2012), p. 041014 (cit. on p. 139).
- [132]D. Hume, C. W. Chou, D. R. Leibbrandt, et al. “Trapped-Ion State Detection through Coherent Motion”. In: *Phys. Rev. Lett.* 107 (2011), p. 243902 (cit. on p. 140).
- [133]I. A. Boldin, A. Kraft, and C. Wunderlich. “Measuring Anomalous Heating in a Planar Ion Trap with Variable Ion-Surface Separation”. In: *Phys. Rev. Lett.* 120 (2018), p. 023201 (cit. on p. 140).
- [134]M. Brownnutt, M. Kumph, P. Rabl, and R. Blatt. “Ion-trap measurements of electric-field noise near surfaces”. In: *Rev. Mod. Phys.* 87 (2015), p. 1419 (cit. on p. 140).
- [135]J. Benhelm, G. Kirchmair, C. F. Roos, and R. Blatt. “Experimental quantum-information processing with $^{43}\text{Ca}^+$ ions”. In: *Phys. Rev. A* 77 (2008), p. 062306 (cit. on p. 140).
- [136]G. Poulsen, Y. Miroshnychenko, and M. Drewsen. “Efficient ground-state cooling of an ion in a large room-temperature linear Paul trap with a sub-Hertz heating rate”. In: *Phys. Rev. A* 86 (2012), p. 051402 (cit. on p. 140).
- [137]M. A. Duncan. “Infrared spectroscopy to probe structure and dynamics in metal ion-molecule complexes”. In: *Int. Rev. Phys. Chem.* 22 (2003), p. 407 (cit. on p. 145).
- [138]T. R. Rizzo, J. A. Stearns, and O. V. Boyarkin. “Spectroscopic studies of cold, gas-phase biomolecular ions”. In: *Int. Rev. Phys. Chem.* 28 (2009), p. 481 (cit. on p. 145).
- [139]E. K. Campbell, M. Holz, D. Gerlich, and J. P. Maier. “Laboratory confirmation of C_{60}^+ as the carrier of two diffuse interstellar bands”. In: *Nature* 523 (2015), p. 322 (cit. on p. 145).
- [140]S. Schlemmer, T. Kuhn, E. Lescop, and D. Gerlich. “Laser excited N_2^+ in a 22-pole ion trap: experimental studies of rotational relaxation processes”. In: *Int. J. Mass Spectrom.* 185/186/187 (1999), p. 589 (cit. on p. 145).

- [141]O. Asvany, K. M. T. Yamada, S. Brünken, A. Potapov, and S. Schlemmer. “Experimental ground-state combination differences of CH_5^+ ”. In: *Science* 347 (2015), p. 1346 (cit. on p. 145).
- [142]D. B. Hume, T. Rosenband, and D. J. Wineland. “High-fidelity adaptive qubit detection through repetitive quantum nondemolition measurements”. In: *Phys. Rev. Lett.* 12 (2007), p. 120502 (cit. on p. 145).
- [143]S. Willitsch. “Experimental Methods in Cation Spectroscopy”. In: *Handbook of High-Resolution Spectroscopy*. Ed. by M. Quack and F. Merkt. Vol. 3. John Wiley & Sons, 2011, p. 1691 (cit. on p. 145).
- [144]F. Wolf, Y. Wan, J. C. Heip, et al. “Non-destructive state detection for quantum logic spectroscopy of molecular ions”. In: *Nature* 530 (2016), p. 457 (cit. on pp. 145, 169).
- [145]M. Sinhal, Z. Meir, K. Najafian, G. Hegi, and S. Willitsch. “Quantum-nondemolition state detection and spectroscopy of single trapped molecules”. In: *Science* 367.6483 (2020), pp. 1213–1218 (cit. on pp. 145, 172).
- [146]D. M. Meekhof, C. Monroe, B. E. King, W. M. Itano, and D. J. Wineland. “Generation of nonclassical motional states of a trapped atom”. In: *Phys. Rev. Lett.* 76 (1996), p. 1796 (cit. on p. 147).
- [147]S. R. Langhoff, C. W. Bauschlicher Jr, and H. Partridge. “Theoretical study of the N_2^+ Meinel system”. In: *J. Chem. Phys.* 87.8 (1987), pp. 4716–4721 (cit. on p. 151).
- [148]M. J. Frisch, G. W. Trucks, H. B. Schlegel, et al. *Gaussian 09 Revision D.01*. Gaussian Inc., Wallingford CT, 2009 (cit. on p. 152).
- [149]M. S. Safronova and U. I. Safronova. “Blackbody radiation shift, multipole polarizabilities, oscillator strengths, lifetimes, hyperfine constants, and excitation energies in Ca^+ ”. In: *Phys. Rev. A* 83.1 (2011), p. 012503 (cit. on p. 154).
- [150]C. T. Schmiegelow, H. Kaufmann, T. Ruster, et al. “Phase-Stable Free-Space Optical Lattices for Trapped Ions”. In: *Phys. Rev. Lett.* 116 (2016), p. 033002 (cit. on p. 157).
- [151]C. Runge. “Ueber die numerische Auflösung von Differentialgleichungen”. In: *Mathematische Annalen* 46 (1895), pp. 167–178 (cit. on p. 158).
- [152]I. S. Vogelius, L. B. Madsen, and M. Drewsen. “Internal cooling of molecular Coulomb crystals by coupling to collective modes”. In: *J. Phys. B: At. Mol. Opt. Phys.* 39 (2006), S1267 (cit. on p. 169).

- [153]D. Patterson. “Method for preparation and readout of polyatomic molecules in single quantum states”. In: *Phys. Rev. A* 97 (2018), p. 033403 (cit. on p. 175).
- [154]Y. Lin, J. P. Gaebler, T. R. Tan, et al. “Sympathetic Electromagnetically-Induced-Transparency Laser Cooling of Motional Modes in an Ion Chain”. In: *Phys. Rev. Lett.* 110 (2013), p. 153002 (cit. on p. 180).
- [155]R. J. M. Bennett. “Hönl–London factors for doublet transitions in diatomic molecules”. In: *Monthly Notices of the Royal Astronomical Society* 147.1 (1970), pp. 35–46 (cit. on p. 200).
- [156]G. Poulsen. “Sideband cooling of atomic and molecular ions”. PhD thesis. Aarhus University, 2011 (cit. on p. 205).

Acknowledgements

The research presented in this thesis is the collaborative effort of many people and the result of fruitful discussions with many more. The thesis would also be impossible if not for the wonderful people around me. Therefore, many thanks are in order:

To **Prof. Dr. Stefan Willitsch** whom I had the great fortune of having as a supervisor. With his patience and his priority always being the learning and development of his students, he has allowed me to grow and explore independently while always being prepared to guide me where needed. You are a role model for how to supervise and teach.

To my collaborators on the QuTe experiment: **Dr. Ziv Meir** whose effort and quality of work has enhanced my own work from the day he joined us. I foresee a continued bright path for you. To **Mudit Sinhal**, **Gregor Hegi** and **Matthias Germann**, thank you for your great work and for making the lab an enjoyable atmosphere. To **Prof. Dr. Michael Drewsen** who welcomed me to his lab for three months. My research was jump-started by the time spent in Aarhus. Thank you for the great experience and the exciting discussions.

To my other colleagues (and now friends) with whom I had the pleasure of working, thank you: **Pascal** for the dancing, **Alex** who would not hesitate to back me up in a fight, **Ardi** for deep conversations, **Uxxi** for fighting, **Patrik** for the energy, **Tomi** for keeping it real, **Arezo** for the kindness, **Moritz** for allowing me to stand on his shoulders, **Alex II** for the Rhine sessions, **Corey** for existing, **Georg** for teaching me, **Ian**, **Ludger**, **Panos**, **Dong**, **Anatoly**, **Grischa**, **Steffen**, **Karin**, **Claudio**, **Christian**, **Dominik** and **Ilia** for the good company.

To my friends who give me the energy: **Princess Kax** 50 points to Hufflepuff, **Zarek** (i will end you) **Silberschmidt** and his anti-infinity theory, **Telma** for being uncompromisingly Telma, **The Clara gang**, **the Greek crew**, **the Italians**, **the Kurdish mafia** and the **Elsi**.

To my extra siblings **Babak**, **Anoush**, **Mina** and **Bahman**. To every **khale**, **amoo**, **amme** and **dayi** I was blessed with. To **my cousins**, near and far.

To **my mother and father** from whom I have learned everything of value. And to **my sister**, an unwavering source of light.

Thank you.

Curriculum Vitae: Kaveh Najafian

Phone No. +41 766 271358, **Email:** kaveh.najafian@unibas.ch

Personal:

Date of birth: March 8, 1987

Nationality: Swedish

Languages: Swedish, English, Persian (advanced)
German (intermediate)

Technical experience:

Lasers and optics, RF-electronics, Vacuum technology, MATLAB,
Wolfram Mathematica, COMSOL, LabVIEW, Python, Arduino

Teaching experience:

Teaching assistant for laboratory courses in Physical Chemistry at the University of Basel. (10 semesters, 20% of full-time employment)
Supervision of Bachelor and Masters students for longer projects of 1-3 months

Education:

Doctoral studies: Physical Chemistry

University of Basel, Switzerland **2014-2020**

Thesis: *“Quantum manipulation of a single trapped molecular ion”*

Master of Science: Physics and Astronomy

Chalmers University of Technology, Sweden **2012-2014**

Thesis: *“Experimental studies of isotope effects in small water clusters”*

Bachelor of Science: Physics

University of Gothenburg, Sweden **2010-2012**

Thesis: *“Can the boundary of a boundary be nontrivial in AdS/CFT?”*

Publications (first author):

From megahertz to terahertz qubits encoded in molecular ions: theoretical analysis of dipole-forbidden spectroscopic transitions in N_2^+

K. Najafian et al., **Phys. Chem. Chem. Phys.** **22**, 23083 (2020)

Identification of molecular quantum states using phase-sensitive forces

K. Najafian et al., **Nat. Comm.** **11**, 4470 (2020)

State-selective coherent motional excitation as a new approach for the manipulation, spectroscopy and state-to-state chemistry of single molecular ions

Z. Meir et al., **Faraday Discuss.** **217**, 561-583 (2019)

Radiative cooling of C_7^-

K. Najafian et al., **J. Chem. Phys.** **140**, 104311 (2014)

Publications (other):

Quantum-nondemolition state detection and spectroscopy of single trapped molecules

M. Sinhal et al., **Science** **367**, 1213-1218 (2020)

Cooling dynamics of carbon cluster anions

H. Shiromaru et al., **J. Phys.: Conf. Ser.** **635**, 012035 (2015)

Inverse internal conversion in C_4^- below the electron detachment threshold

N. Kono et al., **Phys. Chem. Chem. Phys.** **17**, 24732 (2015)